Fakultät für Physik

de Haas-van Alphen effect and magnetic anisotropy in correlated electron systems studied by cantilever magnetometry

Schorsch Michael Sauther

Vollständiger Abdruck der von der Fakultät für Physik der Technischen Universität München zur Erlangung des akademischen Grades eines

Doktors der Naturwissenschaften

genehmigten Dissertation.

Vorsitzender: Prof. Dr. Ulrich Gerland

Prüfer der Dissertation:

1. Prof. Dr. Christian Pfleiderer
2. apl. Prof. Dr. Rudolf Hackl

Die Dissertation wurde am 05.07.2021 bei der Technischen Universität München eingereicht und durch die Fakultät für Physik am 06.12.2021 angenommen.

Abstract

Intriguing electronic and magnetic phenomena arise in solids hosting correlated electron systems, making such materials interesting to both fundamental research and for novel technological applications. A comprehensive understanding of their characteristics is key to the development of reliable methods for controlling and tailoring electronic correlations to the needs of devices. In this thesis, we employ cantilever magnetometry to study the properties of two intermetallic compounds hosting electronic correlations. In the following, we outline the main results.
We investigate the de Haas-van Alphen (dHvA) effect in single-crystal chromium diboride (CrB_2) at temperatures down to 60 mK and magnetic fields up to 35 T. Studies of the angular and temperature evolution allow us to determine eleven distinct dHvA components and eight effective masses. A variety of vague further frequencies is observed. Electronic structure calculations yield a Fermi surface comprising five sheets resulting in an abundance of possible dHvA components. The comparison of experiment and theory leads to ambivalent conclusions, indicating the need for an extension of the theoretical picture.
We further study the magnetic anisotropy of bulk manganese silicide (MnSi). The excellent agreement of torque data with an analytical description of magnetocrystalline anisotropies allows us to report the first comprehensive set of anisotropy constants in the field-polarized state of MnSi. Both leading and next-to-leading order anisotropy constants exhibit non-monotonic dependences on temperature and field magnitude which reflects subtle changes of the multi-sheet Fermi surface. Measurements in the modulated phases reveal two competing mechanisms contributing to the anisotropy of non-collinear magnetic order. We further observe large hysteresis, hinting at the presence of (meta-)stable topological defects.

Inhaltsangabe

Faszinierende elektronische und magnetische Phänomene, die in Festkörpern mit korrelierten Elektronensystemen auftreten, machen solche Materialien interessant sowohl für die Grundlagenforschung als auch für neuartige technologische Anwendungen. Ein umfassendes Verständnis ihrer Charakteristika ist entscheidend für die Entwicklung verlässlicher Methoden zu Kontrolle und Maßschneidern elektronischer Korrelationen für die Bedürfnisse von Apparaturen. In dieser Arbeit nutzen wir Biegebalkenmagnetometrie, um die Eigenschaften zweier intermetallischer Verbindungen mit elektronischen Korrelationen zu studieren. Im Folgenden umreißen wir die Hauptergebnisse.

Wir untersuchen den de Haas-van Alphen-Effekt (dHvA-Effekt) in einkristallinem Chromdiborid bei Temperaturen bis hinunter zu 60 mK und magnetischen Feldern bis zu 35 T. Untersuchungen der Winkel- und Temperaturentwicklung erlauben uns die Bestimmung von elf deutlichen dHvA-Komponenten und acht effektiven Massen. Eine Vielzahl undeutlicher weiterer Frequenzen ist zu beobachten. Berechnungen der elektronischen Struktur ergeben eine Fermifläche, die fünf Schichten umschließt und somit eine Fülle an möglichen dHvA-Komponenten zur Folge hat. Der Vergleich von Experiment und Theorie führt zu ambivalenten Rückschlüssen, was auf die Notwendigkeit hindeutet, die theoretische Darstellung zu erweitern.

Weiterhin untersuchen wir die magnetische Anisotropie von Mangansilizium (MnSi). Die exzellente Übereinstimmung der Drehmomentdaten mit einer analytischen Beschreibung der magnetokristallinen Anisotropien ermöglicht es uns, die erste umfassende Bestimmung von Anisotropiekonstanten im feldpolarisierten Zustand von MnSi zu vermelden. Sowohl die führende wie auch die an zweiter Stelle stehende Anisotropiekonstante zeigen nicht-monotone Abhängigkeiten von Temperatur und magnetischer Feldstärke, was geringfügige Veränderungen der vielschichtigen Fermifläche widerspiegelt. Messungen in den modulierten Phasen zeigen, dass zwei konkurrierende Mechanismen zur Anisotropie von nicht-kollinearer magnetischer Ordnung beitragen. Wir beobachten darüberhinaus große Hysteresen, was die Existenz (meta-)stabiler topologischer Defekte andeutet.

Contents

1 Introduction **3**

2 Theoretical concepts **7**
2.1 Magnetic anisotropy 7
2.1.1 General concept 7
2.1.2 Magnetic anisotropy in cubic chiral helimagnets 8
2.2 The de Haas-van Alphen effect 12
2.2.1 Landau quantization of free electrons 13
2.2.2 Quantum oscillations 15
2.2.3 Transforms between time and frequency domain 17
2.3 Density functional theory 19
2.3.1 Hohenberg-Kohn theorems and Kohn-Sham equations 20
2.3.2 Approximation of V_{XC} and self-consistent solution of the Kohn-Sham equations 21

3 Experimental setups **23**
3.1 Measurement method 23
3.1.1 Longitudinal cantilever magnetometer 24
3.1.2 Torsional cantilever magnetometer 30
3.2 Setups for dHvA measurements 34
3.2.1 Superconducting magnet setups 35
3.2.2 High magnetic field laboratory setup 35
3.3 Setup for anisotropy measurements 36
3.3.1 Rotating field setup 36
3.3.2 Rotating sample setup 40
3.3.3 Orientations 41

4 dHvA effect in single crystal CrB2 **51**
4.1 Introduction to CrB_2 51
4.1.1 Magnetic structure 52
4.1.2 Previous state of work and outline 53
4.2 Experimental conditions and data evaluation 54
4.2.1 Experimental conditions at HFML 54
4.2.2 Data evaluation 55
4.3 Experimental results 62

4.3.1 Angular dependence . . . 64
4.3.2 Temperature dependence . . . 66
4.4 Electronic structure calculations . . . 68
4.4.1 Theoretical methods . . . 68
4.4.2 Magnetic state . . . 69
4.4.3 Fermi surface . . . 73
4.4.4 Implications for the dHvA effect . . . 75
4.5 Comparison of experiment and theory . . . 78
4.5.1 Discussion . . . 84
4.6 Conclusion . . . 88

5 Magnetic anisotropy of MnSi **91**
5.1 Introduction to MnSi . . . 91
5.2 Experimental conditions and data evaluation . . . 94
5.2.1 Rotating sample setup . . . 96
5.2.2 Rotating field setup . . . 99
5.3 Measurements in the field-polarized phase . . . 101
5.3.1 Rotating sample setup . . . 101
5.3.2 Rotating field setup . . . 106
5.3.3 Numerical simulations . . . 109
5.3.4 Discussion . . . 113
5.4 Measurements in modulated phases . . . 121
5.4.1 Field rotations . . . 121
5.4.2 Field scans . . . 123
5.4.3 Discussion . . . 127
5.5 Conclusion . . . 133

6 Summary and outlook **137**
6.1 CrB_2 . . . 137
6.2 MnSi . . . 138

A Magnets, cantilevers and alignment **141**
A.1 Calculation of cantilever bending lines and reduction factors . . . 141
A.2 Beam widths of CuBe cantilevers prepared by wet chemical etching . . . 143
A.3 Generic calibration of cantilevers at HFML . . . 144
A.4 Hall probe measurements within the AMI vector magnet . . . 145
A.4.1 Rotations . . . 145
A.4.2 Field sweeps . . . 149
A.5 X-ray images of a spherical MnSi sample in the Laue camera . . . 151

B DFT calculations on CrB_2 **153**
B.1 Electronic structure of non-magnetic CrB_2 . . . 153
B.2 Alternative representation of the CrB_2 Fermi surface . . . 156
B.3 Extremal orbits on the CrB_2 Fermi surface . . . 158
B.4 Resolution limit of the DFT calculation . . . 161

C Torque in the field-polarized phase of MnSi **163**
C.1 General . . . 163
C.1.1 Benefit of including the K_2-term in the fit function . . . 163
C.2 Rotating sample setup . . . 164
C.2.1 Scaling of high-temperature data from the spherical sample . . 164
C.2.2 Node-correction of data from the cubic sample . . . 166
C.2.3 Measurement errors in the temperature dependence of K_1 and K_2 . . . 168
C.2.4 Torque data from the cubic sample . . . 169
C.2.5 Phenomenological fit to the temperature evolution of K_1 . . . 169
C.3 Rotating field setup . . . 170
C.3.1 Measurements on a cubic sample . . . 171
C.3.2 Spurious features in the capacitive readout induced by magnetic flux jumps . . . 172
C.3.3 Rotational hysteresis . . . 173
C.3.4 Magnetic field dependence of torque and anisotropy constants 174
C.3.5 Additional temperature dependent torque data and anisotropy constants . . . 175
C.3.6 Fit parameters g_i and Γ_{off} . . . 177
C.3.7 Magnitude of field gradients in the AMI vector magnet . . . 178
C.3.8 Measurements at different misalignment γ_{r} . . . 179

D Anisotropic magnetization in the modulated states of MnSi **183**
D.1 Field rotations . . . 183
D.1.1 Full rotation measurement data . . . 183
D.1.2 Temperature evolution at 0.1 T . . . 184
D.1.3 Field dependence at 28.5 K . . . 186
D.2 Field scans . . . 188
D.2.1 Full field scan data . . . 188
D.2.2 Deviation from high symmetry directions . . . 189
D.2.3 Hysteresis above H_{c2} . . . 193
D.2.4 Field scans through the skyrmion lattice phase . . . 195
D.2.5 Temperature evolution for field along $\langle 001 \rangle$ and $\langle 110 \rangle$ . . . 196

Bibliography **201**

Acknowledgments **213**

Scientific collaborations

The work presented in this thesis has been carried out in two independent research groups at the Physics Department of the Technical University of Munich. Since the official affiliation of the author states the chair for the topology of correlated systems for the purpose of this thesis, contributions on the part of the chair of physics of functional multilayers are gratefully acknowledged. In particular, the author wants to mention:

- initial employment and introduction to the academic world
- provision of an office, laboratory space and equipment for getting the thesis started
- the possibility of using the group's clean room for sensor preparation
- good teamwork with administrative, research and technical staff

Parts of the present thesis benefited from further collaborations. The author would like to thankfully acknowledge contributions by the respective people and institutions:

- Dr. Olga Young and Prof. Dr. Uli Zeitler in the High Field Magnet Laboratory at the Radboud University in Nijmegen who made it possible for us to conduct measurements in their 35 T Bitter magnet,
- Prof. Dr. Markus Garst of the Technical University of Dresden and the Karlsruhe Institute of Technology who was a great help with understanding magnetic anisotropy of helimagnets and with the implementation of numerical simulations.

1 Introduction

Modern everyday life is influenced to an overwhelming extent by the omnipresence of microelectronic devices. Since the invention of the first germanium transistor in 1948 [Bar48], the field of semiconductors has permanently grown both as an active research area and, more importantly, in the form of technological applications. The expansion as a research field was crucially facilitated by development of new growth techniques such as, e.g., molecular beam epitaxy [Cho75] or the discovery of novel effects as, e.g., the quantum Hall effect [Kli80]. The technological progress was driven by a continuous spread to more and more areas of application. Early implementations in radios and computers were soon followed by applications in cars and phones. Nowadays, even mundane devices such as refrigerators or washing machines are controlled by microelectronic units. This technological spread benefited from drastic improvements regarding the abilities to manipulate materials' properties and to tailor physical characteristics of different materials into one device.
Technological progress further allowed for constant miniaturization of components. According to the famous law of Moore [Moo65], the number of transistors on integrated circuits doubles every two years. While this prediction has proven true for more than 50 years, we are rapidly approaching an end of the miniaturization era. With current transistor sizes ranging down below 10 nm [Hui17], manufacturers face both technological limits as the resolution of lithography methods as well as physical limits imposed, e.g., by the onset of tunneling processes [Key01].
The semiconductor industry has declared the necessity to explore alternatives regarding both materials and computing architectures more than a decade ago [Ard06]. One possible direction for such investigations is the exploitation of new degrees of freedom. Conventional semiconductor devices rely exclusively on the electric charge of electrons or holes. Novel applications may feature functionalities based on electrons' spin or orbital angular moment. Concepts for both logic as well as memory devices making use of these properties have been proposed [Dat90, Par08], but so far they have not been able to prove commercially viable.
For the successful implementation of novel computational concepts, a new material basis may be indispensable. In this context, materials exhibiting electronic correlations are promising. The term "correlation" describes substantial interactions between electrons, i.e. the single-particle picture commonly used for silicon and similar materials cannot account for the behavior of the electron system. Instead, a description of the material's properties is only possible when the mutual influence of electrons on each other is considered. Strong electronic correlations can lead to drastic changes of the macroscopic properties of the material. For instance, these interactions may induce superconductivity or stabilize novel ground states of complex

magnetic order. Thus it appears natural to look for novel functionality arising from such correlation phenomena.
A detailed understanding of the phenomenology is a prerequisite for the sustainable implementation of device applications. The majority of materials known to host correlated electron systems are compounds of complex composition, often involving transition metals, rare earths or oxygen, which impedes straightforward comprehension. The key to conceiving the macroscopic properties of such a material is a profound knowledge of its electronic structure. In particular, many properties are defined predominantly by the electronic states close to the Fermi energy. The Fermi surface, i.e. the electronic states located at the Fermi energy may be probed in several ways. A powerful tool is the de Haas-van Alphen (dHvA) effect, i.e. quantum oscillations of the magnetization. For temperature and field regime not accessible by the dHvA effect, information on the electronic structure may be obtained, e.g., from measurements of the magnetocrystalline anisotropy (MCA). In this thesis, we employ torque magnetometry to investigate both dHvA effect and MCAs on two intermetallic compounds exhibiting electronic correlations. More precisely, we study the dHvA effect in the antiferromagnetic chromium diboride (CrB_2) and MCAs in the helimagnet manganese silicide (MnSi).
Transition metal diborides comprise a surprising variety of ground states in the same crystallographic structure. In particular, the highest transition temperature for phonon-mediated superconductivity to date has been found in MgB_2 [Nag01]. In this material, a detailed investigation of the electronic properties revealed the origins of the two-band superconductivity with a high T_c in the electronic structure [Xi08]. In contrast, CrB_2 exhibits an antiferromagnetic ground state and does not show a superconducting transition at ambient pressure despite its close similarity to MgB_2. We aim to extend earlier investigations of the electronic structure in CrB_2 [Bra13b] in order to shed light on the origin of this strongly different behavior.
The phase diagram of MnSi exhibits several states of different magnetic order at low temperatures and fields. In particular, MnSi is the first material in which the formation of magnetic vortices known as skyrmions could be observed. The emergent electrodynamics arising due to this phenomenon [Sch12] makes helimagnets highly interesting regarding the search for novel functionalities and applications. Still, the MCAs in MnSi have not been measured directly despite their crucial importance for a variety of phenomena being studied intensely. We aim to fill this gap with the experiments presented in this work.
The thesis is organized as follows: In Ch. 2, we provide the theoretical fundamentals relevant for our experiments. We address magnetic anisotropy considering collinear and non-collinear magnetic order. Further, we introduce the dHvA effect for bulk materials and the concept of electronic structure calculations based on density functional theory. Chapter 3 is dedicated to the experimental setups used in this work. We particularly address experimental shortcomings such as inhomogeneous magnetic fields and misalignment. In Ch. 4, we present measurements of magnetic quantum oscillations in CrB_2 at various angles and temperatures in combination with electronic structure calculations and discuss the results in terms of the Fermi surface. We report

investigations of magnetic anisotropy in MnSi in Chapter 5. We explore the field and temperature dependence of anisotropy constants inferred from measurements in the field-polarized state and pronounced hysteretic behavior observed during experiments in the modulated phases indicating the presence of long-lived topological defects. Finally, we conclude with a summary and a brief outlook in Ch. 6.

2 Theoretical concepts

In this chapter, we introduce the theoretical fundamentals relevant to our experimental work. We address the concept of magnetic anisotropy in Sec. 2.1. In particular, we consider collinear as well as non-collinear magnetic order in cubic chiral helimagnets. After that, we review the Landau diamagnetism of an electron gas in Sec. 2.2. Quantization in high magnetic fields leads to the de Haas-van Alphen effect. We consider finite temperature and disorder in terms of the Lifshitz-Kosevich formalism. Finally, we briefly discuss the concept of density functional theory in 2.3.

2.1 Magnetic anisotropy

This section is dedicated to the phenomenon of magnetic anisotropy. We introduce the general concept in Sec. 2.1.1. Extensive descriptions of microscopic origin, phenomenology and common models of magnetic anisotropy can be found in literature, see e.g. Refs. [Kan63, Chi64, Bru93, Sko08]. Here, we restrict ourselves to basic definitions and remarks. Following that, we address the specific case of cubic chiral helimagnets in Sec. 2.1.2 including a consideration of non-collinear magnetic order.

2.1.1 General concept

The term magnetic anisotropy refers to the fact that the total energy of a magnetic material depends on the direction of its magnetization $\mathbf{M}$. As a consequence, a spontaneous magnetization will align along preferential directions in the absence of magnetic fields. Such directions representing local minima of the magnetic anisotropy energy (MAE) are commonly referred to as easy axes. Conversely, directions corresponding to local maxima of the MAE are denoted as hard axes. It is commonly distinguished between intrinsic and extrinsic contributions to the MAE. An intrinsic source of magnetic anisotropy can be provided, e.g., by the symmetry of the host crystal. Such contributions are mediated by spin-orbit coupling and commonly referred to as magnetocrystalline anisotropy (MCA). As an example of extrinsic origin, stress exerted on the material can lead to magnetoelastic anisotropy. Another standard example for the origin of magnetic anisotropy is the so-called shape anisotropy. For anisotropic geometries, i.e. for any sample shape different from a sphere, dipolar interactions also induce a contribution to the MAE. The minimization of this energy contribution is primarily responsible for the formation of magnetic domains.
The phenomenology of magnetic anisotropy is most commonly introduced by means of its simplest form, i.e. an uniaxial anisotropy with a leading term of second order in

spin-orbit coupling. Within this thesis, we investigate the magnetic anisotropy of the cubic chiral helimagnet manganese silicide (MnSi). Since second-order contributions vanish for cubic systems, we omit the standard introduction and immediately move on to the discussion of MCAs in cubic chiral helimagnets.

2.1.2 Magnetic anisotropy in cubic chiral helimagnets

A number of cubic chiral helimagnets with different crystallographic structures share the space group $P2_13$. While the crystal structures exhibit simple cubic Bravais lattices, the atomic basis is arranged such that the crystals lack inversion symmetry and possess the tetrahedral point group T. The magnetic properties of cubic chiral helimagnets are commonly described by means of an effective Ginzburg-Landau functional for the free energy including ferromagnetic (FM) exchange, Dzyaloshinskii-Moriya interaction (DMI), dipolar interaction and terms of higher order in spin orbit coupling representing magnetocrystalline anisotropies [Gar16]. FM exchange and DMI are invariant regarding rotations of $\mathbf{M}$ with respect to the crystal axes [Eve12]. Anisotropic contributions from dipolar interactions vanish for cubic systems [Joh96] and can thus be deemed negligible in cubic helimagnets. Thus, the intrinsic anisotropy of a uniform magnetization is determined by the higher-order MCAs. The corresponding Landau potential consistent with the tetrahedral point group T reads

$$\mathcal{V}_T = K_1\left(\hat{M}_x^4 + \hat{M}_y^4 + \hat{M}_z^4\right) + K_2\left(\hat{M}_x^2\hat{M}_y^4 + \hat{M}_y^2\hat{M}_z^4 + \hat{M}_z^2\hat{M}_x^4\right) + ... \tag{2.1}$$

with the magnetization unit vector $\hat{M}$. The leading-order term is fourth order in spin-orbit coupling. For $K_1 > 0$, the easy and hard axes are $\langle 111\rangle$- and $\langle 001\rangle$-directions, respectively, for $K_1 < 0$ the situation is reversed. We note that a second fourth-order term, $\hat{M}_x^2\hat{M}_y^2 + \hat{M}_y^2\hat{M}_z^2 + \hat{M}_z^2\hat{M}_x^2$, is equivalent to the K_1-term up to a constant. Further, the K_1-term preserves a fourfold rotation symmetry C_4 that is not contained in T. The same holds true for two next-to-leading-order terms $\hat{M}_x^2\hat{M}_y^2\hat{M}_z^2$ and $\hat{M}_x^6 + \hat{M}_y^6 + \hat{M}_z^6$ which are therefore neglected in the following. In contrast, the next-to-leading-order K_2-term breaks the C_4 symmetry. This term is sixth order in spin-orbit coupling and reflects the chirality of the host crystal. In the shape displayed in Eq. 2.1, it represents a right-handed enantiomer. For a left-handed crystal, the term reads $\hat{M}_y^2\hat{M}_x^4 + \hat{M}_x^2\hat{M}_z^4 + \hat{M}_z^2\hat{M}_y^4$. Terms of eighth and higher order in spin-orbit coupling are neglected as indicated by the dots in Eq. 2.1.
The energies associated with the magnetic anisotropy described by Eq. 2.1 are illustrated in Fig. 2.1. Here, the energy for a given orientation of the magnetization is depicted as distance to the origin. All faces are shown in the same crystallographic orientation as depicted in panel k). Red and blue shadings highlight large and low energies, respectively. All finite anisotropy constants exhibit the same arbitrary absolute value. Note that energy faces in different panels are not scaled equally. From top to bottom, rows correspond to positive, zero and negative values of K_2. From left to right, the first three columns correspond to positive, zero and negative values of K_1. In panels a) - i), a right-handed crystals is described. For comparison,

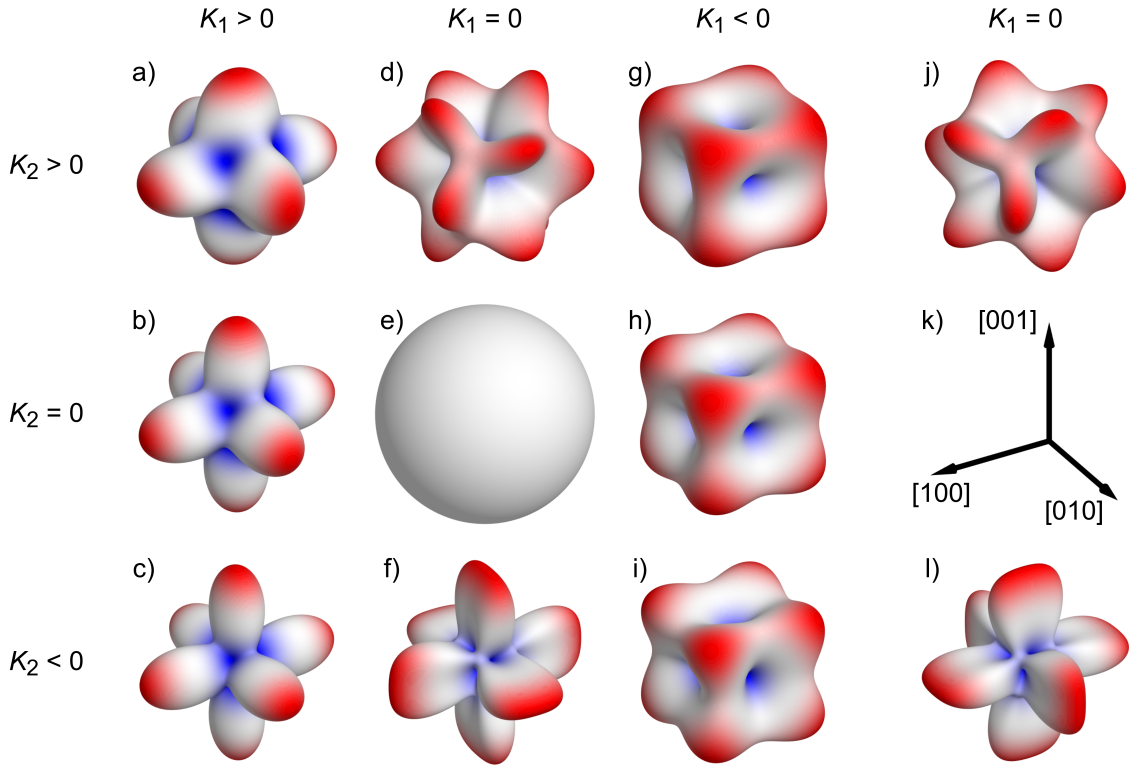

Figure 2.1: Illustration of magnetic anisotropy energy according to Eq. 2.1. Energies in different panels are not to scale. All finite anisotropy constants exhibit the same arbitrary absolute value. Red and blue shading correspond to large and low energies, respectively. a) - i) From left to right, columns correspond to $K_1 > 0$, $K_1 = 0$ and $K_1 < 0$. From top to bottom, rows correspond to $K_2 > 0$, $K_2 = 0$ and $K_2 < 0$. k) shows the crystallographic directions. j) and l) show the same situation as d) and f) but for a left-handed instead of a right-handed crystal.

the energy faces displayed in panels d) and f) are depicted for a left-handed crystal in panels j) and l).
For $K_1 = K_2 = 0$ in panel e), the crystal is completely isotropic which is represented by a sphere. From the energy faces for finite K_1 in panels a) - c) and g) - i), we can infer that $\mathcal{V}_T$ is dominated by K_1 for comparable values of K_1 and K_2. As stated above, positive values of K_1 result in easy axes along $\langle 111 \rangle$-directions and hard axes along $\langle 001 \rangle$-directions. This situation is found, e.g., in MnSi [Ish76]. Conversely, a negative K_1 leads to easy axes along $\langle 001 \rangle$-directions and hard axes along $\langle 111 \rangle$-directions as has been reported, e.g., for the insulating helimagnet Cu_2OSeO_3 [Ada12]. Sign changes of K_1 may occur during changes of environmental conditions. For instance, K_1 changes from positive to negative values with increasing temperature in FeGe [Leb89].
In panels d) and f) where the energy is determined by the K_2-term, we distinctly recognize the absence of a fourfold rotation symmetry C_4 as described above. While this symmetry reduction is barely visible on the displayed energy faces for finite

values of K_1, it is still reflected in the behavior of helimagnets as, e.g., at the helical-to-conical phase transition in MnSi [Bau17]. The energy associated with $K_2 > 0$ ($K_2 < 0$) exhibits minima (maxima) corresponding to easy (hard) axes along $\langle 001 \rangle$-directions. More interestingly, the maxima (minima) for $K_2 > 0$ ($K_2 < 0$) are found for cyclic permutations of $[\pm\sqrt{2}, 1, 0]$ for the right-handed crystal in panels d) and f). For the left-handed enantiomer depicted in panels j) and l), we find identical energy landscapes except for a reversed chirality with minima (maxima) along $\langle 001 \rangle$-directions and maxima (minima) along cyclic permutations of $[\pm 1, \sqrt{2}, 0]$ for $K_2 > 0$ ($K_2 < 0$).

Non-collinear order

Equation 2.1 in the preceding paragraph describes the anisotropy of a uniform magnetization. In other words, $\mathcal{V}_T$ reflects the anisotropy potential experienced by each individual magnetic moment in a sample. In the case of collinear order of microscopic moments, the potential of the resulting macroscopic moment is obviously identical to $\mathcal{V}_T$. If microscopic moments order in a non-collinear fashion, the situation becomes more delicate. The magnetic anisotropy is then determined by the sum over the MAE of all individual moments pointing in various directions. The resulting anisotropy potential for a macroscopic magnetization may deviate significantly from the potential experienced by individual moments. In this thesis, we investigate MnSi which exhibits a helimagnetic ground state, i.e. in the absence of magnetic fields the microscopic moments order non-collinearly. In the following, we briefly recapitulate the implications of such a spin structure for the magnetic anisotropy as discussed in Ref. [Hal18]. With respect to the material investigated in this work, we consider weak magnetic anisotropies compared to the mechanism stabilizing non-collinear order.

Depending on the magnitude of an applied magnetic field, MnSi can exhibit three different states of magnetic order at low temperatures $T \ll T_\mathrm{c}$, i.e. a helical, a conical or a field-polarized state. We treat the helical state and the field-polarized state as limiting cases of a conical helix described by

$$\mathbf{M}(\mathbf{r})/M_s = \hat{e}_3 \cos\alpha + \sin\alpha \, (\hat{e}_1 \cos(\mathbf{kr}) + \hat{e}_2 \sin(\mathbf{kr})) \tag{2.2}$$

with the saturation magnetization M_s, the pitch vector $\mathbf{k} \parallel \hat{e}_3$ and the orthonormal right-handed basis $\hat{e}_1 \times \hat{e}_2 = \hat{e}_3$. The cone angle α denotes the angle between individual moments and the pitch vector. Consequently, the limits $\alpha = 0°$ and $\alpha = 90°$ correspond to the field-polarized and the helical state, respectively. In the absence of distortions of the conical helix, the macroscopic moment resulting from such a structure points in the same directions as the pitch vector $\mathbf{k}$. A variational calculation reported in Ref. [Hal18] yields an effective anisotropy potential for the orientation of the pitch vector given by

$$\mathcal{V}_\alpha(\hat{k}) = K_\mathrm{eff}(\alpha)\left(\hat{k}_x^4 + \hat{k}_y^4 + \hat{k}_z^4\right). \tag{2.3}$$

We note that for this calculation only the leading K_1-term of the potential $\mathcal{V}_T$ has been considered. The potential $\mathcal{V}_\alpha$ exhibits a shape identical to the K_1-term of $\mathcal{V}_T$ but yields an effective anisotropy constant

$$K_{\text{eff}}(\alpha) = \frac{K_1}{64}(9 + 20\cos(2\alpha) + 35\cos(4\alpha)) \tag{2.4}$$

which depends on the cone angle α. In the limit of the field-polarized state, i.e. $\alpha = 0°$, we obtain $K_{\text{eff}} = K_1$ consistent with our consideration above. In the limit of the helical state, i.e. $\alpha = 90°$, we obtain $K_{\text{eff}} = 3K_1/8$. While for an ideal spin helix, the macroscopic magnetization vanishes, the effective anisotropy potential still determines the direction of its pitch vector. The coincident sign of K_1 and $K_{\text{eff}}(90°)$ implies the coincidence of preferential directions for the pitch vector of an ideal helix and an individual magnetic moment. Strikingly, this coincidence is not maintained everywhere in the conical phase. As can be inferred from Eq. 2.4, the effective anisotropy constant changes sign for angles between $\alpha \approx 30°$ and $\alpha \approx 70°$ implying a commutation of hard and easy axes.
At temperatures $T \lesssim T_c$ and small magnetic fields $\mathbf{B}$, an additional phase pocket exists in MnSi, i.e. the skyrmion lattice phase. Here, magnetic moments order in the form of a hexagonal lattice of spin vortices in a plane perpendicular to $\mathbf{B}$. Analogous to the pitch vector of a helix, an effective anisotropy potential can be determined for the normal vector of the hexagonal array. While it has been shown that this potential exhibits, in leading order, the same shape as $\mathcal{V}_\alpha$, no expression has been reported relating the respective effective anisotropy constant to the anisotropy constant K_1 for an individual moment [Ada18].
We emphasize again that the above considerations neglect deviations of magnetic order from its ideal structure. In particular, we will see in Ch. 5 that the magnetization does not vanish in the helical state due to anharmonic effects. The presence of similar deviations is expected for the conical and skyrmionic states. To the best of our knowledge, no theoretical framework exists addressing the influence of anharmonic distortions on the magnetic anisotropy potential.

Experimental implications

The magnetic anisotropy sets preferential directions for the magnetization of a material. In the presence of a magnetic field deviating from the easy axis, the magnetization is tilted away from its zero-field preferential direction towards the field direction due to the Zeeman energy

$$E_Z/V = -\mathbf{M} \cdot \mathbf{B}. \tag{2.5}$$

We note that the Zeeman energy vanishes at $B = 0$ and is therefore not regarded as an anisotropy energy in the classical sense. During our experiments, we measure

magnetic torque in dependence of the orientation of a finite magnetic field. In principle, this torque can be simulated by minimizing the anisotropy energy density

$$\begin{aligned} E_a/V = &- \mathbf{M}\cdot\mathbf{B} + K_1\left(\hat{M}_x^4 + \hat{M}_y^4 + \hat{M}_z^4\right) \\ &+ K_2\left(\hat{M}_x^2\hat{M}_y^4 + \hat{M}_y^2\hat{M}_z^4 + \hat{M}_z^2\hat{M}_x^4\right) \end{aligned} \tag{2.6}$$

numerically and calculating the resulting torque. We present results of such simulations in Sec. 5.3.3. With this procedure, the simulated curve needs to be adjusted to experimental results "by hand" which is rather cumbersome given the large number of measurements. A more convenient approach may be adopted for measurements in the high-field limit, i.e. under the assumption that magnetization and field vector point into the same direction. In this case, we can derive an analytical expression for the torque expected due to the anisotropy potential in Eq. 2.1 via $\Gamma/V = \partial\mathcal{V}_T/\partial\varphi$. Here, the angle φ describes a rotation of $\mathbf{B}$ around a fixed axis. Numerical simulations confirm that in the field-polarized state of MnSi the assumption of the high-field limit is valid for rotations around a crystallographic $\langle 110\rangle$-direction and an anisotropy potential $\mathcal{V}_T$ dominated by K_1. This corresponds to our experimental situation and we obtain

$$\begin{aligned} \frac{\Gamma(\varphi)}{V} = \frac{\partial\mathcal{V}_T}{\partial\varphi} = &\frac{K_1}{2}[1+3\cos(2\varphi)]\sin(2\varphi) \\ &- \frac{K_2}{32}[1+3\cos(2\varphi)]^2\sin(2\varphi) \end{aligned} \tag{2.7}$$

with the sample volume V. The analytical function allows for a simple fitting routine, thus facilitating the extraction of anisotropy constants from experimental torque curves.
We note that for rotations around a $\langle 111\rangle$-direction a similar derivation yields $\Gamma(\varphi) = 0$ when only the K_1-term is considered. This is not confirmed by numerical calculations due to considerable tilts of the magnetization vector $\mathbf{M}$ out of the magnetic field rotation plane and the associated breakdown of the high-field limit assumption.

2.2 The de Haas-van Alphen effect

The quantum oscillatory behavior of the magnetic susceptibility as a function of magnetic field was first observed in bismuth in 1930 [Haa30]. Named after its discoverers, it is nowadays known as the de Haas-van Alphen (dHvA) effect. Being a pure quantum mechanical phenomenon, the dHvA effect provides valuable information on the quantum mechanical ground state of the host and has thus been established as a powerful method to determine the Fermi surface (FS) properties along with effective masses and scattering rates of three dimensional electron systems. In this section a brief overview of the underlying physical concepts is presented. We follow

Ref. [Sho84] which comprises an extensive review on the dHvA effect in metals. Here, we focus on the results which are important for our experiments.

2.2.1 Landau quantization of free electrons

In an external magnetic field, electrons are, in the classical picture, subjected to the Lorentz force. Consequently, the motion perpendicular to the magnetic flux lines is forced on circular orbits while the motion parallel to the field remains unaffected. A quantum mechanical treatment results in the well-known Landau quantization found in standard textbooks as, e.g., Ref. [Gro12]. Due to the crucial importance to our experiments, we recapitulate the main steps below.
A free electron of charge $-e$ and effective mass m^* is considered. In a uniform magnetic field of the form $\mathbf{B} = (0, 0, B_z)$, the Hamiltonian is given by

$$\hat{H} = \frac{\hat{p} + e \cdot \mathbf{A}}{2m^*} \tag{2.8}$$

with the momentum operator $\hat{p} = -i\hbar\nabla$ and the vector potential $\mathbf{A}$. In the Landau gauge the latter is set to $\mathbf{A} = (0, x \cdot B_z, 0)$. The Schrödinger equation (SE) can then be written as

$$\left[\frac{\partial^2}{\partial x^2} + \left(\frac{\partial}{\partial y} - \frac{ieB_z}{\hbar} \cdot x\right)^2 + \frac{\partial^2}{\partial z^2} + \frac{2m^*}{\hbar^2} \cdot E\right]\Psi(x, y, z) = 0. \tag{2.9}$$

and exhibits solutions of the form $\Psi(x, y, z) = e^{[i(\beta y + k_z z)]}u(x)$. Inserting this solution into the SE yields

$$\left[\frac{-\hbar^2}{2m^*}\frac{\partial^2}{\partial x^2} + \frac{m^*\omega_c^2}{2}(x - x_0)^2\right]u(x) = \left(E - \frac{\hbar^2 k_z^2}{2m^*}\right)u(x). \tag{2.10}$$

This is the equation of a harmonic oscillator with the cyclotron frequency $\omega_c = eB/m^*$ and the guiding centre coordinate of a cyclotron orbit in real space $x_0 = -k_y l_B^2$. Here, $l_B = (\hbar/eB)^{1/2}$ denotes the magnetic length and k_i is the i-th component of the wavevector $\mathbf{k}$. Equation 2.10 results in the eigenenergies

$$E_j = \left(j + \frac{1}{2}\right)\hbar\omega_c + \frac{\hbar^2 k_z^2}{2m^*} \quad j = 0, 1, 2, ... \tag{2.11}$$

Apparently, the motion within the (k_x,k_y)-plane, i.e. orthogonal to B, is quantized. The allowed energy states follow circles in reciprocal space. The motion along k_z, i.e. parallel to the magnetic field, is unaffected and the parabolic dispersion of free electrons is recovered. In sum the permitted states form concentric cylinders with an axis parallel to the external field B. These so called Landau levels (LLs) are schematically depicted in Fig. 2.2. A hypothetical Fermi surface is indicated by the shaded sphere. At $T = 0$, only the states inside the sphere are occupied. For a solid state system with arbitrary energy landscape, the tubes representing the LLs are not

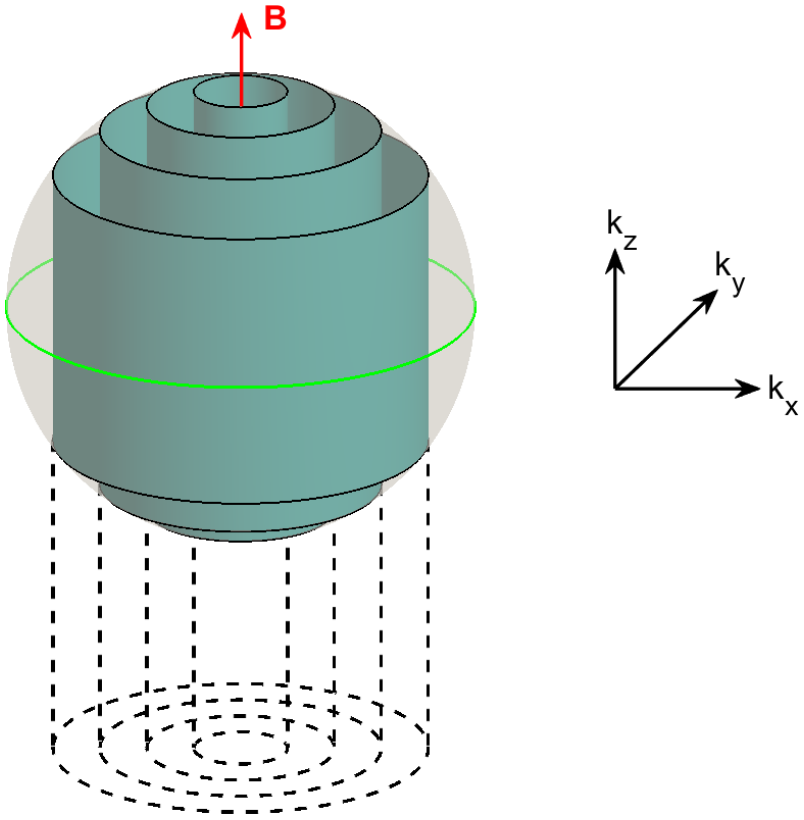

Figure 2.2: Schematic sketch of Landau tubes for a free electron gas. The bright green circle indicates an extremal cross section of the spherical Fermi surface.

necessarily cylindrical or parallel to B [Sho84].
The eigenenergies for a given k_z are degenerate. For a sample area of $\mathcal{A} = L_x \cdot L_y$ parallel to the external magnetic field, the guiding centre coordinates of two neighboring orbits is given by $\Delta x_0 = \Delta k_y l_\mathrm{B}^2 = \left(\frac{2\pi}{L_y}\right)(\hbar/eB)$. This results in a number of states with constant energy $N = \frac{L_x}{\Delta x_0} = L_x L_y eB/\hbar$ for any particular value of k_z. We obtain the degeneracy per unit area

$$N_\mathrm{L} = \frac{eB}{\hbar} \cdot g_\mathrm{s}. \tag{2.12}$$

with the spin degeneracy g_s which equals 2 for spin degenerate systems. From Eqs. 2.11 and 2.12 we see that both energy and degeneracy of Landau levels are linear functions of the field magnitude. Consequently, the density-of-states (DOS) as well as the magnetization of metals are affected by the quantization of the electron motion. This ultimately leads to magnetic oscillations as described in following.

2.2.2 Quantum oscillations

As a starting point for the derivation of the magnetization M, we introduce the thermodynamic potential

$$\Omega = F - \chi N = U - TS - \chi N \tag{2.13}$$

with the chemical potential χ and the particle number N. Further, $F = U - TS$ denotes the free energy which depends on the internal energy U, the entropy S and the temperature T. The differential of Ω is given by

$$\mathrm{d}\Omega = -S\mathrm{d}T - M\mathrm{d}B + N\mathrm{d}\chi \tag{2.14}$$

so that we can derive the magnetization from

$$M = -\left(\frac{\partial\Omega}{\partial B}\right)\bigg|_{T,\chi}. \tag{2.15}$$

Note that we have ignored the vector character of M and B above. In the following, we assume $\mathbf{B} \parallel \mathbf{z}$ without loss of generality. At zero temperature, the thermodynamic potential for an ideal electron system of volume V is given by

$$\Omega = -\frac{VeB}{\pi^2\hbar}\sum_j \int_0^{k_j} (\chi - E_j)\mathrm{d}k_z. \tag{2.16}$$

Here, the sum includes all possible states E_j and the upper integration limit k_j equals the value of k_z for which $\hbar^2 k_j^2/2m^* = \chi - (j + 1/2)\hbar\omega_\mathrm{c}$ is fulfilled. We assume a FS of arbitrary shape and non-interacting electrons. The oscillatory part of the thermodynamic potential is then obtained by execution of the integral and expression in the form of a Fourier series

$$\Omega_\mathrm{osc} = \mathrm{const} \times \frac{B^{5/2}}{\sqrt{P''}} \sum_{p=1}^{\infty} \frac{1}{p^{5/2}} \cos\left[2\pi p\left(\frac{\hbar P}{2\pi eB} - \frac{1}{2}\right) \pm \frac{\pi}{4}\right]. \tag{2.17}$$

Here, P denotes the extremal cross sectional area of the FS perpendicular to the external field. The average curvature of the FS along k_z at the position of the extremal cross section is denoted by P''.
For an intuitive interpretation of Eq. 2.17, we refer to Fig. 2.2. As stated above, the energy of Landau levels grows with increasing field magnitude (cf. Eq. 2.11). Regarding Fig. 2.2 this translates to increasing radii of Landau tubes. As a consequence, the intersections with the spherical Fermi surface move up and down which has little impact on the energy, i.e. the thermodynamic potential. However, when the intersections reach the extremal cross section indicated by the bright green circle, the Landau tube at once leaves the Fermi surface causing a significant change of the energy. Adjacent Landau tubes with energies $\hbar\omega_\mathrm{c}$ subsequently leaving the Fermi surface for steadily increasing field magnitude lead to periodic variations of the

thermodynamic potential which are reflected in Eq. 2.17 by the cosine-terms. The periodicity of the first harmonic, i.e. $p = 1$, is described by

$$\frac{\hbar P}{eB} = 2\pi(n + \gamma) \tag{2.18}$$

with a phase correction γ and an integer n. Apparently, the variations are periodic in $1/B$. The oscillation frequency f is determined by the Onsager relation [Ons52]

$$P_i = \frac{2\pi e}{\hbar} f_i \tag{2.19}$$

which relates f to the extremal Fermi surface cross section. A Fermi surface of arbitrary shape may exhibit multiple extremal cross sections orthogonal to the applied field each of which contributes to the magnetization with an oscillating term described by Eq. 2.17.
As stated above, we can deduce M from Ω by derivation with respect to B (cf. Eq. 2.15). For this operation, the vector character of M and B may no longer be neglected. For convenience, we divide the oscillatory magnetization $\mathbf{M}$ into its components parallel and perpendicular to the magnetic field. We denote these components by $M_\parallel$ and $M_\perp$, respectively, and obtain

$$M_\parallel^0 = \text{const.} \times \frac{f B^{1/2}}{m^* \sqrt{P''}} \sum_{p=1}^{\infty} \frac{1}{p^{3/2}} \sin\left[2\pi p\left(\frac{\hbar P}{2\pi e B} - \frac{1}{2}\right) \pm \frac{\pi}{4}\right] \tag{2.20}$$

$$M_\perp^0 = -\frac{1}{f}\frac{\partial f}{\partial \theta} M_\parallel. \tag{2.21}$$

In both components of the magnetization, the periodic variation of the thermodynamic potential is reflected. We indicate the assumption of a disorder-free electron system at zero temperature by the superscript 0. The factor $\frac{\partial f}{\partial \theta}$ in $M_\perp^0$ accounts for the anisotropy of the Fermi surface. Specifically, it denotes the partial derivative of the oscillation frequency f with respect to the angle θ describing the orientation of the magnetic field. Evidently, $\frac{\partial f}{\partial \theta}$ disappears for a spherical Fermi surface and, consequently, $M_\perp^0$ vanishes in this case.

Lifshitz-Kosevich formalism

The derivation of $M_\parallel^0$ and $M_\perp^0$ sketched above was performed assuming an ideal electron gas at $T = 0$. For real electron systems, finite temperature and disorder lead to amplitude reduction and phase smearing of dHvA oscillations. In order to take these effects into account, the so-called Lifshitz-Kosevich formalism has been established [Lif54, Lif55, Din52a, Din52b, Was96].
The occupation of accessible electronic states at finite temperature is determined by the Fermi distribution

$$\mathcal{F}(E, \chi, T) = \left[1 + \exp\left(\frac{E - \chi}{k_\mathrm{B} T}\right)\right]^{-1}. \tag{2.22}$$

It has been shown that the resulting amplitude reduction of quantum oscillations can be accounted for by including a factor of the form

$$R_{\mathrm{T}} = \frac{X}{\sinh X}, \text{ with } X = \frac{2\pi^2 k_{\mathrm{B}} m^* T}{\hbar e B} \tag{2.23}$$

in Eq. 2.17. As a most beneficial consequence, measuring the oscillation amplitude at various temperatures allows for the determination of the effective mass m^* of charge carriers on the corresponding orbits.
A similar reduction factor R_{D} can be obtained to incorporate the effect of disorder. The magnetization of an electron system with finite relaxation times and at finite temperature is then given by

$$M_{\parallel} = M_{\parallel}^0 R_{\mathrm{T}} R_{\mathrm{D}}, \tag{2.24}$$

$$M_{\perp} = M_{\perp}^0 R_{\mathrm{T}} R_{\mathrm{D}}. \tag{2.25}$$

Including R_{D} enables the determination of finite relaxation times from field magnitude-dependent measurements. No such evaluation has been performed for the experimental data presented in this work.

Magnetic breakdown

Fermi surfaces of complicated shape can arise from the electronic band structures of real metals. If several bands cross the Fermi energy E_F at similar positions in reciprocal space, electrons can tunnel between adjacent orbits. This phenomenon is known as magnetic breakdown [Coh61]. The probability of such a process is described by the Blount criterion [Sho84]

$$\hbar\omega_{\mathrm{c}} \gtrsim \frac{E_{\mathrm{g}}^2}{E_{\mathrm{F}}} \tag{2.26}$$

where E_{g} is the energetic separation of the respective orbits. By connection of orbits corresponding to extremal cross section of the Fermi surface perpendicular to the magnetic field, magnetic breakdown can lead to additional frequencies in the dHvA spectrum. From Eq. 2.26, we infer that observations of such frequencies are expected in large magnetic fields. An exemplary illustration of magnetic breakdown orbits is shown in Figs. 4.19 and 4.20.

2.2.3 Transforms between time and frequency domain

As described above, an abundance of dHvA frequencies can be observed in metals due to complex multi-sheet Fermi surfaces and additional components being introduced by magnetic breakdown. Therefore, it is convenient to transform the oscillating signal to the frequency domain for evaluation. In the following, we briefly review the various methods for such transformations that were employed in this work. For a

graphic illustration of the different spectra resulting from a single set of data due to different transformation techniques see Fig. 4.4.

Fourier transform

The most common approach to analyzing periodically varying data in the frequency domain is considering the Fourier transform. Throughout literature, this wide-spread standard technique is usually introduced in its integral form for continuous functions [Kai94, Rah11]. During our measurements, we obtain discrete sets x of data points. In this case, a discrete Fourier transform y can be calculated via

$$y_k = \sum_{j=1}^{n} \omega^{(j-1)(k-1)} x_j, \text{ with } \omega = e^{-2\pi i/n} \tag{2.27}$$

where n is the number of data points in x, and j and k are indices running from 1 to n. The corresponding frequency data is deduced from the spacing between values in the time domain. By definition, a uniform spacing of data points in the time domain is required. The discrete Fourier transform is usually computed by efficient algorithms subsumed under the name fast Fourier transform (FFT). Therefore, the terms discrete Fourier transform and FFT are often treated as synonyms.
The resolution of a FFT spectrum is determined by the length of the observed interval in the time domain. Consequently, one may improve the nominal resolution by expanding the time interval with data points of value zero. This procedure is called zero padding. The resulting spectrum represents an interpolation of the FFT spectrum without zero padding rather than one with increased resolution, i.e., zero padding may improve the accuracy of displayed maxima positions, but does not yield any additional information [Smi10].

Lomb-Scargle algorithm

The Lomb-Scargle (LS) algorithm is a specific form of the least-squares spectral analysis (LSSA) which is utilized most frequently in the field of astronomy. In general, LSSA relies on least squares fits of sinusoids at various frequencies to the data set under investigation. The LS method was developed by N. Lomb [Lom76] and further elaborated by J. Scargle [Sca82] with the specific objective of treating unevenly spaced data. A recent attempt to provide an intuitive approach to the Lomb-Scargle periodogram is presented, e.g., in Ref. [Van18]. Here, we restrict ourselves to the basic definition. We consider a discrete set x of n data points taken at times t_j. The LS estimate of the power spectral density is then given by

$$P_{\mathrm{LS}}(\omega) = \frac{1}{2\sigma^2} \left\{ \frac{\left[\sum_{j=1}^{n} (x_j - \bar{x}) \cos(\omega(t_j - \tau))\right]^2}{\sum_{j=1}^{n} \cos^2(\omega(t_j - \tau))} + \frac{\left[\sum_{j=1}^{n} (x_j - \bar{x}) \sin(\omega(t_j - \tau))\right]^2}{\sum_{j=1}^{n} \sin^2(\omega(t_j - \tau))} \right\} \tag{2.28}$$

with the mean

$$\bar{x} = \frac{1}{n}\sum_{j=1}^{n} x_j \tag{2.29}$$

and the variance

$$\sigma^2 = \frac{1}{n-1}\sum_{j=1}^{n}(x_j - \bar{x})^2 \tag{2.30}$$

of the data set. The time delay τ defined by

$$\tan(2\omega\tau) = \frac{\sum_{j=1}^{n}\sin(2\omega t_j)}{\sum_{j=1}^{n}\cos(2\omega t_j)}. \tag{2.31}$$

vanishes for data points taken at uniformly spaced t_j. Instead of the circular frequency ω, we discuss our experimental results in terms of the ordinary frequency $f = \omega/2\pi$.

Welch algorithm

The algorithm proposed by P. D. Welch [Wel67] provides an estimate of the power spectral density with strongly reduced variance at the cost of decreased resolution. For this purpose, a discrete data set is divided into a variable number of segments overlapping by a variable amount. The data in each segment is weighted with a window function before the discrete Fourier transform is calculated. Note that the data points must be spaced equally in time in order to enable computation of the Fourier transform. The overlap of windows prevents information loss since most window functions grant larger influence to the center of a segment than to its edge regions. In a final step, the power spectral density is averaged over all segments.
The frequency spectrum obtained from the Welch algorithm is referred to as a modified periodogram due to application of a weighting window function. During the evaluation of data in Ch. 4, we employ a Hamming window function. The number of windows as well as their overlap are varied as described in Sec. 4.2.2.

2.3 Density functional theory

The appreciation of experimental results prevalently requires comparison to predictions derived from some form of theoretical model. For the experiments presented in this work, the appropriate object of comparison is the calculated electronic structure of the examined materials. For an exact computation, the stationary many-body Schrödinger equation [Sho09]

$$\left[-\frac{\hbar^2}{2m}\sum_{i=1}^{N}\nabla_i^2 + \sum_{i=1}^{N}V(\mathbf{r}_i) + \sum_{i=1}^{N}\sum_{j<i}U(\mathbf{r}_i,\mathbf{r}_j)\right]\psi = E\psi \tag{2.32}$$

must be solved. The first term including the electron mass m denotes the kinetic energy of each electron, the second term describes the potential imposed on electrons by the atomic nuclei. Note that the Born-Oppenheimer approximation has been applied. The last term on the left side represents the interaction between different electrons. The electronic wave function ψ depends on the spatial coordinates $\mathbf{r}_1, ..., \mathbf{r}_N$ and E is the ground state energy. For the moment, we disregard the electron spin. The number of electrons N is on the order of 10^{21} for macroscopic samples of solid materials rendering an exact solution of Eq. 2.32 impossible.
In the past decades, a technique known as density functional theory (DFT) allowed for approximations to this solution at a staggering level of success. Instead of the many-body wave function $\psi(\mathbf{r}_1, ..., \mathbf{r}_N)$ depending on $3N$ spatial coordinates, DFT considers the electron density $n(\mathbf{r})$ which is a function of only three spatial coordinates. For wave functions of individual electrons denoted by $\psi_i(\mathbf{r})$, the electron density can be expressed by [Sho09]

$$n(\mathbf{r}) = 2\sum_i \psi_i^*(\mathbf{r})\psi_i(\mathbf{r}). \tag{2.33}$$

Here, the factor 2 represents spin degeneracy. In the following, we briefly review the basic principles of DFT relevant for this work. For an extended account of the technique, see, e.g., Ref. [Mar04], for a rather practical introduction, see Ref. [Sho09].

2.3.1 Hohenberg-Kohn theorems and Kohn-Sham equations

The concept of DFT is based on two theorems proven by Hohenberg and Kohn as well as a set of equations derived by Kohn and Sham. The first Hohenberg-Kohn theorem states that "the ground-state energy from Schrödinger's equation is a unique functional of the electron density" [Hoh64]. In other words, a unique ground-state electron density exists which allows for unambiguous determination of ground-state energy, wave function and further properties of the electron system. The second Hohenberg-Kohn theorem states that "the electron density that minimizes the energy of the overall functional is the true electron density corresponding to the full solution of the Schrödinger equation" [Hoh64], i.e., one may identify the correct ground-state electron density by minimizing the energy functional. We note that in this form the Hohenberg-Kohn theorems are valid for non-degenerate ground states only but can be extended for the degenerate case. Unfortunately, the shape of the ground-state energy functional is not known. Moreover, the functional may still depend on the N wave functions of individual electrons ψ_i making minimization an unfeasible task.
Kohn and Sham were able to show that the correct electron density can be obtained from a set of equations each of which describes a single quasiparticle only [Koh65]. These Kohn-Sham equations read

$$\left[-\frac{\hbar}{2m}\nabla^2 + V(\mathbf{r}) + V_{\mathrm{H}}(\mathbf{r}) + V_{\mathrm{XC}}(\mathbf{r})\right]\psi_i(\mathbf{r}) = \varepsilon_i\psi_i(\mathbf{r}) \tag{2.34}$$

which resembles Eq. 2.32 except for the lack of summations. Again, the first term denotes the kinetic energy of the electron and the second term describes the potential arising from atomic nuclei in the Born-Oppenheimer approximation. The third term denotes the Hartree potential, i.e. the Coulomb repulsion [Sho09]

$$V_{\mathrm{H}}(\mathbf{r}) = e^2 \int \frac{n(\mathbf{r})}{|\mathbf{r} - \mathbf{r}'|} d^3r' \tag{2.35}$$

between the individual electron considered in one equation and the electron density resulting from all electrons. Finally, V_{XC} denotes the exchange-correlation potential which is defined to include all contributions not captured the other terms. In general, this potential is a functional of $n(\mathbf{r})$ of unknown shape.

2.3.2 Approximation of V_{XC} and self-consistent solution of the Kohn-Sham equations

Several ways have been established for the approximation of V_{XC}. The approaches most commonly used include, e.g., the local density approximation (LDA) or the generalized gradient approximation (GGA). In the LDA, the exchange-correlation functional is approximated as a function of the electron density at a specific position:

$$E_{\mathrm{XC}}^{\mathrm{LDA}}[n] = \int d^3r \; e_{\mathrm{XC}}(n(\mathbf{r})) \cdot n(\mathbf{r}). \tag{2.36}$$

In the GGA, the gradient of the local electron density is additionally taken into account by $e_{\mathrm{XC}} = e_{\mathrm{XC}}(n(\mathbf{r}), |\nabla n(\mathbf{r})|)$.
The approximation of V_{XC} enables a self-consistent solution of the Kohn-Sham equations. In a first step, an initial electron density $n^{\mathrm{i}}(\mathbf{r})$ is guessed. This density is then used to compute the potentials V_{H} and V_{XC}. Subsequently, the Kohn-Sham equations are solved. For this purpose, the use of several basis sets for the ψ_i has been established such as, e.g., linear combinations of atomic orbitals (LCAO), linearized augmented plane wave (LAPW) functions or KKR functions. For the calculation in this thesis, augmented plane waves plus local orbitals (APW+lo) functions were employed which assume a localized behavior corresponding to a muffin-tin potential close to atomic nuclei and plane-waves in interstitial regions. From the solution of the Kohn-Sham equations, a final electron density $n^{\mathrm{f}}(\mathbf{r})$ is calculated. In subsequent cycles, the computation of potentials, solution of Kohn-Sham equations and calculation of $n^{\mathrm{f}}(\mathbf{r})$ is repeated while $n^{\mathrm{i}}(\mathbf{r})$ is adjusted before each iteration with respect to the previously obtained $n^{\mathrm{f}}(\mathbf{r})$. This self-consistent calculation is conducted until the difference between $n^{\mathrm{i}}(\mathbf{r})$ and $n^{\mathrm{f}}(\mathbf{r})$ within one cycle falls below an arbitrarily defined convergence threshold.
Despite its tremendous success, there are several systematic shortcomings of DFT. For instance, DFT as described above tackles the ground state of an electronic system and thus yields little information on excited states. Another well-known issue is the underestimation of band gaps in semiconductors and insulators. A

drawback of particular interest for the band structure calculations in this work is that LDA neglects spin fluctuation in the material. As a consequence, the calculated magnetic moment may deviate strongly from experimental observations. There is no standard solution to this problem, yet a number of methods have been established allowing to adjust the calculated moment. Examples include the DFT+U method where an additional Hubbard potential is introduced in the Hamiltonian, fixed-spin-moment calculations which consider a fictitious magnetic field, or the spin scaling approach which employs an additional free scaling parameter for the spin-density in the Kohn-Sham equations. The latter method was applied in this thesis.

3 Experimental setups

In this chapter we present our experimental procedure. We first review the general concepts of the method employed in our experiments in Sec. 3.1. Consequently, we describe the specific setups for measurements of the de Haas-van Alphen effect and magnetic anisotropy in Sec. 3.2 and Sec. 3.3, respectively.

3.1 Measurement method

The magnetization M of a material may be investigated in numerous ways. Naturally, the method of choice depends on the purpose of the study. Throughout this thesis, we performed experiments targeting magnetic quantum oscillations as well as investigations of magnetic anisotropy. In this section, we describe our experimental techniques.
The observation of magnetic quantum oscillations requires high-precision measurements at low temperatures T and in high magnetic fields B. The well established methods are (1) the modulation technique, (2) pulsed field techniques and (3) torque techniques. The modulation technique consists in superimposing a small oscillating magnetic field to the main slowly varying field and detecting the induced electromotive force (EMF) due to the sample's oscillating magnetization with a pick-up coil [Sho64, Gol65, Win66, Sta68, Win68]. As a major advantage, the method allows for phase sensitivity. A similar procedure is adopted in pulsed fields techniques, where the EMF induced by a rapidly changing magnetization is picked up [Pri66]. The utilization of pulses allows for magnetic field regimes not accessible by static fields. In both techniques, not the magnetization but quantities related to its first and higher-order derivatives $\mathrm{d}^k M/\mathrm{d}B^k$ with respect to magnetic field are measured. In contrast, torque techniques measure M statically.
Beside its suitability for the observation of magnetic quantum oscillations, torque magnetometry is also found among the established techniques for experiments targeting magnetic anisotropy. Alternative methods comprise, e.g., ferromagnetic resonance (FMR), vector vibrating sample magnetometers (VVSMs), magneto-optical Kerr effect (MOKE) magnetometry or comparison of hysteresis loops of the isotropic magnetization for different crystallographic directions. While the latter method may require the least effort, it provides little accuracy and is rather suitable for preliminary examinations [Ben06]. In contrast, MOKE magnetometry exhibits high sensitivity but is only applicable for thin films [Qiu00]. VVSMs offer high sensitivity over a wide parameter range but are difficult to implement and operate [Ben06]. Similar to modulation and pulsed field techniques, a VVSM measures the induced EMF related to $\mathrm{d}^k M/\mathrm{d}B^k$ rather than the static magnetization. Ferromagnetic resonance offers

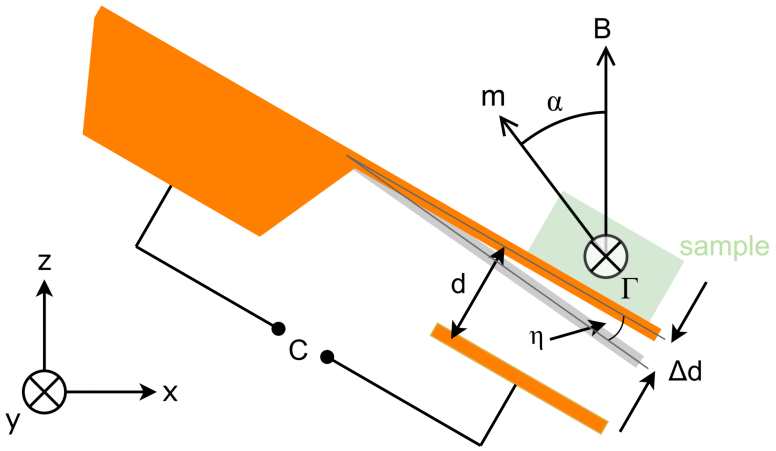

Figure 3.1: Working principle of the longitudinal cantilever magnetometer with capacitive readout. The torque Γ acting on the sample deflects a thin beam. The deflection Δd is reflected in a capacitance change between cantilever paddle and counter electrode.

the advantage of detecting inhomogeneities of the anisotropy energy throughout the specimen under investigation [Chi64]. Regarding magnetic anisotropy, FMR measures the second order derivative of the anisotropy energy with respect to the rotation angle, i.e. the first order derivative of the torque $\mathrm{d}^2E_\mathrm{a}/\mathrm{d}\phi^2 = \mathrm{d}\Gamma/\mathrm{d}\phi$. Torque magnetometry provides a more direct measure of anisotropy and, more importantly, yields the highest accuracy among the established methods. Possible drawbacks such as limited torque range and lack of information on longitudinal magnetization are of minor importance to our anisotropy investigations.
Magnetic torque measurements divide into two methods, i.e. torsional balance and cantilever magnetometer. The former was used during the first discovery of the de Haas-van Alphen effect in bismuth [Haa30] and essentially consists in a wire or fiber attached to the sample being twisted by a torque or force in a homogeneous or inhomogeneous magnetic field. Several sophisticated concepts have been proposed [Haa84, Eis85b, Eis85a, Tem88, Wie98, Mat04]. Throughout this thesis, cantilever magnetometry has been employed. In this section, we give details on the general concept of these techniques. The specific implementation in our various setups will be presented in the following sections.
Cantilever magnetometers can be operated in a longitudinal bending mode and a torsional mode. Our investigations of the de Haas-van Alphen effect rely solely on the longitudinal bending option whereas we employed both variants for our anisotropy measurements. Longitudinal operation is described in Sec. 3.1.1, the torsional method is addressed in Sec. 3.1.2.

3.1.1 Longitudinal cantilever magnetometer

The working principle of a longitudinal cantilever magnetometer is schematically shown in Fig. 3.1. The sample is attached to a paddle at the free end of a flexible,

singly clamped beam. In a homogeneous magnetic field $\mathbf{B}$, the magnetic moment $\mathbf{m}$ of the sample results in a torque

$$\boldsymbol{\Gamma} = \mathbf{m} \times \mathbf{B}\,. \tag{3.1}$$

As a consequence, the cantilever beam is deflected from its equilibrium position by an angle η. For small deflections Hooke's law holds true and Eq. 3.1 transforms to

$$\Gamma = k\eta = k\frac{\Delta d}{L} \tag{3.2}$$

with the spring constant k and the effective length of the cantilever beam L. The deflection Δd is proportional to the exerted torque Γ. Various methods of measuring the deflection have been established as, e.g., interferometric [Gib93, Spr06], piezoresistive [Wil98, Lup99] or capacitive readout schemes. We employ the capacitive method sketched in Fig. 3.1. Before discussing the details of readout technique and calibration procedure, we briefly consider some peculiarities of the experimental method relevant for our experiments.

- As follows from Eq. 3.1, a non-zero component of the sample magnetization perpendicular to $\mathbf{B}$ is a prerequisite for measuring a torque. Consequently, the dHvA effect may only be observed in the torque signal in materials with anisotropic Fermi surfaces as can be inferred from Eq. 2.21. For a fully isotropic Fermi surface, the factor $\frac{\partial f}{\partial \theta}$ and thus $M_\perp$ amounts to zero. Strictly speaking, this is also the case for magnetic field applied along symmetry axes of the FS, i.e. the high symmetry directions of the crystal. In practice, these blind spots are a weak limitation since dHvA oscillations can usually be tracked up to field directions very close to symmetry axes.

- Fig. 3.1 insinuates a torque pointing in y-direction as a result of external field and magnetization both lying within the x-z-plane. In general, the magnetization can point into any direction in 3D space and thus yield a non-zero torque component in the x-z-plane which will result in a torsion of the cantilever. Such a torque and its detection are suppressed by our cantilever design and readout method as assessed in [Alb15]. A torque along the cantilever beam yields only a capacitance change on the order of $\lesssim$1 % compared to a torque of identical magnitude in y-direction. As a consequence, we mainly measure the projection of the actual magnetic torque onto the y-direction. This insight is particularly important for the evaluation of our experiments concerning magnetic anisotropy in Ch. 5.

- In the presence of a magnetic field gradient, an additional force

$$\mathbf{F} = \nabla(\mathbf{m} \cdot \mathbf{B}) \tag{3.3}$$

  acts on the sample. In the specific case of a uniform magnetization and a field gradient pointing along the field direction, $\mathbf{F}$ is parallel to $\mathbf{B}$ and scales with

the isotropic part of the magnetization $M_{\parallel}$. Measuring both $M_{\perp}$ and $M_{\parallel}$ then yields the full magnetization $\mathbf{M}$[1]. However, collinearity of $\mathbf{B}$ and $\nabla\mathbf{B}$ is not warranted in our experiments. Throughout this thesis, we aim to investigate solely the torque, i.e. the anisotropic part of the magnetization $M_{\perp}$. The influence of field gradients is discussed in detail for each of our setups in the following sections.
Strictly speaking, a force as in Eq. 3.3 may also result from spatial variations of the magnetization in a homogeneous magnetic field. We consider our samples to be magnetized homogeneously on a macroscopic level so that we can neglect such a situation.

Readout and calibration

The cantilever deflection can be measured, e.g., by interferometric [Gib93, Spr06], piezoresistive [Wil98, Lup99] or capacitive [Gri73, Sch00] means. The advantages of capacitive readout consist in easy wiring and fast integration of different cantilever designs. Moreover, the achieved readout resolution is rarely a limiting factor in our experiments. We thus employ the capacitive technique throughout the present work as indicated in Fig. 3.1. For this purpose, the cantilever is placed on a printed circuit board in such a way that the paddle and a counter electrode on the circuit board form a plate capacitor. Assuming parallel plates, the equilibrium capacitance C_0 is given by

$$C_0 = \frac{\epsilon_0 A}{d} \tag{3.4}$$

with A the area of paddle and counter electrode and d the distance between them. A change Δd in the plate distance is thus reflected in the capacitance. For small deflections $\frac{\Delta d}{d} \ll 1$ we can expand C as

$$C(d+\Delta d) = \frac{\epsilon_0 A}{d+\Delta d} = \frac{\epsilon_0 A}{d}\left(1+\frac{\Delta d}{d}\right)^{-1} \tag{3.5}$$

$$\approx C_0\left(1-\frac{\Delta d}{d}+...\right). \tag{3.6}$$

Comparing the proportionality of capacitance change ΔC and deflection Δd to Eq. 3.2 yields a linear relation between a torque causing a cantilever deflection and the resulting capacitance change:

$$\Gamma = K\Delta C\,. \tag{3.7}$$

[1]Note that magnetic moment $\mathbf{m}$ and magnetization $\mathbf{M} = \mathbf{m}/V$ are exchangeable since we know the volumes V of our samples.

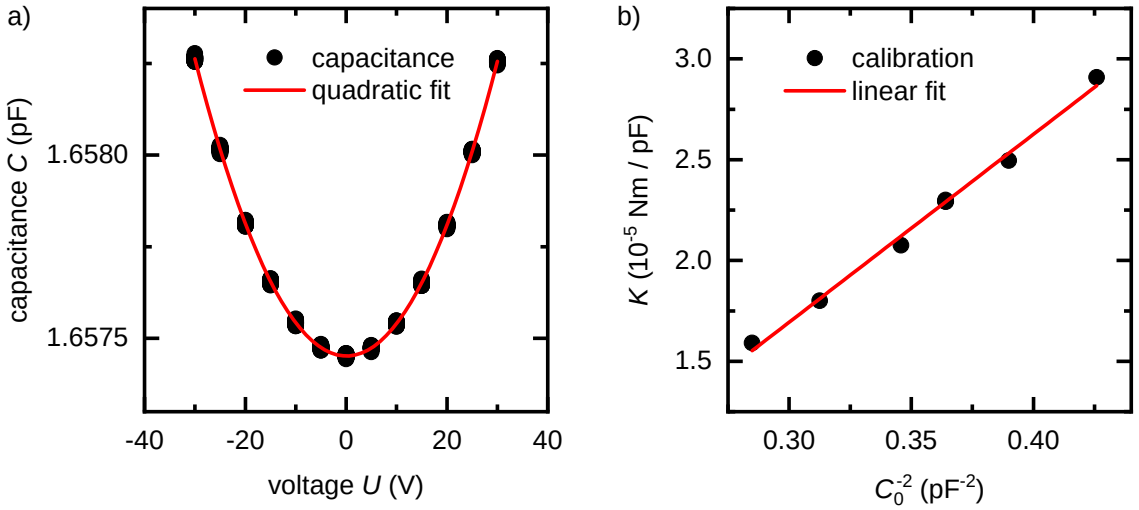

Figure 3.2: a) Measured capacitance (black circles) as a function of applied voltage between cantilever and counter electrode. The red line denotes a quadratic fit from which κ is determined. Experimental error bars are smaller than symbols and relative errors of the fit are smaller than 10^{-3}. b) Calibration constant K as determined from electrostatic calibrations (black circles) versus capacitance at zero voltage C_0. The red line depicts a linear fit from which the constants K_a and K_b for direct conversion of capacitance to torque following Eq. 3.16 are determined. Error bars of data points are smaller than symbols, relative errors of K_a and K_b amount to 0.103 and 0.034, respectively.

The proportionality constant K can be determined *in situ* by an electrostatic calibration routine. For this purpose an external dc voltage U is applied between cantilever and counter electrode which results in an attractive force

$$|F| = \frac{C_0 U^2}{2d_0}\,. \tag{3.8}$$

In turn, the electrostatic force exerts an effective torque

$$\Gamma = \beta |F| L = \frac{\beta C_0 L U^2}{2d_0} \tag{3.9}$$

on the cantilever. The factor β accounts for the reduced mechanical response of the cantilever to a force acting on the beam as compared to a torque [Sch00, Wil04]. It depends on the material as well as on the dimensions of the cantilever. Equations for calculation of this reduction factor can be found in appendix A.1. In this work, β ranges from 0.68 to 0.80 as we will point out in detail in the following section on cantilever design. Combining Eq. 3.9 with Eq. 3.7, we obtain

$$\Delta C = \kappa U^2 \quad \text{with} \quad \kappa = \frac{\beta C_0 L}{2d_0 K}\,. \tag{3.10}$$

In order to determine κ, we measure C as a function of applied voltage. This is exemplarily shown in Fig. 3.2 a) where the black circles represent measured data and the red curve depicts a quadratic fit from which we can extract κ. We replace d_0 in Eq. 3.10 and obtain

$$K = \frac{\beta C_0^2 L}{2\epsilon_0 A \kappa}\,. \tag{3.11}$$

In Eqs. 3.8 to 3.11, C_0 is the capacitance at $U = 0$. For small changes $\Delta C \ll C_0$ during the experiment, we can assume a constant K independent of the zero-voltage capacitance. It is then sufficient to perform a single measurement of $\Delta C(U)$, determine the corresponding K with Eq. 3.11 and calculate the torque via Eq. 3.7. In the case of large capacitance changes, it is advisable to consider the dependence of K on C_0. We transform Eq. 3.7 to

$$K = \frac{\Gamma}{\Delta C} = \frac{\Gamma d_0}{\Delta d C_0}\,. \tag{3.12}$$

With $d_0 \propto 1/C_0$ and the fact that the deflection $\Delta d \propto \Gamma$ is independent of the capacitance, we can write

$$K \propto \frac{1}{C_0^2} \tag{3.13}$$

and consequently

$$K(C) = K_\mathrm{a} + \frac{K_\mathrm{b}}{C^2}\,. \tag{3.14}$$

The calibration parameters K_a and K_b are determined by extracting K from $\Delta C(U)$ as described above at multiple points C_0. An example is shown in Fig. 3.2 b), where K is plotted versus $1/C_0^2$ (black circles). We use a linear fit (red curve) to obtain K_a and K_b and employ the integral form of Eq. 3.7 to calculate the torque

$$\Gamma(C) = \int_{C_0}^{C} K(C')\,\mathrm{d}C' \tag{3.15}$$

$$= K_\mathrm{a}(C - C_0) + K_\mathrm{b}\left(\frac{1}{C_0} - \frac{1}{C}\right). \tag{3.16}$$

Here, C_0 is again the capacitance at $\Gamma = 0$ which is usually determined by starting or ending each measurement at $B = 0$.

Cantilever design

Selecting proper dimensions is key in conducting a successful cantilever experiment. While high resolution is usually the main objective, also robustness must be considered. For measurements on low-dimensional electron systems, e.g., resolutions better than 10^{-15} J/T are accessible [Her15]. For the phenomena investigated in this work, a resolution of 10^{-10} J/T is sufficient. However, our cantilevers must withstand larger stress from samples' weight und magnetization.
In the course of this thesis, two different types of longitudinal cantilevers were

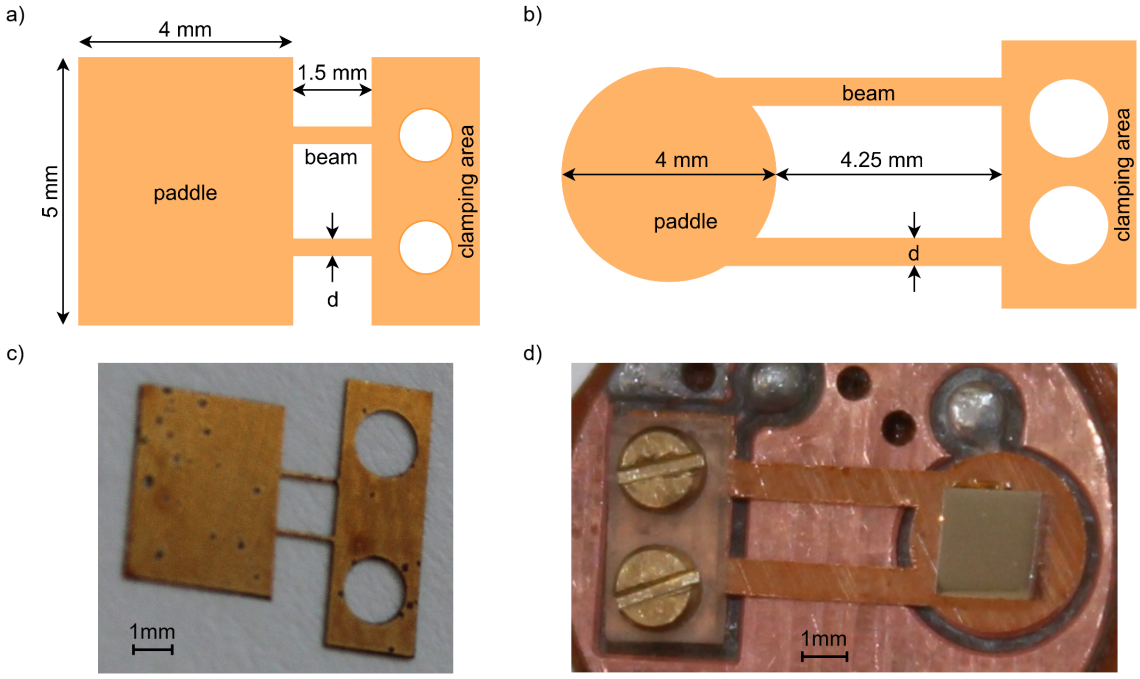

Figure 3.3: Shape and dimensions of the CuBe cantilevers used a) at TUM and b) at HFML in Nijmegen. The beam width d is set to 0.2 mm or 0.6 mm for the TUM cantilever design and 0.2 mm or 0.8 mm for the HFML cantilever design. The thickness is 50 µm for the TUM design and 80 µm for the HFML design. c) and d) show photographs of the cantilevers sketched in a) and b), respectively.

employed. Both types were fabricated from copper beryllium (CuBe) foil with different manufacturing techniques as well as different shapes and dimensions. The designs are sketched in Fig. 3.3 a)-b) and illustrated by photographs in Fig. 3.3 c)-d). The cantilevers shown in a) and c) were used during experiments at TUM. The shape was transferred to a 50 µm thick foil by optical lithography and released in a wet chemical etching process. Due to poor precision during this process regarding the control of tiny structures, the beam width d that was set to 0.2 or 0.6 mm was less uniform and up to 0.1 mm smaller than targeted. Microscope pictures of wet-etched CuBe cantilever beams are shown in appendix A.2. As we calibrate each of these cantilevers *in situ* during the experiment, the decreased beam width merely affects the reduction factor β for electrostatic calibration. We calculate β following [Wil04] and obtain 0.785 for 0.2 mm and 0.750 for 0.6 mm, respectively. Both values increase by less than 1.5 % when the beam width is adjusted to the uncertainty limit.
The cantilevers shown in Fig. 3.3 b) and d) were employed during experiments at the High Field Magnet Laboratory (HFML) in Nijmegen. The shape was laser-cut from an 80 µm thick foil, the beam width d was set to 0.8 or 0.2 mm. The reduction factor β was not needed, since no calibration was performed with these cantilevers (cf. Sec. 3.2.2). Moreover, the calculation of β following [Wil04] requires a rectangular paddle. For the sake of comparison to the TUM design, we roughly estimate β for the HFML design assuming a quadratic paddle of side length 3.5 mm and uniform

beams of length 4.5 mm and obtain 0.684 for 0.8 mm and 0.701 for 0.2 mm beam width, respectively.

3.1.2 Torsional cantilever magnetometer

The torsional cantilever magnetometer used in this work is part of a commercially available setup sold by *Quantum Design*. This physical property measurement system (PPMS) enables easy temperature and magnetic field control for exchangable measurement options as, e.g., specific heat or ac and dc magnetic susceptibility. For our experiments, we combined the horizontal rotator and torque magnetometer options. We limit the discussion in this section to a brief depiction of working principle and readout scheme followed by a description of the calibration routine. Problematic issues of the setup will be discussed in Sec. 3.3.2.
Fig. 3.4 a) shows a photograph of the torque option chip including cantilever and circuitry for calibration and readout. The general shape of the cantilever resembles the levers shown in Fig. 3.3, but instead of a metallic material, chip and cantilever of the torsional sensor are fabricated from silicon. According to the torque magnetometer option user's manual [Man17], two constantan piezoresistors are placed on the beams for readout. The paddle further features a single copper coil loop for calibration. The horizontal rotator option enables rotation of the whole chip around the x-axis with the magnetic field applied in the PPMS pointing along the z-axis. Fig. 3.4 b) shows the optional 3-leg modification of the sensor: A third beam connects the paddle to the chip top plane on the side opposed to the two standard beams. This modification prevents flexion of the cantilever and increases its torsional spring constant thus allowing for higher torques to be measured.
The working principle of the magnetometer is illustrated in Fig. 3.4 c). Alike the longitudinal case, the sample is mounted on the free-standing paddle of a flexible beam. At zero field, the magnetization M points along the easy axis (ea) of the material. When a magnetic field is applied, M is tilted away from the easy axis and the resulting torque tilts the paddle by an angle η. In contrast to the longitudinal case, the torsional cantilever is constructed to sense a torque in x-direction, i.e. along the beam. For this purpose, a piezoresistive readout scheme is employed which utilizes that any tilt of the cantilever paddle creates stress in the beams and is therefore reflected by changes of the piezoresistors R_1 and R_2. *Quantum Design* claims that the resistance changes are directly proportional to the exerted torque [Man17]. We discuss the validity of this assumption in later sections.
As indicated in Fig. 3.4 a) and b), the piezoresistors on the cantilever beams are incorporated into a Wheatstone bridge circuit that is integrated on the chip. The two high-precision resistors R_3 and R_4 completing the bridge are located in close vicinity to the cantilever. Placing all resistors in the same environment helps to diminish measuring errors due to field and temperature dependent resistance changes. The Wheatstone bridge is operated in constant current mode with an alternating dc current. Fig. 3.4 d) shows a circuit diagram of the bridge. During fabrication, the resistors are tuned to exhibit almost identical resistances so that the bridge is nearly

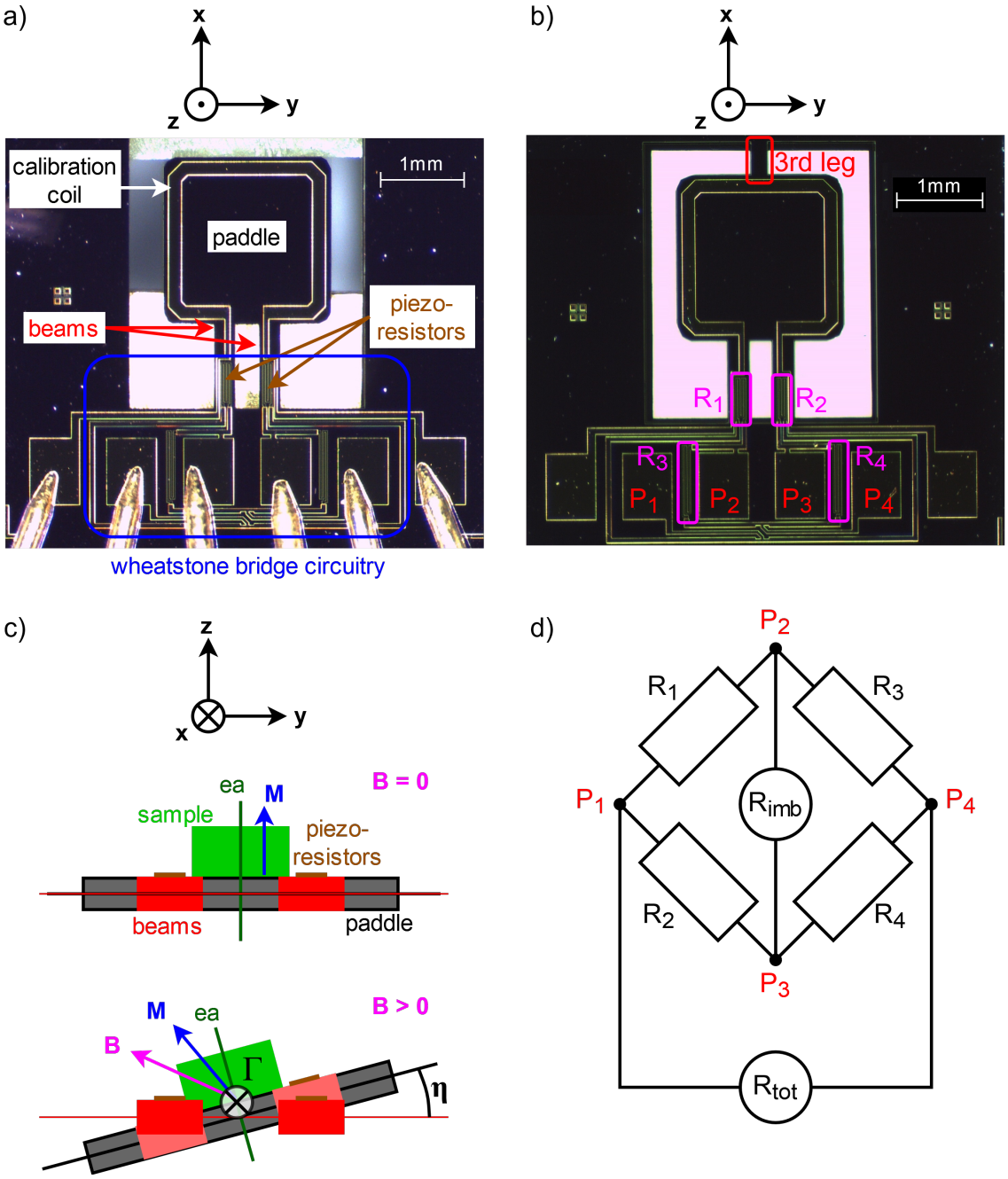

Figure 3.4: Torsional cantilever magnetometer. a) Photograph of the chip with lever and readout circuitry. b) 3-leg modification of the cantilever for higher moment. c) Working principle: At $\mathbf{B} = 0$ (upper sketch) the magnetization $\mathbf{M}$ points along the easy axis. At finite field, the equilibrium direction of $\mathbf{M}$ points between $\mathbf{B}$ and easy axis and the cantilever is twisted by a torque, resulting in different distortions of the two piezoresistors. The deviation is measured via a Wheatstone bridge integrated on the chip. d) Circuit diagram of the Wheatstone bridge where the resistors R_1 and R_2 are the piezoresistors on the beams and R_3 and R_4 are high-precision resistors on the chip as marked in b).

balanced, i.e., the bridge imbalance R_{imb} is close to zero without any torque applied. At this point, R_{imb} is proportional to small changes of individual resistors and the two arms of the bridge contribute to the imbalance with opposing signs [Sch07]:

$$R_{\mathrm{imb}} \propto \Delta R_1 - \Delta R_2 \,. \tag{3.17}$$

Consequently, a pure flexion of the lever, as shown in Fig. 3.1, does not contribute to the imbalance since the identical distortion of both piezoresistors cancels out. In contrast, when the cantilever is twisted by a magnetic torque as depicted in Fig. 3.4 c), the piezoresistors on the beams are distorted in opposing directions. The resulting bridge imbalance is proportional to the difference of both resistances and the bridge ratio r_{b}, i.e., the ratio of R_{imb} to the total resistance of the bridge R_{tot} scales linearly with the exerted torque:

$$\Gamma \propto \Delta\left(\frac{R_{\mathrm{imb}}}{R_{\mathrm{tot}}}\right) = \Delta r_{\mathrm{b}} \,. \tag{3.18}$$

Here, Δ denotes the difference from the zero-torque value which is usually finite due to residual mismatch of the resistances or external influences as, e.g., distortion by sample weight. In analogy to the capacitive readout of longitudinal operation, the piezoresistive readout for torsional operation favors the detection of a torque in x-direction over a torque in y-direction and we measure a projection of the full magnetic torque.

Calibration

Equation 3.18 can be rewritten as

$$\Gamma = c_\tau \cdot \left(r_{\mathrm{b}} - r_{\mathrm{b}}^0\right) \tag{3.19}$$

with the torque coefficient c_τ and the bridge ratio at zero torque r_{b}^0. The software supplied with the torque option allows for an automated calibration routine which aims to determine both c_τ and r_{b}^0 over the full temperature range accessible by the PPMS. In a first step, the temperature is set to its maximum and the horizontal rotator is positioned such that the normal on the cantilever paddle is orthogonal to the PPMS' magnetic field direction. From this state, the bridge ratio at zero field and zero current through the calibration coil is measured while the temperature is lowered to its minimum. The resulting curve is shown as red solid line in Fig. 3.5 a) and referred to as "baseline". As no field is applied, it represents the bridge ratio at zero torque $r_{\mathrm{b}}^0(T)$. The value measured during this process is subtracted from the bridge ratio for every measurement before conversion to torque. Once the minimum temperature is reached, the magnetic field is set to its maximum. An alternating dc current I is sent through the calibration coil inducing a magnetic moment

$$m = I \cdot A \,, \tag{3.20}$$

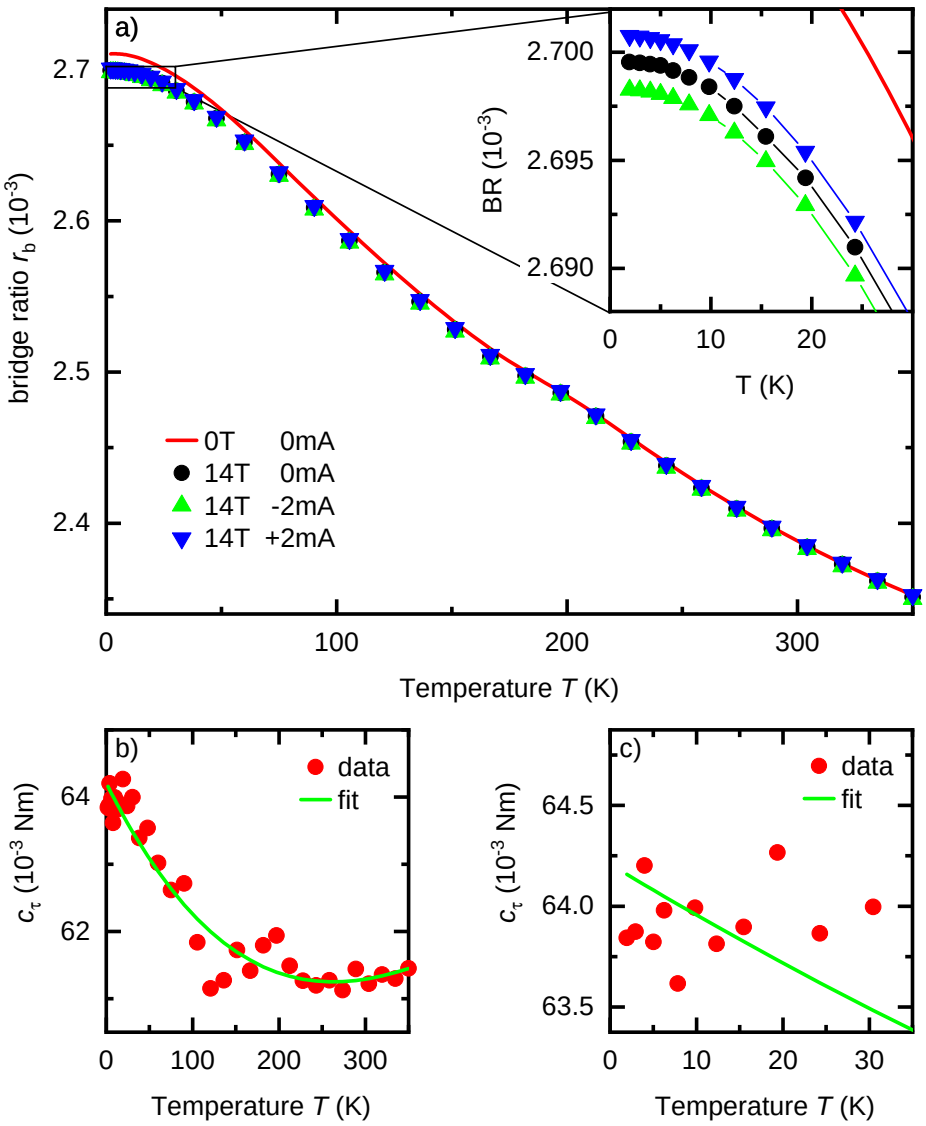

Figure 3.5: a) Bridge ratio measured during calibration procedure versus temperature. The red curve is measured during cooldown, data depicted by symbols is measured during warm-up. Magnetic field and current through the calibration coil are applied during warm-up to determine the torque coefficient c_τ. The inset shows a blow-up of the low temperature regime. b) Torque coefficients calculated from the data shown in a). c) Low temperature blow-up of b).

where A is the area enclosed by the coil. Consequently, a torque

$$\Gamma_{\text{coil}} = IAB \sin\theta \tag{3.21}$$

acts on the cantilever where θ is the angle between field B and moment m. As stated above, B points along the z-direction whereas m is orthogonal to the cantilever plane and thus perpendicular to B. The torque coefficient is then given by

$$c_\tau = \frac{2IAB}{\Delta r_{\text{b}}}\,, \tag{3.22}$$

where Δr_{b} denotes the bridge ratio difference for positive and negative current. This procedure is repeated at preselected temperature increments while the chip is warmed up to maximum temperature. The bridge ratio values measured at positive, negative and zero current during this phase are depicted as blue triangles, green triangles and black circles in Fig. 3.5 a), respectively. While the overall shape follows the zero-field curve closely, we observe a distinct deviation towards low temperatures. Fig. 3.5 b) and c) show the torque coefficients calculated from the bridge ratio values in a). The green solid lines depict a "best fit" applied by the PPMS software. Neither the fit function nor the residuum of the fit are given by the software, yet the maximum deviation of data points from the fit is smaller than 1.5 %. Similar to $r_{\text{b}}(T)$ in Fig. 3.5 a), the slope of $c_\tau(T)$ appears to tend to zero in the low temperature regime. This behavior is not reflected in the fit.

3.2 Setups for dHvA measurements

In order to probe the Fermi surface of a material via the dHvA effect, the prerequisites of high sample quality, high magnetic fields and low temperatures need to be met. Details on our samples will be provided in Sec. 4.1. Here we present the various setups employed in order to meet the temperature and field requirements. Together with technical details, we will also give estimates of the resolution for each setup. The minimum detectable magnetic moment change δM is calculated via

$$\delta M = \frac{\delta\Gamma}{B} = K \cdot \frac{\delta C}{B}\,, \tag{3.23}$$

where K is the calibration constant and δC is the smallest detectable capacitance change. As both K and δC depend on the angle of the sample stage, estimates are given exemplary at specific angles and fields. For the extraction of dHvA frequencies, the magnetic field resolution, i.e., the data point density during field sweeps must be considered as well since it limits the observable frequency range.
We pursued investigations in three different experimental environments. All magnets exhibit homogeneities sufficient to justify neglection of forces due to field gradients. Moreover, the oscillations we aim to observe are present in $M_\parallel$ as well (cf. Eq. 2.20) so that contributions of $M_\parallel$ tend to enlarge the oscillatory signal. In all setups, lon-

gitudinal CuBe cantilevers with capacitive readout were utilized and the capacitance was measured with an Andeen-Hagerling AH2700A capacitance bridge. We describe the setups featuring superconducting magnets in Sec. 3.2.1 and the resistive Bitter magnet setup in Sec. 3.2.2.

3.2.1 Superconducting magnet setups

For our investigations of the dHvA effect, we acquired data using two different superconducting magnet setups. In both, the TUM cantilever design with rectangular paddle shown in Fig. 3.3 a) was utilized. The beam width d was set to 0.2 mm. The cantilevers were calibrated at a single point C_0 since the overall capacitance changes were well below 10 % (cf. Sec. 3.1.1).
In a first experiment we combined an *ICE Oxford Ltd* ^{3}He-insert with a *Cryogenic Ltd* 15 T axial magnet. The insert allows for temperatures down to ∼280 mK and is equipped with a mechanically rotatable sample stage allowing for *in situ* rotation of the cantilever with respect to the magnetic field. The current position of the stage is monitored via a mechanical counter coupled to the rotation mechanism. A calibrated *Cernox* temperature sensor was mounted on the stage. The homogeneity of the magnet is specified to $5 \cdot 10^{-5}$ within 1 cm^3 around the field centre. In order to minimize the noise level, the cryostat was suspended on an active vibration-damping system. At $B = 10$ T and an angle of 82° between magnetic field and cantilever normal, we found a resolution of $\sim 5 \cdot 10^{-12}$ J/T.
In a second setup we employed a Joule-Thomson (JT) ^{3}He/^{4}He dilution refrigerator insert and a 14 T axial magnet both fabricated by *Oxford Instruments plc.* The insert allowed for temperatures down to ∼60 mK. The sample stage was set to a fixed angle and equipped with a batch-calibrated ruthenium oxide temperature sensor. The resolution at $B = 10$ T and an angle of 70° between magnetic field and cantilever normal was estimated to $\sim 1 \cdot 10^{-11}$ J/T.
Both magnets are superconducting solenoids immersed in liquid helium. As their operation does not produce an appreciable amount of heat, the liquid helium boil-off rate is low enough so that the magnets can maintain their maximum field for days without disruption. Thus the setups allow for almost arbitrarily slow magnetic field variation and, with regard to our experiments, for very high data point density. To keep measurement duration at a reasonable scope, we recorded data at 1-5 points per mT.

3.2.2 High magnetic field laboratory setup

In addition to our experiments with superconducting magnets, we performed a number of measurements in the High Field Magnet Laboratory (HFML) in Nijmegen in the Netherlands which provides access to Bitter type magnets. These resistive solenoids are constructed of slotted copper plates separated by insulating layers [Web16]. De-ionized water is pressed through the slits at high flow rates to dissipate the enormous amounts of heat produced during operation. The high-throughput

water-cooling results in high mechanical noise levels compared to typical laboratory magnet setups. The magnet used for our measurements provides fields up to 35 T at a homogeneity of $\sim 1 \cdot 10^{-3}$ within 1 cm^3 around the field centre.
The cantilever design with circular shaped paddle shown in Fig. 3.3 b) was used with beam widths d of 0.2 and 0.8 mm. Cantilevers were mounted on a mechanically rotatable stage equipped with a *Cernox* temperature sensor and a Hall sensor for accurate angle determination. In addition, the Hall sensor was used to position the sample exactly in the field centre. The rotation stage was mounted in a bespoke sample-in-liquid ^{3}He-system allowing for temperatures down to 300 mK. We employed an active damping suspension for the probe to counteract mechanical noise.
Due to limited time in the facility, no electrostatic calibration was performed. A generic calibration for the HFML cantilevers can be found in appendix A.3. Using the value given for $d = 0.2$ mm, the resolution was estimated to $\sim 6 \cdot 10^{-10}$ J/T at 30 T and 85° between field and cantilever normal. Due to limitations of cooling, the employed magnet can maintain fields above 25 T for rather limited time periods only. Consequently, the field range from 25 to 35 T had to be covered within ∼45 minutes limiting data point density to ∼0.13 points per millitesla.

3.3 Setup for anisotropy measurements

The most direct way to investigate the magnetic anisotropy of a material is to measure the angular dependence of the magnetic torque $\Gamma(\varphi)$. A well controlled rotation of sample and magnetic field with respect to each other is essential for such experiments. We pursued two different approaches to fulfill this requirement. In Sec. 3.3.1 we describe our setup with magnetic field rotating around a fixed sample, Sec. 3.3.2 is dedicated to the alternative approach of a rotating sample in a fixed field. Finally, we give details on the alignment of magnets, cantilevers and samples in Section 3.3.3.

3.3.1 Rotating field setup

Our experiments with rotating field employed longitudinal CuBe cantilevers with capacitive readout. The cantilever design with rectangular paddle was used with beam widths d of 0.2 mm and 0.6 mm (cf. Fig. 3.3 a)) and the capacitance was measured by an Andeen-Hagerling AH2700A capacitance bridge. During measurements, the capacitance changed by up to 30 %. We therefore determined $K(C_0)$ conducting a number of electrostatic calibrations and assuming a linear relation between K and C_0^{-2} (cf. Sec. 3.1.1). Resolutions were estimated in the manner described in Sec. 3.2. At 1 T and 0° between field and cantilever we obtain resolutions better than $\sim 7 \cdot 10^{-11}$ and $\sim 12 \cdot 10^{-11}$ for $d = 0.2$ mm and $d = 0.6$ mm, respectively.
A ^{3}He-insert fabricated by *Oxford Instruments plc* was utilized allowing for temperatures from ∼280 mK up to ∼50 K. Earlier experiments using this probe and featuring a calibrated temperature sensor mounted directly on the sample stage demonstrated negligible temperature gradients between sample stage and ^{3}He pot. Therefore, no

temperature sensor was mounted on the sample stage for our experiment to reduce electrical noise. Instead, the temperature was monitored by two sensors located at the ^{3}He pot roughly 11 cm above the sample. Temperatures down to 2 K were measured by a *Cernox* sensor, at temperatures below 2 K a calibrated RuO_2 sensor was employed. Measuring head, i.e. the part of the probe below the ^{3}He pot, and sample stage were machined from copper. The angle of the stage was fixed without the possibility of *in situ* rotation.
Additional measurements were performed using a different ^{3}He insert. The information given on the first probe holds true for the second insert except that measuring head and sample stage were made of the machinable ceramic Macor. Unfortunately, one of the capillaries necessary for low temperature operation turned out to be magnetic on this insert. Its magnetization was reflected in our measurements rendering proper evaluation of data acquired with this system nearly unfeasible.
To generate the rotating magnetic field, we used a superconducting vector magnet purchased from *American Magnetics Inc.* The system consists of a 9 T solenoid for vertical field fastened in the centre of a 4.5 T split coil for horizontal field. The specified homogeneities within a 1 cm diameter spherical volume (DSV) around the field centre are $1 \cdot 10^{-3}$ and $5 \cdot 10^{-3}$ for solenoid and split coil, respectively. The joint operation of both coils allows for an angular resolution of well below 1° at 100 mT.

Hall probe investigation

Due to constructional adjustments on the cryostat, we conducted a Hall sensor study of the magnet system prior to our experiments. The major objective of this investigation was to determine the exact vertical distance of both magnet coils' field centres to the cryostat top flange. As an additional benefit, the data yields a possibility to estimate the field gradients along the vertical axis. In the following we refer to the vertical direction, i.e. the field direction of the solenoid as z-direction and the horizontal field direction of the split coil as y-direction.
In order to examine the magnet, a probe equipped with three Hall sensors was inserted into the cryostat. The sensors were arranged orthogonal to each other and, due to the design of the probe, at different distances to the probe end. As a consequence, only one Hall sensor could be placed in the field centre at a time. By construction, one Hall sensor was adjusted to sense magnetic field in the z-direction. A second one was adjusted to sense field in y-direction by using its signal in a field applied only by the split coil. The third Hall sensor thus monitored the x-direction, i.e. the direction orthogonal to both y and z. During a full field rotation at 1 T, the x-sensor showed a maximum signal of 1 % compared to the y-direction Hall sensor. For a field aligned perfectly in y-direction, this corresponds to a misalignment of the Hall probe of $\sim$0.6°. An angular error of this size is easily introduced during our manual adjustment of the probe. We thus consider residual field components in x-direction as negligible and dicuss data on y- and z-directions only.
To determine the field centre position, we changed the height of the probe within the cryostat in steps of 1 mm and measured the Hall resistance at each position.

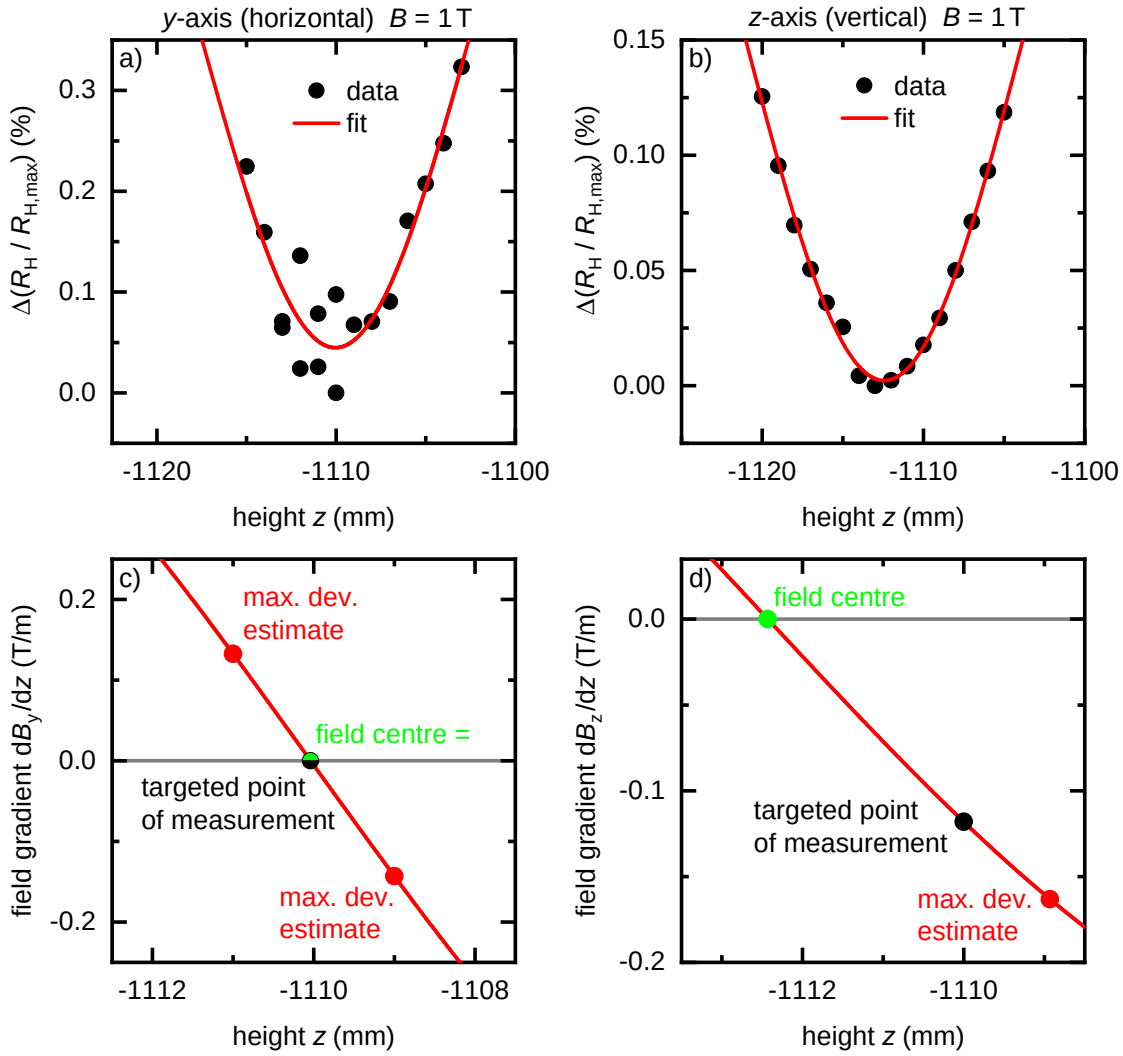

Figure 3.6: a)-b) Relative change of Hall voltage versus height z below cryostat top flange for horizontal (left) and vertical (right) field. Black circles depict data points, red curves display Gaussian fits. c)-d) Field gradients in z-direction as obtained from the Gaussian fits' first order derivatives.

This process was performed twice, once with a magnetic field in the z-coil and once with magnetic field in the y-coil only. The data obtained is shown as black circles in Fig. 3.6 a) for field and sensor in y-direction and Fig. 3.6 b) for field and sensor in z-direction. The values are expressed as relative changes compared to the maximum Hall resistance and the height is measured from the cryostat top flange. The data for the horizontal y-direction exhibits significantly higher fluctuations. These may stem from tiny rotations around the z-axis introduced during manual height adjustments. In a phenomenological approach, Gaussian fits are applied to the data and depicted as red curves in Fig. 3.6 a) and b). The field centres are determined from the fits' minimum positions to be located at -1110 mm for the y-coil and at -1112.5 mm for the z-coil. Strikingly, the field centres of solenoid and split coil are separated by

more than 2 mm.
In order to decide where to locate our sample during measurements, we consider the impact of field gradients along z. For this purpose, the derivatives of the Gaussian fits are depicted in Fig. 3.6 c) and d) for y-coil and z-coil, respectively. Here, they are expressed in units of absolute field gradients, i.e. T/m, at the applied field of $B = 1\,\mathrm{T}$. Since these gradients grow proportional to the applied magnetic field, we discuss their magnitudes in terms of gradient per field in the following, i.e. estimates are given in units of $(\mathrm{T/m})/\mathrm{T} = \mathrm{m}^{-1}$.
The field gradient of the y-coil grows more than twice as fast with distance from the field centre compared to the z-coil. We consequently decide to locate our sample in the centre of the y-coil for measurements and accept the smaller gradients imposed by the distance to the z-coil field centre. This is illustrated by highlighted data points in Fig. 3.6 c)-d). For the y-coil, the field centre and the targeted point of measurement, i.e. the position of our sample, coincide (black and green circle). For a systematic uncertainty of $\pm 1\,\mathrm{mm}$ in the location of our sample, we expect a maximum field gradient of $0.15\,\mathrm{m}^{-1}$ from the split coil (red circles). For the solenoid, the sample is placed $\sim$2.5 mm above the field centre (black and green circles). Together with the height uncertainty, we expect a maximum field gradient of $0.17\,\mathrm{m}^{-1}$ (red circle).
Apart from gradients along z, field gradients along x- and y-directions may influence our measurements. As we have no position dependent Hall sensor data for these directions, we assess their contributions based on the magnet specifications and experimental conditions. For a rough estimate, we assume a linear decrease of the field from its centre to the edge of the 1 cm DSV for which the homogeneity is specified. Field changes of 0.5 % and 0.1 % for y-coil and z-coil then yield field gradients within this volume of $1\,\mathrm{m}^{-1}$ and $0.2\,\mathrm{m}^{-1}$, respectively[2]. Our measurement geometry favors the detection of forces in z-direction over forces along x and y by factors of $\sim$60 and $\sim$10, respectively (cf. Sec. 3.3.3 and Ch. 5). Consequently, horizontal gradients of the z-coil are neglected since their contributions to the measurement signal are small compared to the expected gradient in z-direction as well as to its uncertainty. The same holds for x-directed gradients of the y-coil. The only relevant contribution from horizontal gradients is thus the y-directed gradient of the split coil. A value of $1\,\mathrm{m}^{-1}$ is a reasonable upper boundary considering that the assumptions used for estimation hold for a gradient along z as well which according to the derivative of the fit shown in Fig. 3.6 amounts to roughly $0.6\,\mathrm{m}^{-1}$ at 5 mm distance to the field centre.
In addition to the height dependent measurements of Hall resistances at fixed fields, we recorded the Hall sensor signals of sweeps and rotations of the magnetic field as applied during sample measurements. The results are shown in appendix A.4. For the most part, the observed signals resembled the expected behavior. While the curves exhibits some minor disturbances, we did not encounter any irregularities on a scale relevant to our experimental results.

[2] A Gaussian bell shape as shown in Fig. 3.6 a) and b) is a more realistic shape for the field decrease around its centre. While such a curve exhibits steeper slopes at the DSV edges, the slope in the field centre is zero. A linear decrease is thus an acceptable assumption for a rough estimate of the gradient.

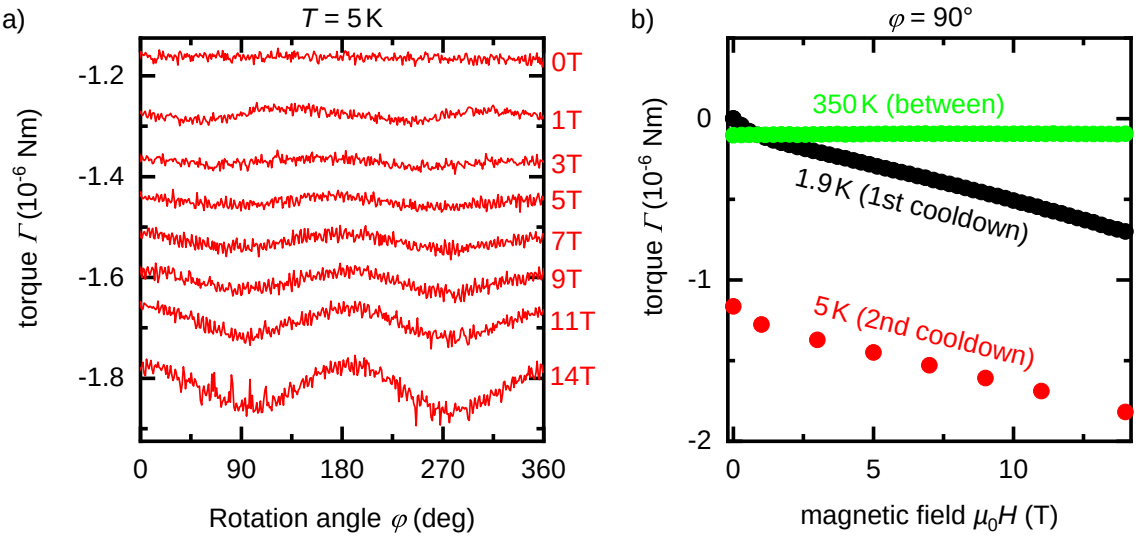

Figure 3.7: Torque signal of an empty 3-leg cantilever. a) Angular dependence measured at $T = 5\,\mathrm{K}$ and in various magnetic fields. Note that data for different fields are not "shifted for clarity". b) Magnetic field dependence measured at different temperatures. Data depicted as green and black circles has been recorded at $\varphi = 90°$ during the calibration process. The red circles represent the mean values of the rotation curves shown in a).

3.3.2 Rotating sample setup

Complementary to our experiments in the vector magnet, we performed anisotropy measurements in an environment with fixed magnetic field and rotating sample. We employed a commercially available *Quantum Design* PPMS equipped with horizontal rotator and torque magnetometer options. The setup allows for temperatures from 1.9 K up to 400 K and magnetic fields up to 14 T. The field is applied in vertical direction and the homogeneity of the solenoid is specified to 10^{-3} within a 1 cm DSV around the field centre. The torque magnetometer option utilizes the torsional cantilever with piezoresistive readout described in Sec. 3.1.2. The magnetic moment resolution at 14 T is specified to $7 \cdot 10^{-11}$ J/T. The chip is placed in the setup such that the cantilever senses torque in a direction perpendicular to the magnetic field. The horizontal rotator option enables rotation of the cantilever around this projection axis. Possible deviations of projection axis and rotation axis are discussed in the following section. An angular resolution of 0.005° is specified for the rotator.
For each deployed cantilever chip, we conducted the calibration routine described in Sec. 3.1.2. A fault in the software incorrectly scaling the torque coefficients by a factor of ∼1.38 could be corrected. Yet several conceptual drawbacks remain in the setup. As sample and cantilever are rotated around a horizontal axis, gravity effects may influence the measured signal during rotations. Further, a force due to a field gradient may be superimposed to the magnetic torque. Both effects follow a single-fold sine curve during rotation.
Further disturbances arise from resistance changes in the readout circuit due to variations of temperature and magnetic field. We illustrate these issues with the

aid of Fig. 3.7. Graph a) shows the torque as measured by the PPMS software obtained from an empty 3-leg cantilever during rotation at 5 K and various fields. The angle φ denotes the angle between cantilever normal and magnetic field. We immediately make two main observations: First, the torque varies distinctly with the angle. Second, the mean value around which the angular dependency unfolds shifts systematically with magnetic field magnitude. This second observation is illustrated further in graph b) where the field dependence of torque is shown. The mean values of the rotational measurements in a) are depicted as red circles. Here, we notice the third important observation: The torque at zero field is not at or even near zero. The green and black circles denote torque data from field sweeps at 90° between field and cantilever normal and 350 K resp. 1.9 K. As denoted in the graph, the low temperature field scan was measured before the field scan at 350 K. The rotations were recorded last. While the low temperature field scan exhibits a similar field dependence compared to the mean values of the rotation scans, it is distinctly shifted. The black curve begins at zero torque by construction, since the depicted field sweep was recorded during the calibration routine and thus contains the exact value of the baseline r_b^0 at zero field. The high temperature curve is almost constant over the whole field range but has a non-zero value at zero field.
The main conclusion drawn from the above observations is that the concept of the baseline r_b^0 described in Sec. 3.1.2 is inadequate. The idea of r_b^0 is to measure a zero-torque reference for the bridge ratio r_b. However, r_b depends on angle and magnitude of the magnetic field as well as on the temperature and its history. Consequently, we need to renew the zero-torque reference after every temperature change. Moreover, it is important to keep the empty-cantilever signal's dependence on the field magnitude and angle in mind when evaluating data from sample measurements.
In addition to the data shown in Fig. 3.7, we measured field dependent torque curves in the same temperature state as the depicted rotations at several angles. All of them showed a very similar field dependence in close coincidence with the mean values of the rotation scans. The curves are not shown in the graph for the sake of clarity, yet they clearly imply that the angular dependence of the empty-cantilever signal develops evenly around the field-dependence. From the curves in Fig. 3.7 a) we infer a two-fold rotation symmetry of the magnetoresistive contribution to our signal.So far, we have discussed gravitational and field gradient forces, magnetoresistance and thermal cycling as possible causes for measurement errors. The list is extended by the uncertainty of the torque coefficients c_τ discussed in Sec. 3.1.2. All in all, we may expect a large systematic error for measurements in the PPMS. The systematics of individual erroneous contributions still allows us to obtain a comprehensible set of data. We discuss the data handling with respect to these errors in Sec. 5.2.1.

3.3.3 Orientations

During the experiments described in the foregoing sections, the alignment of sample, cantilever and magnet with respect to each other is of paramount importance. Following the experimental conditions, we address the alignment of sample and

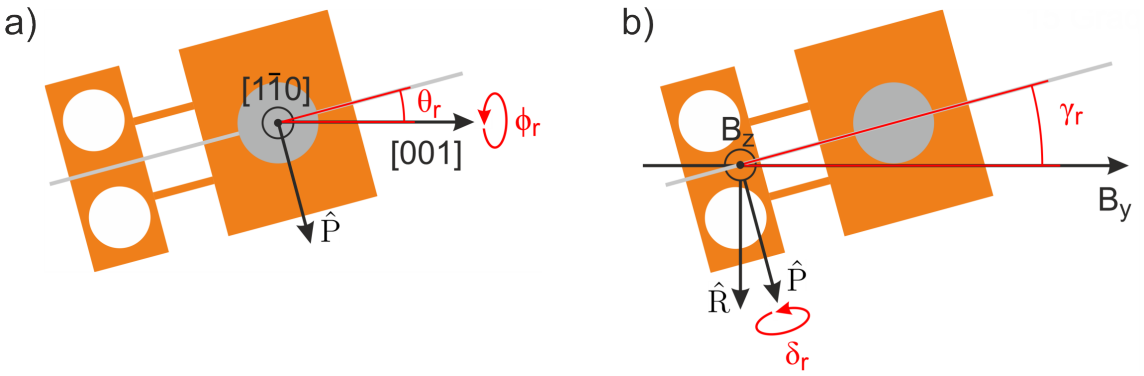

Figure 3.8: Definition of misalignment angles for longitudinal cantilevers in the rotating field setup. a) Misalignment of sample and cantilever. Crystal directions are given exemplary for the MnSi sphere. For the orientation of the cubic sample, see main text. b) Misalignment of cantilever and magnet.

magnet not directly but in terms of a two-step process: First we discuss the orientation of our sample's crystallographic axes with respect to the cantilever. Then we turn to the adjustment of the cantilever's projection axis and magnetic field rotation axis.
In our anisotropy experiments, we employed samples with cubic and spherical shapes all of which exhibit a cubic crystal structure. Samples of both shapes have been used with both setups. We define the situation where the crystallographic [110]-direction is parallel to both the cantilever projection axis $\hat{P}$ and the rotation axis $\hat{R}$ as ideal alignment. In the following, we describe our efforts to determine and minimize deviations from the ideal orientation for each combination of sample and setup. Before giving details on the practical implementation, we define all potential misalignment angles.
For ideal alignment, the [1$\bar{1}$0]-direction as well as the [001]-direction are orthogonal to $\hat{P}$. Deviations from this ideal are sketched in Fig. 3.8 a) for a spherical sample on a longitudinal cantilever. The angles ϕ_r and θ_r describe rotations around the [001]- and [1$\bar{1}$0]-directions, respectively. The sketch in Fig. 3.8 b) illustrates alignment of a longitudinal cantilever in the vector magnet system. For ideal alignment, $\hat{P}$ and $\hat{R}$ are parallel to each other. Rotations around the vertical magnet axis B_z are denoted by γ_r. A rotation around the projection axis is denoted by δ_r. While such a tilt does not change the relative orientation of $\hat{P}$ and $\hat{R}$, it changes the rotation plane with respect to the crystal unless γ_r is zero and must therefore be included in our consideration. Rotation of the cantilever around an axis along its beams is prohibited by construction of the sample stage.
The alignment of a sample on a torsional cantilever in the rotating sample setup is represented in Fig. 3.9. The adjustment of the crystal axes with respect to $\hat{P}$ is depicted in sketch a) in full analogy to the longitudinal cantilever. An analog to δ_r is prohibited by construction of the probe. Instead, a deviation of $\hat{P}$ from $\hat{R}$ around an axis parallel to the cantilever normal is possible as shown in Fig. 3.9 b). We denote this deviation by β_r. A rotation around an axis perpendicular to $\hat{P}$ and the

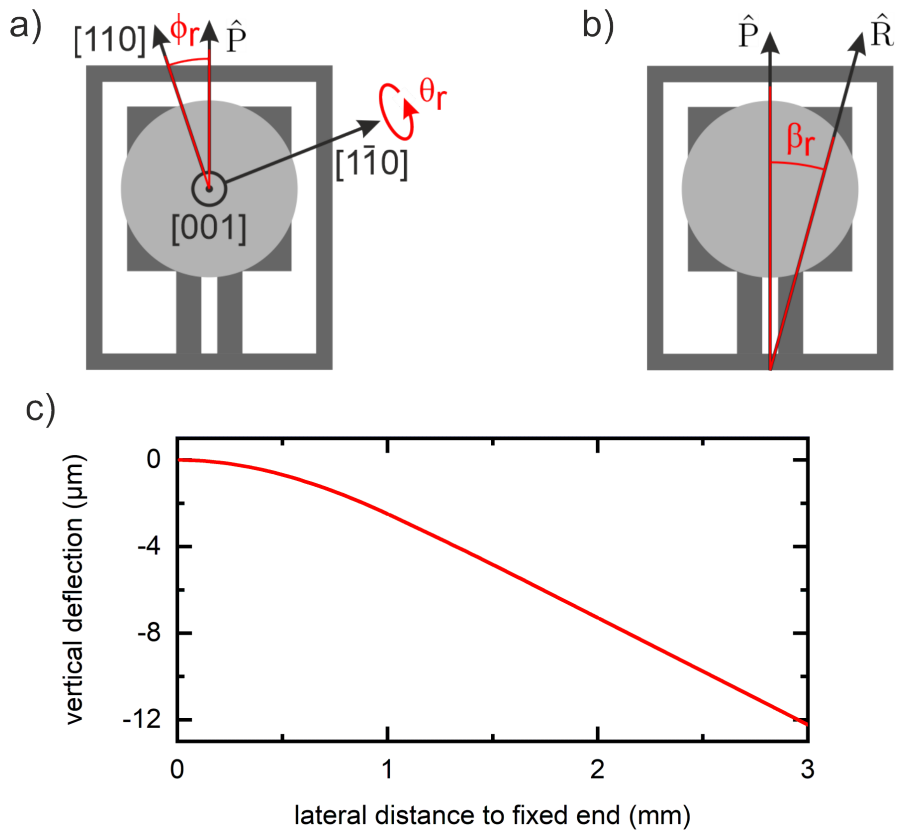

Figure 3.9: Definition of misalignment angles for torsional cantilevers in the rotating sample setup. a) Misalignment of sample and cantilever analogous to the longitudinal case. b) Misalignment of cantilever projection axis and rotation axis. c) Longitudinal bending of a torsional cantilever due to sample weight. The maximum misalignment angle is smaller than 0.3°.

cantilever normal in Fig. 3.9 b) constitutes a misalignment of the cantilever chip analogous to γ_r. While such a rotation is prohibited for the chip by construction, longitudinal bending of the cantilever can introduce a deviation in this direction. We used the formulas given in appendix A.1 to calculate the bending of our torsional cantilever due to sample weight. The result is shown in Fig. 3.9 c) for our heaviest sample of 31 mg. According to the calculation, the paddle bends down no more than ∼12 µm and thus creates a maximum deviation of less than 0.3°. Estimates on the magnitude of the other misalignment angles will be given for each specific sample and setup in the following sections.

Alignment of samples on cantilevers

As stated above, we employed both spherical as well as cubic samples with both longitudinal and torsional cantilevers. The potential misalignment is identical for both cantilever types. The orientation of cubic samples on cantilevers was done by hand aligning the cube edges parallel to the paddle edges by visual estimate.

1 Detection screen
2 X-ray ejection tip
3 Rail
4 x-z-Translation stage
5 Vacuum pump
6 Sample holder connector for vacuum pump
7 Goniometer
8 x-y-z-Positioning tool for cantilever
9 Sample-mounting face of sample holder
10 Cantilever holder
11 platform holder for PPMS cantilever mounting
12 alternative holder with CuBe cantilever

Figure 3.10: Laue camera setup for aligned attachment of spherical samples to cantilevers.

Microscope images show tilts ϕ_r and θ_r of less than 1° on a longitudinal and less than 2° on a torsional cantilever. We note that for the cubic sample on the longitudinal cantilever the [001]- and [1$\bar{1}$0]-direction perpendicular to the projection axis were not parallel to the cube's edges. The cube mounted on a torsional cantilever was tilted by ∼13° around an axis along the beam. Both changes merely introduce a linear shift of the rotation angle to the data as long as the direction of $\hat{R}$ with respect to $\hat{P}$ is not considerably affected. We discuss such deviations in the next section.
The orientation of spherical samples represents a more challenging task. As no crystallographic directions are noticeable by eye, we employed an x-ray setup to visualize and adjust the crystal orientation. A photograph of the so-called Laue camera is shown in Fig. 3.10 together with a description of its principal parts. The ejection tip (2) directs an x-ray beam into the chamber, the detection screen (1) collects photons scattered back from the sample. A rail (3) is fastened on an x-z-translation stage (4) and aligned parallel to the x-ray beam. A three-axis goniometer (7) allowing for arbitrary rotations is mounted on the rail. For our specific purpose,

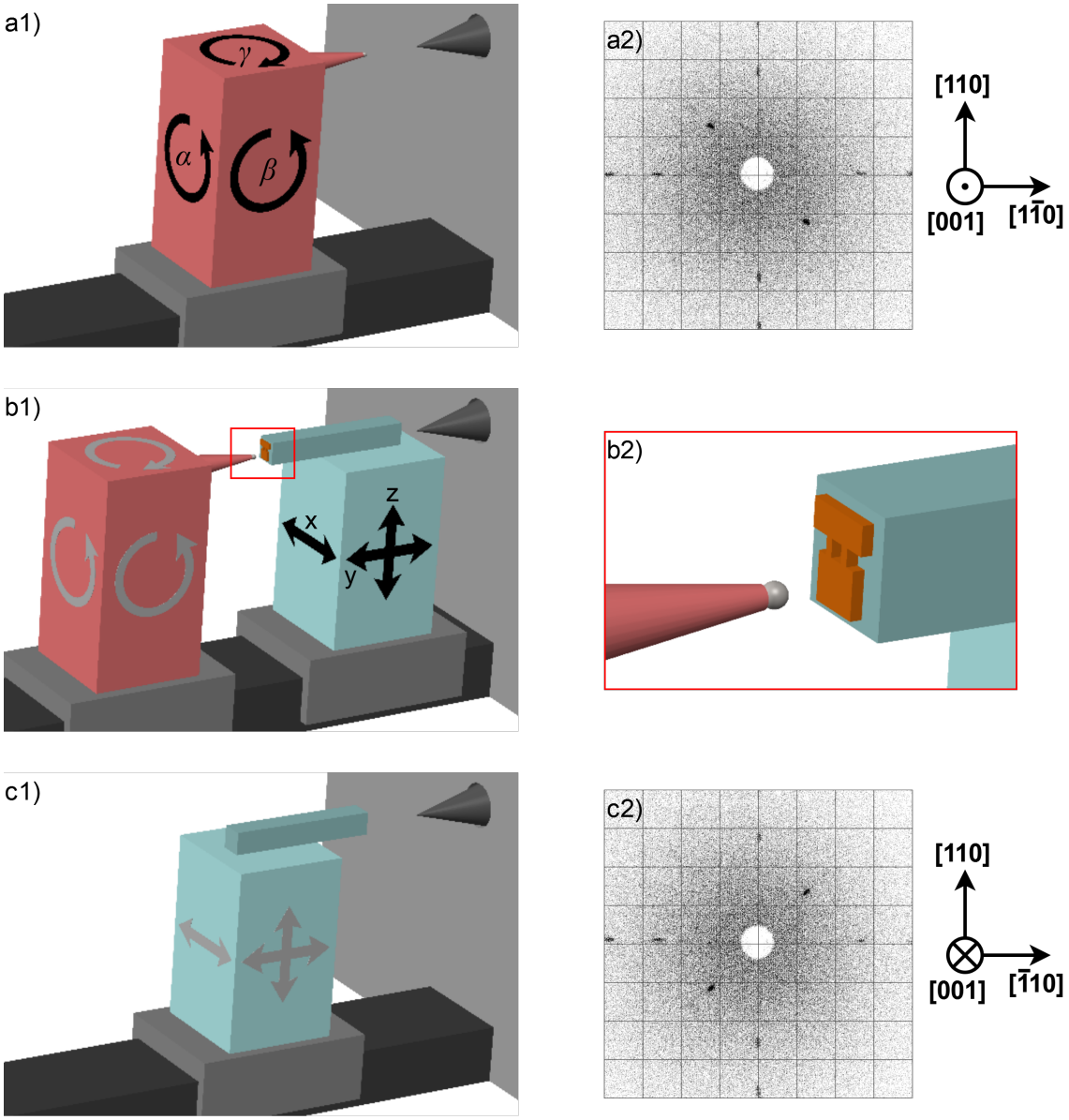

Figure 3.11: Schematic of the attaching process for spherical samples on cantilevers. a1) The sample is mounted on a three-axes goniometer and aligned with respect to the x-ray beam. a2) X-ray image of the well aligned sample on the goniometer. b1) The angles α, β and γ are fixed on the goniometer and the cantilever is positioned with the x-, y- and z-translation stages. b2) Blow-up of sample and cantilever in b1). c1) After the sample is attached to the cantilever, the orientation is checked again. The corresponding x-ray image is shown in c2).

we utilize a vacuum pump (5) connected to a hollow sample holder (6) that carries the sphere (9) and is fitted to the goniometer. We further constructed a bespoke three-axis translation stage (8) that can be mounted on the rail. Different holders can be installed on this positioning tool in order to carry torsional (10,11) or longitudinal cantilevers (12).
The sample mounting process in sketched in Fig. 3.11. In a first step, the sample is mounted on the goniometer. Instead of being glued to the sample holder, it is held in place by the suction of the vacuum pump allowing for instantaneous and complete detaching once the pipe is vented. This is of particular importance since our mechanically sensitive cantilevers are easily damaged by the mechanical forces which an adhesive on the sample holder might exert during separation. While the sphere is mounted on the goniometer, the sample's crystallographic axes are aligned with respect to the x-ray beam as schematically depicted in Fig. 3.11 a1). An exemplary x-ray image obtained during this process in shown in Fig. 3.11 a2) together with the inferred crystallographic directions. Once the sample is adjusted as desired, the x-rays are turned off and the goniometer angles are fixed. We then mount the x-y-z-positioning tool carrying a cantilever on the rail. As depicted in Fig. 3.11 b1) and b2), the translation stage is constructed such that the cantilever approaches the sample exactly along the x-ray beam path. The cantilever paddle is adjusted to meet the sample by x- and z-translations and glue is applied to the paddle surface before the two parts are brought into contact. After the glue has dried, the vacuum pipe is vented and cantilever and sample are carefully removed from the goniometer. Finally, the correct orientation of the sample on the sensor is again probed with the x-ray beam as depicted in Fig. 3.11 c1) and c2).
The described process was performed once for each a longitudinal and a torsional cantilever. The corresponding x-ray images are shown together with inferred crystal directions in appendix A.5. From the scattering pattern we can also extract the misalignment angles ϕ_r and θ_r. On the longitudinal cantilever, both angles amount to less than 0.5°. On the torsional cantilever, ϕ_r is similarly small while θ_r amounts to $\sim$1°.

Cantilever and magnet

The orientation of the probe in the cryostat, i.e. the cantilever-to-magnet alignment was accomplished in different ways for each setup configuration. In the PPMS setup, height and orientation of the probe inside the cryostat are fixed by construction. As stated above, no analog to δ_r is possible and the gravity induced γ_r is smaller than 0.3°. A misalignment around the cantilever normal β_r can be realized by improper mounting of the cantilever chip on the rotator platform. While a deviation of 4° is the maximum possible value, careful handling of the chip implies an upper boundary of $\lesssim$1°.
The alignment of longitudinal cantilevers in the vector magnet setup is less straightforward. In addition to γ_r and δ_r, the correct height of the probe has to be considered. We employed the ^{3}He insert with copper sample stage for measurements on a spherical

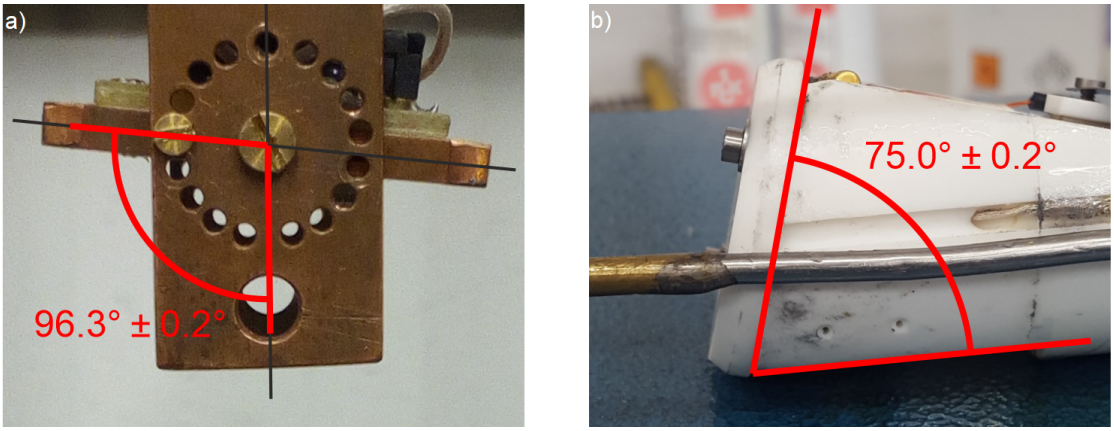

Figure 3.12: Angle between sample stage and probe axis in the ^{3}He system used for measuring a) a spherical sample and b) a cubic sample. Following the definition of δ_r in Fig. 3.8, the displayed angle is roughly $90°+\delta_\mathrm{r}$ in a) and $90°-\delta_\mathrm{r}$ in b).

sample and the insert with Macor stage for a cubic sample. The angle δ_r can be inferred from photographs for both probes as depicted in Fig. 3.12. The picture in a) shows the ^{3}He insert with the copper sample stage, b) depicts the one made from Macor. Following our definition, we obtain values for δ_r of $\sim$6° and $\sim$15°, respectively. As stated before, at $\gamma_\mathrm{r} = 0$ the deviation δ_r merely shifts the measured data along the rotation angle. In contrast, γ_r can strongly distort our torque signal. Therefore we did not attempt to minimize δ_r but focus on γ_r. For this purpose as well as for the height adjustment, we pursued different approaches with the two probes. Following the chronology of our experiments, we begin with the Macor probe used for measuring a cube.

Our measurements on the cubic sample preceded the Hall probe investigation described in Sec. 3.3.1. We attempted to infer the correct installation depth of the insert as well as a position with minimal γ_r directly from torque measurements. The graph in Fig. 3.13 a) shows typical torque data acquired during field rotation at a temperature of 1.5 K and magnetic field amplitude of 0.65 T. The field was rotated by 360° in both senses as indicated by the arrows. The angle φ is measured from the positive field direction of the horizontal split coil, i.e. the y-direction towards the positive field direction of the vertical solenoid, i.e. the z-direction. The green, black and red lines denote measurements between which the probe was rotated around the vertical field axis, i.e. γ_r was changed. We observe distinctly different amplitudes of the minimum close to 0° and 180°, i.e. where the field approaches the horizontal axis. The black line exhibit the largest signal at the minimum. The red and green lines correspond to positions deviating from the position of the black curve in opposing directions. We conclude that γ_r is minimal for the position yielding the largest signal for horizontal field, i.e. the position corresponding to the black line.

In order to determine the position of the field centre, we measured the angular dependence of the torque as shown in Fig. 3.13 a) at several installation depths and evaluated the integral over full 360° rotations. While the integral of a pure

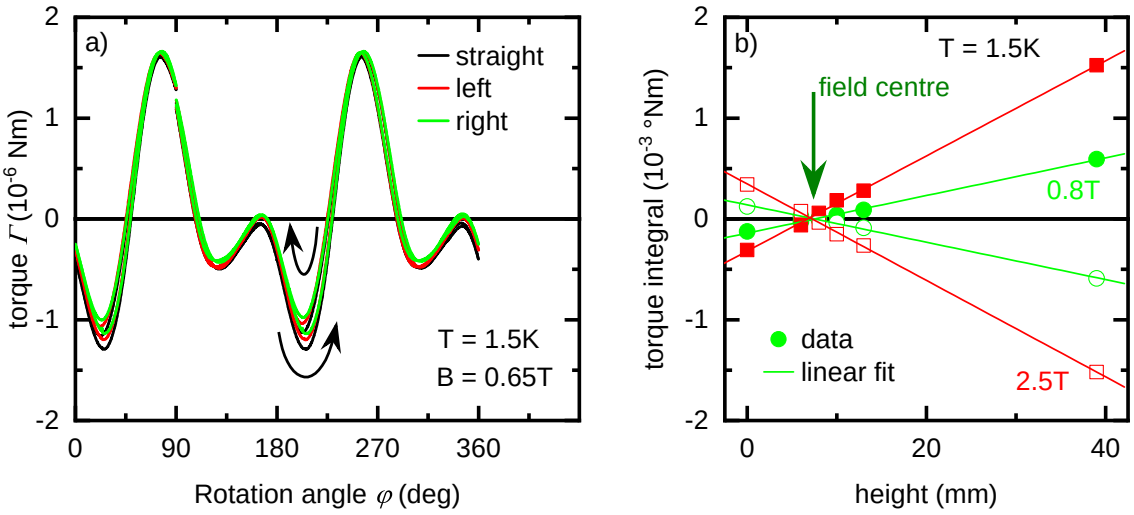

Figure 3.13: a) Torque signal versus angle at 1.5 K and 0.65 T. The probe has been rotated partly around its axis in the cryostat between measurements. The position with the largest signal (black curve) is taken to be the one with the best alignment of cantilever and magnet. b) Integral of the torque during a 360°-field rotation versus height over the bottom position measured at 1.5 K and 0.8 T (green circles) resp. 2.5 T (red squares). Solid lines represent linear fits. Filled symbols depict positive rotation sense, empty symbols depict negative rotation sense. The field centre is taken to coincide with the intersection of all linear fits at zero.

magnetic torque signal is expected to amount to zero over a 360° rotation, forces due to field gradients introduce asymmetric signals resulting in finite torque integrals. Corresponding data is shown in Fig. 3.13 b) where the torque integral is plotted versus the height of the probe above its lowest possible position. All data was recorded at 1.5 K. Red squares depict data from rotations with field magnitude of 2.5 T, green circles depict measurements at 0.8 T. Angular scans in positive and negative rotation sense were recorded. Filled symbols in the graph depict positive rotation sense, empty symbols depict negative rotation sense. All data sets were fitted with a linear function. Field gradients are expected to be zero in the field centre and increase their magnitude with opposing sign when moving away from the field centre in opposing directions. We therefore conclude from Fig. 3.13 b) that the field centre coincides with the height where the four linear fits intersect at zero. All sample measurements were consequently performed at this height of ∼7 mm.
While the described procedure appears as a comfortable method to adjust the probe within the cryostat, it suffers from two major blind spots. The conducted process neither allows any quantitative estimate of residual errors regarding γ_r and the installation depth nor does it enable us to make an educated guess regarding the influence of potential field gradients. Furthermore, it relies on our measurement technique without considering possible disturbances. As we mentioned above, the probe used during this process disturbed our measurements due to the magnetization of a capillary. Thus both the minimization of γ_r and the height adjustment performed

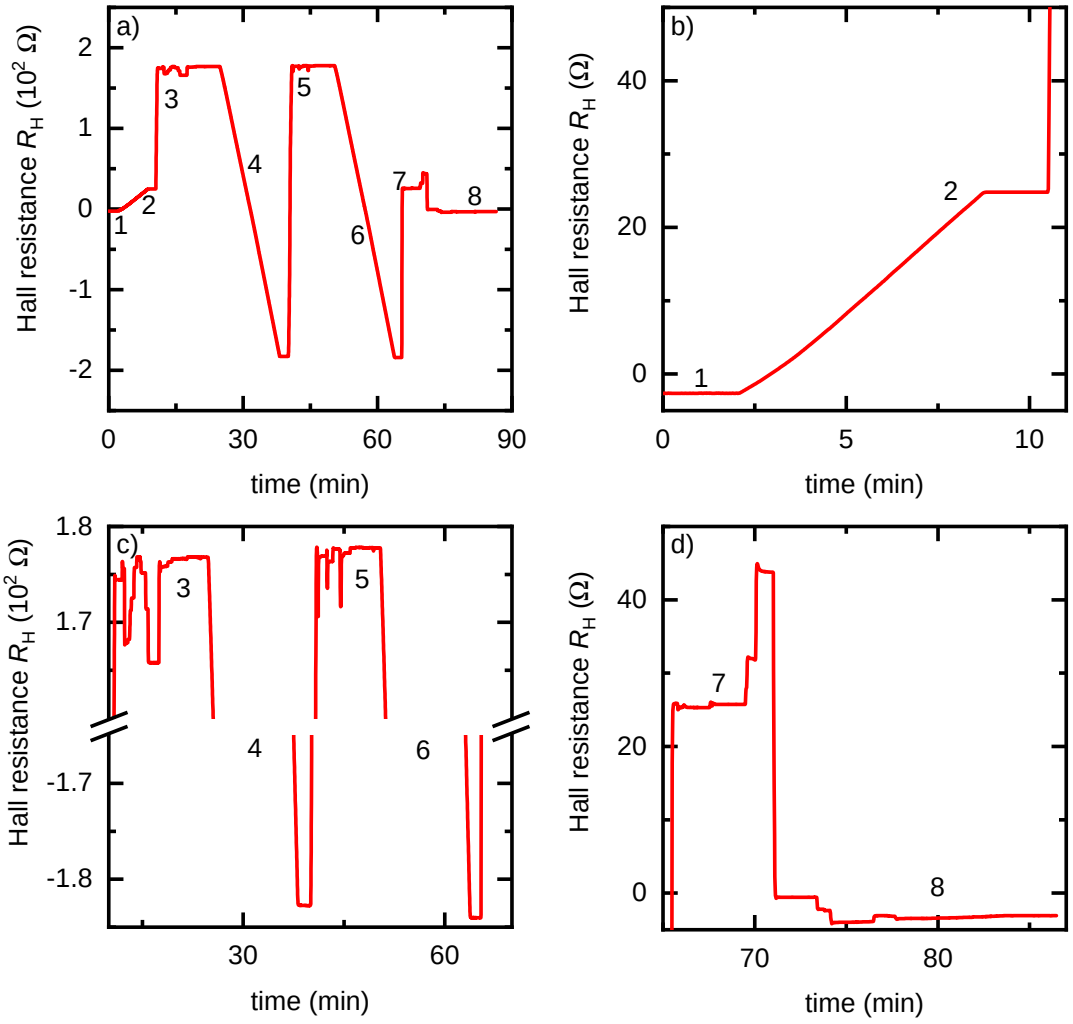

Figure 3.14: a) Hall resistance measured during rotation of the probe around its axis. b)-d) are blow-ups of a) for clarity.

during this experiment are intrinsically flawed. We thus pursued a different approach for measurements on a spherical sample.
The measurements using the ^{3}He insert with copper stage were performed subsequent to the Hall probe investigations so that the installation depth could be inferred from measuring the distance of the sample to the top flange on the probe. As mentioned before, we detected a vertical distance of more than 2 mm between the field centres of the magnet coils. The vertical gradient of the split coil's horizontal field, i.e. $\mathrm{d}B_y/\mathrm{d}z$, grows considerably faster with increasing distance to the field centre compared to the vertical gradient of the solenoid's vertical field, i.e. $\mathrm{d}B_z/\mathrm{d}z$ (cf. Fig 3.6). We thus decided to centre our sample in the split coil in order to minimize the vertical field gradients. In order to determine γ_r, we attached a Hall sensor to the end of the probe. The sensor is oriented to sense horizontal field and mounted such that the Hall resistance is zero at $\gamma_\mathrm{r} = 0°$ and exhibits a maximum for $\gamma_\mathrm{r} = 90°$. Unfortunately, this

adjustment was made towards the end of our experiment. Thus most measurements were performed at finite γ_r and only a small count of reference measurements was recorded near $\gamma_r = 0$. However, the Hall sensor measurement enables us to accurately determine the value of γ_r during the majority of our measurements which is a great asset for the evaluation of our data.
The recorded Hall resistance is shown in Fig. 3.14. Graph a) displays the full measurement, graphs b)-d) contain blow-ups of various parts. We start at zero field and the system positioned as during the preceding measurements. In this stage, the Hall sensor displays only a small zero offset (1). In a first step, the horizontal field is ramped up to +1 T resulting in the expected linear increase of the Hall resistance (2). Next, we rotate the probe around the vertical axis in order to find the maximum of the Hall resistance (3). We mark the position as $\gamma_r = 90°$, then we and ramp the field down to -1 T (4) and rotate the probe to find the maximum Hall resistance again (5). This position is marked as $\gamma_r = -90°$. The horizontal field is ramped back to +1 T (6) and the insert is rotated back to its initial measuring position (7). Finally, the probe is rotated such that the Hall resistance is reverted back to its zero offset at the finite field of +1 T (8). This position is marked as $\gamma_r = 0°$ and used for subsequent measurements. From the recorded Hall resistance, we calculate a misalignment of $\gamma_r \approx 9°$ for the preceding measurements.

4 De Haas-van Alphen effect in single crystal CrB_2

In this chapter we present our results on chromium diboride (CrB_2). We employed torque magnetometry to investigate the de Haas-van Alphen (dHvA) effect and density functional theory (DFT) to perform electronic structure calculations. Parts of the presented experimental and theoretical work have been carried out as part of the Master theses of Matthias Dodenhöft and Arthur Niedermayr, respectively. The chapter is organized as follows: In Sec. 4.1 we provide an introduction to CrB_2 including a brief review of the previous state of work on its Fermi surface as well as an outline of the work conducted in the course of this thesis. We describe the experiment and the data evaluation process in Sec. 4.2. The main experimental and theoretical results are presented in Sec. 4.3 and Sec. 4.4, respectively. This is followed by a thorough comparison and discussion of both in Sec. 4.5. Conclusions are drawn in Sec. 4.6.

4.1 Introduction to CrB_2

Transition metal (TM) diborides have been studied for decades. Early investigations were driven by their mechanical and thermal stability, chemical inertness and high electrical and thermal conductivity [Kny76, Gor75] which make the materials suitable for technical applications. More recently, large interest has been triggered by the discovery of superconductivity in MgB_2 [Nag01, Buz01]. This compound exhibits the record-high transition temperature $T_c \approx 39\,\mathrm{K}$ among conventional superconductors and has become the prime example for two-band superconductivity. Like many TM diborides, it crystallizes in the $C32$ structure introduced below. While so far none of the TM diborides that are isostructural to MgB_2 has shown superconductivity at ambient conditions without doping, these materials exhibit a wide spectrum of magnetic properties including non-magnetic ground states as well as ferro-, ferri- and antiferromagnetism [Mor09, Nov07, Kas70, Avi03]. Thus, a variety of ground states can be studied in an unmodified crystallographic environment.
In this work the itinerant antiferromagnet chromium diboride (CrB_2) was investigated. CrB_2 crystallizes in the $C32$ structure with lattice constants $a = 2.97\,\text{Å}$ and $c = 3.07\,\text{Å}$. The hexagonal unit cell is shown in Fig. 4.1. Closest-packed chromium layers and honeycomb boron layers alternate along the [001]-direction. The covalent B-B-bonds are very strong compared to the rather ionic Cr-B-bonds giving the material a somewhat two-dimensional character [Vaj01, Che01].
The CrB_2 single crystal was prepared by optical float zoning. Since ^{10}B is a strong

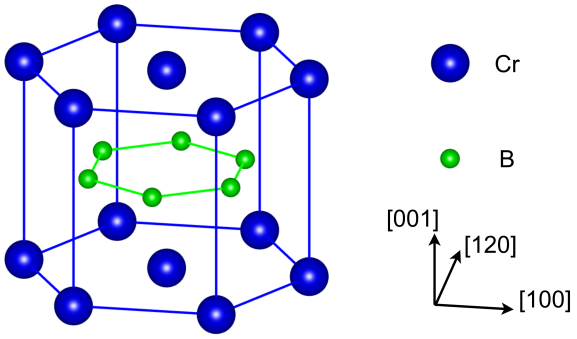

Figure 4.1: *C*32 crystal structure of CrB_2. Closest-packed chromium layers and honeycomb boron layers alternate along the [001]-direction.

neutron absorber [Ama36], 99 % isotopically enriched ^{11}B was used during growth to allow for neutron scattering experiments. Details of the preparation process are described in Ref. [Bau14b]. The authors further report an extensive characterization by means of resistivity, Hall effect and specific heat. The results demonstrate an excellent sample quality. The RRR values of 11 along [100] and 31 along [001] are the highest reported to date. For temperatures approaching zero, the resistivity drops to only a few $\mu\Omega$cm. In contrast to most earlier reports, no evidence for Fe impurities was observed. For the experiments presented in this thesis, a cuboid with dimensions of $2.45 \times 2.2 \times 0.8\,\mathrm{mm}^3$ parallel to the [001] $\times$ [100] $\times$ [120]-directions was cut from the ingot with a wire saw and oriented by Laue x-ray diffraction. The high quality of the crystal is corroborated by the first observation of de Haas-van Alphen oscillations in CrB_2 [Bra13b]. The authors investigated the very same sample as used in our experiments and report, to the best of our knowledge, the first experimental attempt to determine the CrB_2 Fermi surface properties prior to the present work.

4.1.1 Magnetic structure

Chromium diboride orders antiferromagnetically below $T_\mathrm{N} = 88\,\mathrm{K}$ [Bar69]. Early NMR studies on powder samples claimed that CrB_2 is located in the middle of the local moment and the weakly antiferromagnetic limits [Kit78, Kit80]. In contrast, more recent investigations carried out on single crystals describe CrB_2 as "weak itinerant antiferromagnet par excellence" [Bau14b]. The itinerant character was inferred primarily from the remarkable stability of resistivity, specific heat and magnetization in magnetic fields.
Although antiferromagnetic order in CrB_2 has been established decades ago, the microscopic details are still under debate. A first report suggested a spin density wave along $0.26\,\mathbf{q}_{001}$ [Liu75] where $\mathbf{q}_{001}$ is the reciprocal lattice vector along the c-axis with $|\mathbf{q}_{001}| = 2\pi/c$. This idea was quickly rejected by Funahashi *et al.* who proposed the formation of a spin cycloid [Fun77]. Based on single crystal neutron diffraction, they inferred an ordered moment $m_\mathrm{s} = 0.5 \pm 0.1\,\mu_\mathrm{B}$/Cr rotating in the a-c-plane along $0.285\,\mathbf{q}_{110}$. Here, $\mathbf{q}_{110}$ is the reciprocal lattice vector along [110], hence $|\mathbf{q}_{110}| = 2\pi/(a/2)$. For years, this suggestion has been widely accepted with

only minor adjustments as, e.g., a tilting of the rotation plane out of the a-c-plane by a few degrees [Kay09]. On the contrary, the results of NMR measurements on CrB_2 single crystals could not be accounted for by a simple cycloid [Mic07]. Recent neutron diffraction experiments shed new light on the question of the microscopic spin structure [Reg19]. Considering a number of single-k, double-k and triple-k spin structures, an extensive magnetic structure refinement was performed. The authors further report a representation analysis based on the nuclear structure of the material. The best fit is obtained for a complex incommensurate triple-k state that corresponds to a $\mathbb{Z}_2$ vortex lattice. This topologically non-trivial spin structure can be understood as a superposition of three spin cycloids propagating along $0.286\,\mathbf{q}_{110}$, $0.286\,\mathbf{q}_{\bar{2}10}$ and $0.286\,\mathbf{q}_{\bar{1}20}$, respectively. In contrast to the simple cycloid, the spins rotate in three dimensions rather than within a 2D plane. Moreover, not only the direction but also the magnitude of the moment changes when moving from one Cr atom to another. The average moment size can be interpreted as the ordered moment $m_\mathrm{s} \approx 0.59\,\mu_\mathrm{B}/\mathrm{Cr}$.
The single-k cycloid proposed by Funahashi *et al.* is not found among the primary results of the analysis presented in [Reg19]. However, the authors stress that their experimental data are consistent with such a structure and the proposed magnetic multi-k state of CrB_2 closely resembles simple cycloids along a-directions of the crystal. Thus, for our electronic structure calculations presented in Sec. 4.4 we considered a single-k cycloid, since the incorporation of incommensurate multi-k states into DFT calculations is beyond the scope of this thesis.

4.1.2 Previous state of work and outline

Prior to this work, there has been one experimental study of the CrB_2 Fermi surface by Brasse *et al.* [Bra13b] which was conducted using torque magnetometry in magnetic fields up to 14 T and at temperatures down to 300 mK. The very same sample as investigated in the present work was used. The authors were able to track three distinct dHvA frequencies around 300 T, 1600 T and 1950 T in the basal plane ([100]-[120]-plane), two of which showed a 60°-symmetry. The oscillation at 1.6 kT was also observed in the [120]-[001]-plane where it exhibited a two-fold symmetry. The authors further determined the effective masses of the corresponding orbits to $1.22\,m_\mathrm{e}$, $0.86\,m_\mathrm{e}$ and $1.07\,m_\mathrm{e}$. Band structure calculations were carried out for a non-magnetic state as well as for a single-k spin cycloid. At a propagation vector of $\mathbf{q} = 0.3\,\mathbf{q}_{110}$ the authors found three Fermi sheets and an ordered moment of $m_\mathrm{s} \approx 1.3\,\mu_\mathrm{B}/\mathrm{Cr}$. Comparison of experiment and calculations yielded a mass enhancement of 2 - 2.3 for B-$p_{x,y}$ states. A more complex spin structure as discussed in Sec. 4.1.1 was not considered.
Within the present work, the dHvA effect has been measured using torque magnetometry in magnetic fields up to 35 T and temperatures down to 60 mK. We covered an angular range of 60° within the basal plane and observed up to 11 distinct frequencies. The effective masses of 8 dHvA components were determined from experiment. In addition, DFT calculations assuming both non-magnetic and single-k

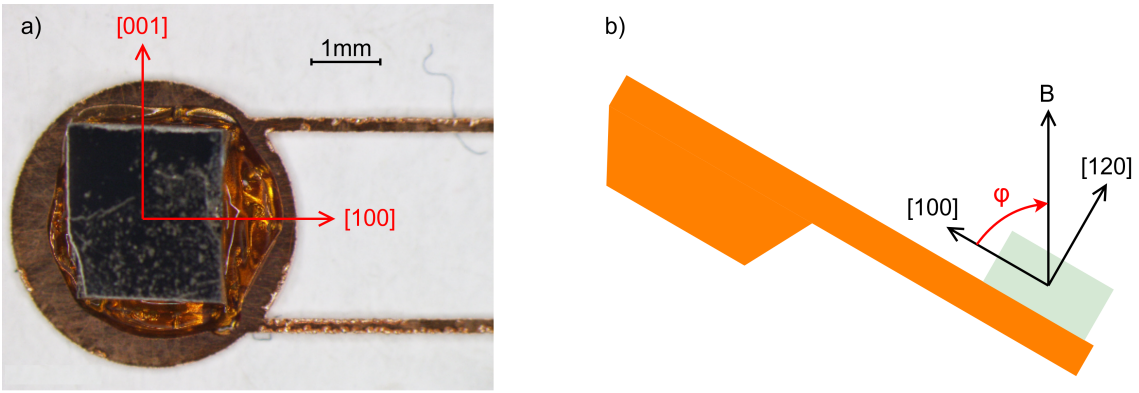

Figure 4.2: Orientation of the CrB_2 single crystal on the cantilever. a) Microscope picture of the sample on the cantilever at the HFML. The [120]-direction is pointing out of the plane. b) Schematic side view of cantilever and sample. The measurement angle is enclosed by the [100]-direction and the magnetic field.

spin cycloid states have been performed. We adjusted the propagation vector to the experimentally observed value of $\mathbf{q} = 0.286\,\mathbf{q}_{110}$ and employed the spin scaling approach [Ort12] to account for the reduced magnetic moment of $m_s \approx 0.59\,\mu_B/\mathrm{Cr}$. As a result we obtained five Fermi surface sheets which were analyzed with respect to our experimental findings. Calculations considering a multi-k spin structure are beyond the scope of this thesis.

4.2 Experimental conditions and data evaluation

In the present work, torque magnetometry on a CrB_2 single crystal was carried out in three different experimental environments. Parts of these experiments were performed by Matthias Dodenhöft as part of his Master thesis. First, measurements at a single field direction in the basal plane were carried out in a superconducting 14 T magnet at temperatures as low as 60 mK. Second, measurements within a 60° angular range in the basal plane were performed in a superconducting 15 T magnet at temperatures down to 280 mK. Third, measurements in magnetic fields up to 35 T and temperatures down to 300 mK were conducted in a resistive Bitter magnet at the High Field Magnet Laboratory (HFML) in Nijmegen in the Netherlands. Since the results from both superconducting magnet setups are fully and consistently contained in those obtained at HFML, we will limit our discussion to the high field data in the following. In this section we describe the experiment at HFML and the data handling.

4.2.1 Experimental conditions at HFML

The HFML cantilever design with round paddle was used for the high field experiments. Most measurements were carried out with a sensor with a beam width of 0.2 mm, a few with a less sensitive sensor of 0.8 mm beam width. As already stated

in Sec. 3.2.2, we did not perform an electrostatic calibration due to time constraints. Looking to investigate the dHvA effect, we are mainly interested in frequencies and relative amplitudes of oscillating signals whereas the absolute torque value is less important. Therefore we neither considered the generic calibration shown in appendix A.3 for data evaluation, but directly analyzed the capacitance data. Since the absolute capacitance changes were smaller than 3 %, the approximation of direct proportionality of capacitance and torque could be applied (cf. Sec. 3.1.1).
Figure 4.2 shows the orientation of the sample on the cantilever. The CrB_2 cuboid was oriented such that the [100]-direction pointed along the cantilever beams with the [001]-direction pointing orthogonal to the beams lying in the cantilever plane. This way, the magnetic field was applied within the hexagonal basal plane. The measurement angle φ is defined as the angle enclosed by the [100]-direction and the magnetic field. The highest measurement temperature was $4.2\,\mathrm{K} \ll T_\mathrm{N}$, so that the experiment exclusively addressed the antiferromagnetic phase of CrB_2.

4.2.2 Data evaluation

The signal-to-noise ratio of the dHvA data taken at HFML was varying between different magnet runs. In order to consistently extract the dHvA oscillation frequencies from the observed capacitance signal, it was found necessary to perform an extensive evaluation process for each field sweep. Most of the process was automated, yet the frequencies still had to be determined from the resulting diagrams "by hand". In this subsection, we describe the automated data preparation process and give examples for our selection procedure.

Preparation process

The data preparation process was automated with MATLAB code. Starting from the raw capacitance data for each field sweep, the code output consists of four types of diagrams. From these diagrams we extract the oscillatory components of the signal. The automated process is sketched in Fig. 4.3. In the first step, the non-oscillatory part of the signal, i.e., the magnetic background, is removed from the capacitance raw data. We model this background with two different methods: We either smooth the raw data over a sufficiently large number of data points or we perform a polynomial fit. In the latter case, the data at low field is cut off before the fit to improve the fit accuracy, since at very low fields the signal often behaves non-polynomial or exhibits excessive noise. The background obtained by smoothing or fitting is then subtracted from the original signal to obtain the oscillating part of the signal ΔC.
After background subtraction, the low field part of the signal is cut off. Since the dHvA oscillation amplitude grows with magnetic field, while the mechanical noise in the signal becomes larger with decreasing field, it is handy to analyze the data only above a certain field threshold. In the case of the polynomial fitting method, an additional reason is to avoid the boundary of the fit region. Since dHvA oscillations are periodic as a function of inverse field, the data is then transferred from field dependence $\Delta C(B)$ to inverse field dependence $\Delta C(1/B)$.

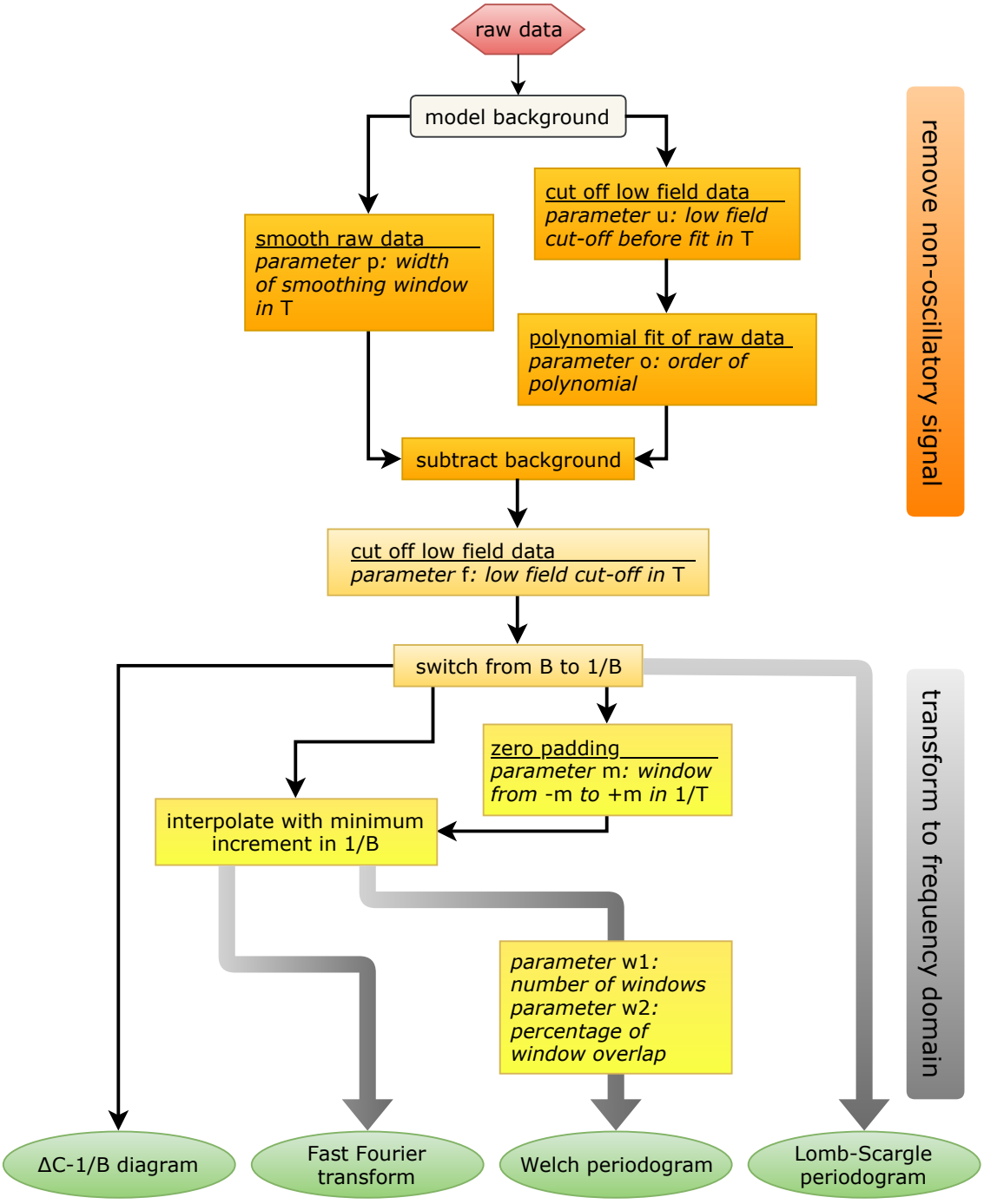

Figure 4.3: Sketch of the automated preparation process of our experimental data. The raw capacitance data is turned into four types of diagrams. The main tasks are the removal of the non-oscillatory magnetic background and the transformation of the oscillatory signal to the frequency domain. The values of parameters used during the process are summarized in Tab. 4.1.

At this point, the data flow splits into four different paths. The most direct way is to display the data in a ΔC-$1/B$-diagram. In principle, this representation contains all relevant oscillations. In practice, it is very hard to determine all frequencies and especially to distinguish oscillations with similar frequencies from such a plot. Therefore we choose to additionally transform the data to the frequency domain. This can be achieved with each of the three algorithms described in Sec. 2.2.3. The Lomb-Scargle periodogram can be calculated directly from the capacitance and inverse field data. For the FFT and Welch algorithms, the data first needs to be interpolated to obtain evenly spaced field data. The number of interpolation points is chosen such that the field data is spaced with the minimum increment present in the original data. In the case of the FFT algorithm, we can optionally add the step of zero padding discussed in Sec. 2.2.3. The code automatically generates several versions of all four types of diagrams with different parameter sets. The choice of parameters is described in the following section.

Parameters

The result of the preparation process can depend strongly on a number of parameters. Concerning the smoothing method, the main parameter is the number of data points over which the moving average is calculated. Since the data point density differs between different measurements, we specify this parameter in terms of the field width p covered by the respective number of data points. Parameter p determines a focus frequency range, since for large p low frequency oscillations are well visible while the signal-to-noise ratio is rather low at higher frequencies, whereas for small p low frequency oscillations are smoothed away while higher frequency components may appear much clearer in the frequency spectrum.
Regarding the polynomial fitting method, we have two parameters: the order of the polynomial o and the low field threshold u at which the raw data is cut off before the fit. Both parameters influence the accuracy of the fit. While a too low order polynomial can prevent the fit from following the data well, a too high order

p [T]	**f [T]**
2	2
1	5
0.75	7.5
0.5	10
0.4	15
0.3	20
0.2	25
0.1	30

o	**u [T]**	**f [T]**
2	4	8
3	8	10
4	X	X
5		
6		
7		
8		
9		

m [T^{-1}]	**w1**	**w2 [%]**
0.25	1	0
0.5	2	10
0.75	5	25
1	8	33
1.5	10	50
2	20	66
3	35	75
5	50	99

Table 4.1: Parameter values used in the preparation process.

polynomial may oscillate around $C(B)$. The latter would introduce low frequency oscillations in ΔC that are not present in the actual signal. The low-field cut-off is important to restrict the data to a regime where the noise is sufficiently low and the background behaves sufficiently similar to a polynomial.
After background removal the low field portion of the data is cut off a second time at a threshold f. This parameter is crucial, since, on the one hand, the larger the field range covered by the data is, the higher the resolution of the resulting frequency spectra becomes. On the other hand, a cut-off is still necessary to remove the noise-dominated low field portion of the data. The right balance between signal-to-noise ratio and data range is key to obtain a good frequency spectrum.
Zero padding before a FFT introduces an additional parameter m where the zero padding window ranges from -m to +m. In the case of the Welch periodogram, we can adjust two more parameters: w1 is the number of windows in which the signal is split, w2 is the percentage of overlap between these windows.
The parameter values used in the automated process are given in Tab. 4.1. The left part shows values for background modelling with the smoothing method. Values for p range from 2 T to 0.1 T, values for f from 2 T to 30 T. All possible pairs of the listed p and f values are applied. The values for the fitting method parameters are given in the middle of Tab. 4.1. Polynomials of the orders o = 2 to 9 are used. We apply fits of all orders for u = 4 T and u = 8 T. The X implies that, for some sweeps, u is individually adjusted to improve the outcome. For the fitting method, f is standardly set to 8 T for u = 4 T and to 10 T for u = 8 T. Again, the X implies individual adjustments for a couple of measurements. Values for the parameters m, w1 and w2 are given in the right part of Tab. 4.1. They are applied after the smoothing method with p = 1 T and f = 5 T. For all versions of $\Delta C(1/B)$ resulting from other background modeling parameters, we set m = 2, w1 = 5 and w2 = 50 %.
A ΔC-$1/B$-diagram is automatically produced when applying the fitting method. For all background models produced with the methods and parameters described above, the code automatically generates a Lomb-Scargle and Welch periodogram as well as FFT spectra with and without zero padding. In total, this data preparation process leaves us with a couple of hundreds of plots resulting from one single field sweep. To complete the evaluation, we assess these plots to determine the dHvA frequencies in the signal.

Frequency selection

The evaluation process described above results in a manifold of frequency spectra for each single field sweep. The final evaluation step is to extract frequency peaks from these spectra and discriminate between dHvA signal and false peaks induced by noise or the evaluation process. Since the transition from signal to noise is fluent, we categorize the peaks present in the spectra instead of drawing one fixed line between them. We illustrate this procedure on the example of a field sweep from 35 T to 0 T at $\varphi = 20°$ and $T = 0.3$ K.
Figure 4.4 displays a selection of several frequency spectra obtained from this data

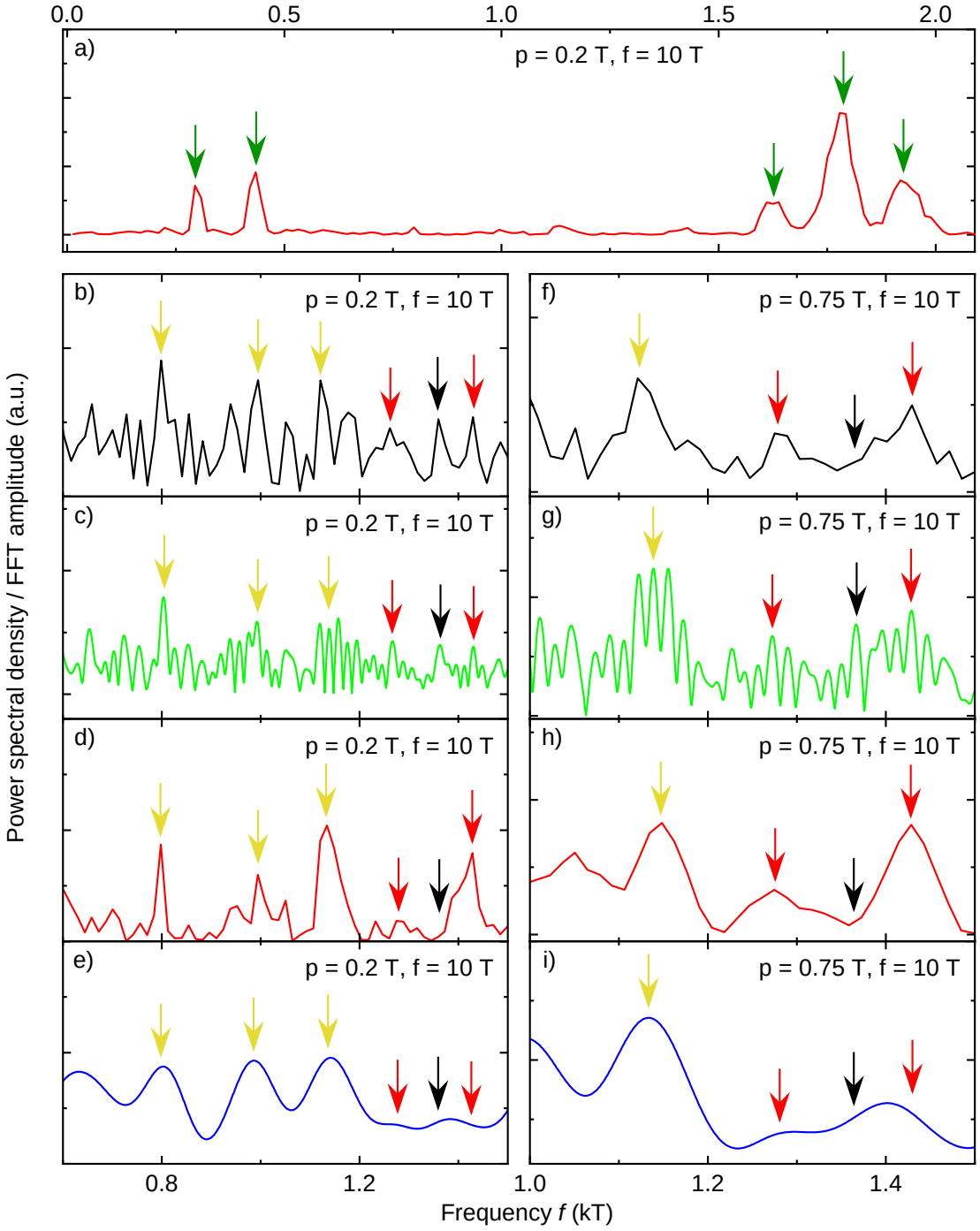

Figure 4.4: Exemplary frequency spectra selection obtained from a field sweep from 35 T to 0 T at $\varphi = 20°$ and $T = 0.3$ K. Black and green lines represent Fourier transforms without and with zero padding, respectively, red and blue lines show Lomb-Scargle and Welch periodograms, respectively. Green arrows mark obvious frequency peaks, yellow arrows mark peaks that are less obvious but stable throughout parameter variation. Red arrows mark less stable peaks which still appear regularly while black arrows mark peaks appearing occasionally.

set. Figure 4.4 a) shows the Lomb-Scargle diagram for p = 0.2 T and f = 10 T over a large frequency range from 0 to 2.1 kT. Five frequency components marked by the green arrows are clearly visible at frequencies of ∼300 T, ∼430 T, ∼1625 T, ∼1777 T and ∼1935 T. They are similarly well recognizable in spectra resulting from FFT and Welch's methods. We consolidate such prominently pronounced peaks as undoubtedly real dHvA signal in category A.
The remaining graphs on the left of Fig. 4.4 show a smaller section of the spectra obtained with the same background model p = 0.2 T and f = 10 T for FFT without zero padding in b), FFT with zero padding in c), the Lomb-Scargle method in d) and the Welch method in e). While the spectra differ strongly in resolution and signal-to-noise ratio, there are still common features. The three peaks marked by yellow arrows at ∼800 T, ∼985 T and ∼1150 T can be recognized in each of the four spectra. They are also stable against variation of parameters p and f, which is not shown here for clarity. In contrast to the large peaks in Fig. 4.4 a), these three peaks are barely recognizable in the broader spectrum. Such peaks which are not obviously recognizable in the full spectrum, but well visible in a smaller frequency region and stable over a broad preparation parameter range are assessed as reliable signal and consolidated in category B.
The red arrows in Fig. 4.4 b) - e) mark positions of less stable or less pronounced peaks. This assessment is substantiated by the remaining graphs on the right of Fig. 4.4. They contain spectra obtained with a different background model, namely p = 0.75 T and f = 10 T, and again various transforms with FFT without zero padding in f), FFT with zero padding in g), the Lomb-Scargle method in h) and the Welch method in i). While the yellow marked peak at ∼1150 T is well pronounced in all spectra from b) to i), the spectra differ at the positions of the red arrows. At ∼1270 T, there is a peak visible in FFT and Lomb-Scargle spectra which is considerably lower than the yellow marked peaks. In the Welch spectra, it is barely recognizable. At ∼1430 T we see a comparatively larger signal for Lomb-Scargle spectra, similar signal strength in FFT spectra and in the Welch spectra, the peak is visible, but shifted in frequency. These peaks, which exhibit a very weak signal strength or are unstable against changing preparation parameters, are assessed as unreliable, yet possibly real dHvA signal and consolidated in category C.
Finally, there are peaks which are both rather weak and very unstable against parameter changes. An example is marked by the black arrows in Fig. 4.4 at ∼1360 T. While a signal clearly appears in graphs b), c) and g), there is no recognizable peak in graphs d), f) and h). In the Welch spectra in graphs e) and i), the peak is shifted and, with regard to the other spectra, is rather attributed to the signal marked by the red arrow at ∼1430 T. Such weak and apparently randomly appearing peaks are not considered in the analysis.
At this point, it is worth noting that, while the nine graphs in Fig. 4.4 are supposed to give an impression of the categorization process, the actual number of graphs considered for each field sweep is ∼350. Moreover, at almost all measurement angles, we have at least two field sweeps (up- and downsweep), for which we can perform the whole analysis independently and then compare the results. Thus the

stability of peaks against preparation parameters is tested much more rigorously than the foregoing description may imply. No frequency components above 5 kT were evaluated due to the limit imposed by the experimental data point density. In the following, we will refer to categories A and B as reliable frequencies whereas category C contains possibly complementing results.

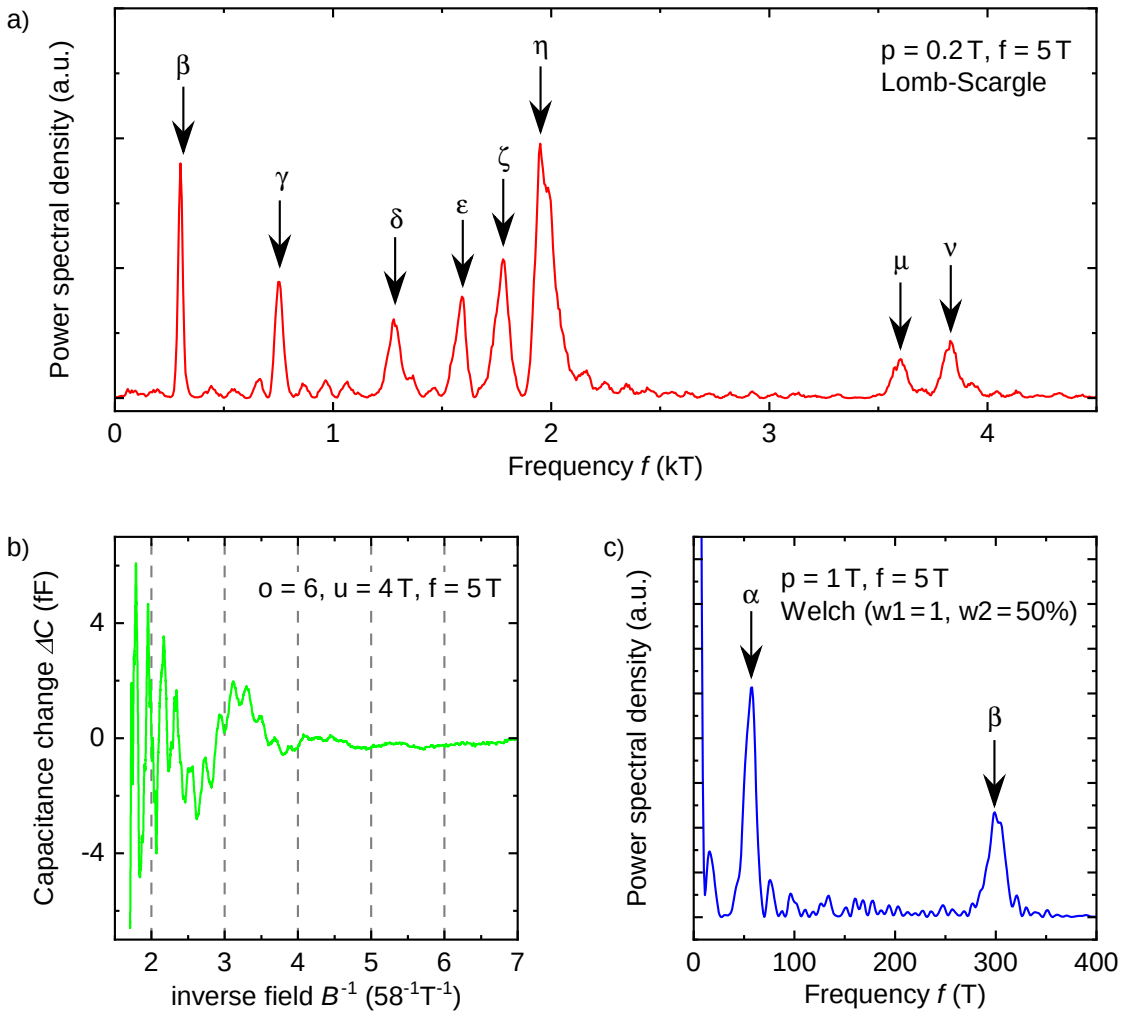

Figure 4.5: Exemplary experimental result at $\varphi = 5°$ and $T = 0.3\,\mathrm{K}$. a) Lomb-Scargle periodogram after smoothing with p = 0.2 T and f = 5 T. Category A peaks are marked with arrows and enumerated by greek letters. The corresponding frequency values are given in Tab. 4.2. b) ΔC-1/B-diagram after fitting with o = 6, u = 4 T and f = 5 T. The inverse field axis is scaled to match the period of a dHvA oscillation α with a frequency of 58 T. c) Welch periodogram with w1 = 1 and w2 = 50 % after smoothing with p = 1 T and f = 5 T. Complementary to a), an additional peak corresponding to α is visible at 58 T.

4.3 Experimental results

In this section we present our experimental findings. We investigated the dHvA effect at various angles and temperatures. Concerning the angular dependence, we covered the range from 0° to 60° in steps of 5° with additional measurements at 11°, 26°, 49° and 90°. All these measurements were performed at a base temperature of ∼0.3 K. In addition, we performed measurements at seven temperatures from 0.35 K to 3.15 K at an experimental angle $\varphi = 5°$.
Figure 4.5 displays the result for $\varphi = 5°$ and $T = 0.3\,\mathrm{K}$. The graph in Fig. 4.5 a)

shows the Lomb-Scargle periodogram obtained with the smoothing method with p = 0.2 T and f = 5 T. We observe eight category A frequency peaks which are marked with arrows and enumerated by greek letters. As discussed in Sec. 2.2, each of these frequencies corresponds to an extremal orbit on the Fermi surface with a cross-sectional area of $P_i = 2\pi e/\hbar f_i$ (cf. Eq. 2.19). There is no clear peak recognizable for frequencies below the peak marked β at ∼305 T.
In Fig. 4.5 b) we show the ΔC-$1/B$-diagram after a fit with o = 6 and u = 4 T. Here we can clearly observe a low frequency oscillation. The axis of the inverse field is scaled to the period of a 58 T oscillation which appears to match the oscillations in the graph. In Fig. 4.5 c) we present the Welch periodogram with parameters p = 1 T, f = 5 T, w1 = 1 and w2 = 50 %. We can easily identify the peak α at 58 T which confirms our observation from the ΔC-$1/B$-diagram.
All dHvA frequencies observed at this angle are given in Tab. 4.2. In addition to the nine category A frequencies shown in Fig. 4.5, we observe one category B frequency which we enumerate as f with roman letters as indices and two category C frequency which are enumerated as f with arabic numbers as indices.
Not all frequencies occuring at 5° can be tracked over the full angular regime. In return, there are frequencies visible at several or individual other angles which are not present at $\varphi = 5°$. As a full tabular list of all frequencies at all angles would lack lucidity, we refer to Sec. 4.3.1 and Fig. 4.6 for this purpose.

Orbit	Frequency (T)	Category
α	58	A
β	305	A
f_1	440	C
γ	760	A
f_a	1130	B
δ	1280	A
ϵ	1580	A
ζ	1775	A
η_1	1950	A
η_2	1995	A
f_2	2935	C
μ	3600	A
ν	3830	A

Table 4.2: Frequencies found experimentally at $\varphi = 5°$ and $T = 0.3$ K.

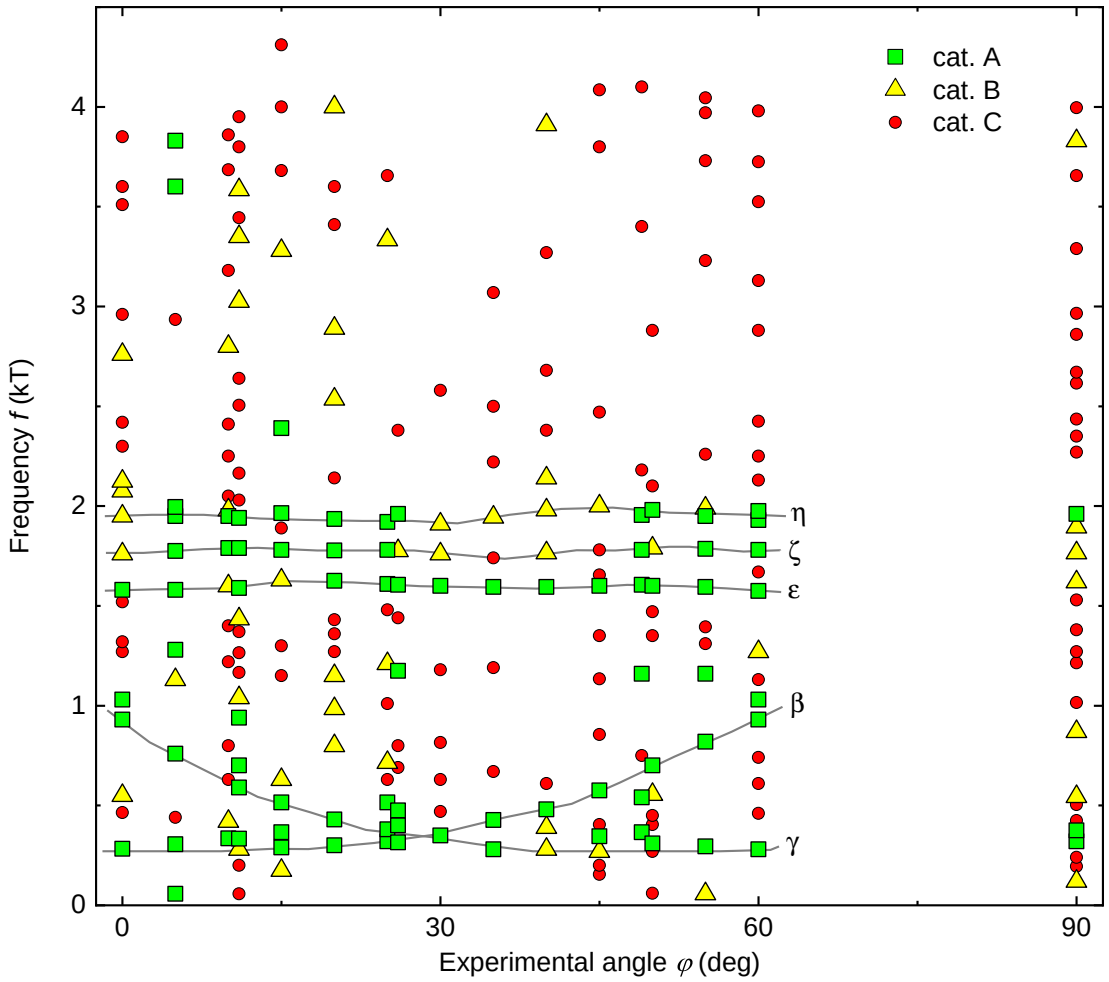

Figure 4.6: Angular distribution of experimentally observed dHvA frequencies. Gray lines are a guide to the eye.

4.3.1 Angular dependence

We studied the angular dependence of the dHvA effect over a 60° range in the basal plane. Figure 4.6 shows the resulting frequency versus angle map. The large signals of category A are represented by green squares, the stable peaks of category B are displayed as yellow triangles and the possible frequency components of category C are shown as red circles. The gray lines are a guide to the eye.
The most prominent feature in the graph is a cluster of three frequency branches between 1.5 and 2 kT. These frequency components, labeled as ϵ, ζ and η, are visible in practically all measurements and appear to change their frequencies only slightly. For some angles, η splits up into a double peak. Two of these orbits, i.e. ϵ and η, have already been observed in earlier experiments [Bra13b].
Similarly distinct branches are marked as β and γ. These branches are also visible over the full investigated angular range and exhibit stable signal. The variation in frequency is somewhat larger, reaching from ∼270T up to ∼930T. The branches

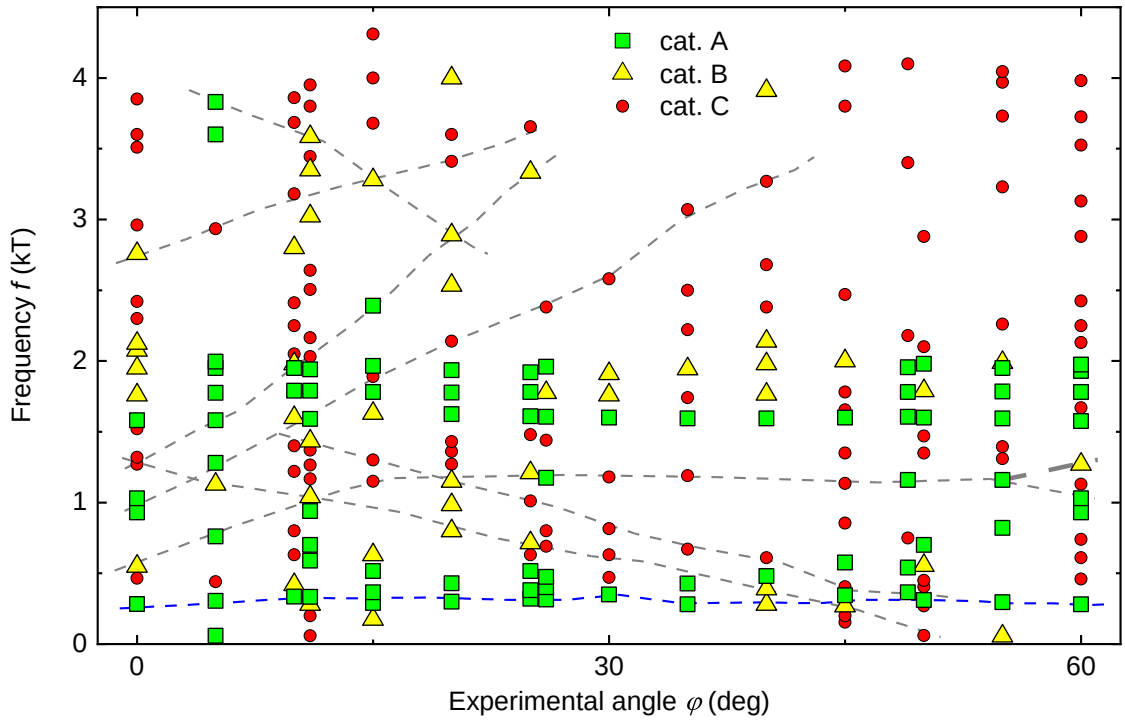

Figure 4.7: Angular distribution of experimentally observed dHvA frequencies. Gray dashed lines hint at possible but not verifiable frequency branches. The blue dashed line indicates an assignment from an earlier work [Bra13b].

appear to be symmetric to each other with respect to $\varphi = 30°$ and cross each other at that angle.

Apart from these quite distinct features, the large angular step size makes it difficult to follow an observed frequency. A lot of branches are thinkable to fit to our observations as we illustrate in Fig. 4.7. Here, several conceivable frequency branches are indicated by hand-drawn lines. None of these are verifiable with our experimental data alone. We particularly point to the hypothetical branch marked by the blue dashed line. Similar to the orbits ϵ, ζ and η, experimentally observed frequencies that could be attributed to this branch are visible in all measurements with only small frequency changes. Together with ϵ and η, these frequencies have been observed in earlier experiments and were attributed to one small closed Fermi surface pocket [Bra13b]. In contrast, we regard this observation as being due to two symmetric frequency branches crossing at 30° as discussed above.

In addition to the ambiguity of frequency branches, the small range covered by our measurements prevents the observation of a specific symmetry as well as discrimination between open and closed Fermi surface sheets. A more elaborate discussion of these results is postponed to the comparison with DFT calculations in Sec. 4.5.

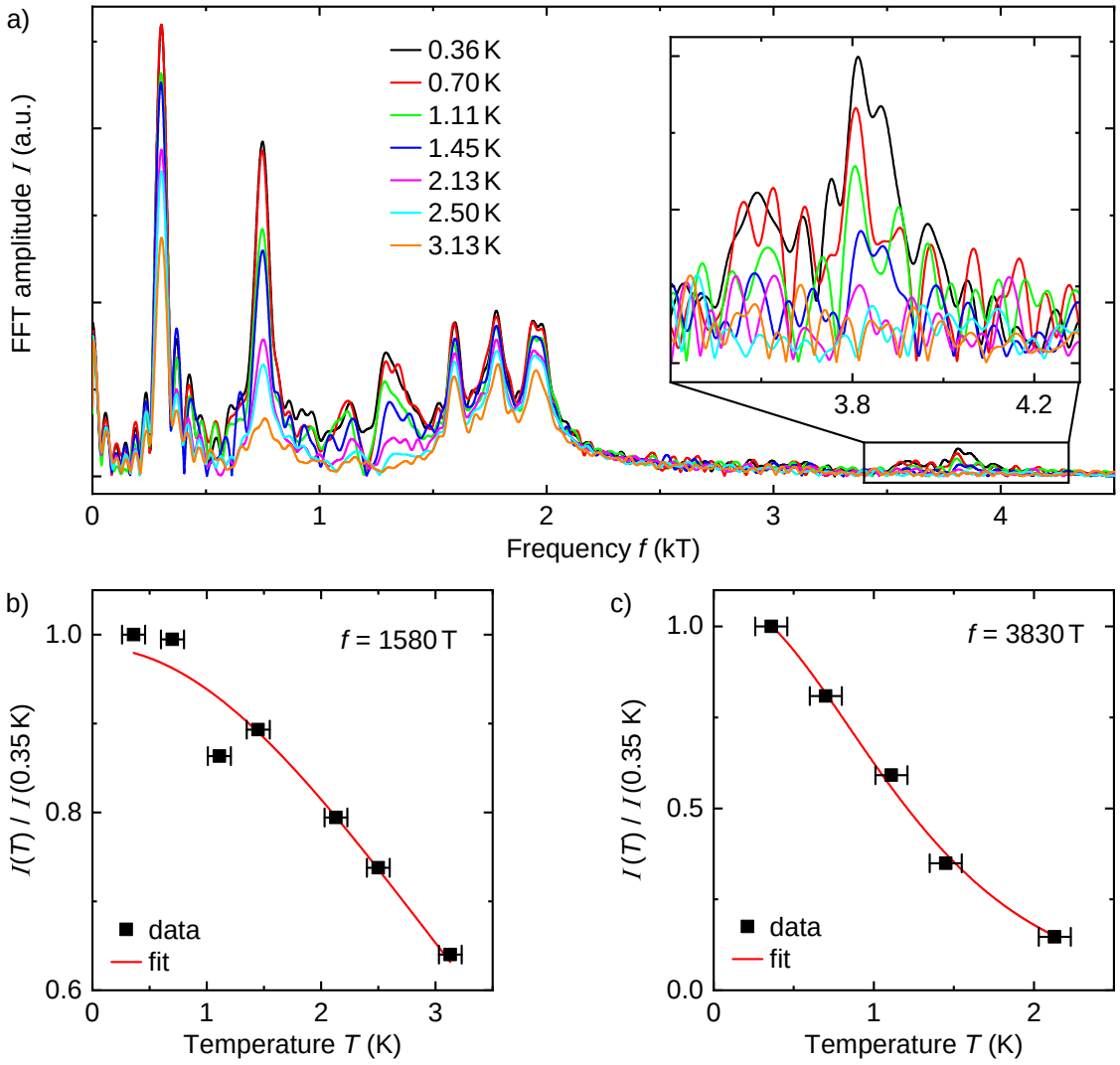

Figure 4.8: Temperature dependence of the dHvA signal in CrB_2 at $\varphi = 5°$. a) FFT spectra after smoothing with p = 1.15 T and f = 20 T and zero padding with m = 1 for all measured temperatures. Before the smoothing, the raw data were interpolated to make evaluation of different sweeps more comparable. b) Normalized FFT amplitudes versus temperature for the frequency component at 1580 T. The Lifshitz-Kosevich fit yields $m^* = (0.94 \pm 0.06)\, m_e$. c) Normalized FFT amplitudes versus temperature for the frequency component at 3830 T. The Lifshitz-Kosevich fit yields $m^* = (3.32 \pm 0.10)\, m_e$.

4.3.2 Temperature dependence

We investigated the temperature dependence of dHvA oscillation amplitudes present at an experimental angle of $\varphi = 5°$. For this purpose we measured the torque at temperatures of 0.35 K, 0.70 K, 1.11 K, 1.45 K, 2.13 K, 2.45 K and 3.15 K. From the relative amplitude change of the oscillatory signal, the effective quasiparticle mass can be determined (cf. Sec. 2.2.2). The individual measurements comprising a temperature series must thus be evaluated on an equal footing, i.e., the influence

of external parameters must be kept at a minimum. Unfortunately, the noise level fluctuates strongly from one measurement to the other which hampers the precise determination of effective masses. We estimate an upper bound for the error bar due to systematic errors of 10 %.
The amplitude I of the peak in a frequency spectrum can depend on experimental parameters as, e.g., the magnetic field sweep rate as well as on preparation parameters as, e.g., the low field cut-off f. We therefore need to control these parameters very carefully and keep them as stable as possible during all measurements. As a consequence, we only considered magnetic field upsweeps for evaluation, since the experimental parameters during downsweeps could not be kept consistent between single measurements. To keep the influence of the preparation process as small as possible, we added an additional step before the background modeling which consists of interpolation of the raw data. In this way, all data sets exhibit the same point density. The data was then evaluated with the smoothing method with p = 1.15 T and f = 20 T and transformed using FFT with zero padding and m = 1. The high value for f was chosen to avoid the influence of sweep rate changes below 20 T.
The FFT spectra obtained in this manner are shown in Fig. 4.8 a). We can clearly see the peak amplitude decrease with rising temperature. As discussed in Sec. 2.2.2, this decrease is described by the Lifshitz-Kosevich formalism and is commonly used to determine the effective mass m^* of charge carriers on the corresponding orbit.
Figure 4.8 b) and c) show the decrease of the peak amplitude with temperature exemplarily for the peaks ϵ and ν at 1580 T and 3830 T, respectively. While the signal of orbit ϵ is suppressed by less then 40 % at $T = 3.15$ K, the signal of orbit ν vanishes completely at $T = 2.5$ K. Since the absolute peak amplitude is not of interest, the values have been normalized with respect to the lowest measurement temperature. In this way, the data points can be fitted with a function of the form

$$\frac{I(T)}{I(0.35\,\mathrm{K})} = M_0 \frac{X}{\sinh(X)} \tag{4.1}$$

where I is the FFT peak amplitude and $X = 2\pi^2 k_\mathrm{B} m^* T/\hbar e B$ contains the effective mass m^*. Fits of this form are included in the graphs as red lines. We can see a remarkable outlier for orbit ϵ at 1.1 K. This substantiates the difficulties mentioned

Orbit	eff. mass / m_e
β	1.17 ± 0.03
γ	2.10 ± 0.07
f_a	1.95 ± 0.09
δ	2.54 ± 0.10

Orbit	eff. mass / m_e
ϵ	0.94 ± 0.06
ζ	0.88 ± 0.03
η	0.88 ± 0.04
ν	3.32 ± 0.10

Table 4.3: Effective masses of orbits as obtained from the temperature dependence with Lifshitz-Kosevich fits. The given uncertainties arise solely from the fit and do not include any possible amplitude uncertainty due to differences in measurement or preparation parameters.

above in comparability of the individual measurements. On the other hand, the fit appears to perfectly cut through all data points for orbit ν.
The fits shown in Fig. 4.8 b) and c) yield effective masses of $(0.94 \pm 0.06)\, m_\mathrm{e}$ and $(3.32 \pm 0.10)\, m_\mathrm{e}$ for orbit ϵ and ν, respectively. They are listed together with the other effective masses that could be determined in Tab. 4.3. The given uncertainties originate only from the fit accuracy and do not reflect possible uncertainties in the peak amplitude.
As stated before, the orbits we labeled as β, ϵ and η have already been observed by Brasse *et al.* [Bra13b]. The authors also determined the effective masses for these orbits. They obtain $m^*_\beta = (1.22 \pm 0.12)\, m_\mathrm{e}$, $m^*_\epsilon = (0.86 \pm 0.07)\, m_\mathrm{e}$ and $m^*_\eta = (1.07 \pm 0.06)\, m_\mathrm{e}$ in good agreement with our results.

4.4 Electronic structure calculations

Band structures and Fermi surfaces for CrB_2 were calculated to support and complement our experimental results. Parts of these calculations were carried out by Arthur Niedermayr as part of his Master thesis. In this section we report the outcome of our calculations. We briefly introduce the applied methods in Sec. 4.4.1 and discuss the considered states in Sec. 4.4.2. In Sec. 4.4.3 we present the resulting Fermi surface and compare it to that of Brasse *et al.* [Bra13b]. Finally, we analyze the implications for the dHvA effect following from the calculated Fermi surface in Sec. 4.4.4.

4.4.1 Theoretical methods

The calculations performed in this work employed the Elk code[1]. In this software package the full potential linearized augmented plane wave method is utilized to solve the Kohn-Sham equations of density functional theory. The local spin density approximation (LSDA) of Perdew-Wang/Ceperley-Alder [Per92] was used for the exchange-correlation potential and the experimental lattice constants $a = 2.969\,\text{Å}$ and $c = 3.066\,\text{Å}$ were supplied as input parameters.
We performed band structure calculations for a paramagnetic state as well as for several cycloidal states with propagation vectors of different length along $\mathbf{q}_{110}$. Among others, we considered $\mathbf{q} = 0\,\mathbf{q}_{110}$ and $\mathbf{q} = 0.5\,\mathbf{q}_{110}$ which are equivalent to collinear ferromagnetic and antiferromagnetic order, respectively. For the non-collinear, but single-k spin structures, the generalized Bloch theorem allows for implementation without the need for large supercells [San91]. On the contrary, a multi-k spin structure as the suggested $\mathbb{Z}_2$ vortex state (cf. Sec. 4.1.1) does not fulfil this condition and could thus not be implemented within this work. Spin-orbit-coupling (SOC) could not be considered in our calculations as a consequence of applying the generalized Bloch theorem.
We note that instead of the experimentally observed spin cycloid, where the spin rotation axis is slightly tilted out of the a-b-plane [Kay09], the Elk code assumes

[1] http://elk.sourceforge.net

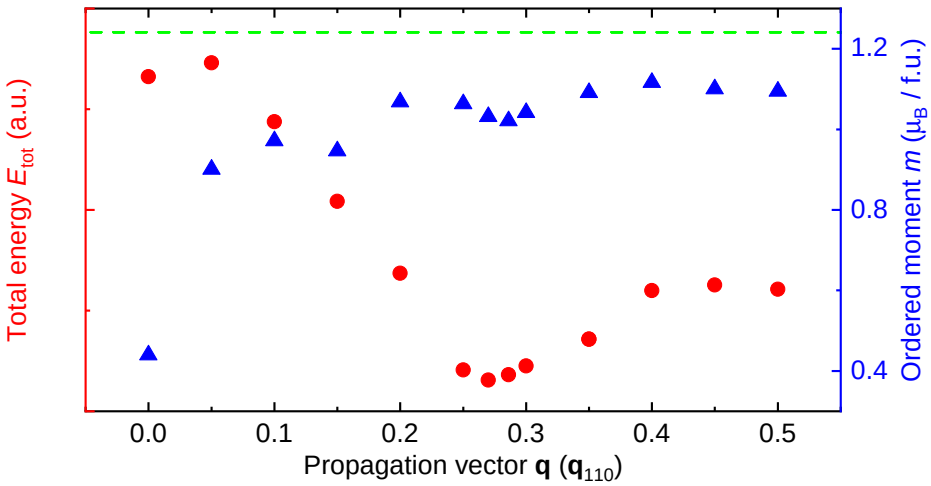

Figure 4.9: Total energy (red circles) and ordered magnetic moment per unit cell (blue triangles) as a function of the propagation vector length along $\mathbf{q}_{110}$. The green dotted line represents the total energy in the paramagnetic state.

a spin spiral with the rotation axis parallel to the *c*-direction. However, due to the absence of spin-orbit-coupling in our calculations, the electronic structure is identical for both states. The spin spiral with the experimental propagation vector $\mathbf{q} = 0.286\,\mathbf{q}_{110}$ was additionally treated using the spin scaling approach [Ort12] to match the ordered moment of $0.59\,\mu_B$/Cr found in experiments [Reg19].
We analyze the implications of the calculated band energies for the dHvA effect using the SKEAF (Supercell K-space Extremal Area Finder) tool [Rou12]. For a given field direction with respect to the crystal axis, this numerical algorithm returns the expected dHvA frequencies together with band masses and curvatures of the corresponding orbits. The code treats each band individually and is consequently limited to orbits residing on a single band. Energetic degeneracies or magnetic breakdown can allow extremal orbits to reside on FS sheets of multiple bands. DHvA frequencies corresponding to such orbits are not included in the SKEAF output. We defer a detailed discussion of further limitations of our calculation to the next section.

4.4.2 Magnetic state

The band structure of non-magnetic CrB_2 was calculated in order to assess the sensitivity of individual Fermi surface pockets to magnetic order. The results are shown in appendix B.1. They match perfectly with those presented by Brasse [Bra13a], substantiating the author's two main statements: First, the four bands crossing the Fermi energy have almost exclusively Cr-*d* character, with the exception of two bands crossing E_F close to the A-point which exhibit strong B-*p* character. Second, these B-*p*-like pockets are merely spin-split and shifted in reciprocal space, but hardly altered in shape and size by the introduction of magnetic order, while Cr-*d* bands are highly sensitive to the spin structure.

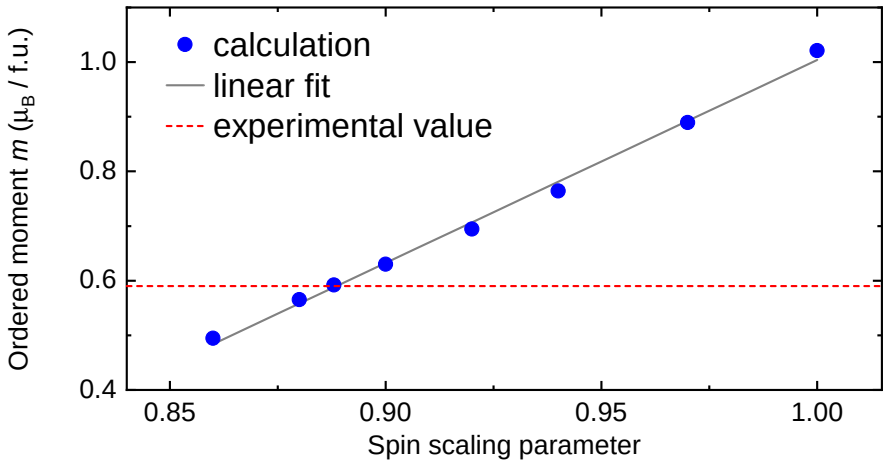

Figure 4.10: Ordered magnetic moment per unit cell (blue circles) as a function of the spin scaling parameter. The gray solid line displays a linear fit through the calculated moments. The red dashed line represents the experimentally observed value of $0.59\,\mu_B$/Cr.

We further performed band structure calculations for single-k spin cycloids with different propagation vector magnitudes along $\mathbf{q}_{110}$. We varied the length of $\mathbf{q}$ from $0\,\mathbf{q}_{110}$, i.e., the ferromagnetic state, to $0.5\,\mathbf{q}_{110}$, i.e., the collinear antiferromagnet. The resulting total energies are shown as red circles in Fig. 4.9. The energy of the paramagnetic state is included as green dashed line. According to our calculations, any considered magnetic order is favorable over the non-magnetic state. The ferromagnetic state is energetically much less favorable than antiferromagnetic order. The total energy exhibits a minimum at $0.27\,\mathbf{q}_{110}$ which is very close to the experimentally observed propagation vector $0.286\,\mathbf{q}_{110}$ [Reg19].
The ordered moments resulting from the calculations are shown in Fig. 4.9 as blue triangles. For finite propagation vector, they vary between 0.90 and $1.12\,\mu_B$/Cr. In particular, at the experimental length of $\mathbf{q}$, the moment is as high as $1.02\,\mu_B$/Cr as opposed to the experimentally observed value of $0.59\,\mu_B$/Cr. As a crucial advance compared to previous work, we employed the concept of spin scaling [Ort12] in our calculation in order to resolve this mismatch. Figure 4.10 displays the variation of the ordered moment with changing spin scaling parameter. The dependence is roughly linear, as illustrated by the fit. The experimental value is best matched for a spin scaling parameter of 0.888. Consequently, we constrain our detailed discussion of the electronic structure to the calculation with $\mathbf{q} = 0.286\,\mathbf{q}_{110}$ and spin scaling parameter 0.888 representing the best fit to the real experimental situation.
Considering a single-k spin structure, the sixfold symmetry of the Brillouin zone (BZ) is reduced. This is schematically depicted in Fig. 4.11. Here, e.g., the points M and M' are no longer equivalent. The same holds for L and L'. The importance of this consideration is illustrated by means of the band structure. Figure 4.12 a) shows the band structure along the red path in Fig. 4.11, Fig. 4.12 b) contains the band structure along the cyan path. Obviously, we obtain the identical picture for the overlapping part of the paths between Γ and A. Interestingly, also the paths

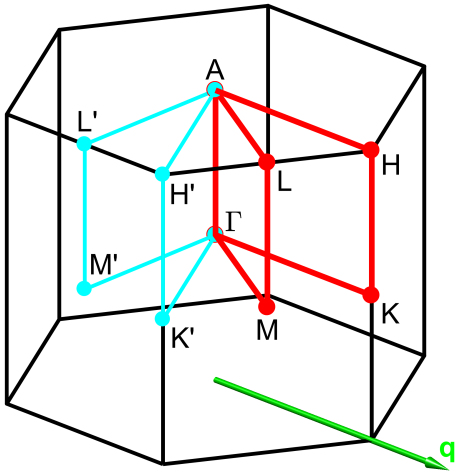

Figure 4.11: Brioullin zone of a hexagonal Bravais lattice. The magnetic order with propagation vector **q** reduces the symmetry so that points like M and M' oder L and L' are no longer equivalent. The red and cyan lines represent the paths along which the band structure is plotted in Fig. 4.12.

$\overline{\mathrm{KH}}$ and $\overline{\mathrm{K'H'}}$ are still identical, but moving away from the Brillouin zone boundary, we observe different structures for $\overline{\Gamma\mathrm{K'}}$ and $\overline{\Gamma\mathrm{K}}$ resp. $\overline{\mathrm{H'A}}$ and $\overline{\mathrm{HA}}$. In the band structure shown in Fig. 4.12 a), only three bands cross the Fermi energy, namely the blue, cyan and purple ones. The bands colored green and red come close to, but never actually touch the Fermi level in this plot. On the contrary, in Fig. 4.12 b), these bands both clearly cross the Fermi energy. Consequently, we have five bands contributing to the Fermi surface. Following the naming convention of the Elk code, we label them bands 19 (red) to 23 (green).

Before presenting the corresponding Fermi surface sheets, we discuss some of the limitations of our theoretical approach. A natural issue is the limited resolution. In numerical approaches, a trade off between calculation time and spatial resolution is necessary. In our Fermi surface calculation, e.g., the energy eigenvalues were calculated on a $50\times50\times50$ k-mesh within the reciprocal unit cell (RUC). A limited resolution can become critical, e.g., when a band exhibits an extremum very close to the Fermi energy. This is the case for our band 23 about halfway between Γ and K as marked by the magenta arrow in Fig. 4.12 a). According to our band structure calculation, band 23 does not yield a Fermi surface pocket at this point. However, the calculated band minimum resides less than 15 meV above the Fermi energy while the energetic difference between neighboring k-points around the minimum is on the order of 15 - 20 meV. In the band structure calculation, the path $\overline{\Gamma\mathrm{K}}$ is covered by $\sim$170 k-points, whereas the Fermi surface calculation contains less than 30 k-points on the same path. This is owed to the fact that computation time grows linearly with the number of k-points per reciprocal length in the one-dimensional band structure calculation but with the third power of that number for the three-dimensional FS calculation. Consequently, for band extrema similarly close to $\mathrm{E_F}$ that do cross the Fermi energy, the corresponding FS pockets might not be correctly resolved.

The DFT code used in this work does not follow particular bands, but simply enumerates the energy eigenvalues at each k-point. Thus, whenever bands cross, the calculated bands switch numbers. The bands involved exhibit kinks at the crossing point. The labeling thus corresponds to a situation where all band crossings are

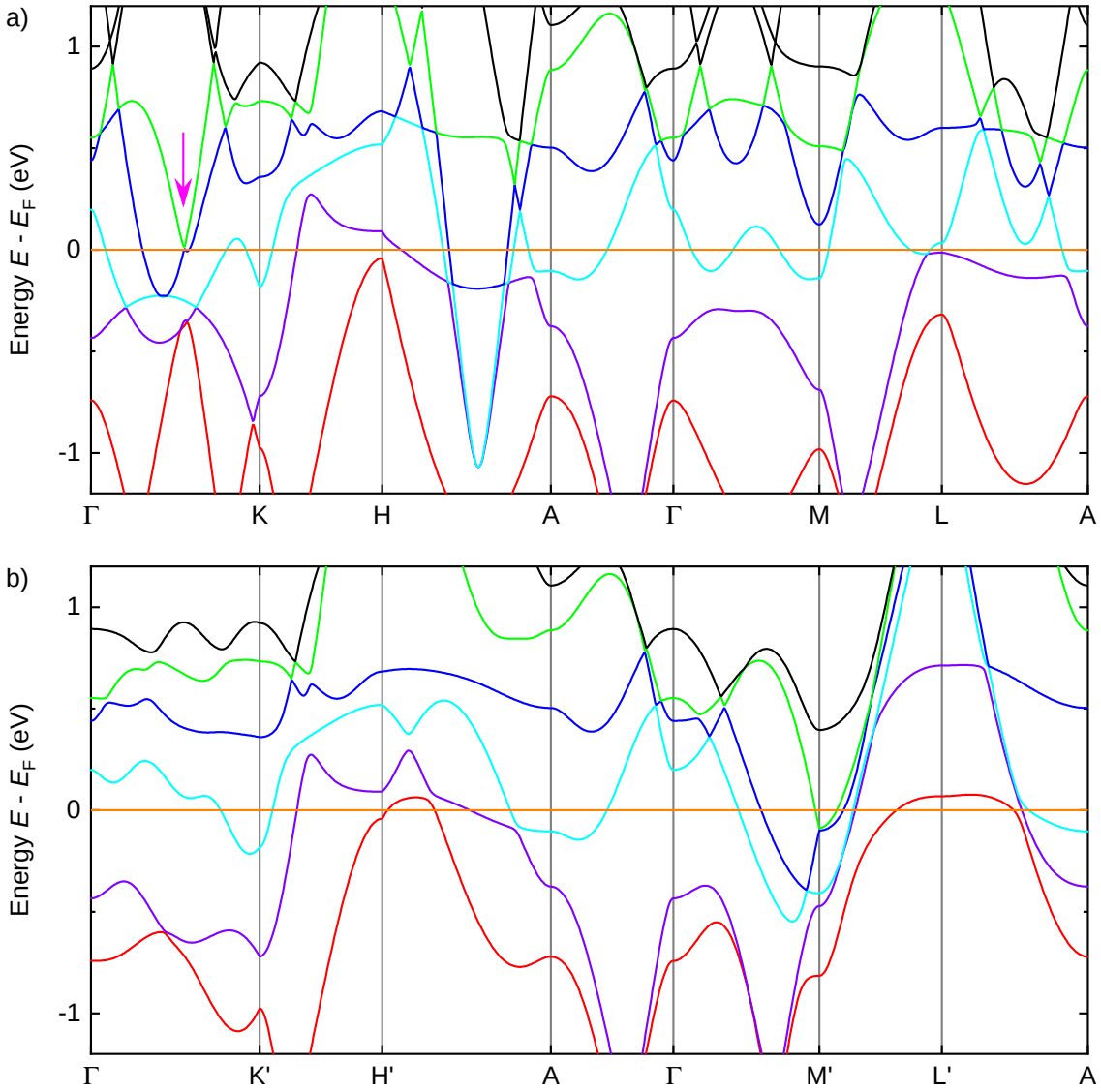

Figure 4.12: Band structure calculated for a cycloidal spin structure of CrB_2. The structure is calculated along the paths indicated in Fig. 4.11 with the red path in a) and the cyan path in b). The orange straight line represents the Fermi energy. In a) only three bands cross the Fermi energy, in b) five bands do.

avoided, regardless of whether or not they cross at a point of degeneracy. There are many examples visible in Fig. 4.12 as, e.g., the minimum of band 23 close to E_F between Γ and K. In many cases, spin-orbit-coupling lifts the degeneracy at crossing points since the SOC-induced mixing of bands promotes avoided crossings. As a consequence, the calculated band structure and Fermi surface may look more similar to reality than we can expect from our procedure. A quantitative assessment of the gap sizes between FS sheets is only possible with high-resolution calculations including SOC. Still, spin-orbit-coupling might alter the band dispersion and consequently the shape of the Fermi surface also away from band crossing points.

Finally, we considered a single-k cycloidal spin structure as suggested already by early neutron scattering experiments. More recent work suggests that CrB_2 might actually have a more complex spin structure (cf. Sec. 4.1.1). As we stated above and will again demonstrate below, the CrB_2 Fermi surface is very sensitive to the details of its magnetic structure. Thus, it is likely that the FS for such a multi-k spin structure differs strongly from the result of our calculations.

4.4.3 Fermi surface

The Fermi surface obtained from our calculation is shown in Fig. 4.13 (i) to (v). Sheets arising from different bands are plotted separately for clarity. The colors correspond to the colors of the bands in Fig. 4.12. Directions and symmetry points in the reciprocal unit cell are illustrated in Fig. 4.13 (ix). An illustration of all bands within the same reciprocal unit cell as well as in the Brillouin zone is presented in appendix B.2.
The bands 19 and 20, depicted in red and purple, are shown in Fig. 4.13 (i) and (ii), respectively. They both yield a single large pocket centered around the L'-point. While the red sheet has a rather smooth topography, the purple sheet exhibits several pronounced extrusions. The cyan colored band 21 shown in Fig. 4.13 (iii) results in a complicated Fermi surface sheet. There are two copies of a sphere located between A and L', one flat, plus-sign shaped pocket centered around M' and a large, multiply connected sheet spread through the whole reciprocal unit cell. The band 22 is depicted in blue and shown in Fig. 4.13 (iv). The reciprocal unit cell contains five pockets. Alike band 21 in Fig. 4.13 (iii), there are two copies of a sphere between A and L'. Further, two copies of a dumbbell shaped pocket are located between Γ and M'. Last, there is one pocket around M' elongated along $\mathbf{q}_{1\bar{1}0}$. The green band 23 is shown in Fig. 4.13 (v). It yields a single small pocket around M' which appears almost planar in the $\mathbf{q}_{110}$-$\mathbf{q}_{001}$-plane.
Bands 19 and 20 are hole-like sheets, bands 22 and 23 are electron-like. Band 21 has mixed character, yet the spherical pocket is clearly electron-like. As mentioned before, the presented sheets are almost exclusively of Cr-d character. The only exceptions are the spherical pockets in Fig. 4.13 (iii) and (iv) which exhibit predominantly B-p character. As stated above, single copies of these pockets are present around the A-point in a non-magnetic calculation. By introduction of magnetic order, they are spin-split and shifted in reciprocal space, but not altered significantly in shape and size. In contrast, the Cr-d-like sheets are sensitive to magnetic order.
We now compare our results to those presented by Brasse *et al.* [Bra13b]. The authors employed the WIEN2k software package and presented results for a spin cycloid with an ordering wave vector $\mathbf{q} = 0.3\,\mathbf{q}_{110}$. Their calculation yielded an ordered moment of $1.3\,\mu_B$/Cr, i.e., more than twice the experimental value. The Fermi surface resulting from their calculation is shown in Fig. 4.13 (vi) to (viii). In contrast to our results, they only obtain sheets from three bands. The bands 19 and 23 in our description do not cross the Fermi energy in their calculation. The purple colored sheet in Fig. 4.13 (vi) looks similar to our band 20 but misses some extrusions,

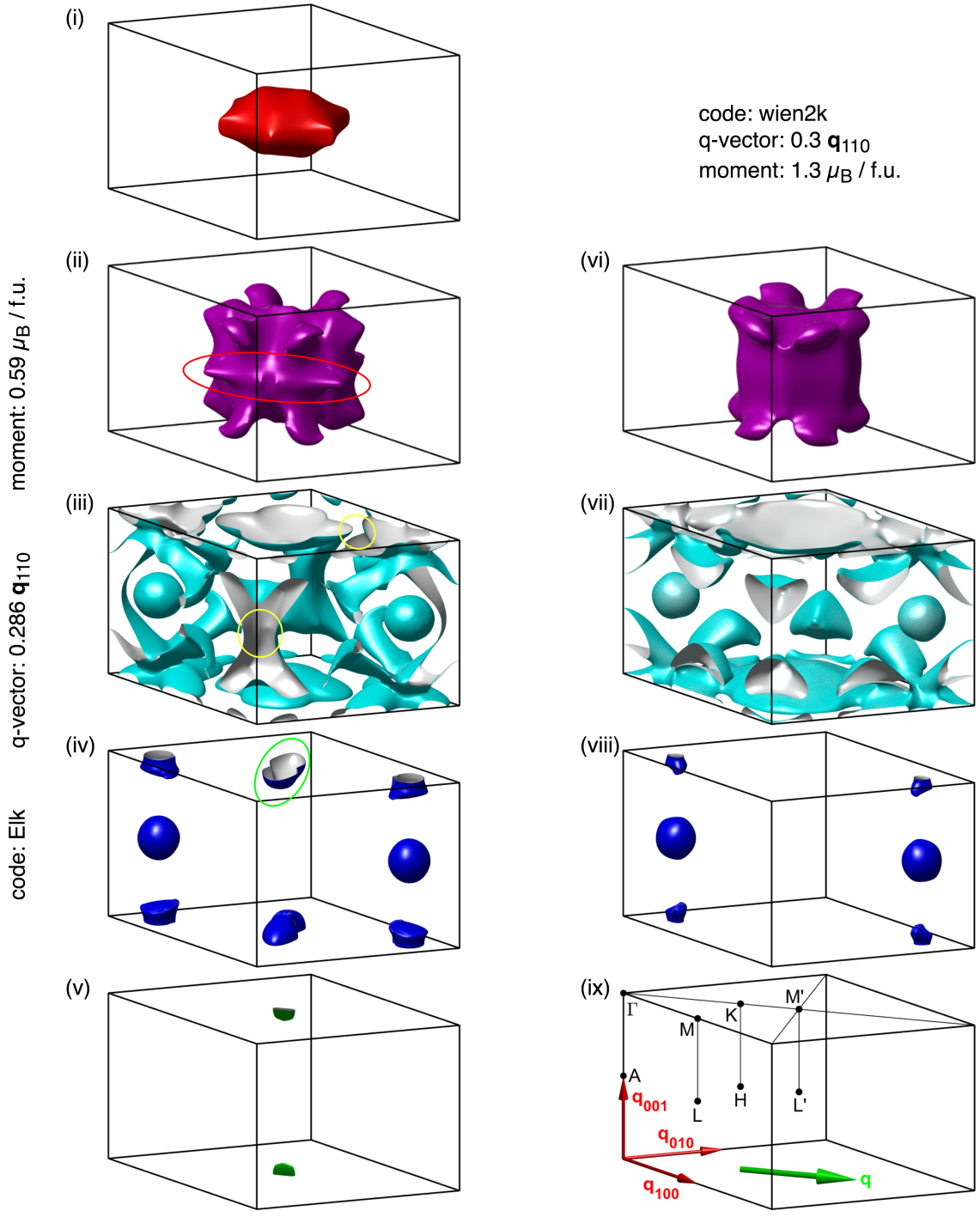

Figure 4.13: Fermi surfaces calculated in this work ((i)-(v)) and previous work ((vi)-(viii)) [Bra13b]. Prominent differences are marked by the red, yellow and green circles. Our calculation yields sheets from two more bands than previously reported. (ix) Symmetry points in the reciprocal unit cell with respect to the propagation vector of the spin cycloid. The reciprocal lattice vectors $\mathbf{q}_{100}$, $\mathbf{q}_{010}$ and $\mathbf{q}_{001}$ (red) are scaled to half their length with respect to the cell for clarity.

as marked by the red circle in Fig. 4.13 (ii). The cyan colored bands in Fig. 4.13 (iii) and (vii) also look somewhat similar, but there are notable differences as, e.g., the connection of several pockets as marked by the yellow circles in Fig. 4.13 (iii). Notably, the spherical pockets appear almost identical in both calculations. The blue colored sheet in Fig. 4.13 (viii) consists of spheres and dumbbells like our band 22, but misses the M'-centered pocket as marked by the green circle in Fig. 4.13 (iv). While the B-*p*-like spherical pockets look very similar in shape and size, the rather Cr-*d*-like dumbbell-shaped pockets are notably altered between the two calculations. The direct comparison presented above substantiates the sensitivity of Cr-*d*-like Fermi surface sheets to the details of the magnetic structure. Compared to the previous results, we significantly improved the adjustment of the calculation to the experimental values of ordering wave vector and magnetic moment in the present work.

4.4.4 Implications for the dHvA effect

In this section we discuss the implications of the calculated Fermi surface for our experiment. We employed the SKEAF tool to extract the expected dHvA frequencies for a given field direction as well as the effective masses and curvatures of the corresponding orbits. Possible additional dHvA components due to orbits residing on multiple bands are not discussed in this section. We address this issue in Sec. 4.5.1. In Fig. 4.14 we show the frequencies obtained for magnetic fields in the (001)-plane as a function of the experimental angle φ. In this representation, the field is parallel to the ordering wave vector for $\varphi = 0°$. Again, we notice that the six-fold symmetry of the crystal structure is lifted by the magnetic order. Since a two-fold symmetry is preserved by the cycloidal structure, we only show the angular region from 0° to 180°.

The expected frequencies range from a few Tesla up to more than 30 kT. The corresponding effective masses range from $0.21\,m_\mathrm{e}$ up to over $12\,m_\mathrm{e}$. The topologically and topographically simple Fermi sheets originating from bands 19 and 23 each result in a single frequency branch present over the whole angular range. The Fermi surface of band 20 is singly connected, but has a rich topography which leads to splitting of the frequency branch for certain directions. Band 22 has several separated Fermi pockets, resulting in one continuous branch for each pocket. The one arising from the M'-centered sheet splits between 60° and 120°. Band 21 with its complex Fermi surface sheet results in a manifold of possible extremal orbits. The branches differ widely in frequency as well as their angular variation. Moreover, band 21 yields a number of frequency branches that exist only on small segments of the angular regime. Except for the split-offs of bands 20 and 22, the branches originating from other bands are continuous through the whole angular regime.

The frequency spectrum presented in Fig. 4.14 assumes a magnetic state with a single propagation vector in $\mathbf{q}_{110}$-direction. Due to the six-fold symmetry of the crystal, the sample can exhibit further domains with the spin cycloid propagating along vectors rotated by ±120° with respect to $\mathbf{q}_{110}$, i.e. along $\mathbf{q}_{1\bar{2}0}$ and $\mathbf{q}_{\bar{2}10}$, respectively.

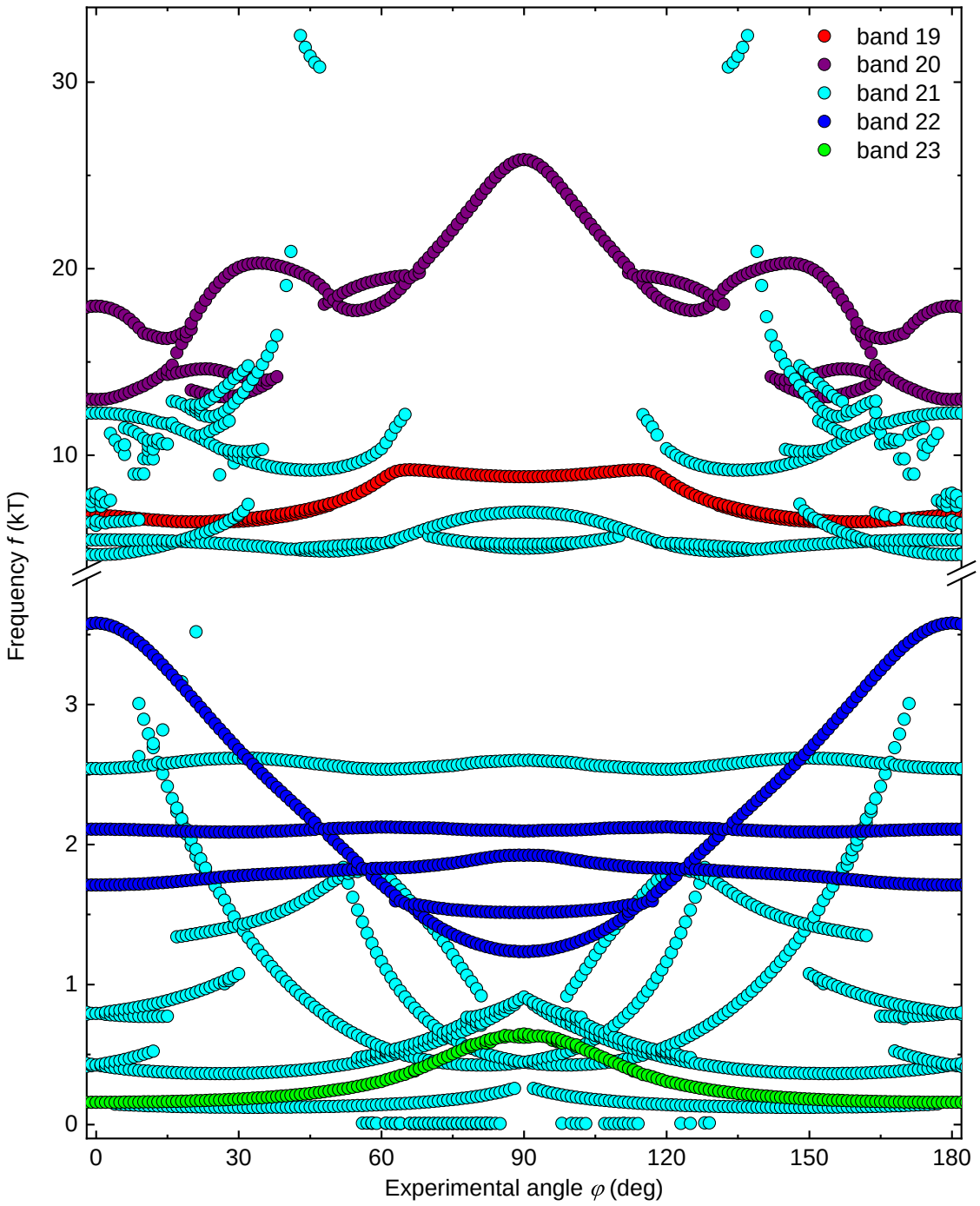

Figure 4.14: Frequencies of dHvA oscillations as expected from our calculated Fermi surfaces for magnetic fields applied in the (001)-plane. φ is the experimental angle defined in Fig. 4.2 b). In this representation, the ordering wave vector is parallel to the field at $\varphi = 0°$. Orbits crossing between multiple sheets are not considered.

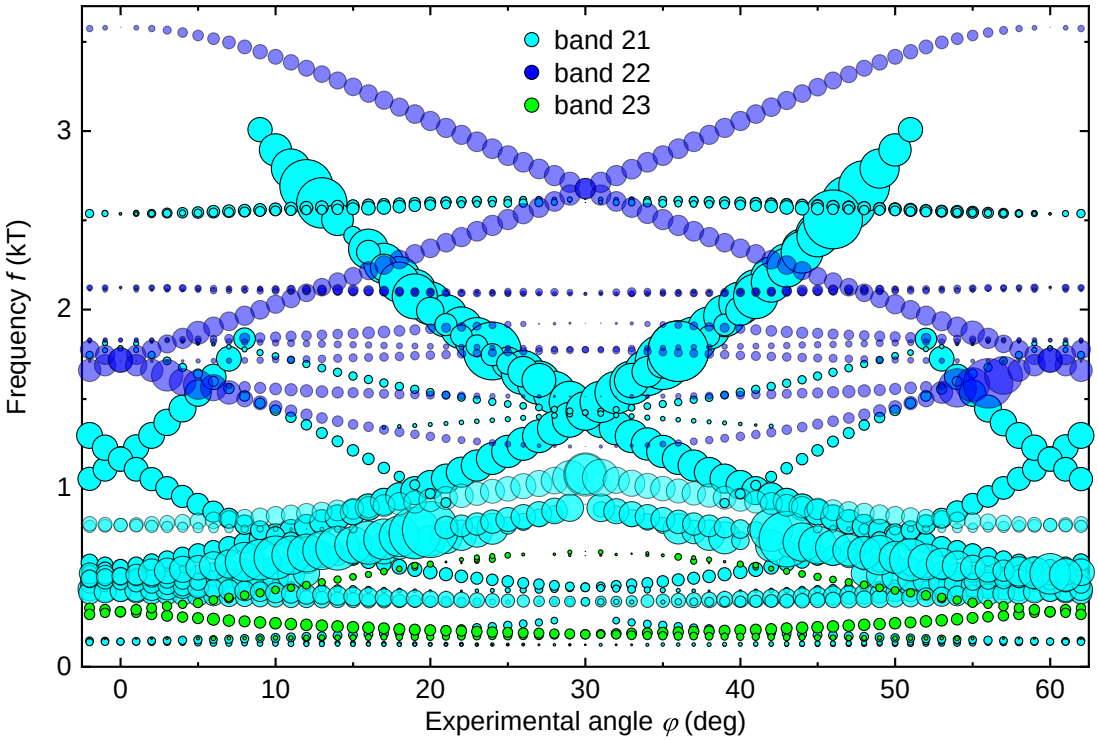

Figure 4.15: Frequencies expected in the dHvA effect from our calculations. The point size resembles the relative expected amplitude. The frequencies from three magnetic domains are included.

Considering three equally populated domains, the six-fold symmetry is restored in the frequency spectrum. Adding the dHvA frequencies following from the additional domains to Fig. 4.14 is equivalent to shifting the components displayed in the angular ranges from 60° to 120° and from 120° to 180° to the regime between 0° and 60°. Thus, the number of expected frequencies for a given field direction is drastically increased. For a more elaborate estimate of what we expect to observe in experiment according to our calculation, we additionally consider the strength of the oscillating signal.

As described in Sec. 2.2, the amplitude of magnetic quantum oscillations depends on effective mass m^* and curvature P'' of the corresponding orbit. The resulting torque additionally depends on the angular variation of the frequency. At finite temperature T, the Lifshitz-Kosevich factor has to be considered. We calculated

$$S = \left| \frac{\partial f}{\partial \varphi} \cdot \frac{1}{m^* \sqrt{P''}} \cdot \frac{X}{\sinh X} \right| , \quad \text{with} \quad X = \frac{2\pi^2 k_\mathrm{B} T}{\hbar e B / m^*} \tag{4.2}$$

to obtain a measure S for the expected signal strength of a particular frequency. For this calculation we assumed an experimental temperature of 0.3 K and a magnetic field of 15 T.

In Fig. 4.15 we show the calculated frequencies as circles. S is included as data point

size. For clarity, we only show frequencies in the range relevant for our experiment. The graph includes the calculated frequency branches for all three domains. There are roughly ∼30 frequencies present at each angle. While some of them are well separated from other branches, there is a lot of overlap especially at frequencies below 1 kT. E.g., for angles close to 0°, several frequency branches approach each other around $f = 0.5$ kT. In such a case, it is particularly hard to distinguish the individual frequencies from experimental data. We find distinct differences in the expected signal strengths. Band 21 yields the branches with the strongest, but also those with the weakest signal. The expected signals of bands 22 and 23 are relatively small compared to the strong band 21 branches. A more detailed discussion is presented in the following section along comparison with experimental results.

4.5 Comparison of experiment and theory

In this section we combine the results from measurements and calculations presented above. We begin with dHvA frequencies and their angular evolution. In Figs. 4.16 and 4.17 we show experimentally observed and calculated frequencies versus the measurement angle φ. Figure 4.16 contains the calculated result for band 21, Fig. 4.17 shows the results for bands 22 and 23. Experimentally obtained frequencies are depicted as squares. Large red squares show reliable frequencies whereas small magenta squares represent the more uncertain results of category C (cf. Sec. 4.2.2). Calculated frequencies are depicted as circles. The circle size is scaled with S, i.e. proportional to the expected amplitude. Note that the colors of the calculated data no longer refer to the FS sheet, but are intended to help to distinguish between orbits around different pockets or in different locations in the RUC on the same sheet. An exemplary illustration of extremal orbits on the CrB_2 Fermi surface is given in appendix B.3.
The plots are confined to the range covered experimentally. As stated above, we did not evaluate any frequencies above 5 kT due to the limited data point density. We can therefore not expect to observe any oscillations corresponding to orbits on bands 19 or 20. The experimental conditions also require a lower frequency limit which in our case was ∼20 T. Slower oscillations could not clearly be separated from the non-oscillatory background. An angular range of 60° was covered in experiment. All calculated frequencies are contained in this range due to the six-fold symmetry in the three domain configuration.
In Fig. 4.16 we discriminate between three types of calculated orbits. The blue circles represent the orbit around the spherical B-*p*-like pocket of band 21, the green circles resemble an orbit centered around M on the multiply-connected sheet. The gray colored data points represent a bunch of orbits on the same sheet located alongside the connection of M and L. On first glance, there is a lot of overlap between experiment and calculation. The detailed investigation given in the following shows, however, that this does not result in unique assignments for the majority of observed orbits.
Strikingly, there is no obvious experimental candidate for the branches with the

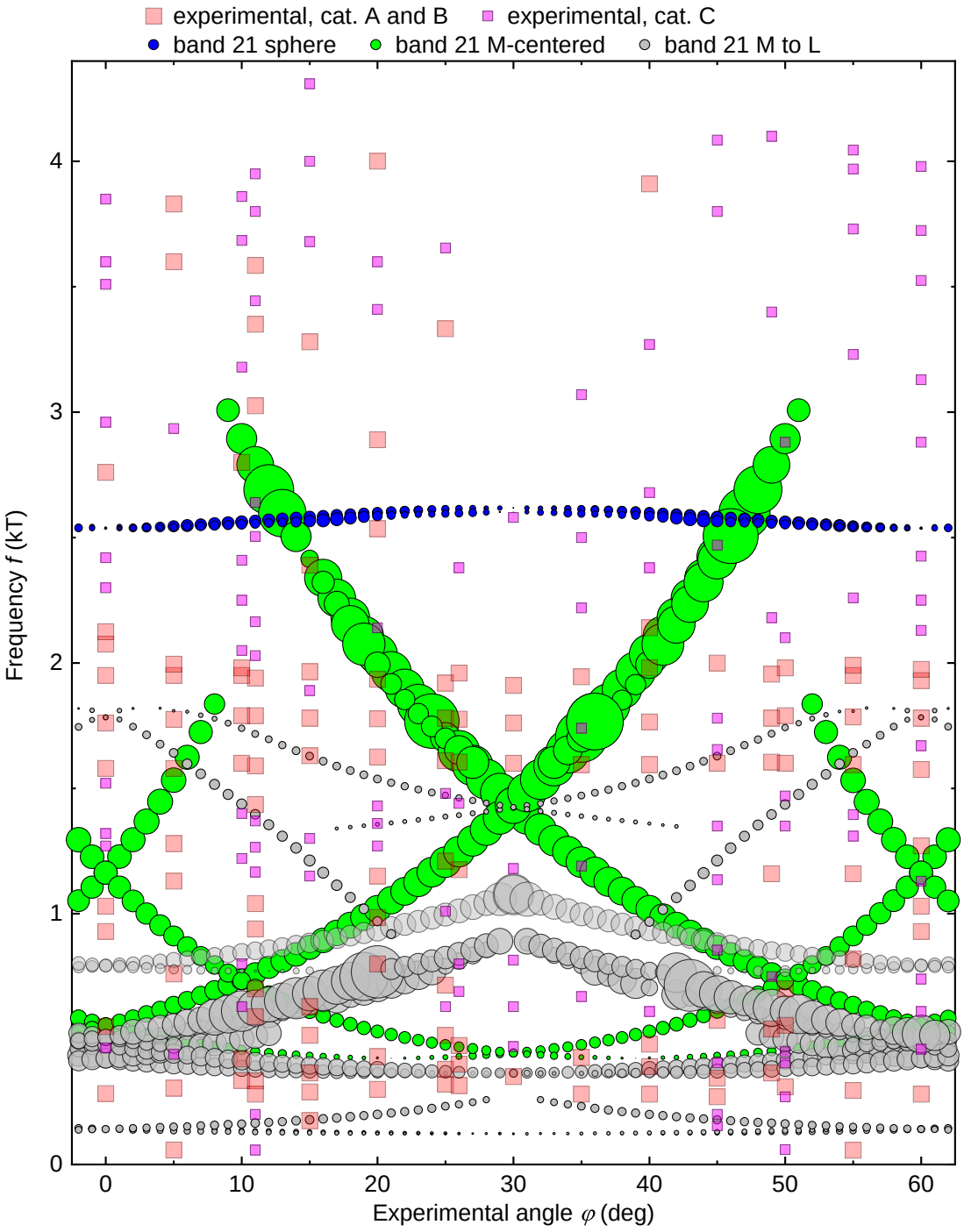

Figure 4.16: Comparison of experimental results and calculation for band 21. Circles represent calculated frequencies. The colors correspond to different locations in the reciprocal unit cell, the point size illustrates the calculated relative amplitude. Squares represent experimental data. Large red squares are reliable frequencies whereas small magenta colored squares represent the more uncertain category C results.

largest expected signal strength, namely the green colored component centered around M which appears at 3 kT and quickly drops with φ. While there are good matches at individual angles, we find no clear evolution of any measured frequency component resembling the calculated behavior. In different domains, the same branches run reasonably close to the experimental branches labeled β and γ in Fig. 4.6, but exhibit distinctly smaller relative signal strength S.
The frequency components colored gray show a lot of overlap with experimental data. Yet there is no obvious match of any particular branch leaping to the eye. Above 0.6 kT, the overlap with experiment is rather occasional. Below that value, several calculated branches overlap, hindering an unambiguous assignment. There is additional overlap with band 23 shown in Fig. 4.17. The lowest branch in frequency appears to be an exception. It runs fairly separate from the large frequency cluster making it the candidate closest to the lowest measured frequencies. However, one calculated frequency branch at 5 - 15 T (cf. Fig. 4.14) is not included in the plot. This additional branch arises from a rather flat part of the band close to the Fermi energy, so that a tiny alteration to E_F or the magnetic structure might easily shift it closer to the experimental values than the gray branches shown in the plot. Also, this low frequency branch has a much higher expected amplitude than the ones shown in the graph. Still, we excluded this branch from the plot for two reasons. First, it lies below the experimental low frequency threshold. Second, the calculated orbit is so small that its appearance is governed by the strong interpolation performed within the SKEAF algorithm rather than by the energy eigenvalues obtained from the FS calculation. This is briefly illustrated in appendix B.4. We thus assess this orbit as an unreliable result due to the limited resolution of our DFT calculation. Yet a shift of less than 10 meV in E_F is sufficient to increase the calculated frequency to match the lowest experimental values. Thus, while it is not reliably resolved in our calculation, this additional orbit might represent a better candidate for the lowest experimentally observed frequencies than the components presented in Fig. 4.16.
The frequency arising from the orbit around the sphere shows almost no variation with changing angle. The closest experimental frequencies with similar stability are found between 1.5 and 2 kT. While Brasse *et al.* allocated the experimental frequency labeled η in our work to the spherical pocket of this band [Bra13b], we refrain from such a statement for several reasons. The frequency mismatch is roughly 20 %. We showed that the B-*p*-like spheres are very stable against alteration of the magnetic state. Thus the frequency mismatch is unlikely to be created by a misrepresentation of the structure in our calculation. To account for the difference by the Fermi energy, a shift as large as 100 meV is necessary which lacks physical justification. Finally, there are better candidates for the measured frequency as we will show below.
In Fig. 4.17 we discriminate between orbits arising from different FS pockets. The green circles represent the orbits around the small band 23 pocket. The blue, yellow and cyan colored circles correspond to the orbits around the sphere, the dumbbell and the elongated M'-centered pocket of band 22, respectively. As pointed out for the gray colored frequencies in Fig. 4.16, the calculated values for band 23 lie close to a lot of experimental data points, yet due to the overlap of several branches, a

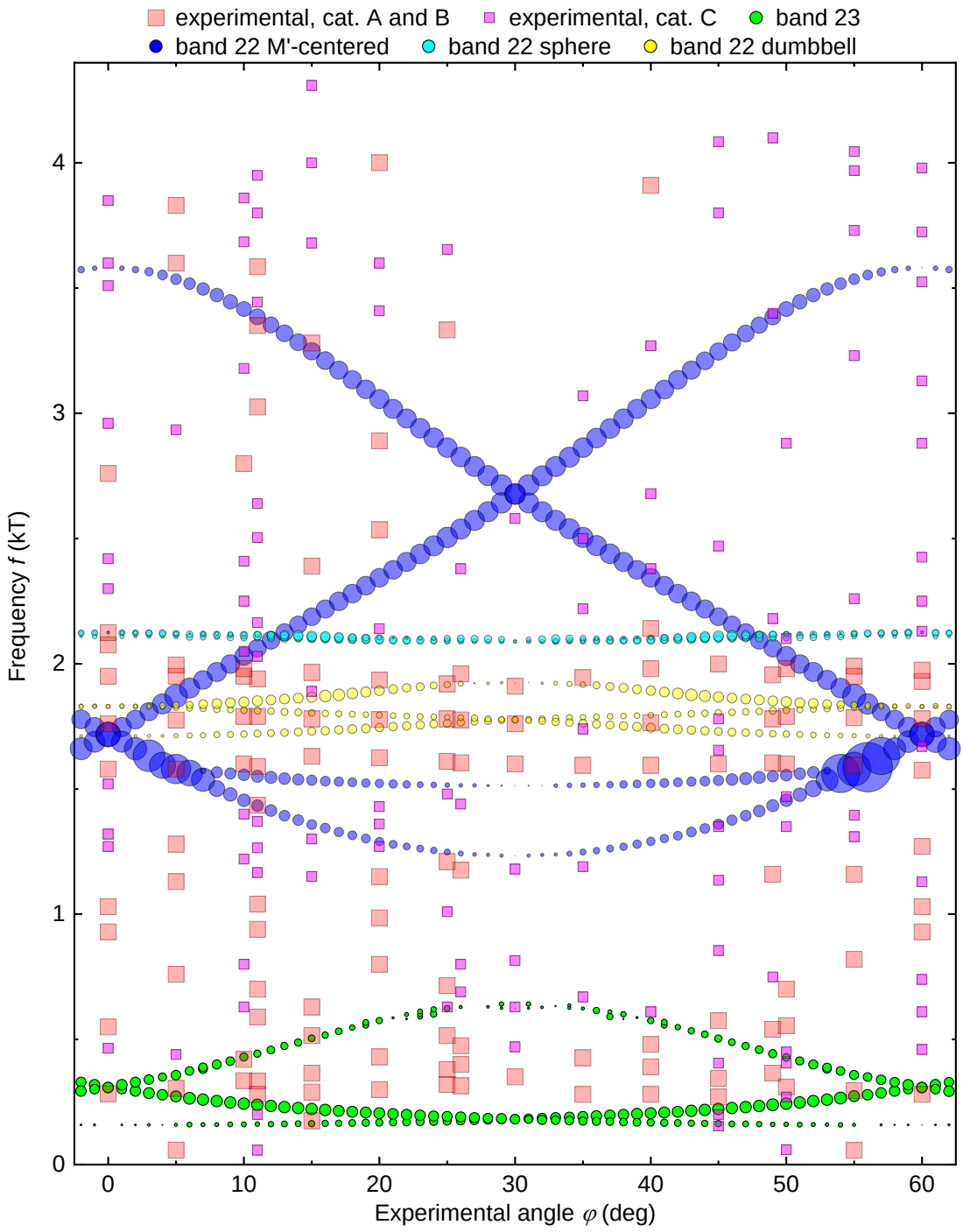

Figure 4.17: Comparison of experimental results and calculation for bands 22 and 23. Circles represent calculated frequencies. Different colors correspond to different FS pockets. The point size illustrates the calculated relative amplitude. Squares represent experimental data. Large red squares are reliable frequencies, small magenta colored squares represent the more uncertain category C results.

clear assignment cannot be made. For band 22, a more detailed look is necessary. The branches with the largest signal strength S are the blue ones arising from the elongated Fermi pocket around M'. In two domains, this pocket yields a single orbit which alters its frequency from ∼1.7 kT to over 3.5 kT. Similar to the M-centered orbits with large signal strength of band 21, there are occasionally good matches with measured frequencies at individual angles, but the calculated behavior is not clearly reflected in any measured frequency branch. In the third domain, the orbit splits into two branches with considerably smaller signal strength and smaller frequency variation. The lower-frequency branch extends from 1.2 to 1.7 kT. Although dHvA frequencies close to this branch are observed at most experimental angles, a definite assignment is not possible due to overlap with the branches calculated for band 21. The higher-frequency split-off is almost constant in frequency around ∼1.5 kT.
The spherical and the dumbbell-shaped pocket of band 22 both yield frequencies in the range from 1.7 to 2.2 kT which do not change much with φ. Together with the split-off of the elongated pocket at ∼1.5 kT, they comprise a number of components which are present over the whole angular regime with very little change in frequency. These fit well to the experimental frequencies between 1.5 kT and 2 kT labeled ϵ, ζ and η in Fig. 4.6. These experimental branches too are visible over the whole angular range with almost no change in frequency. At individual angles, several of these experimental values also match well with calculated branches of higher frequency variation, but the remarkable stability in the experimental frequencies suggests that they belong to rather isotropic Fermi pockets, i.e. that the calculated branch should resemble the stability in frequency.
We emphasize the discrepancy between the experiment and the calculated signal strength. The stable frequency components between 1.5 and 2.2 kT which match the experimental data best have rather small signal strength in the calculation. In contrast, the largest signal is expected for several orbits on bands 21 and 22 which show a large frequency change. These orbits can not clearly be recognized in the experimental data. Moreover, we observed several dHvA frequencies in experiment which are nowhere near any calculated value.
Beside frequencies, charge carrier masses were both calculated and determined from experiment. In Fig. 4.18 we show the calculated band masses (squares and triangles) together with the effective masses obtained from measurements (red circles). The symbol colors for calculated values help discriminate between values originating from orbits around different FS pockets or in different locations in the RUC. Again, the graph is constrained to the experimentally relevant frequency and mass regimes.
An intriguingly good match is found for two measured components between 1.5 and 2 kT. For the experimentally observed dHvA oscillation ϵ, both frequency and mass match exceptionally well to a calculated orbit around the M'-centered Fermi pocket of band 22 (blue squares) with a difference of less than 2 %. For the dHvA oscillation ζ, the experimental value is closely surrounded by the three orbits calculated for the dumbbell-shaped pocket of band 22 (yellow squares) with a maximum mismatch of less than 4 % in frequency and less than 10 % in mass. For the third experimental component in this frequency range η, a comparison to the same pocket still yields

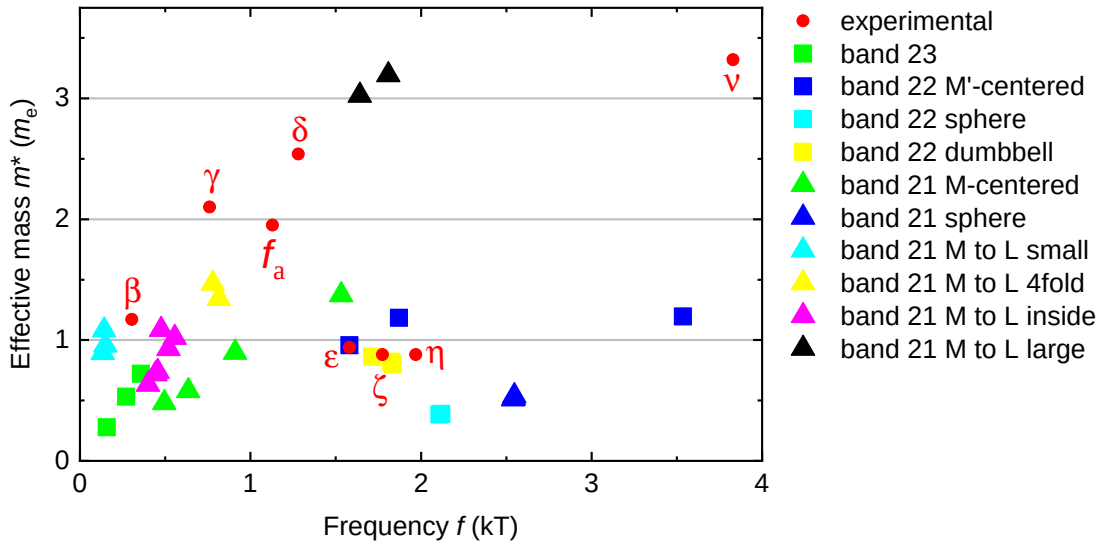

Figure 4.18: Effective masses versus frequencies of extremal orbits. Red circles represent experimental values, squares and triangles represent calculated values. Colors discriminate between orbits around different FS pockets or in different locations in the RUC.

a good match with values differing by less than 7 % in frequency and 10 % in mass for the closest calculated value. From the frequency-versus-angle map we rather suggest an allocation of η to the spherical pocket of band 22 (cyan squares). Here, the frequency differs by less than 8 %, but the calculated mass amounts to only 44 % of the measured value. DFT is known to often underestimate effective masses due to negligence of interactions between charge carriers and collective lattice excitations such as, e.g., phonons or magnons. Thus, considering an allocation of η to the spherical pocket of band 22 is still reasonable. We note that we do not observe an obvious experimental candidate for the sphere arising from band 21 (blue triangles). Regarding the frequency components below 1 kT, β and γ, there are several reasonable candidates among the calculated orbits. For β, the closest candidates in frequency originate from the band 23 FS (green squares). The frequencies are off by 10 % and 20 % and the mass is enhanced by factors of 2.2 and 1.6, respectively. Comparison to orbits originating from band 21 (cyan and magenta triangles) yields a better match of the mass at the cost of a larger frequency mismatch. Considering the angular dependence in Fig. 4.16, β fits best to an M-centered orbit on band 21 (green triangles) for which frequency mismatch and mass enhancement are larger than 60 % and 2.4, respectively. For γ, the closest candidates arise from orbits along the connection of M and L on the FS of band 21 (yellow triangles). They yield a mass enhancement of 1.4 and 1.6 at frequency mismatches of less than 3 and 7 %, respectively. Again, with respect to Fig. 4.16, we also consider an orbit centered around M on the same FS sheet (green triangles). Here, the frequency mismatch and the mass enhancement amount to 20 % and 2.3, respectively.
Between 1 and 1.5 kT, we observed two dHvA frequencies, but no theoretical values are found in this range. The closest calculated frequencies to the experimental

components f_a and δ correspond to the M-centered orbit on band 21 (green triangles). The frequency mismatch amounts to 20 % for both f_a and δ, the masses are enhanced by factors of 2.2 and 1.9, respectively. Above 3 kT there are only one observed dHvA component ν and one calculated component arising from the M'-centered pocket of band 22 (blue square). A comparison yields a frequency mismatch of less than 8 % and a mass enhancement of 2.8. Given that we observed another dHvA oscillation much closer to the calculated value (cf. Fig. 4.17), we do not suggest an assignment of ν to the elongated band 22 pocket despite the reasonably small frequency difference.

4.5.1 Discussion

So far, we considered frequency, angular dependence and charge carrier masses. Another important criterion for assigning experimental observations to calculated orbits is their uniqueness, i.e. the (non-)existence of other calculated values close to a measured frequency. Unfortunately, this requirement is given for almost none of our candidates. The only exception is the cluster of ϵ, ζ and η and the orbits on band 22 between 1.5 and 2.2 kT. While the frequencies and masses agree remarkably well, the main argument for an allocation is the small variation of the frequency in the investigated angle range found for all three experimental and calculated components. Similar behavior is not found for any other calculated orbit in that frequency range. We thus suggest an assignment of η to the spherical pocket, ζ to the dumbbell-shaped pocket and ϵ to the elongated pocket of band 22.
Apart from these three components, no unique match is found. The comparison of frequency branches is in particular hindered by the large experimental angle step size which prohibits definite tracking of particular frequencies with changing angle. The ambiguity is demonstrated by the example of the experimental branch β. The angular dependence indicated in Fig. 4.6 resembles an M-centered orbit on band 21. However, this orbit yields a frequency mismatch of >60 % and a mass enhancement of >2.4 at $\varphi = 5°$. In contrast, the frequency is matched with <11 % deviation at a mass enhancement of 2.2 for an orbit on band 23. Further, an orbit alongside $\overline{\mathrm{ML}}$ on band 21 matches the mass to less than 10 % at a frequency mismatch of 56 %. None of the latter two orbits exhibits an angular dependence resembled by experimental data. Similar difficulties are encountered for the other remaining experimental components. We thus refrain from any definite assignment beside ϵ, ζ and η.
It appears odd that the mass is matched well for the allocations of ϵ and ζ whereas a mass enhancement of 2.3 is found for η. We attribute this to the character of the corresponding FS pockets. The spherical FS sheet originates from B-p states for which strong mass enhancement has been reported [Bra13b]. The authors allocated, following our nomenclature, component η to the spherical pocket of band 21 and ϵ to the spherical pocket of band 22. By analogy with MgB_2 where B-$p_{x,y}$ electrons form a superconducting condensate, strong electron-phonon coupling for these states was inferred for CrB_2 from the mass enhancement. In contrast, the dumbbell-shaped and M'-centered pockets arise from Cr-d states where no similar enhancement has been reported. While we suggest a different allocation than Ref. [Bra13b], the argument

of strong electron-phonon coupling for B-p states still persists for η and the band 22 sphere.
No statement about the electron-phonon-coupling of Cr-d states has been made in Ref. [Bra13b]. Considering our allocation of ϵ and ζ to orbits arising from such states, we find an accurate match rather than an enhancement of the mass. This is in contrast to the remaining experimental results. All calculated orbits with frequencies below 2 kT arise from Cr-d states, yet the best candidates for the measured frequencies below 1.5 kT yield mass enhancements of 1.4 - 2.3. These orbits arise from the FS sheets of bands 21 and 23, whereas we allocated ϵ and ζ to band 22. Differing strengths of electron-phonon-coupling for different bands may deliver an explanation, but our investigations do not yield any indication of a physical origin of such a difference. We note that, while an orbit residing on the band 23 FS is the best frequency fit to β, all observed frequencies below 1.5 kT may be accounted for by band 21. It is thus possible that the difference only persists between band 22 and band 21. Yet the only apparent difference is that while band 22 and 23 give rise to electron-like FS pockets, band 21 has a mixed character between electron- and hole-like states.
An enhanced mass reduces the dHvA signal strength. Thus, an effect enhancing the charge carrier masses of orbits on band 21 but not on band 22 could also deliver an explanation for the discrepancy concerning the expected signal strengths addressed above. However, at least a factor of $\sim$50 would be necessary to account for the discrepancy which is about 20 times larger than an estimate of the potential mass enhancement.
As stated before, we do not consider the only calculated orbit above 3 kT in Fig. 4.18 a good match for ν. Above, we argued that there are better experimental candidates for the calculated value as can easily be seen in Fig. 4.17. The assessment is further corroborated by the fact that the calculated orbit originates from the same FS pocket for which we find the perfect match with ϵ. In contrast, a mass enhancement of 2.8 is found for an orbit around that pocket when compared to ν which appears highly implausible. Given that, we do not find any candidate for our experimental observation ν in the SKEAF results. In summary, we have experimentally observed several orbits that cannot be accounted for in the calculations of single-sheet orbits in terms of frequency value and dispersion, effective mass and relative signal strength. We therefore consider orbits residing on multiple FS pockets which are not contained in the SKEAF output in the following.
Figure 4.19 displays the Fermi surfaces of bands 21 and 22 in the Brillouin zone cut open along the $\mathbf{q}_{110}$-direction. Four extremal orbits are shown. They reside in the cutting plane for $\varphi = 30°$. The orbits depicted as green and red solid lines are calculated by SKEAF for bands 21 and 22, respectively. The black and magenta dashed lines illustrate orbits where charge carriers swap from one band to the other and back. These orbits can not be found by SKEAF, since the code treats each band individually. Yet both orbits may be physically valid when swapping charge carriers from one band to another is allowed. In our calculation, the bands are actually degenerate at the crossing point, but even when the band degeneracy is lifted, e.g., by

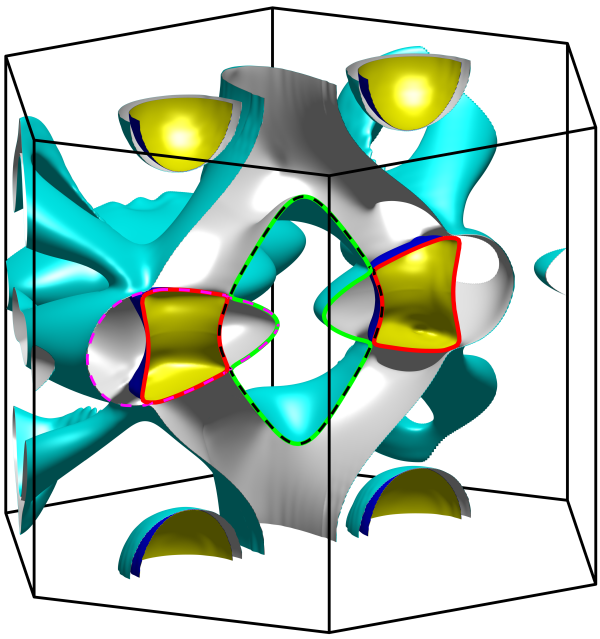

Figure 4.19: Fermi surfaces of bands 21 (cyan/white) and 22 (blue/yellow) in the Brillouin zone cut along $\mathbf{q}_{110}$ with selected extremal orbits for magnetic field along $\mathbf{q}_{1\bar{1}0}$. The two orbits on individual sheets (red and green solid lines) have been calculated by SKEAF. The two orbits crossing between FS sheets (magenta and black dashed lines) cannot be found by SKEAF.

the inclusion of spin-orbit-coupling, the dashed orbits may still exist due to magnetic breakdown [Coh61]. Naturally, an occupation of these orbits decreases the number of charge carriers running on and thus the signal strength of the single-sheet orbits. In the limit where all charge carriers cross bands at all breakdown junctions, the orbits depicted solid green and red vanish from the dHvA frequency spectrum. Instead, the magenta and black dashed orbits would dominate the frequency spectrum in this limit. The breakdown probability can be assessed via Eq. 2.26. Due to the lack of spin-orbit-coupling in our calculation, we can neither state whether the band degeneracy is lifted nor estimate the size of a potential energy gap. Therefore we are limited to the qualitative statement that the real dHvA frequency spectrum of CrB_2 might be altered by magnetic breakdown. The spectra presented in Sec. 4.4.4 may both lack existing frequencies arising from multi-sheet orbits as well as display non-existent frequencies suppressed by the depopulation of single-sheet orbits. Moreover, the signal strengths of orbits involved in magnetic breakdown might be changed.
For the situation shown in Fig. 4.19, we can determine the dHvA frequencies corresponding to the multi-sheet orbits. The black orbit results in a dHvA frequency of 6.57 kT which is well above our experimental limit. The magenta orbit encloses a FS cross-section corresponding to 3.90 kT which is very close to ν. However, ν is measured at $\varphi = 5°$ whereas the situation in Fig. 4.19 corresponds to $\varphi = 30°$. The angular dependence of the frequencies arising from breakdown orbits is unclear since we could not trace the extremal orbit away from high symmetry planes. Looking

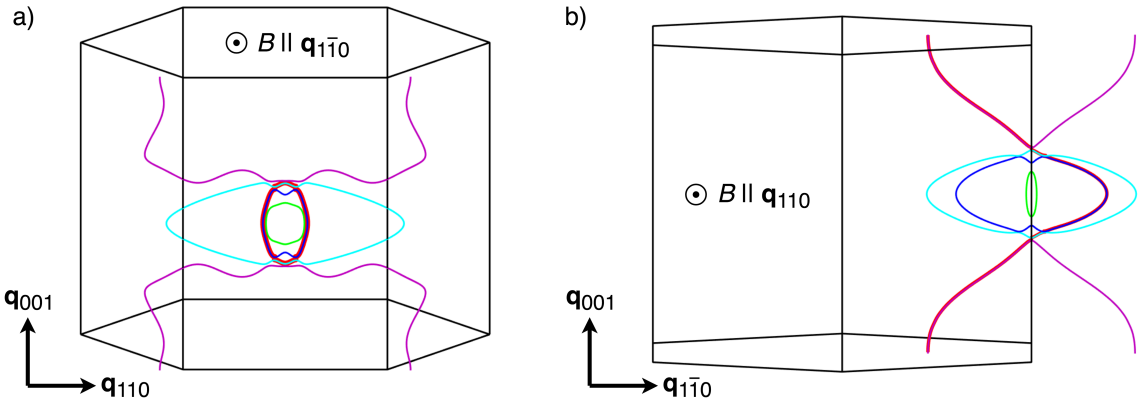

Figure 4.20: 2D slices of selected FS sheets of bands 20 (purple), 21 (cyan), 22 (blue) and 23 (green) in the planes containing M' and L' as well as a) K' and b) Γ. The orbits along the plotted lines are extremal on single bands for magnetic field along a) $\mathbf{q}_{1\bar{1}0}$ and b) $\mathbf{q}_{110}$. The red lines indicate possible orbits on multiple bands.

at the Fermi sheets, it appears likely that, when rotating the field, the magenta orbit will convert to an open orbit, causing the corresponding dHvA oscillation to disappear.
Another candidate for multi-sheet orbits is given by the two spherical pockets of bands 21 and 22. As can be seen in Fig. 4.19, the spheres appear to touch at their highest and lowest points in $\mathbf{q}_{001}$-direction, thus providing possible band crossing points for any magnetic field direction in the basal plane. In the limit of constant band crossing, only one frequency branch is expected instead of the two branches calculated by SKEAF. This may explain the experimental observation of one spherical FS pocket instead of two. The frequency and quasiparticle mass of the multi-sheet orbit would reside in the middle of the single-sheet values. Regarding our assignment of η to a spherical FS pocket, the frequency mismatch would consequently increase from 8 to 18 % and the mass enhancement would decrease from 2.3 to 1.9. Considering dispersion and uniqueness of the observed and calculated frequencies, we stand by the assignment.
While the orbits displayed in Fig. 4.19 are rather easy to find at this particular angle, there might be more hidden multi-sheet orbits not contained in our calculation. Furthermore, we can not determine the corresponding frequencies, masses and signal strengths at arbitrary angles for these orbits as we did for non-breakdown orbits. Consequently, it is possible, that ν corresponds to a breakdown orbit that we have not discovered. We stated that single-sheet orbits may be depopulated by magnetic breakdown. In the particular case discussed on Fig. 4.19, one of these single-sheet orbits runs around the dumbbell-shaped pocket of band 22 for which we found a remarkably good match of theory and experiment. In a second example, we look at possible breakdown orbits involving the M'-centered pocket of band 22 for which we found the best agreement of calculation and measurement.
Figure 4.20 shows two-dimensional slices of selected FS sheets in two planes both containing M'. The FSs are sliced perpendicular to $\mathbf{q}_{1\bar{1}0}$ in Fig. 4.20 a) and perpendicular

to $\mathbf{q}_{110}$ in Fig. 4.20 b). The purple, cyan, blue and green lines represent bands 20, 21, 22 and 23, respectively. The red lines indicate possible breakdown orbits involving the elongated band 22 pocket. The configuration in Fig. 4.20 a) corresponds to $\varphi = 30°$ and the orbit along the blue line results in the lowest blue frequency branch in Fig. 4.17. The suggested breakdown orbit resides on band 22 for the most part and merely crosses to band 21 at the top and bottom. As a result, the frequency increases from ∼1.23 kT to ∼1.39 kT. While this is a notable change, we can assume that in this case the frequency branch is shifted uniformly and the frequency spectrum is not altered fundamentally. This is not the case in Fig. 4.20 b) where $\varphi = 0°$ and the orbit along the blue line results in the highest blue frequency in Fig. 4.17. The indicated orbit crosses from band 22 to band 21 and runs on to band 20 resulting in an open orbit. Consequently, there is no dHvA oscillation corresponding to this orbit. In the limit where all charge carriers cross bands, the calculated frequency around that angle vanishes completely without another component appearing in return.

4.6 Conclusion

We have presented the results of torque magnetometry and DFT calculations on CrB_2. Experimentally, we observed up to 11 reliable dHvA frequencies for magnetic field within the basal plane. The effective masses of 8 dHvA components were determined. In addition, we observed a manifold of less distinct but possibly real dHvA components. Theoretically, we obtained Fermi surface sheets from five bands by closely matching the DFT calculations to the experimental values for the spiral propagation vector and the size of the ordered moment. The calculated FS sheets result in an abundance of expected dHvA frequencies.
The comparison of theory and experiment is ambivalent. On the one hand, we obtain very well fitting candidates from our calculation for three experimentally observed frequency branches between 1.5 and 2 kT. On the other hand, the large overlap among calculated frequencies renders a clear allocation of further measured frequencies unfeasible. Apart from that, several issues remain unresolved including (1) several well pronounced frequencies found in experiment that can not be accounted for by our calculation, especially above 2 kT, (2) the strong discrepancy in signal strength, i.e., we clearly observe dHvA oscillations for which a small signal is expected whereas we can not recover the branches in our experimental data for which the largest signal is calculated, (3) the effect of magnetic breakdown; while this might account for some experimental frequencies which can not be allocated to single-sheet orbits, it might also diminish the appearance of the few orbits we obtained a good match for, and (4) the differences in mass enhancement; while a strong electron-phonon-coupling for B-*p* states, analogous to MgB_2, appears reasonable, we have no physical explanation for a mass enhancement ranging from 0 to 2.4 for orbits on Cr-*d*-like bands.
All in all, we improved both the experimental as well as the theoretical state of the art with our approach to determine the CrB_2 Fermi surface. While our investigations suggest a partial agreement of the real Fermi surface with our theoretical result, the number of open questions also points towards several distinct deviations. Further ex-

perimental and theoretical efforts are necessary to resolve these issues. Theoretically, DFT calculations including spin-orbit-coupling are crucial for a conclusive understanding of the Fermi surface. Moreover, the incorporation of the suggested triple-k state in electronic structure calculations is essential for a comprehensive analysis. Experimentally, measurements over a larger angle range and within symmetry planes other than the basal plane can give a deeper insight into the dHvA spectrum and the underlying Fermi surface. A combination of these theoretical and experimental advances may help to resolve the question of the microscopic spin structure and yield a clear picture of the CrB_2 Fermi surface. This in turn will be helpful for the global understanding of itinerant antiferromagnetism and related phenomena.

5 Magnetic anisotropy of single crystal MnSi

In this chapter we present our work on manganese silicide (MnSi). We performed torque measurements in various setups and on different samples in order to thoroughly investigate the magnetocrystalline anisotropy (MCA) of MnSi in the field-polarized state as well as in its modulated magnetic phases. We begin the chapter with an introduction to the material in Sec. 5.1 including a brief review of previous work on its MCA as well as a short outline of our investigations. This is followed by a description of the experimental conditions and data evaluation in Sec. 5.2. The results of measurements in the field-polarized state are discussed in Sec. 5.3. We include results of numerical simulations in order to compare our experimental findings to theory. Measurements in the modulated phases of MnSi are presented in Sec 5.4. We conclude the chapter with summary and outlook in Sec. 5.5.

5.1 Introduction to MnSi

Manganese silicide (MnSi) nowadays is the prime example for a cubic chiral helimagnet. These compounds have been under investigation since the 1970s. Early studies on MnSi targeted long-wavelength helimagnetism as subject of research [Ish76]. Despite the identification of its helical ground state, MnSi was widely regarded as a weak itinerant ferromagnet and deemed of high importance in developing a self-consistent renormalization theory for such systems [Jan08, Mor85]. In later decades, interest in MnSi was renewed by the discovery of the additional A-phase [Leb95] and a non-Fermi liquid state under moderate hydrostatic pressure [Pfl97]. The past decade has probably been influenced most intensely by the first time experimental observation of skyrmion lattice states in MnSi [Mü09].
Like many cubic chiral magnets, MnSi crystallizes in the $B20$ structure. The corresponding space group $P2_13$ lacks inversion symmetry and allows for two enantiomers with opposite chirality. The right-handed version of the crystal is exemplarily illustrated in Fig. 5.1 a). In the simple cubic Bravais lattice, atoms are positioned at (u, u, u)a, $(\frac{1}{2}+u, \frac{1}{2}-u, -u)$a, $(\frac{1}{2}-u, -u, \frac{1}{2}+u)$a and $(-u, \frac{1}{2}+u, \frac{1}{2}-u)$a with lattice constant $a = 4.558\,\text{Å}$ and displacements $u_{\text{Mn}} = 0.137$ and $u_{\text{Si}} = 0.845$ in right-handed MnSi or $u_{\text{Mn}} = 0.863$ and $u_{\text{Si}} = 0.155$ in left-handed MnSi [Gri10]. As indicated in the figure, the configuration of each four Mn and Si atoms within the unit cell can be regarded as two distorted tetrahedra opposed to each other. In this perception, the structure resembles a distorted GaAs structure.
The magnetic phase diagram of MnSi has been studied extensively. Details can be

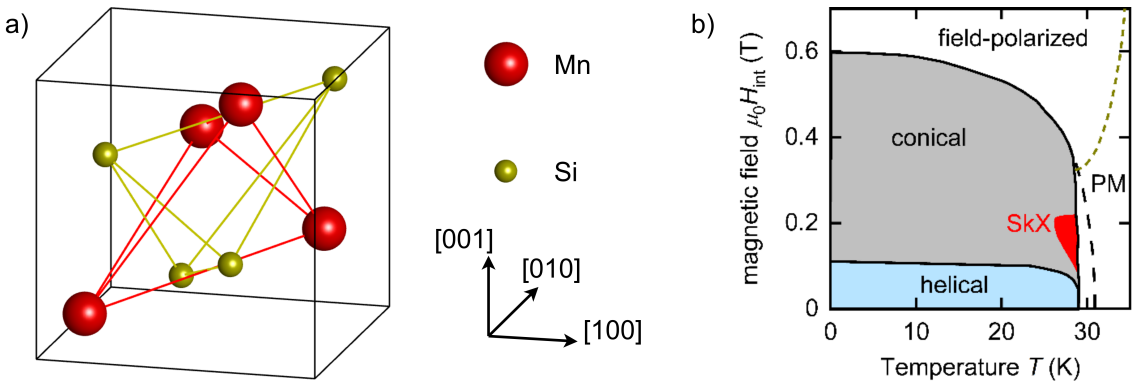

Figure 5.1: a) $B20$ crystal structure of MnSi. In the simple cubic Bravais lattice, atoms are positioned at (u, u, u)a, $(\frac{1}{2}+u, \frac{1}{2}-u, -u)$a, $(\frac{1}{2}-u, -u, \frac{1}{2}+u)$a and $(-u, \frac{1}{2}+u, \frac{1}{2}-u)$a with the lattice constant a. In right-handed MnSi as shown here $u_{\rm Mn} = 0.137$ and $u_{\rm Si} = 0.845$, in left-handed MnSi $u_{\rm Mn} = 0.863$ and $u_{\rm Si} = 0.155$ [Gri10]. b) Phase diagram of MnSi for field along $\langle 100 \rangle$. The yellow dashed line denotes a crossover between the paramagnetic regime at high temperatures and the field-polarized phase at high magnetic fields. The white region between the black dashed line and the modulated phases (helical, conical, skyrmion lattice) represents a fluctuation-dominated regime. Picture adapted from [Bau16c].

found, e.g., in Refs. [Bau12, Bau16c]. Here, we constrain ourselves to a brief review of the low temperature phases. For magnetic field applied along the $\langle 100 \rangle$-direction, the phase diagram is shown in Fig. 5.1 b). At zero field, the magnetic moments order helically below $T_{\rm c} \approx 29\,{\rm K}$ with an ordered moment of $\sim 0.4\,\mu_{\rm B}$/f.u. and a wavelength of $\sim 180\,{\rm \AA}$. The chirality of the helix is determined by the chirality of the atomic crystal [Gri10, Dmi12] and the helix pitch vector points along $\langle 111 \rangle$-directions. At a magnetic field of $\mu_0 H_{\rm c1} \approx 0.1\,{\rm T}$, the system transitions into a conical state. The pitch vector reorients to point along the field direction and the magnetic moments cant towards the field while the periodicity of the helix remains almost unaltered. With increasing field, the angle enclosed by moments and helix pitch vector decreases until the transition to a field-polarized phase is reached at $\mu_0 H_{\rm c2} \approx 0.6\,{\rm T}$.
The origin of long-range helical order in MnSi is commonly discussed in terms of a specific hierarchy of contributions to the free energy. On the largest scale, ferromagnetic exchange (FM) favors collinear alignment of moments. On an intermediate scale, the Dzyaloshinskii-Moriya interaction (DMI) acts in favor of perpendicular spin alignment [Dzy58, Mor60]. This rotationally invariant interaction arises from chiral spin-orbit coupling due to the lack of inversion symmetry in the crystallographic structure [Dzy64]. The competition of FM and DMI stabilizes the observed helix [Bak80]. In addition to these interactions, cubic magnetocrystalline anisotropies (MCAs) are present on the weakest scale. Regarding helical order, these higher order spin-orbit coupling terms are responsible for pinning the pitch vector to preferred crystal symmetry directions [Bau17].
The area colored red in Fig. 5.1 b) represents the skyrmion lattice phase where a hexagonal array of spin vortices forms in a plane orthogonal to the external field. The skyrmion phase pocket exists for fields applied along all major symmetry directions

and has been shown to be stabilized by thermal fluctuations [Mü09, Buh13]. This contrasts early predictions of magnetic skyrmions stabilized by strong anisotropies [Bog89, Bog94]. As shown by Adams *et al.*, the weak MCAs in MnSi cause small deviations of the skyrmion lattice normal vector $\hat{N}$ from the field direction and are responsible for fixing the lattice regarding rotations around $\hat{N}$ [Ada18].
Despite their minor relevance for the formation of non-collinear order, MCAs are of great importance for the global understanding of helimagnets. Besides determining preferential directions of helix pitch or skyrmion lattice normal vectors [Bau17, Ada18], they decisively influence, e.g., the anisotropy of temperature and field range of skyrmion phases [Mü09, Ada11, Lam06, Bau13], the formation of different skyrmion lattice morphologies [Kar16, Nak17] or dispersion and damping of spin waves [Sch15, Sta17]. Further substantiation of the significance of MCAs has been found in the magnetoelectric insulator Cu_2OSeO_3 (CSO). While it exhibits a more complex crystal structure as compared to MnSi, CSO crystallizes in the same space group $P2_13$. Its phase diagram qualitatively resembles that of MnSi shown in Fig. 5.1 b) with a skyrmion pocket stabilized by thermal fluctuations found just below T_c. As in MnSi, this phase pocket is isotropic in the sense that it exists for fields applied along all major symmetry directions [Bau16c]. Recently, a second skyrmion pocket has been discovered in this material in the low-temperature high-field corner of the conical regime [Cha18, Hal18]. In contrast to the conventional high-temperature skyrmion phase (HTS), this new low-temperature skyrmion phase (LTS) is found to be stabilized by cubic anisotropies. As a remarkable consequence, the LTS is highly anisotropic in that it exists for field along the $\langle 100 \rangle$-direction only.
Several phenomena closely connected to MCAs are subject of ongoing research. Thus, proper interpretation of new experimental findings can depend crucially on a precise quantitative knowledge of the weak cubic anisotropies. Still, little effort has been expended in order to precisely determine their magnitudes. A first claim to present "the anisotropy energy in the high-field 'ferromagnetic' state" inferred from torque measurements was issued already in 1969 [Con69]. Yet up to the present day no anisotropy constants have been reported for the field-polarized phase in bulk MnSi to the best of our knowledge. Differently, effective anisotropy constants have been reported rather recently for modulated phases in bulk MnSi as well as for MnSi thin films. Bauer *et al.* employed small angle neutron scattering (SANS) as well as magnetization and AC susceptibility measurements to determine first and second order effective anisotropy constants for the pitch vector in the helical phase [Bau17]. Adams *et al.* performed SANS measurements in the skyrmion phase and reported a first order effective anisotropy constant for the skyrmion lattice normal vector [Ada18]. As discussed in Sec. 2.1.2, these effective anisotropy constants result from the orientation of a large number of non-collinear magnetic moments and thus reflect the magnetocrystalline anisotropy only indirectly. Anisotropy constants of field-polarized MnSi thin films have been determined by SQUID magnetometry [Kar12] and torque magnetometry [Bra13a]. The anisotropy of such films is governed by uniaxial contributions arising from strain and sample shape so that magnetocrystalline anisotropy was not addressed by these experiments. Further,

torque measurements on field-polarized bulk MnSi were carried out within our own group [Wil20b]. However, these experiments targeted the dHvA effect and thus measured the variation of magnetic torque with the applied field's magnitude rather than its orientation. The field magnitude dependent torque was also investigated by Birkelbach for a single orientation and with a focus on the region of modulated states [Bir09]. Field scans along the ⟨001⟩-direction featured hysteresis both above and below H_{c2}. In the conical phase, this hysteresis mostly vanishes with increasing temperature already below T_c.
In principle, magnetic anisotropy constants due to magnetocrystalline anisotropy can also be obtained from ab initio band structure calculations. In MnSi, however, the cubic anisotropies are too small to be calculated reliably [Kar12]. In turn, precise measurements of anisotropy constants may serve as a benchmark for electronic structure calculations and thus contribute to the development of a comprehensive theoretical description of the electronic structure. This procedure has been pursued, e.g., for the weak itinerant ferromagnet Ni_3Al [Sig82, Mat85].
In this thesis, we aim to provide the high precision data for such an operation. We employ torque magnetometry in order to investigate MCAs in bulk MnSi and measure the angle-dependent torque in the field-polarized as well as modulated states. Our measurements in the field-polarized state allow us to extract values for the anisotropy constants in leading and next-to-leading order. We further investigate their dependence on temperature and field magnitude as well as the influence of a cubic shape anisotropy. Comparison with numerical simulations allows for a diligent assessment of erroneous influences on our measurements.
We also perform field scans where the field magnitude is swept back and forth through the modulated phases at fixed orientations, from one field-polarized state to the opposing one. We observe hysteresis below as well as above H_{c2} which exhibits severe quantitave and qualitative changes with temperature. We discuss these observations in the context of topological defects.

5.2 Experimental conditions and data evaluation

In this work, we performed measurements on three MnSi single crystals all prepared via optical float zoning. We denote our samples by OFZ54, OFZ67 and OFZ125 consistent with Ref. [Bau14a] where growth process and sample characterization methods are described. Further details on crystal growth can be found in Refs. [Neu11, Bau16b, Bau16a], a study of the achieved sample quality is presented in Ref. [Rei16]. Before discussing details of the investigated specimens, we note that crystal orientations are presented in terms of equivalent directions of the cubic Bravais lattice. While the cubic symmetry is reduced by the atomic basis of MnSi, discriminating between, e.g., [100]-, [010]- and [001]-directions using Laue diffraction is difficult in practice. Further, the chirality of our single crystals is unknown. The influence of this property on the torque will be discussed in Sec. 5.3.3.
Sample OFZ54 exhibits a RRR of ∼300. Detailed magnetization and susceptibility data on this crystal are presented in [Bau12]. For our experiments, the specimen

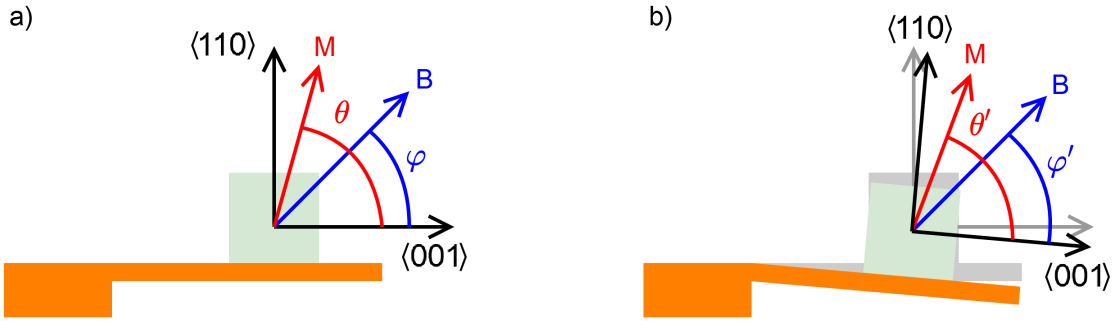

Figure 5.2: Definition of measurement angles. a) The angles φ and θ are measured from the crystallographic $\langle 001\rangle$-direction at zero torque towards magnetic field and magnetization, respectively. b) The angles φ' and θ' include changes of φ and θ due to rotation of the sample caused by a finite torque.

was oriented with Laue x-ray diffraction and consecutively cut into cubic shape with a side length of 1 mm and edges aligned along $\langle 110\rangle$-, $\langle 211\rangle$- and $\langle 111\rangle$-directions. Sample OFZ67 was prepared with 1 % manganese excess. It exhibits a RRR of ∼100 and was also oriented via Laue x-ray diffraction and cut with a wire saw to a $1 \times 1 \times 1\,\mathrm{mm}^3$ cube. For this specimen, the edges are aligned along $\langle 110\rangle$-, $\langle 100\rangle$- and $\langle 010\rangle$-directions. To allow for measurements unaffected by shape anisotropy, sample OFZ125 with the lowest RRR of ∼80 was prepared in spherical shape with a diameter of ∼2.1 mm. The orientation process is described in Sec. 3.3.3.
Both longitudinal cantilevers in the rotating field setup and torsional cantilevers in the rotating sample setup were used as described in Sec. 3.3. The spherical sample OFZ125 was investigated in both setups. Measurements on cubic samples were performed in the rotating field setup with OFZ54 and in the rotating sample setup with OFZ67. The rotating field setup was employed mainly for rotation and field scans through the modulated states. The rotating sample setup allowed for higher fields and faster measurements and was employed mainly for rotation scans in the field-polarized phase.
During the measurements, we record torque as a function of the angle φ enclosed by the $\langle 001\rangle$-direction of the crystal and the applied field $\mathbf{B}$ as illustrated in Fig. 5.2 a). The relevant angle for investigations of magnetic anisotropy is enclosed by the $\langle 001\rangle$-direction and magnetization $\mathbf{M}$ as denoted in the sketch by θ. Due to the competition of Zeeman and anisotropy energy, the angles φ and θ are never identical in practice except for the field vector pointing along a high symmetry axis. This issue has frequently been addressed in literature [Cal60, Bur77, Sig82, Hub98]. For known magnitudes of Γ, $\mathbf{M}$ and $\mathbf{B}$, the angle θ can easily be calculated from φ.
Using torque magnetometry, we have to be aware of a second source of angular distortion that has not been addressed as widely in literature. As the measurement method relies on detecting the deviation of the sample from its initial position, this deviation simultaneously changes the orientation of the sample with respect to the external field. This is illustrated in Fig. 5.2 b) for the case of a longitudinal cantilever. While the applied field $\mathbf{B}$ retains its orientation, the crystal directions are rotated

by the torque and thus the angle between field and ⟨001⟩-direction changes from φ to φ'. Due to this variation, the orientation of $\mathbf{M}$ also changes with respect to the crystal axes, i.e. θ changes to θ'.
In our experiments, the difference between θ' and φ' is almost negligibly small. In contrast, the difference between φ and φ' can have substantial influence on our results. Unfortunately, we lack the information necessary for the calculation of θ'. Consequently, we stick to the angle φ as a reference when presenting our experimental results. We discuss the spurious influence of angular distortion on the extraction of anisotropy constants thoroughly in Sec. 5.3.4.
In the following, we present details on experimental procedure and data processing for the various configurations employed in our anisotropy investigations. For convenience, we will refer to the rotating sample setup and data as PPMS setup and data and to the rotating field setup and data as AMI setup and data.

5.2.1 Rotating sample setup

The PPMS setup has been described in Secs. 3.1.2 and 3.3.2. Further details can be found in the corresponding manuals [Man00, Man17, Man16]. Here we present the procedure during our measurements and the consequent data treatment. Parts of the experiments were carried out by Michelle Hollricher and Dr. Vivek Kumar.

Experimental procedure

The horizontal rotator option provides an angular range of 380°, i.e., accessible angles ϕ reach from -10° to 370° where ϕ denotes the angle enclosed by cantilever normal and magnetic field direction. Due to backlash of the rotation mechanism, the cantilever normal typically points 5-6° away from the field direction at the nominal position $\phi = 0°$. Instead of ϕ, we use φ as a reference for our torque data as defined in the foregoing section.
As stated above, we performed measurements on a cubic and a spherical sample. The cubic sample was mounted on a standard 2-leg cantilever, the spherical sample was mounted on a 3-leg modified cantilever due to its larger volume. Both sensors were calibrated following the routine described in Sec. 3.1.2. For both samples, we aimed to align the ⟨110⟩-direction along the cantilever projection axis and the ⟨001⟩-direction along the cantilever normal. As discussed in Sec. 3.3.3, all relevant misalignment angles are estimated to be less than 2°. The influence of misalignment on our measurements is assessed in Sec. 5.3.3.
Each measurement consists of a stepped and a swept rotation scan. During a stepped scan, we change ϕ from -10° to 370° at a rate of ∼12.0°/s. At discrete steps of 2°, rotation is halted and a torque value is recorded that is the result of an internal averaging process in the PPMS software including 25 single measurements. Measurements with different step sizes and angular rates were performed and yielded identical results. After the stepped scan, ϕ is continuously swept back to -10° at a rate of ∼4.8°/s while torque values are recorded without internal averaging. Again, different sweep rates were tested and found not to influence the torque signal. Since

stepped and swept scans yield identical results, we only present stepped scans which provide better angular resolution.
In the PPMS setup, we performed rotation scans exclusively in collinear phases. We recorded scans at field magnitudes from 0.65 T to 14 T and temperatures from 2 K up to 51 K. Additionally, rotation scans at zero field were performed at each temperature to account for gravity and the erroneous baseline calibration (cmp. Sec. 3.3.2). To avoid influences of field and temperature history, all measurements were started from well defined states, i.e. well outside the region of modulated phases in the phase diagram. We pursued two different approaches relying either on high field or high temperature to warrant this precondition. In most measurements, the sample was heated up to 50 K before approaching the measurement temperature at zero field. Then a rotation scan was recorded at 0 T followed by scans at finite fields in ascending order. In some measurements on the cubic sample, measurement temperatures were approached at 4 T and scans were performed at fields in descending order, finishing with a scan at 0 T. The consistency of our data implies success for both alternatives. We further performed a small number of field scans along high symmetry directions of the samples. As their results are consistent with the field scans obtained in the AMI setup, we do not discuss them separately.

Data evaluation

The PPMS data correction process is illustrated in Fig. 5.3. It consists of three principal steps the first two of which are identical for all measurements whereas the final step is different for data on spherical and cubic samples, respectively. In a first step, we account for the impact of gravity and the erroneous calibration in terms of the baseline. For this purpose, the torque curve measured at a given temperature and finite field and that at zero field and identical temperature are interpolated in the range from $\phi = 0°$ to $\phi = 359.5°$ with steps of 0.5°. Subsequently, the zero field torque curve is subtracted from the data at finite field as illustrated in Fig. 5.3 a) for a torque curve measured on the spherical sample at 2 K and 1 T. In a second step, we remove a remaining non-zero mean value of the torque data[1]. Such an offset can be induced by various effects such as, e.g., field gradients or magnetoresistance effects in the readout circuitry. Without such disturbances, we expect the integral over the torque during a full rotation to be zero in the absence of rotational hysteresis. As illustrated in Fig. 5.3 b), this shift is usually small compared to both the overall torque signal as well as the shift imposed in the first step.
The third step is illustrated in Fig. 5.3 c) and d) for the spherical and the cubic sample, respectively. For the spherical sample, torque data acquired at temperatures above 16.5 K is scaled by a fixed factor of 7/8 in order to ensure consistency of the temperature dependent data. Necessity and justification of this step are described in appendix C.2.1. In the case of the cubic sample, we subtract a two-fold sine-shaped signal from torque curves to account for the angular dependence induced by the

[1]Note that the mean value is identical to the torque integral over the full rotation as data is beforehand interpolated on an evenly spaced set of angle values.

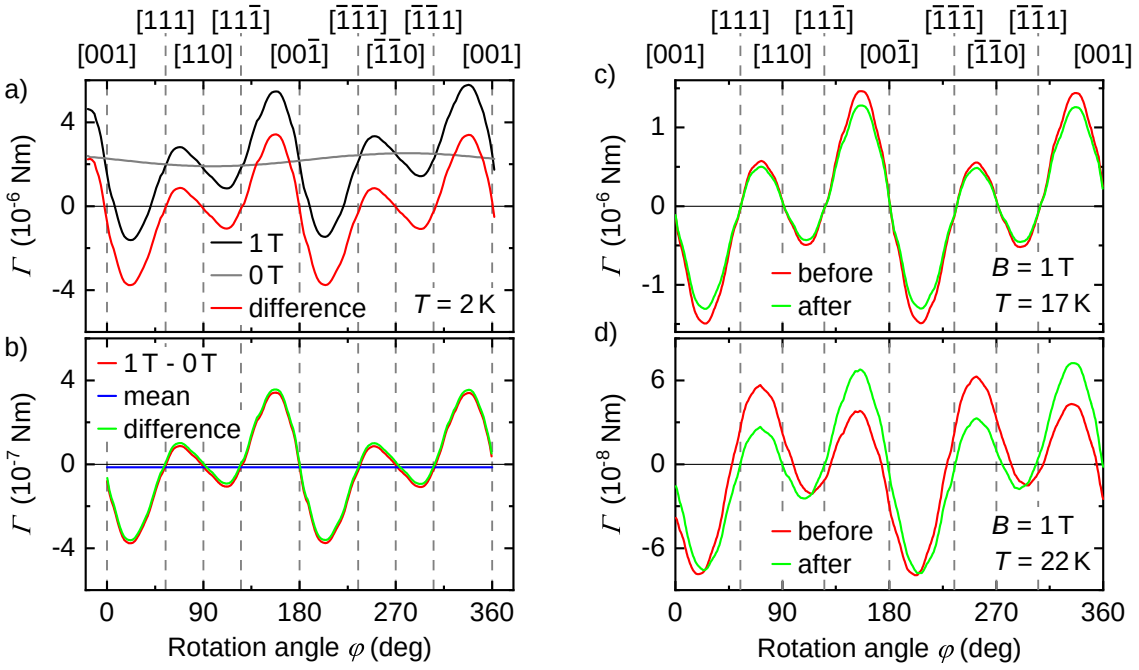

Figure 5.3: Illustration of data processing for the rotating sample setup. a) The zero-field torque is subtracted from the torque at 1 T. b) The mean value is subtracted from the resulting curve. c) Exemplary high-temperature torque curve measured on a spherical sample before and after scaling. d) Exemplary torque curves measured on a cubic sample before and after node-correction.

sensor (cf. Sec. 3.3.2 and Fig. 3.7). The procedure for estimating the size of this contribution is described in appendix C.2.2. In principle, the same correction can be performed for data on the spherical sample. Due to the larger volume of the sphere and likewise larger absolute torque signal, the influence of the sensor's angular dependence can be neglected in this case.
Subsequent to the data correction described above, we extract the anisotropy constants K_1 and K_2 from the torque curves by fitting. We adjust Eq. 2.7 to match our experimental conditions and use

$$\begin{aligned}\Gamma = \Big[&\frac{K_1}{2}[1+3\cos(2\phi-\delta_\mathrm{r})]\sin(2\phi-\delta_\mathrm{r}) \\ &-\frac{K_2}{32}[1+3\cos(2\phi-\delta_\mathrm{r})]^2\sin(2\phi-\delta_\mathrm{r})\Big]\cdot V+\Gamma_\mathrm{off}\end{aligned} \tag{5.1}$$

as a fit function. Here, V is the sample volume, δ_r accounts for the deviation of φ from ϕ mainly due to backlash of the rotator and Γ_off allows for a torque offset. While we shift the curves' mean values to zero in our correction process, this offset can still be finite due to deformation of torque curves from the ideal shape. In practice, we obtain values well below 10° for δ_r and 10^{-8} Nm for Γ_r.

5.2.2 Rotating field setup

The AMI setup has been described in Sec. 3.3.1. We performed measurements on a spherical and a cubic sample. As stated before, data on the cubic sample was acquired with a probe featuring a magnetic capillary which strongly disturbed our measurements. Moreover, the misalignment of cantilever and magnet as well as the sample position relative to the field centre were poorly controlled (cf. Sec. 3.3.3). As a consequence, we do not further consider data from these measurements for evaluation. An example for the disturbances caused by magnetic capillary and misalignment can be found in appendix C.3.1. In the following, we present our procedure and data treatment for measurements on the spherical sample.

Experimental procedure

For measurements in the AMI setup, we employed longitudinal cantilevers with rectangular paddles. A beam width of ∼0.6 mm was chosen and the electrostatic calibration routine described in Sec. 3.1.1 was carried out. Due to large capacitance changes of up to 30 %, a capacitance-dependent calibration constant $K(C)$ was determined. The temperature was monitored at the ^{3}He-pot roughly 11 cm above the sample. To avoid temperature drifts during measurements, the temperature was allowed to settle for ∼30 minutes after each temperature change. In contrast to the PPMS setup, we did not start our measurements in the AMI setup from well defined states by heating the sample above T_c in advance.
The MnSi sphere was oriented with the ⟨110⟩-direction along the cantilever's projection axis and the ⟨001⟩-direction parallel to the cantilever beams with a misalignment of $\lesssim$0.5°. The alignment error of cantilever and magnet was larger and not equal for all measurements. The misalignment angle δ_r (cf. Fig. 3.8) was fixed to ∼6° whereas measurements were performed at $\gamma_r = 9°$ as well as $\gamma_r = 0°$. All rotation scans presented in this chapter were recorded at $\gamma_r = 9°$ since only few rotation scans at $\gamma_r = 0°$ were performed. A brief comparison of both cases is presented in appendix C.3.8. Field scans presented in this chapter were recorded at $\gamma_r = 0°$. Similar measurements have been performed at $\gamma_r = 9°$ with matching results.
We present rotation scans carried out in several magnetic phases at fields from 50 mT up to 4 T and temperatures from 0.3 K up to 50 K. During rotation scans, the field vector was continuously changed at a rate of 0.15 T/min. First, the solenoid field was ramped from zero to the desired magnitude. Consequently, the field was rotated by 720° in one rotation sense, 720° in the opposite rotation sense and 720° in the original rotation sense again. For convenience, we will refer to the initial rotation sense as positive and the opposite as negative rotation sense. Finally, the field was ramped to zero along the starting direction. Our procedure allowed us to ensure reproducibility and check for rotational hysteresis.
We further present field scans between $B_{max} = \pm 1$ T along ⟨001⟩-, ⟨110⟩-, ⟨111⟩- and ⟨11$\bar{1}$⟩-directions at temperatures from 0.3 K up to ∼33.3 K. During field scans, the field vector's angle was kept constant while the magnitude was continuously changed at 0.15 T/min. The field was first swept from zero to $B_{max} > 0$, then twice down to

$-B_{\mathrm{max}}$ and back to $+B_{\mathrm{max}}$. Finally, the magnitude was ramped back to zero. This procedure allowed us to ensure reproducibility and check for dependences on field and temperature history.

Data evaluation

The capacitance raw data from all measurements was converted into torque via Eq. 3.16. For rotation scans, the value C_0 was obtained for each individual measurement from the starting value at zero field. To check for capacitance drifts, C_0 was compared to the final value at zero field which yielded satisfactory results. The field direction of the solenoid where rotation starts and ends corresponds to $\varphi \approx 96°$. Rotations with different starting angles yielded identical results.
As stated in the foregoing section, our procedure for rotation scans allowed us to check for reproducibility and rotational hysteresis. Except for minor disturbances in individual measurements, our torque curves were well reproducible within the limits of uncertainty. Examples of minor disturbances are presented in appendix C.3.2. For field magnitudes below H_{c2}, we observe a large rotational hysteresis. Due to the good reproducibility, we only present the last full rotations for each rotation sense. Consistent with our nomenclature, we plot the positive rotation sense with increasing and negative rotation sense with decreasing angle. At larger field magnitudes, rotational hysteresis was small enough to be attributed to the magnet system as shown in appendix C.3.3. We interpolate the last full rotation for each rotation sense on angles from $\varphi = 0$ to $\varphi = 359.5°$ with steps of $0.5°$ and average over both curves. In order to extract anisotropy constants K_1 and K_2 from the resulting mean curve, we extend Eq. 5.1 to

$$\begin{aligned}\Gamma = &\Big[\frac{K_1}{2}[1+3\cos(2\phi-\delta_{\mathrm{r}})]\sin(2\phi-\delta_{\mathrm{r}}) \\ &-\frac{K_2}{32}[1+3\cos(2\phi-\delta_{\mathrm{r}})]^2\sin(2\phi-\delta_{\mathrm{r}})\Big]\cdot V+\Gamma_{\mathrm{off}} \\ &+g_1[1+\cos(2\phi)]+g_2\sin(2\phi)+g_3[1-\cos(2\phi)]\,.\end{aligned} \tag{5.2}$$

The additional terms g_1, g_2 and g_3 represent the influence of forces imposed by magnetic field gradients $\partial B_{\mathrm{y}}/\partial y$, $\partial B_{\mathrm{y}}/\partial z$ and $\partial B_{\mathrm{z}}/\partial z$, respectively. Equation 5.2 is overdefined which allows for readjustment of g_1, g_3 and Γ_{off} after fitting. We discuss this in detail along with the fit results in Sec. 5.3.2 and appendix C.3.7.
For field scans, C_0 was determined by interpolating the field magnitude dependent capacitance raw data to $B = 0$ for each individual sweep. After conversion to torque, the data is divided by the field magnitude to obtain the anisotropic magnetization $M_\perp$. We note that we only measure the projection of $M_\perp$ on the plane orthogonal to the cantilever projection axis $\hat{\mathrm{P}}$.
Our measurement procedure for field scans allows us to check for reproducibility and history dependence. While the shape of the first upsweep and, in some cases, also that of the first downsweep show a dependence on field and temperature history, the following scans were in most cases perfectly reproducible. In the rare remaining cases,

the measured capacitance exhibited discontinuous jumps pointing at a technical rather than a sample-related explanation. Since temperature and field history before field scans were not well controlled, an interpretation of the initial response during a first upsweep is unfeasible within the scope of this thesis. Thus we only present well reproducible consecutive up- and downsweeps.

5.3 Measurements in the field-polarized phase

In this section, we present our results on the field-polarized phase of MnSi. We begin with measured data from the PPMS setup in Sec. 5.3.1. This is followed by experimental data from the AMI setup in Sec. 5.3.2. We present numerical simulations and assess the influence of misalignment on our measurements in Sec. 5.3.3. The section ends with a thorough discussion of our findings in Sec. 5.3.4.

5.3.1 Rotating sample setup

In the following, we present experimental results acquired in the PPMS setup at fields above H_{c2}. We investigate the dependence on field magnitude and temperature. In the respective sections, we only present data acquired on the MnSi sphere. To assess the influence of cubic shape anisotropy, we compare the results to measurements on a cubic sample.

Field magnitude dependence

In order to investigate the magnetic field magnitude dependence, we conducted rotation scans at the lowest possible temperature of $T = 2\,\mathrm{K}$ and field magnitudes of $0.65\,\mathrm{T}$, $0.8\,\mathrm{T}$ and integer values from $1\,\mathrm{T}$ up to $14\,\mathrm{T}$ in steps of 1-2 T. The corresponding torque curves are shown in Fig. 5.4 a). We make three key observations: (i) all curves exhibit the expected shape corresponding to Eq. 2.7, (ii) a small amplitude modulation with high frequency is superimposed to this shape, and (iii) the evolution of the torque with increasing field magnitude apparently can be divided into three regimes.
The qualitative agreement with the expected shape allows us to extract quantitative values for the anisotropy constants K_1 and K_2 by fitting as described in Sec. 5.2.1. This is illustrated in Fig. 5.4 b) where the measured torque curve is shown for $T = 2\,\mathrm{K}$ and $B = 1\,\mathrm{T}$ as orange solid line and the fitted curve is shown as black dashed line. The fit matches the experimental data extremely well and yields values of $K_1 \approx 500\,\mathrm{J/m^3}$ and $K_2 \approx -920\,\mathrm{J/m^3}$.
The high-frequency signal superimposed to the expected shape is ignored during evaluation. The amplitude of this disturbance is susceptible to changes of field magnitude and temperature, yet remains unaltered for changes of the angular step size or sweep rate. However, we found a similar modulation on torque curves recorded during rotation scans on the ferromagnetic Heusler compound Cu_2MnAl. While the origin of the signal remains unresolved, we suggest a technical explanation owed to the

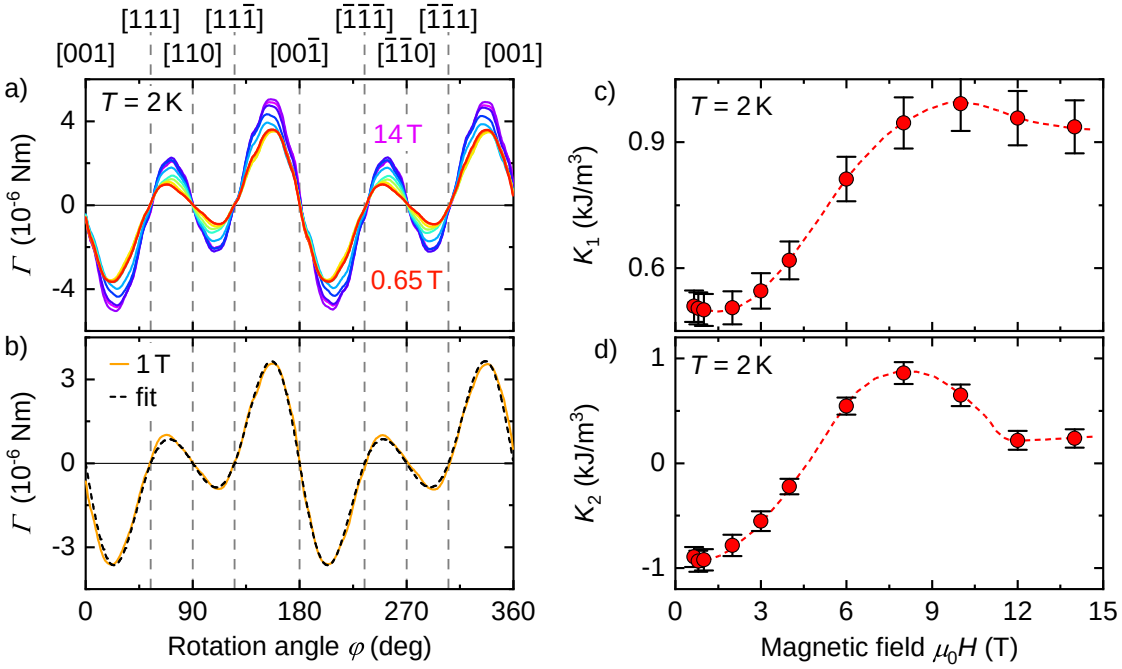

Figure 5.4: Field dependence of torque and anisotropy constants. a) Processed torque curves at $T = 2\,\mathrm{K}$ and magnetic fields from $B = 0.65\,\mathrm{T}$ to $B = 14\,\mathrm{T}$. b) Torque at $T = 2\,\mathrm{K}$ and $B = 1\,\mathrm{T}$ and fit according to Eq. 5.1. c)-d) Anisotropy constants K_1 and K_2 obtained from the curves in a).

setup due to its kindred occurrence in measurements on two very different materials. Fortunately, the phenomenon is only a minor disturbance to our experiments that can readily be neglected.

We discuss the evolution of measured torque curves with field magnitude in terms of low, intermediate and high field regimes. For fields up to 4 T, the torque remains almost unaltered around the ⟨001⟩-direction. In particular, the global extrema neither increase nor decrease. In contrast, the torque around ⟨110⟩-direction changes both size and shape. While the curve at 0.65 T (red) looks almost linear between the local extrema, it gradually approaches a sine-shape with increasing field while the local extrema are increased. Simultaneously, the positions of the extrema shift towards the ⟨110⟩-direction. At higher fields, the torque curve increases rather homogeneously, i.e. the shape remains intact while the torque signal continuously increases between 4 T and 10 T. This evolution is reversed with the local extrema decreasing again above 10 T and the global extrema decreasing from 12 T to 14 T.

The described evolution of the torque signal with field magnitude is reflected in the anisotropy constants. The extracted values of K_1 and K_2 are shown as red circles in Fig. 5.4 c) and d), respectively. Dashed lines are drawn by hand as a guide to the eye. Error bars include the fits' 95 % confidence bounds, a relative error of 5 % and a static error of $5\,\mathrm{J/m^3}$ for K_1 and 10 % for K_2, respectively. We consider these error estimates to account for the minor uncertainties imposed by high-frequency modulation, calibration uncertainty and errors during data evaluation. However,

neither the influence of angle correction and misalignment nor the scaling effect described in appendix C.2.1 are included. We defer a proper estimation of the full error to the discussion of angle corrections in Sec. 5.3.4.
The intermediate and high field regimes described above are well notable in Fig. 5.4 c) and d). Both K_1 and K_2 exhibit a strong increase at intermediate fields followed by a smaller decrease at high fields. The correlation to the behavior described for the low field regime is less evident. Here, K_1 changes moderately from $\sim 510\,\mathrm{J/m^3}$ at 0.65 T to $\sim 620\,\mathrm{J/m^3}$ at 4 T while K_2 is negative and shrinks by more than 75 % in the same field range. This corresponds to the observation that, for comparable magnitudes of K_1 and K_2, a change of K_1 rather scales the torque curve as a whole. A change of K_2 mainly alters the relative height of global and local extrema. Neither a shift of the local extrema positions nor a change of shape can straighforwardly be explained by a change in anisotropy constants. Thus, we regard the obtained values as preliminary results. We discuss their reliability in more detail in Sec. 5.3.4.

Temperature dependence

We investigate the temperature evolution of the torque signal at six different magnetic field magnitudes from $B = 0.65\,\mathrm{T}$ up to $B = 4\,\mathrm{T}$. We carried out rotation scans at temperatures from $T = 2\,\mathrm{K}$ up to $T = 49\,\mathrm{K}$ in steps of 1-2 K. A representative set of torque curves is shown in Fig. 5.5 a) at temperatures up to 35 K and a magnetic field of $B = 1\,\mathrm{T}$. The curve at $T = 2\,\mathrm{K}$ is identical to that in Fig. 5.4 b). Apparently the expected shape is preserved with increasing temperature. We again observe the high frequency modulation which remains negligible for our evaluation. Similar to the field magnitude dependence, the temperature evolution can be divided into three regions of low, intermediate and high temperatures.
At low temperatures, the torque signal slightly increases with rising temperature. Analogous to the low field regime of the field magnitude evolution, the torque around the ⟨110⟩-direction transitions from an almost linear to a rather sine-shaped behavior in this region. At temperatures above ∼8 K, the amplitude of the angular torque variation decreases drastically with increasing temperature. In this intermediate temperature regime, the qualitative shape of the curves remains unchanged. Finally, the torque is inverted at ∼25 K in that maxima change into minima and vice versa. This is further illustrated in Fig. 5.5 b) where the torque curves at $B = 1\,\mathrm{T}$ and temperatures of $T = 24\,\mathrm{K}$ and $T = 29\,\mathrm{K}$ are shown as solid lines together with corresponding fits depicted by dashed lines. We confirm that the measured torque exhibits the expected shape also at elevated temperatures. Deformations from the ideal are more salient as compared to low temperatures, yet the agreement of fits and measured torque is still adequate. The torque curves observed at 24 K and 29 K exhibit similar amplitudes but opposite signs.
The inversion of the torque signal corresponds to the sign change of an anisotropy constant. The temperature evolution of K_1 is presented in Fig. 5.5 c). The low and intermediate temperature regimes are clearly reflected in K_1 which for all investigated

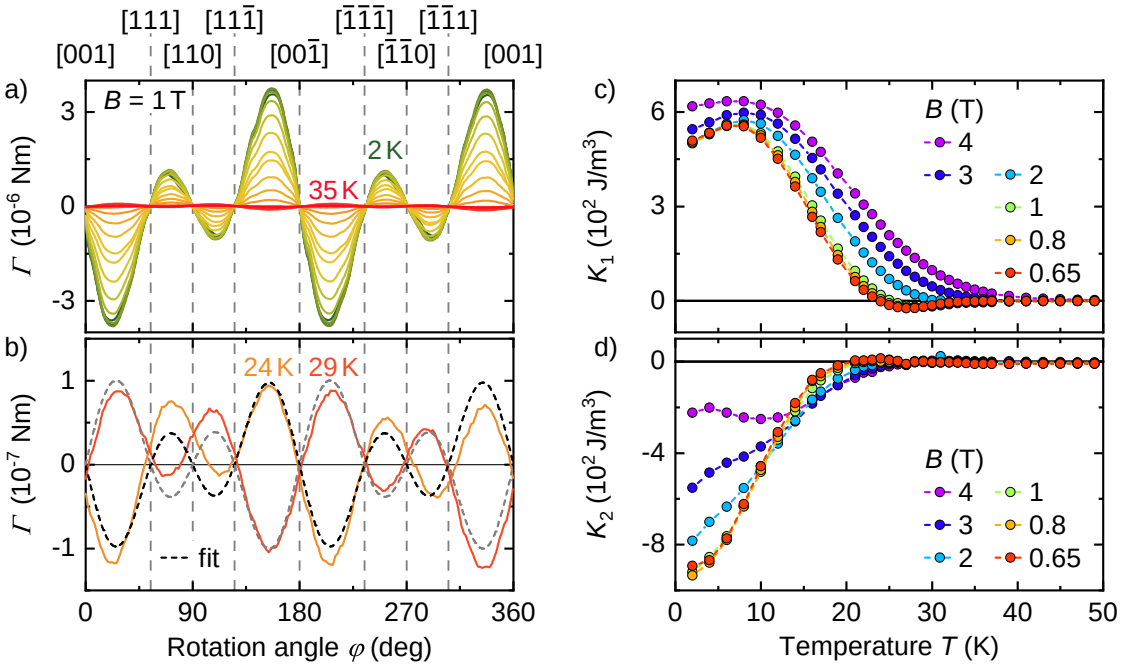

Figure 5.5: Temperature dependence of torque and anisotropy constants. a) Processed torque curves at $B = 1\,\mathrm{T}$ and selected temperatures from $T = 2\,\mathrm{K}$ to $T = 35\,\mathrm{K}$. b) Torque at $B = 1\,\mathrm{T}$ and temperatures of $T = 24\,\mathrm{K}$ and $T = 29\,\mathrm{K}$. Dashed lines represent fits according to Eq. 5.1. c)-d) Anisotropy constants K_1 and K_2 at magnetic fields from $B = 0.65\,\mathrm{T}$ to $B = 4\,\mathrm{T}$ versus temperature.

field magnitudes exhibits a slight increase at low temperatures followed by a strong decrease. In contrast, the sign reversal at high temperatures is only observed for fields up to 2 T. At these lower fields, K_1 passes a minimum and then approaches zero at negative values. At 3 T and 4 T, K_1 has no minimum and approaches zero with the initial positive sign. In the low and intermediate temperature regimes, K_1 exhibits a similar evolution at different field magnitudes. As a tendency, the low temperature values are larger and the decay is slightly slower at higher field magnitudes.

The temperature evolution of K_2 is shown in Fig. 5.5 d). The different temperature regimes are not notably reflected. A slight increase of its magnitude at low temperatures is only found at 4 T. Beside that, K_2 simply decreases to zero with rising temperature. No sign change is observed in the investigated field range. As discussed for the field magnitude dependence, K_2 possesses larger magnitude at smaller fields for low temperatures. As for K_1, the decay of K_2 is slower at higher field magnitudes. In Fig. 5.5 c) and d), error bars have been left out for clarity. For the sake of comparison to Fig. 5.4 c) and d), the respective graphs with error bars as well as blow-ups of the high-temperature regime can be found in appendix C.2.3. As stated before, we discuss the full error in Sec. 5.3.4.

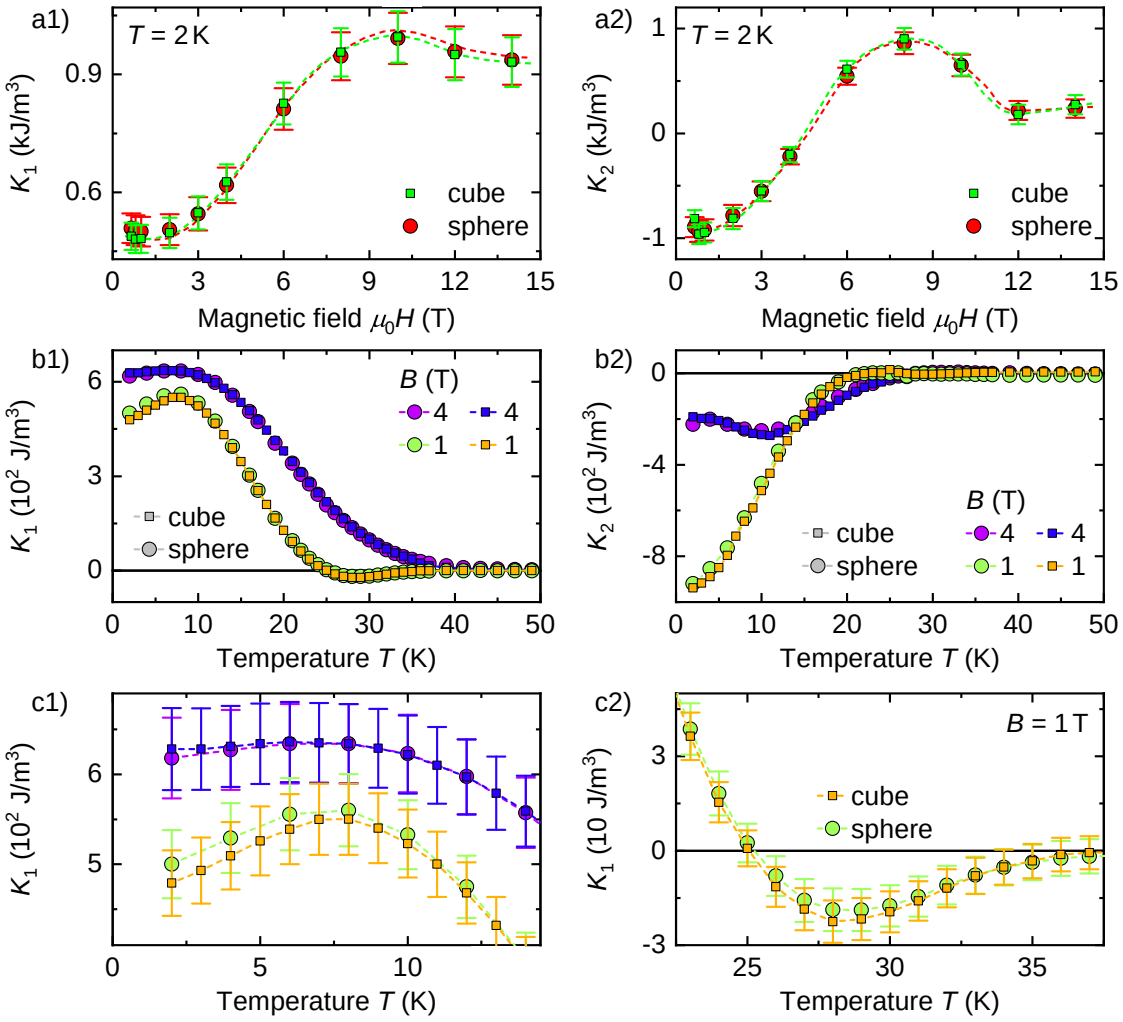

Figure 5.6: Comparison of anisotropy constants extracted from measurements on spherical and cubic sample. a1)-a2) Field dependence of anisotropy constants K_1 and K_2 at $T = 2\,\mathrm{K}$. b1)-b2) Temperature dependence of K_1 and K_2 at $B = 1\,\mathrm{T}$ and $B = 4\,\mathrm{T}$. c1)-c2) Blow-ups of b1) for the low-temperature regime and the zero-transition regime of K_1.

Sample shape

So far we have presented data on a spherical sample only. In this section, we investigate the influence of cubic shape anisotropy. Similar to the measurements described in the foregoing sections, we carried out rotation scans at various field magnitudes from 0.65 T up to 14 T at $T = 2\,\mathrm{K}$ and various temperatures from 2 K up to 51 K at field magnitudes of $B = 1\,\mathrm{T}$ and $B = 4\,\mathrm{T}$. The torque data are not shown here for readability and can be found in appendix C.2.4.
Analogous to the spherical sample, we extracted K_1 and K_2 from the measured curves. The results are summarized in Fig. 5.6 together with corresponding results from the spherical sample. In all graphs, cirlces represent data from the sphere and squares depict data from the cube. Panels a1) and a2) show the field magnitude

dependence of K_1 and K_2, respectively. Likewise, panels b1) and b2) illustrate the temperature evolution of K_1 and K_2, respectively. In panels c1) and c2), blow-ups of K_1 in the low temperature and high temperature regimes are presented. As above, error bars include the 95 % fit confidence bounds, a 5 % relative error and static errors of $5\,\mathrm{J/m^3}$ and $10\,\mathrm{J/m^3}$ for K_1 and K_2, respectively.
The common finding from all graphs is that the agreement of both data sets is far better than the uncertainty of our results. It seems natural to conclude that cubic shape anisotropy is small compared to the magnetocrystalline anisotropy in MnSi. However, this insight can not be extended to other shapes or materials offhand.
As an additional benefit of the comparison, our findings regarding field and temperature evolution of the magnetic anisotropy are reproduced with a second sample. For further assessment, we consider data acquired in a different setup in the following.

5.3.2 Rotating field setup

In this section we present the results of our measurements in the AMI setup. Since we applied no magnetic field higher than 4 T, the field magnitude dependence is of minor significance. We present field magnitude dependent anisotropy constants extracted from AMI data in appendix C.3.4. Here, we focus on the temperature evolution.
We carried out rotation scans at temperatures from $T = 0.3\,\mathrm{K}$ up to $T = 35\,\mathrm{K}$ at magnetic fields of $B = 1\,\mathrm{T}$ and $B = 4\,\mathrm{T}$. Torque curves recorded at $B = 1\,\mathrm{T}$ and temperatures from $T = 0.3\,\mathrm{K}$ up to $T = 35\,\mathrm{K}$ are shown in Fig. 5.7 a). At first glance, we observe the expected shape at low and intermediate temperatures. In particular, the temperature evolution resembles the behavior described for the PPMS data. At low temperatures, the torque slightly increases and the linear passage around $\langle 110 \rangle$ becomes sine-shaped. At intermediate temperatures, the overall amplitude strongly decreases.
In contrast to this agreement, the torque signal appears to deviate severely from the expected shape towards high temperatures. This is further illustrated in Fig. 5.7 b) where torque curves recorded at $T = 24\,\mathrm{K}$ and $T = 30\,\mathrm{K}$ are shown as green and orange solid lines, respectively. These curves no longer follow the expected shape but rather resemble sinusoidal curves with small modulations. We attribute this sinusoidal shape to the presence of substantial field gradients and assume that only the contribution perceived as comparatively small modulation results from magnetocrystalline anisotropy. If this contribution follows the expected shape, we can fit the torque curves via Eq. 5.2. Respective fits are depicted as dashed lines in Fig. 5.7 b) and yield good agreement with experimental data.
In order to validate our procedure, we subtract Γ_g, i.e. the part of the fit including only the gradient terms g_1, g_2 and g_3, from the measured torque. The resulting curves are plotted as solid lines in Fig. 5.7 c). In agreement with our evaluation approach, they exhibit the expected behavior described by Eq. 5.1. Respective fits match the data very well as depicted by the dashed lines in Fig. 5.7 c).
Despite the good agreement of fit and measured torque, a closer look at Γ_g reveals

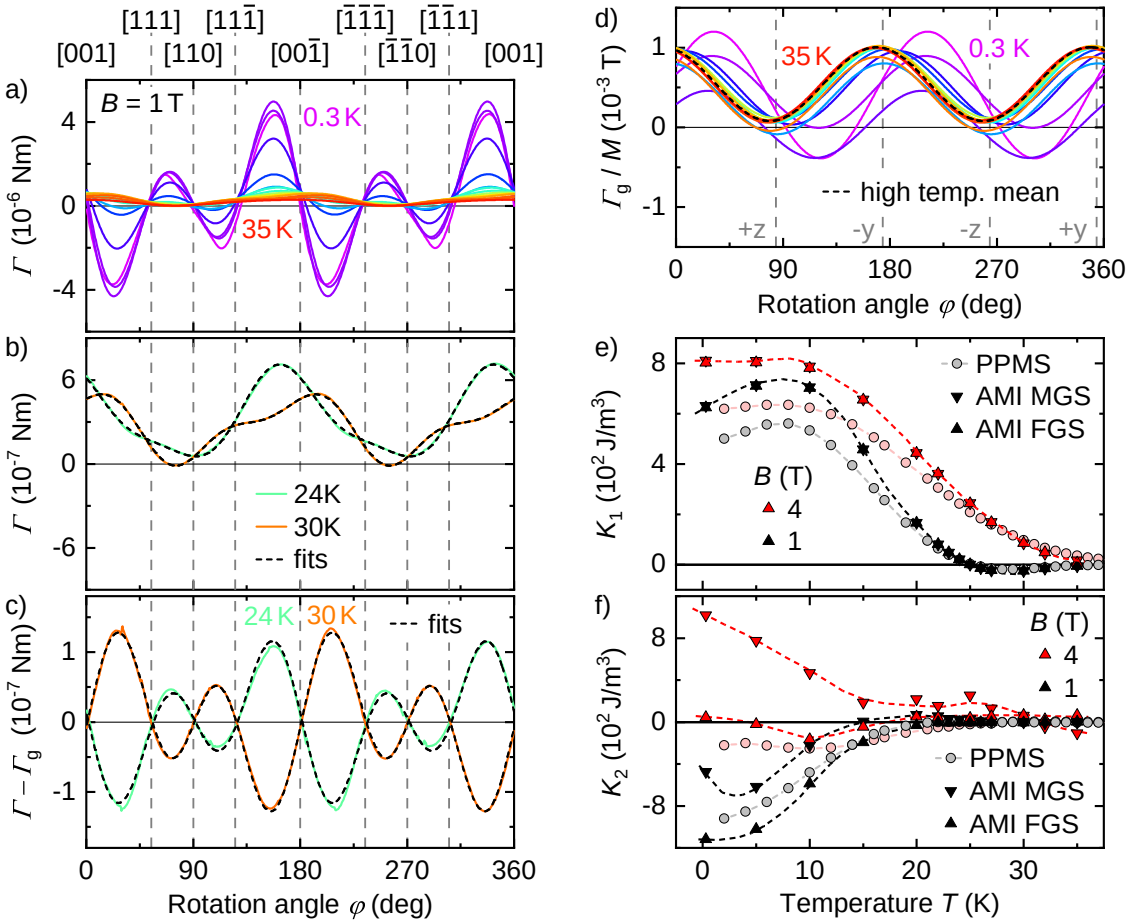

Figure 5.7: Temperature dependence of torque and anisotropy constants. a) Torque curves as measured in the rotating field setup at $B = 1\,\mathrm{T}$ and temperatures from $T = 0.3\,\mathrm{K}$ to $T = 35\,\mathrm{K}$. b) Torque as measured at $B = 1\,\mathrm{T}$ and $T = 24\,\mathrm{K}$ and $T = 30\,\mathrm{K}$. Dashed lines represent fits according to Eq. 5.2. c) Torque at $B = 1\,\mathrm{T}$ and $T = 24\,\mathrm{K}$ and $T = 30\,\mathrm{K}$ after subtraction of fitted gradient contributions. Dashed lines represent fits according to Eq. 5.1. d) Fitted gradient contributions to the torque at $B = 1\,\mathrm{T}$ and temperatures from $T = 0.3\,\mathrm{K}$ to $T = 35\,\mathrm{K}$. The dashed line represents the mean of four gradient torque curves at high temperatures. e)-f) Anisotropy constants at K_1 and K_2 at magnetic fields of $B = 1\,\mathrm{T}$ and $B = 4\,\mathrm{T}$ versus temperature.

a distinct flaw in our evaluation. The evolution of the applied magnetic field is identical for measurements at different temperatures. Consequently, the field gradients imposed to the sample must also be identical and Γ_g should only scale with the ordered moment of the material. In order to check whether our procedure fulfills this condition, we divide the contribution Γ_g obtained from fitting by the magnetic moment M of the sample. For this purpose, we interpolate values of M measured in a PPMS for field applied along a $\langle 001 \rangle$-direction at multiple field magnitudes and temperatures [Bau10] to match our experimental conditions. The normalized gradient contributions Γ_g/M are presented in Fig. 5.7 d) as a function of the measurement angle φ. Strikingly, we find a manifold of different curves.

The marked positions ±y and ±z in Fig. 5.7 d) correspond to the field directions of the split coil and the solenoid, respectively. For a gradient dominated by one of the magnets, the respective direction should be close to the extrema of the gradient contribution. We expect the gradient contribution to be dominated by the split coil (cf. Sec 3.3.1) and thus maxima of the gradient in vicinity of ±y. This appears to be the case rather at high temperatures. Further, Γ_g/M varies only slightly above 25 K. As an approach to model a fixed torque contribution resulting from a unique set of field gradients, we average over the four best matching curves of Γ_g/M at high temperature. The resulting mean gradient contribution per moment is depicted as black dashed line in Fig. 5.7 d). We evaluate our experimental data on the basis of this fixed gradient by scaling the mean contribution with the respective magnetic moment and subtracting it from the measured torque at each temperature. The resulting curves are fitted via Eq. 5.1. A second fixed field gradient was modeled based on the data at $B = 4\,\mathrm{T}$. The respective torque data are is shown in appendix C.3.5. As field gradients scale linearly with applied field magnitude, the modeled fixed gradients can easily be applied to measurements at different fields.
We now discuss the extracted anisotropy constants. As described above, we can obtain K_1 and K_2 either by fitting the measured torque via Eq. 5.2 or by subtracting a gradient contribution and employing Eq. 5.1 as a fit function. We have further described three variants of gradient contributions for subtraction, i.e. Γ_g obtained for each specific measurement or the two modeled fixed field gradients. All in all, we obtain four sets of temperature dependent values for K_1 and K_2. For clarity, we only include two of them in Fig. 5.7. A comparison of all four sets is presented in appendix C.3.5.
Extracted values of K_1 and K_2 are shown in Fig. 5.7 e) and f), respectively. We present the set where individually fitted gradient terms have been subtracted before fitting (FGS) as upward pointing triangles and the set where the mean gradient term modeled from data at $B = 1\,\mathrm{T}$ has been subtracted (MGS) as downward pointing triangles. Dashed lines are drawn by hand as a guide to the eye. For comparison, values obtained from the PPMS data are included as semi-transparent circles. Symbols filled red correspond to data taken at $B = 4\,\mathrm{T}$, black symbols correspond to $B = 1\,\mathrm{T}$.
The two sets of K_1 obtained from the AMI setup are practically identical. The same holds for the two sets that are not shown here (cf. appendix C.3.5). Qualitatively, we observe the same behavior as described for the PPMS data. However, at low temperatures the AMI data is larger by ∼30 % compared to the PPMS data. At high temperatures, both curves approach each other. In particular, K_1 at $B = 1\,\mathrm{T}$ changes sign at the same temperature for values from both setups.
We find large differences between the data sets obtained for K_2 from the AMI setup. At $B = 1\,\mathrm{T}$, the curves show qualitatively the same behavior except for the lowest temperature at which K_2's magnitude increases with the mean gradient method but decreases with the fitted gradient method. The overall shape still resembles the evolution found with the PPMS setup, yet the two AMI data sets are off by ∼30 % in opposite directions. At $B = 4\,\mathrm{T}$, K_2 starts large and positive with the mean gradient

method and hesitates to drop to zero with increasing temperature. In contrast, it starts close to zero and only briefly extends towards negative values before falling back to zero with the fitted gradient method. Neither of both curves resembles the behavior found with the PPMS setup other than that all curves eventually converge to zero. The values obtained by fitting the torque as measured are not included in the figure for clarity. They also differ from both presented data sets (cf. appendix C.3.5). The large spread of values obtained for K_2 with different evaluation methods points towards poor reliability of the extracted data. The different gradient contributions obtained from fits of various measurements hints at some additional perturbation especially at low temperatures which is not considered by our evaluation. Moreover, we obtain large values for the gradient parameters as well as for Γ_{off} from our fits which lack physical justification. For a detailed discussion of the fit parameters g_1, g_2, g_3 and Γ_{off} see appendices C.3.6 and C.3.7.
The volatility of K_2 suggest that uncertainties are larger than the actual values. K_1 appears more stable, especially due to its qualitative agreement with the PPMS data. Yet it must be viewed with caution due to the problems mentioned above. In Fig. 5.7 e) and f), we did not present any error bars. That is mostly due to the fact that the uncertainties are hard to estimate, one of the main reasons being that the influence of substantial misalignment on our experiment is not accounted for during the fitting process. In order to assess the impact of such misalignment, we turn to numerical simulations of our experiments.

5.3.3 Numerical simulations

In the foregoing sections, we evaluated torque data by means of an analytic fitting function that is derived in the high field limit for ideal alignment. Since the presented measurements were performed in the field-polarized state, we can assume the condition of collinear moments aligned along the external field direction to be fulfilled in our experiments. In contrast, our alignment deviated significantly from the ideal situation. In order to obtain an estimate of the measurement error introduced by misalignment, we model our experiment in MATLAB code and simulate torque curves for various experimental conditions. These simulations further allow us to investigate the role of the sample's unknown chirality as well as to quantitatively relate fit parameters g_1, g_2 and g_3 in Eq. 5.2 to physical quantities $\mathrm{d}B_\mathrm{y}/\mathrm{dy}$, $\mathrm{d}B_\mathrm{y}/\mathrm{dz}$ and $\mathrm{d}B_\mathrm{z}/\mathrm{dz}$. We first describe our procedure and the incorporated parameters. Then we discuss simulation results with respect to our experiments.

Procedure

In a first step, we model the experimental geometry in the coordinate system of the crystal. For this purpose, we define the unit vectors $\hat{\mathrm{R}}$ along the field rotation axis, $\hat{\mathrm{P}}$ along the cantilever projection axis and field directions $\hat{B}_\mathrm{y}$ and $\hat{B}_\mathrm{z}$ along the crystal's $\langle 001\rangle$- and $\langle 110\rangle$-directions, respectively, for ideal alignment (cf. Figs. 3.8 and 3.9). Then we consecutively rotate these vectors to account for misalignment angles δ_r and γ_r in the AMI setup or β_r in the PPMS setup, followed by rotations

reflecting ϕ_r and θ_r for both setups. The relative rotation of field and sample is then simulated by defining the field vector

$$\mathbf{B} = B \cdot \left(\hat{B}_\mathrm{y} \cos(\phi) + \hat{B}_\mathrm{z} \sin(\phi)\right) \tag{5.3}$$

and setting the rotation angle ϕ to values from 0° to 359.5° in steps of 0.5°. At each angle step, we minimize the energy density functional

$$\begin{aligned} E_a/V = &- \mathbf{M} \cdot \mathbf{B} + K_1\left(\hat{M}_x^4 + \hat{M}_y^4 + \hat{M}_z^4\right) \\ &+ K_2\left(\hat{M}_x^2\hat{M}_y^4 + \hat{M}_y^2\hat{M}_z^4 + \hat{M}_z^2\hat{M}_x^4\right) \\ &+ K_3\left(\hat{M}_x^6 + \hat{M}_y^6 + \hat{M}_z^6\right) \end{aligned} \tag{5.4}$$

with respect to the orientation of the magnetization vector $\mathbf{M}$. The magnitude of $\mathbf{M}$ is fixed during this process. As already described in Sec. 5.3.2, we utilize values obtained from magnetization measurements in a PPMS setup for field along the ⟨001⟩-direction of a high-quality MnSi crystal [Bau10]. These reference values are interpolated to match the desired field and temperature of our simulation. After the minimizing direction is determined, we calculate the magnetic torque density ($\mathbf{M} \times \mathbf{B}$) and the force density $\nabla(\mathbf{M} \cdot \mathbf{B})$ due to field gradients. For direct comparison with measurements, both densities are multiplied with the sample volume and projected on the respective axes, i.e. $\hat{P}$ for the torque and the cantilever normal for the force. Finally, the torque contribution due to the gradient force is calculated and added to the magnetic torque.
Equation 5.4 describes a right-handed MnSi crystal. As discussed in Sec. 2.1.2, only the K_2-term exhibits chiral shape. For a left-handed crystal, it changes to

$$K_2\left(\hat{M}_x^4\hat{M}_y^2 + \hat{M}_y^4\hat{M}_z^2 + \hat{M}_z^4\hat{M}_x^2\right). \tag{5.5}$$

We further included an additional term K_3 in Eq. 5.4 which has not been discussed before. This term is presented here for the sake of completeness since it has been implemented in our code. However, the torque contribution resulting from the K_3-term resembles that of the K_1-term closely so that both contributions can not be separated. We thus set $K_3 = 0$ in our simulations and do not consider K_3 during our experimental data evaluation.

Parameters

Our simulations require a considerable number of input parameters. In the following, we list them and briefly describe their purpose where necessary.

- The **anisotropy constants** K_1, K_2 and K_3 determine the energy landscape for the magnetization vector. As mentioned above, we set $K_3 = 0$ in all our simulations. K_2 is the only term reflecting the chirality of the material. For comparable values of K_1 and K_2, the contribution of K_1 dominates the observable torque.

- The **magnetic field magnitude** B is directly required for minimization of the energy and calculation of the magnetic torque. A further use is the determination of the appropriate magnetization magnitude M.
- The **temperature** T is solely reflected in our simulations by means of the magnetization magnitude. Reference values of M at various temperatures and field magnitudes are interpolated to the desired conditions for our simulations.
- The **misalignment angles** θ_r and ϕ_r describing the alignment of sample and cantilever are required as input parameters as well as the angles describing misalignment of cantilever and magnet, i.e. γ_r and δ_r for the AMI setup and β_r for the PPMS setup.
- If applicable, the **field gradients** $\mathrm{d}B_\mathrm{y}/\mathrm{dy}$, $\mathrm{d}B_\mathrm{y}/\mathrm{dz}$ and $\mathrm{d}B_\mathrm{z}/\mathrm{dz}$ must be provided in units of gradient per applied field. If gradients are non-zero, the **reduction factor** β is also required in order to calculate the torque contribution resulting from the gradient force (cf. Sec. 3.1.1).
- Finally, **sample volume** and **chirality** are required. The volume is necessary to scale the torque density and enable comparison with measurements. The chirality determines the shape of the K_2-term.

Naturally, our simulation is a better model for our experimental situation compared to our fit function, yet due to its complexity, a complete matching of simulation and experiment is unfeasible. Further, not all parameters are known as, e.g., we do not know the chirality of our crystal. We utilize simulations to assess the uncertainties of extracted anisotropy constants due to effects not accounted for by the fitting routine.

Comparison of experiments and simulation

Several input parameters of the simulation are fixed by experimental conditions. In particular, we know the values of ϕ_r, θ_r, δ_r and γ_r in our various experiments. For β_r we estimated a maximum value. For direct comparison with experiments, we inserted the respective temperature and field magnitude as well as the anisotropy constants obtained from fitting experimental data. For simulations not utilized for direct comparison, we choose $T = 2\,\mathrm{K}$ and $B = 1\,\mathrm{T}$. Other values were tested and yielded consistent results. As stated above, our comparison of experimental and simulated data has three objectives: i) assess the uncertainties of K_1 and K_2 due to misalignment, ii) investigate the influence of chirality and iii) enable quantitative interpretation of fitting parameters g_1, g_2 and g_3.
We begin with the analysis of field gradient parameters. For the purpose of quantitative interpretation, we simulate the torque at zero anisotropy, i.e. $K_1 = K_2 = 0$, but finite gradients. Fitting the resulting torque curves via Eq. 5.2 yields appropriate factors for conversion of g_1, g_2 and g_3 into $\mathrm{d}B_\mathrm{y}/\mathrm{dy}$, $\mathrm{d}B_\mathrm{y}/\mathrm{dz}$ and $\mathrm{d}B_\mathrm{z}/\mathrm{dz}$, respectively. We note that it is crucial for this procedure to include the experimental misalignment angles since the contribution to the measured torque depends strongly on γ_r

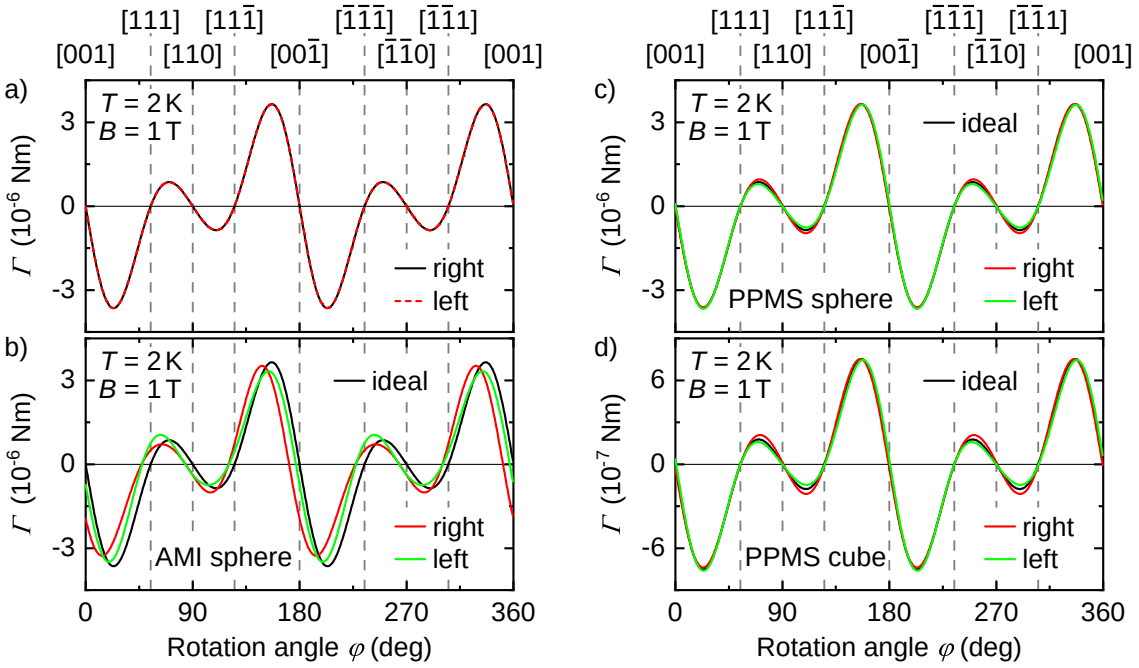

Figure 5.8: Simulated torque curves at $B = 1\,\mathrm{T}$ and $T = 2\,\mathrm{K}$. a) Torque for right-handed and left-handed MnSi in the case of ideal alignment. b)-c) Comparison of torque curves simulated for ideal alignment and experimental misalignment angles in our various experiments in the case of right- and left-handed MnSi.

and δ_r. Field gradients obtained from the fitting routine are discussed in detail in appendix C.3.7. They are not consistent with our maximum estimates in Sec. 3.3.1. Next we discuss the influence of chirality. For perfect alignment of $\hat{\mathrm{R}}$ along $\langle 110 \rangle$, we do not expect a difference of left- and right-handed MnSi. This is illustrated in Fig. 5.8 a) where we show torque simulated for zero misalignment and zero field gradients. Right-handed MnSi is represented by the black continuous line, left-handed MnSi is depicted as red dashed line. No difference between both curves can be observed. We review the situation at finite misalignment individually for each experiment. The situation in the AMI setup is shown in Fig. 5.8 b). The black line depicts torque simulated for perfect alignment, the red and green lines represent simulations including experimental misalignment for right- and left-handed MnSi, respectively. No field gradients are included. We observe distinct differences between all three curves. Independent of chirality, the global extrema around $\langle 001 \rangle$ are decreased by misalignment. The local extrema around $\langle 110 \rangle$ both shift towards negative (positive) values for right-handed (left-handed) MnSi when misalignment is included. Finally, the whole curves are slightly shifted in horizontal direction due to the finite δ_r. Further simulations show that for small ϕ_r and θ_r a change of chirality alters the observed torque almost in the same way as a sign change of γ_r. As a consequence, measurements at different angles γ_r could allow us to determine our sample's chirality. Unfortunately, this was not possible with our results. Respective simulated and experimental data is presented in appendix C.3.8.

In Fig. 5.8 c) and d) we present simulations of our experiments in the PPMS setup with spherical and cubic sample, respectively. Again, black lines denote ideal alignment, red and green lines represent experimental misalignment for right- and left-handed crystals. The region of the global extrema around $\langle 001 \rangle$ remains almost unaffected by misalignment. Small differences between the curves are visible around $\langle 110 \rangle$. Here, the local extrema are increased (decreased) by misalignment for a right-handed (left-handed) crystal. Similar to γ_r in the AMI setup, a sign change of β_r has almost the same effect on the torque as a change of chirality for small ϕ_r and θ_r. As the sign of β_r is unknown, a determination of the sample's chirality is still not possible.
We now compare the anisotropy constants K_1 and K_2 extracted from experimental and simulated data. For this purpose, we apply the fitting procedure described for the evaluation of experimental data to simulated torque curves. For consistency, we use the same convergence criteria as for experimental data. As a result, the anisotropy constants obtained from the fitting routine deviate from those used for simulation. Even for zero gradient and ideal alignment, we find differences of $\sim$1 % for K_1 and $\sim$3.5 % for K_2.
Our experiments in the PPMS setup featured small misalignment and negligible field gradients. The error introduced by misalignment amounts to $\sim$7 % and $\sim$10 % for K_1 obtained from the spherical and the cubic sample, respectively. For K_2, the respective errors amount to $\sim$20 % and $\sim$32 %. Experiments in the AMI setup featured larger misalignment, yet the introduced errors are comparable to the PPMS experiments with $\sim$10 % for K_1 and $\sim$23 % for K_2. However, additional uncertainties may be introduced by misjudgement of gradients.

5.3.4 Discussion

In this section, we appraise the presented results regarding magnetic anisotropy in the field-polarized phase of MnSi. We begin with a consideration of angular distortion of measured torque data. As stated in Sec. 5.2, a full angular correction needs to account for two erroneous contributions, i.e. the rotation of the sample and the angular mismatch of $\mathbf{M}$ and $\mathbf{B}$. The correction procedure for the latter part is well established. Following the nomenclature defined in Fig. 5.2, we use

$$\theta' = \varphi' - \arcsin\left(\frac{\Gamma(\varphi')}{mB}\right) \tag{5.6}$$

where m is the magnetic moment of the sample and B is the applied field magnitude. We employ the same method to find appropriate values of m as described for our numerical simulations. In order to obtain $\Gamma(\varphi')$ from $\Gamma(\varphi)$, we need to determine the angle by which the sample is rotated by the magnetic torque. The most straightforward approach is to calculate

$$\varphi' = \varphi - \frac{\Gamma(\varphi)}{\kappa} \tag{5.7}$$

where κ is a torsional spring constant relating torque and angular distortion. In general, we do not know the spring constants of our sensors. The manufacturer of our torsional cantilevers provides a value of $\kappa_{\mathrm{QD}} = 9.3 \cdot 10^{-7}\,\mathrm{Nm/deg}$ obtained from a single-shot bench test measurement on a 2-leg sensor at room temperature. No information is available regarding variability between different chips, changes towards low temperatures or values for 3-leg sensors. Depending on the fabrication process of the cantilevers, a variation of κ by a factor of $\sim$2 between individual chips can be deemed realistic. Thus we consider half the bench test value, i.e. $\kappa = 4.65 \cdot 10^{-7}\,\mathrm{Nm/deg}$, for our cubic sample on the 2-leg sensor in order to estimate a maximum error. For our spherical sample on the 3-leg sensor, we scale that value by the ratio of torque coefficients c_τ obtained during the calibration routine for 3-leg and 2-leg sensors. With a ratio of $\sim$3.6, we obtain $\kappa = 16.75 \cdot 10^{-7}\,\mathrm{Nm/deg}$.
For longitudinal cantilevers, we have no such experimental reference value of κ. Instead, we utilize the formulas found in the appendix D of Ref. [Wil04] to calculate the bending line due to the measured torque at each angle φ. From these bending lines we determine the angular distortion $\varphi' - \varphi$. For torsional cantilevers, we lack an equivalent mathematical framework and numeric simulations of the angular distortion are beyond the scope of this work. Therefore a direct comparison of both approaches is not possible.
We present torque curves before and after angular correction in Fig. 5.9 a) - c). Red continuous lines represent data with no angular correction (AC), blue dashed lines depict torque data after full AC. Graph a) shows a measurement in the AMI setup at $T = 5\,\mathrm{K}$ and $B = 0.65\,\mathrm{T}$. Almost no difference between the to curves can be recognized. The maximum angular distortion found through all measurements in this setup amounts to less than 1°. Consequently, the anisotropy constant K_1 changes by only $\lesssim$2 %. Changes of K_2 reach up to $\sim$25 % which is still moderate compared to variations between our different evaluation methods for AMI data.
Figure 5.9 b) and c) show measurements in the PPMS setup at $T = 2\,\mathrm{K}$ and $B = 4\,\mathrm{T}$ on the spherical and cubic sample, respectively. As stated above, we employed spring constants of $\kappa_{\mathrm{QD}}/2$ for the 2-leg sensor and $3.6\kappa_{\mathrm{QD}}/2$ for the 3-leg sensor. Here, the differences are more pronounced than in the AMI setup. While differences between θ' and φ' are still less than half a degree, the presumed rotation of our samples due to magnetic torque may amount up to $\sim$5°. As a consequence, extracted anisotropy constants can change substantially. We illustrate this in Fig. 5.9 d) - g) where anisotropy constants K_1 and K_2 are shown for $B = 4\,\mathrm{T}$ at various temperatures. Red circles correspond to uncorrected curves, blue triangles depict values obtained from torque curves after full angular correction with spring constant $\kappa_{\mathrm{QD}}/2$ or $3.6\kappa_{\mathrm{QD}}/2$, respectively. For comparison, we also include values obtained with the full bench test value κ_{QD} resp. $3.6\kappa_{\mathrm{QD}}$ as semi-transparent triangles. Graphs d) and e) show data obtained from the spherical sample, graphs f) and g) correspond to data on the cubic sample. In both cases, the qualitative behavior of K_1 is maintained and we find that values obtained from corrected torque data are larger by up to $\sim$8 %. In contrast, changes of K_2 are on the order of $\sim$100 %. In the case of the spherical sample, we observe a sign change of K_2 at low temperatures due to angular correction. Moreover,

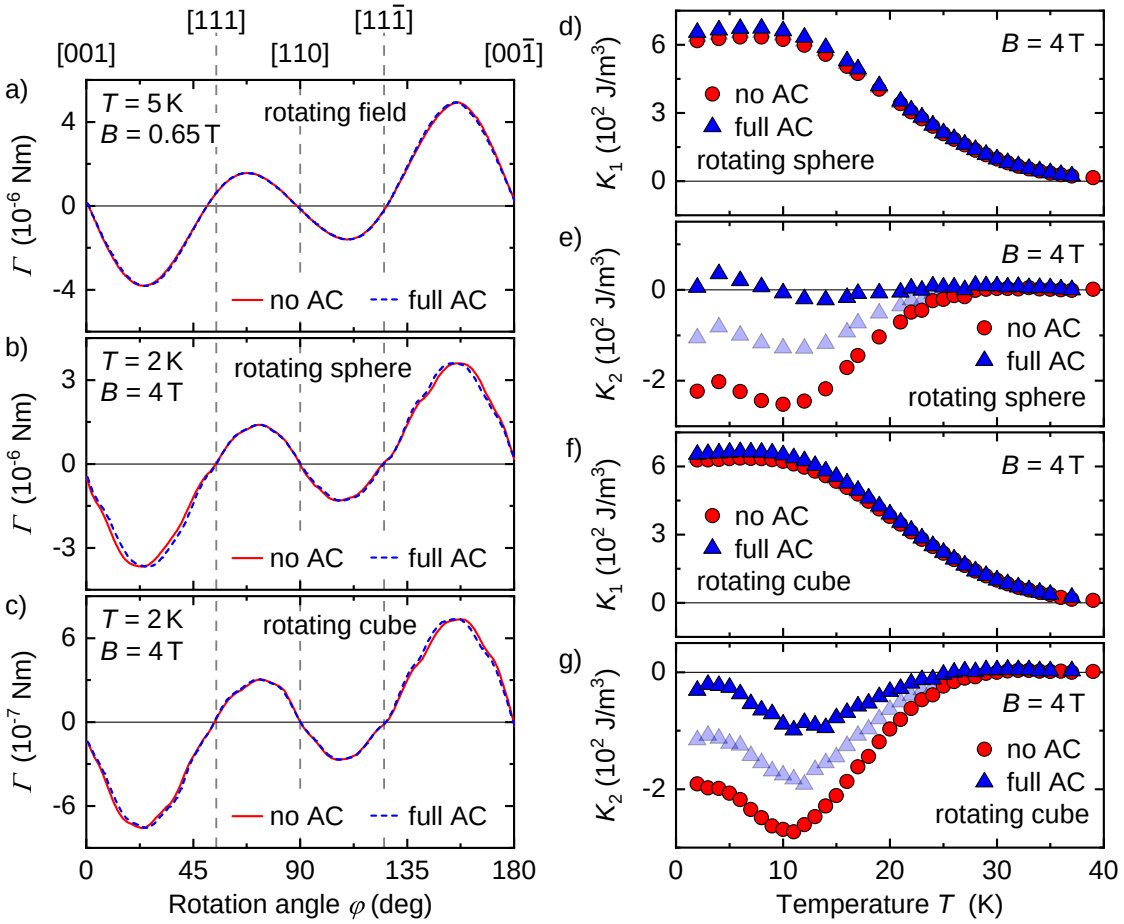

Figure 5.9: a)-c) Comparison of measured torque curves with and without AC from φ to θ' in our various experiments. For PPMS data, we employed $\kappa = 16.75 \cdot 10^{-7}$ Nm/deg for the spherical sample and $\kappa = 4.65 \cdot 10^{-7}$ Nm/deg for the cubic sample. d)-g) Comparison of anisotropy constants K_1 and K_2 obtained from fitting Eq. 5.1 to torque curves with and without AC. For the full AC, half the values of the bench test have been used for κ as in b) and c). Semi-transparent symbols correspond to the full bench test value of κ.

the values obtained from spherical and cubic sample no longer coincide. Performing the angular correction with κ_{QD} yields only half the absolute shift for K_1 and K_2 as compared to $\kappa_{\mathrm{QD}}/2$.

As stated above, we regard the situation shown in Fig. 5.9 as an extreme case of large angular distortion. The relative changes of K_2 in Fig. 5.9 e) and g) are further boosted by the fact that K_2 is relatively small at $B = 4\,\mathrm{T}$. For instance, K_2 is larger by a factor of 4−5 at $B = 1\,\mathrm{T}$ at low temperatures. Performing angular correction with identical spring constants, we find similar absolute shifts of 200−300 J/m^3 for both field magnitudes at low temperatures and consequently a smaller relative change of 25−55 % at $B = 1\,\mathrm{T}$. The same holds true for K_1 where we observe shifts of 40−45 J/m^3 at low temperatures. We infer that angular correction imposes an absolute shift towards positive values on extracted anisotropy constants rather

than a relative change. This is consistent with our observation that doubling the spring constant yields half the absolute shift for anisotropy constants. With rising temperature, the absolute changes diminish similarly fast as the respective anisotropy constants.
The above discussion once again demonstrates how sensitive extracted values of K_2 are to details of experiment as well as data evaluation. We already showed in Sec. 5.3.2 that K_2 obtained from AMI data depends primarily on the method of evaluation due to unexplained perturbations to the measured torque. For PPMS data, we find a strong dependence of K_2 on the unknown spring constant κ. We further note that the good agreement of K_2 extracted from data on spherical and cubic samples shown in Fig. 5.6 may be coincidental. These observations yield uncertainties of K_2 that may range from less than 10 % to more than 100 %. In particular, an error introduced by a poorly estimated spring constant κ may be larger than that of disregarding angular correction altogether. While we suggest that the actual behavior of K_2 still resembles that shown in Figs. 5.4 and 5.5 with values shifted towards positive values by up to $\sim$300 J/m^3, our data is not sufficient to reliably substantiate this presumption. Therefore, we refrain from a detailed discussion of temperature and field evolution of K_2. Still, we conclude that K_2 is negative at small fields and low temperatures and strives towards zero considerably faster than K_1 with increasing temperature.
In the following, we discuss uncertainty, temperature evolution and field magnitude dependence of K_1. AMI and PPMS setups yield qualitatively consistent results especially regarding temperature evolution, but K_1 extracted from PPMS data is smaller by $\sim$30 % at low temperatures. We attribute this quantitative discrepancy to disturbances of unknown origin in the AMI setup. Field gradients and misalignment are already included in our simulations. Further approaches coming into mind include physical origins as, e.g., the de Haas-van Alphen effect or technical issues as, e.g., temperature oscillations. However, none of them can account for the observed perturbation. We thus suggest a thorough investigation of the AMI setup in the future in order to identify the flaw disturbing our experiments. For the following discussion, we focus on K_1 as obtained from PPMS data.
In Figs. 5.4 c) and 5.6 c1) - c2), we presented error bars including the 95 % confidence bounds of the fits, a 5 % relative error and a 5 J/m^3 absolute error. As stated in Sec. 5.3.1, these error estimates are expected to cover minor uncertainties imposed by (i) the high-frequency modulation, (ii) inaccurate calibration and data evaluation, (iii) influences of residual gradients and (iv) magneto-resistive effects in the readout circuitry. As discussed above, our values of K_1 further exhibit an error of $\sim$7 % due to misalignment and an error of $\lesssim$8 % due to angular distortion. An additional source of inaccuracy is the sample volume. During our evaluation, we calculated a spherical volume from the measured diameter $d_{\mathrm{sphere}} = 2.1\,\mathrm{mm}$. In comparison, the volume obtained by dividing the measured sample weight $m_{\mathrm{sphere}} = 30.0\,\mathrm{mg}$ by the density of MnSi $\rho_{\mathrm{MnSi}} = 5.74\,\mathrm{mg/mm^3}$ is larger by 7.8 %.
Considering all uncertainties mentioned above, we find an overall error of $\lesssim$30 % at temperatures below 15 K for all applied field magnitudes. At highest temperatures,

K_1 approaches zero and the uncertainty is governed by the static error of $5\,\mathrm{J/m^3}$. In the intermediate temperature regime, the relative error becomes larger than 30 % for small K_1 only where the absolute error is smaller than $20\,\mathrm{J/m^3}$. The actual errors of our results may be smaller than our estimate since different contributions might cancel each other. For example, an underestimated volume yields too large values of K_1 whereas omission of angular correction yields too low anisotropy constants.
During our discussion of uncertainties, we did not consider a contribution due to the scaling effect discussed in appendix C.2.1 since the nature of its occurrence clearly suggests a technical issue scaling all torque data by a fixed factor. The excellent agreement of results from spherical and cubic samples for K_1 which is rather robust regarding details of experiment and evaluation implies that our procedure of scaling high temperature data down to the level of low temperature measurements is sufficient to account for this error.
Including this scaling of ∼14 %, our overall error still remains smaller than 50 % in the low temperature regime where K_1 is largest. We consider the maximal possible value consistent with our measurements and error analysis to estimate the maximum energy difference between two otherwise identical states with different directions of magnetization. Even including a similar extreme value of K_2 to increase the difference, this maximum estimate lies far below $1\,\mu\mathrm{eV}$ per unit cell which is a lower boundary for typical resolutions in state-of-the-art DFT calculations. Our experiments thus confirm the statement in Ref. [Kar12] that cubic anisotropies in MnSi are too small to be calculated reliably from DFT.
As an adverse consequence, no theoretical work exists regarding not only the size of these anisotropies but also their temperature dependence. We therefore turn to the work on similar materials in order to find a suitable description. As we mentioned in Sec. 5.1, magnetic anisotropy in the weak itinerant ferromagnet Ni_3Al has been addressed both experimentally and theoretically. Ni_3Al shows a similar decrease of K_1 with temperature but neither an increase at low nor a sign change at high temperatures [Sig82]. However, in the theoretical work the experimentally obtained anisotropy was reproduced from band structure calculations by adjusting Fermi energy and *d*-electron number per atom in order to match the experimental findings [Mat85]. While we encourage similar calculations for MnSi, their realization is beyond the scope of this thesis.
For a broader range of theoretical approaches, we turn to nickel as a prime example of itinerant magnetism. In this material, K_1 resembles our findings for MnSi in that it decreases with temperature and changes sign before converging to zero, but differs in that it does not increase at low temperatures [Boz51]. Several attempts to calculate $K_1(T)$ ab initio have been presented with varying degrees of success. Most approaches do not yield analytical expressions and are therefore not applicable for interpretations of our experiments [Mor69, Mor74, Szp84]. In a few papers, low order polynomials are suggested [Ono77, Mit97]. However, these studies exclusively address the low temperature regime where MnSi and Ni exhibit qualitatively different behavior and are therefore not suitable for interpretation of our data either. Instead of ab initio calculations, we consider a phenomenological approach.

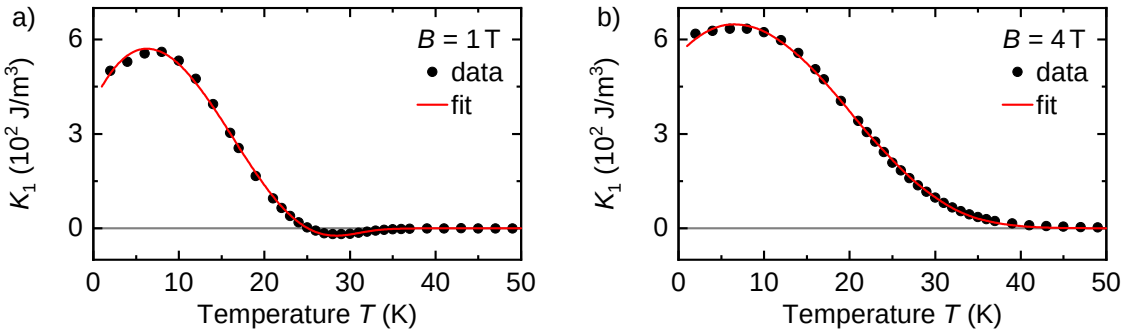

Figure 5.10: Temperature evolution of anisotropy constant K_1 at a) $B = 1\,\mathrm{T}$ and b) $B = 4\,\mathrm{T}$. Red lines denote fits according to Eq. 5.8.

Throughout literature, the temperature dependence of magnetic anisotropy constants is most commonly discussed in terms of a power law, i.e. $K(T)/K(0)$ is supposed to decrease proportional to $[M(T)/M(0)]^n$. Several models exist that yield different exponents n such as, e.g., the single-ion and two-ion models yielding $n = 2$ and $n = 3$ [Sko08, Kob16]. The decrease described by these models is distinctly slower than observed for MnSi. The Zener model was initially developed for localized moments and suggests $n = l(l+1)/2$ where l is the respective anisotropy constant's order in spin-orbit coupling [Vle37, Zen54, Kef55]. We obtain $n = 10$ for a fourth-order K_1 which is the leading term also in the elemental ferromagnets iron, cobalt and nickel. While $K_1(T)$ in Fe is well described by this model, both Co and Ni exhibit sign changes in $K_1(T)$ which can not be accounted for by the simple power law. The temperature evolution of anisotropy in Co could be modeled by extending the power law by a prefactor $(1 - bT/T_\mathrm{c})$ where b could be derived from the thermal expansion of the material [Car58]. A similar factor also allowed to model $K_1(T)$ in Ni, but the prefactor could neither be explained by thermal expansion nor was it justified in a different fashion. However, adjusting a power law by terms of indeterminate physical meaning in order to match experimental findings has been established as common practice [Car58, Tat65, Bir77, Mer59]. For instance, Birss *et al.* proposed a factor of $\exp[-(T/T_\mathrm{c})^n]$ with no physical explanation [Bir77]. Merkle suggested a prefactor linear in T despite obtaining a quadratic term in leading order from calculations [Mer59]. Due to the similarity of $K(T)$ in MnSi and Ni, we stick to the factor $(1 - bT/T_\mathrm{c})$ proposed by Carr [Car58]. To account for the increase at low temperatures, we add an additional factor of $(1 + aT/T_\mathrm{c})$ and obtain

$$K_1(T) = K_1(0) \cdot \left(1 + a\frac{T}{T_\mathrm{c}}\right)\left(1 - b\frac{T}{T_\mathrm{c}}\right)\left[\frac{M(T)}{M(0)}\right]^n \tag{5.8}$$

as a fit function with $a, b \geq 0$. In Fig. 5.10, we present the temperature evolution of K_1 at $B = 1\,\mathrm{T}$ in panel a) and $B = 4\,\mathrm{T}$ in panel b). Black circles represent values obtained from our experiments, red lines illustrate fits according to Eq. 5.8. The overall temperature dependence of our experimental results is reproduced very well by the fit. In particular, the function is capable of describing both the sign change

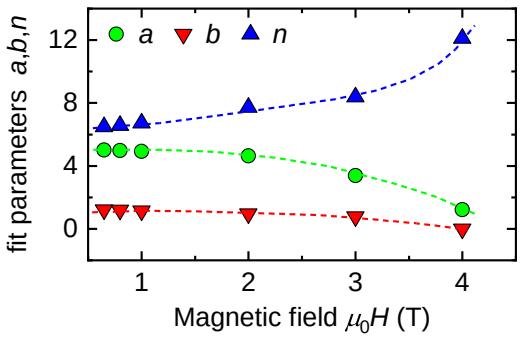

Figure 5.11: Evolution of fit parameters a, b and n as a function of field magnitude.

and minimum at $B = 1\,\mathrm{T}$ as well as the monotonous decrease at $B = 4\,\mathrm{T}$ at high temperatures. On the contrary, the low temperature increase is overstated by the fit. Identical graphs for further field magnitudes are presented in appendix C.2.5.
Values obtained for the free fit parameters a, b, and n are shown in Fig. 5.11. We note that a and b approach zero with increasing field which might result in a temperature evolution strictly following a simple power law at higher fields. At the same time, n increases at a progressive rate from $\sim$6.5 at $B = 0.65\,\mathrm{T}$ to more than 12 at $B = 4\,\mathrm{T}$. An exponent $n \gg 10$ at higher fields as implied by this behavior does not correspond to any existing phenomenological model. Since we can link neither a and b nor n to a physical explanation, a closer discussion is futile at this point.
Our error analysis shows that the sign change in $K_1(T)$ at low fields does not occur "within the margin of error" but with proper significance. Moreover, it is well recognizable in the torque curves as shown in Fig. 5.5 c). We conclude that this part of the evolution is indeed intrinsic to K_1 and corresponds to a real alteration of the anisotropy landscape in MnSi. We illustrate this in Fig. 5.12 where energy is plotted as a function of magnetization direction as obtained from our data at $B = 1\,\mathrm{T}$. Axes and colorization are scaled identically throughout the figure and K_2 as obtained from our fits is included for consistency. Graph a) corresponds to the low temperature situation at $T = 24\,\mathrm{K}$. Here, K_1 is positive and we find the lowest energy along $\langle 111 \rangle$- and highest energy along $\langle 001 \rangle$-directions. For comparison, graph b) shows the anisotropy at $K_1 = K_2 = 0$ which is represented by a fully isotropic sphere. Graph c) corresponds to the high temperature situation at $T = 29\,\mathrm{K}$ where K_1 is negative and we find the lowest energy along $\langle 001 \rangle$- and highest energy along $\langle 111 \rangle$-directions. Similar changes of magnetic anisotropy have been observed in the ferromagnets Co and Fe, but also in the helimagnet FeGe which is isostructual to MnSi [Leb89]. In the case of FeGe, the change of the easy direction has been observed in the helical state at zero field. For MnSi, we observe this change below T_c in the field-polarized state and at lower temperatures for lower fields. Extrapolation to zero field suggests a change of the easy direction in the helical phase at zero field as well. However, no such shift has been observed in MnSi despite numerous studies (see [Bau17] and refs. therein). Apparently, extrapolation of behavior studied in the field-polarized phase to the region of modulated states is not warranted in MnSi. Unfortunately, neither

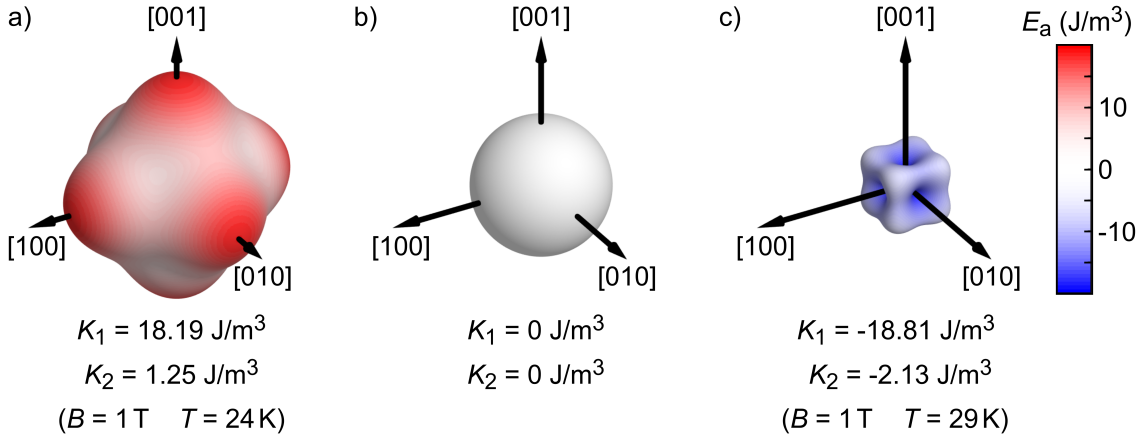

Figure 5.12: Anisotropy energy around the zero-transition of K_1. Axes and colorization are scaled identically in all plots. a) Anisotropy energy with $K_1 = 18.19\,\mathrm{J/m^3}$ and $K_2 = 1.25\,\mathrm{J/m^3}$ as obtained from the torque at $B = 1\,\mathrm{T}$ and $T = 24\,\mathrm{K}$. b) For $K_1 = K_2 = 0$, the energy landscape is represented by a sphere. c) Anisotropy energy with $K_1 = -18.81\,\mathrm{J/m^3}$ and $K_2 = -2.13\,\mathrm{J/m^3}$ as obtained from the torque at $B = 1\,\mathrm{T}$ and $T = 29\,\mathrm{K}$.

is the determination of anisotropy constants in non-collinear magnetic states from torque measurements as we will discuss in Sec. 5.4.

Contrary to the sign change at high temperatures, the low temperature behavior of K_1 is somewhat ambiguous in that the observed increase is distinctly smaller than the uncertainties of our experimental values. However, the major contributions to these uncertainties are systematic shifts that affect the absolute values of K_1 rather than its evolution. Further, we observe an increase for all field magnitudes, on both spherical and cubic samples and even in the AMI setup. It thus appears unlikely that this observation is an artifact due to measurement or evaluation errors. Still, it remains unclear whether the increase is intrinsic to K_1. In the following, we suggest an alternative explanation.

We reported a changing shape of measured torque curves around $\langle 110 \rangle$-directions in the region of low temperatures and low fields. In this regime, the torque between local extrema exhibits a rather linear behavior that becomes more sinusoidal with increasing field magnitude or temperature. This linear behavior between two extrema is reminiscent of a sawtooth shape which mathematically can be modeled by summing up harmonics of sinusoidal oscillations. We thus suggest that the torque is significantly influenced by higher order contributions to the anisotropy potential at low fields and temperatures. Beside an alteration of the magnetic torque's shape, a considerable influence of higher order terms may also result in the perception of smaller K_1. As an example, we consider a sixth order term $K_3(\hat{M}_x^6 + \hat{M}_y^6 + \hat{M}_z^6)$ as in Eq. 5.4. As mentioned before, such a term in the anisotropy potential results in a torque signal similar to that of the K_1-term. Consequently, a negative K_3 may be reflected in our data evaluation as a reduction of K_1.

Regarding temperature dependence, observations of K_2 as well as the Zener model

imply that higher order anisotropy constants decay much faster with increasing temperature than the leading order term. Consequently, we expect the torque signal to be increasingly dominated by the leading order K_1-term with increasing temperature. A higher order term decreasing our extracted values of K_1 and decaying quickly with temperature can thus be responsible for the observed increase of K_1 at low temperatures. We emphasize that this scenario is a mere speculation at this point that deserves further investigation.
We observe a similarly changing shape at low temperatures when increasing the field magnitude. As for the temperature dependence, this change is accompanied by a moderate increase of K_1. Within the frame of our suggested explanation, this implies that the dominance of K_1 over higher order anisotropy constants grows with increasing field magnitude as well. At larger field magnitudes, K_1 grows by more than 90 % between $B = 2\,\mathrm{T}$ and $B = 10\,\mathrm{T}$ and then decreases again. For this behavior we can not present any explanation at this point. However, it has been suggested that the anisotropy of metals may be dominated by degenerate or nearly degenerate electronic states in the vicinity of E_F [Kon74]. Band structure calculations reveal that several such (near-)degeneracies exist close to E_F in MnSi [Wil20a]. A proper explanation of the field magnitude dependence of K_1 may thus require extensive investigations of the band structure and its alteration with increasing magnetic fields.

5.4 Measurements in modulated phases

In this section, we present our results concerning the non-collinear magnetic phases of MnSi. We begin with rotation scans at constant field magnitude $B < \mu_0 H_{\mathrm{c}2}$ in Sec. 5.4.1. Field scans at fixed orientations are addressed in Sec. 5.4.2. We discuss the results of both in Sec. 5.4.3. All data presented in this section has been recorded with the spherical MnSi sample in the rotating field setup. Rotation scans and field scans were recorded at misalignment angles of $\gamma_\mathrm{r} = 9°$ and $\gamma_\mathrm{r} = 0°$, respectively. Measurements on a cubic sample as well as experiments in the rotating sample setup yielded consistent results. Examples thereof are presented in appendix D.2.3. Throughout this section, we discuss the anisotropic magnetization $M_\perp = \Gamma/B$ instead of the measured torque Γ. This is particularly advantageous for field scans through zero since, by its very nature, Γ vanishes at $B = 0$ whereas $M_\perp$ does not.

5.4.1 Field rotations

In order to investigate the various modulated phases of MnSi, we performed rotation scans at several temperatures and field magnitudes. In particular, measurements were carried out at temperatures from $T = 0.3\,\mathrm{K}$ up to $T = 35\,\mathrm{K}$ for fixed field magnitudes of $B = 0.1\,\mathrm{T}$ and $B = 0.3\,\mathrm{T}$ as well as for field magnitudes from $B = 0.05\,\mathrm{T}$ up to $B = 0.3\,\mathrm{T}$ at the fixed temperature of $T = 28.5\,\mathrm{K}$. As described in Sec. 5.2.2, we present consecutive rotations. Since these scans do not include reorientation after a reversal of the rotation sense, displayed curves may be completely disjoint due to rotational hysteresis. A full set of rotation scan magnetization curves including

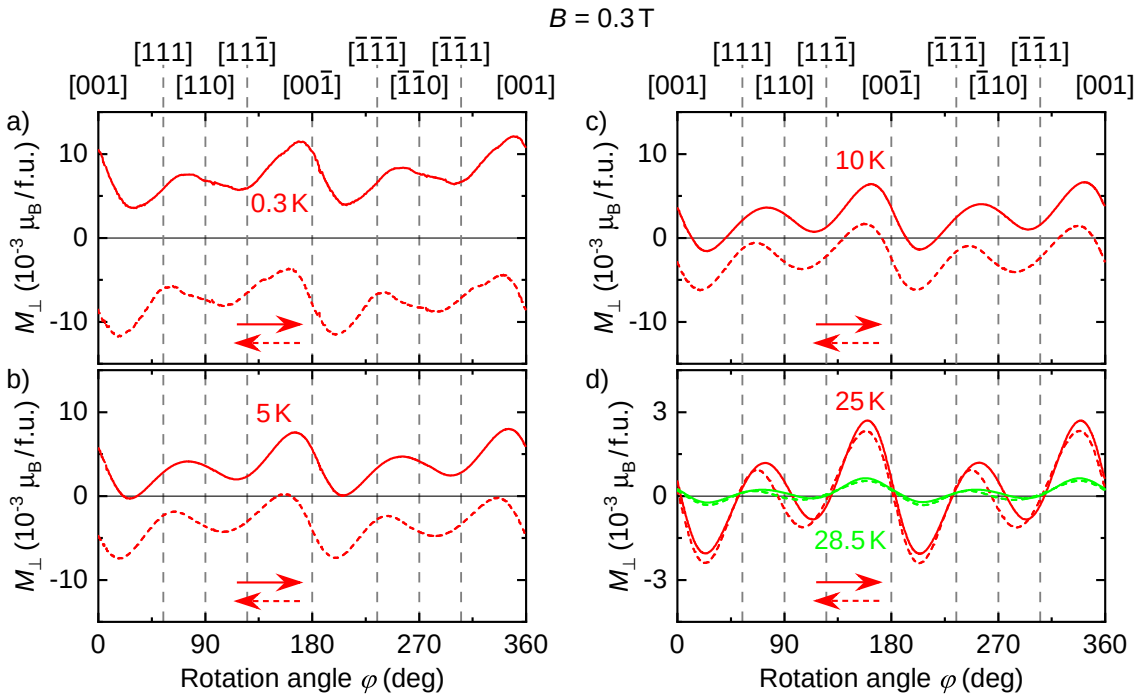

Figure 5.13: Anisotropic magnetization $M_\perp$ during field rotations at $B = 0.3\,\mathrm{T}$ and temperatures from $T = 0.3\,\mathrm{K}$ up to $T = 28.5\,\mathrm{K}$. Solid lines denote positive rotation sense, dashed lines denote negative rotation sense.

regimes of reorientation after rotation sense reversal is shown in appendix D.1.1.
We present the anisotropic magnetization $M_\perp$ measured at $B = 0.3\,\mathrm{T}$ and $T = 0.3\,\mathrm{K}$ in Fig. 5.13 a). The continuous and dashed lines correspond to positive and negative rotation sense, respectively. The most striking observation is a large rotational hysteresis. The curve measured for positive rotation sense is entirely positive whereas the curve recorded for negative rotation sense resides at strictly negative values. Both curves closely resemble the shape described by Eq. 5.1 but with symmetry lines shifted away from zero in opposite directions. Minor irregularities are visible, especially between the local extrema around $\langle 110\rangle$. On closer inspection, the rotation hysteresis does not consist in a vertical translation of the same curve, but rather in two shifted curves related by an inversion operation with respect to the origin. This is best recognized by the local extrema. For positive rotation sense, the local maximum is located roughly in the middle between $\langle 111\rangle$- and $\langle 110\rangle$-directions whereas the local minimum much closer to the $\langle 11\bar{1}\rangle$- than the $\langle 110\rangle$-direction. For negative rotation sense, we observe the inverted situation: The local maximum is positioned close to the $\langle 111\rangle$-direction whereas the local minimum resides in the middle of $\langle 110\rangle$- and $\langle 11\bar{1}\rangle$-directions.
In Fig. 5.13 b) - d), we show rotation scans at $B = 0.3\,\mathrm{T}$ and elevated temperatures. Again, continuous and dashed lines denote positive and negative rotation sense, respectively. Up to the highest investigated temperature of $T = 28.5\,\mathrm{K}$, the shape described by Eq. 5.1 is maintained for all curves. The minor irregularities observed

at $T = 0.3\,\mathrm{K}$ are no longer visible at temperatures of $5\,\mathrm{K}$ and above. Further, the hysteresis decreases drastically with increasing temperature. At $T = 5\,\mathrm{K}$, $M_\perp$ begins to change sign during rotation. At $T = 28.5\,\mathrm{K}$, the rotational hysteresis is small enough to be attributed to the magnet hysteresis (cf. Sec. C.3.3).
The measurements presented above exclusively address the conical phase of MnSi. In appendix D.1.2, we show rotation scans at a field magnitude of $B = 0.1\,\mathrm{T}$ which further involve the helical state. We make similar observations regarding rotational hysteresis at its temperature dependence as for $B = 0.3\,\mathrm{T}$. However, the curves strongly deviate from the shape described by Eq. 5.1. We attribute this in part to phase transitions between helical and conical state during rotation due to anisotropy of the critical field $H_{c1} \approx 0.1\,\mathrm{T}$. Similarly, transitions between conical state and skyrmion lattice phase may occur during rotation scans at a temperature of $T = 28.5\,\mathrm{K}$ and various field magnitudes. Corresponding magnetization curves are presented in appendix D.1.3. Consistent with the temperature dependent measurements at fixed field magnitudes, we find only little rotational hysteresis. For field magnitudes addressing solely the conical or skyrmion lattice phase, a behavior described by Eq. 5.1 is observed. At intermediate field magnitudes, magnetization curves exhibit distinct deviations from this shape. Measurements involving solely the helical state show a drastically different behavior.

5.4.2 Field scans

We performed field scans between $B_{\mathrm{max}} = \pm 1\,\mathrm{T}$ for field vectors applied along $\langle 001\rangle$-, $\langle 110\rangle$-, $\langle 111\rangle$-, and $\langle 11\bar{1}\rangle$-directions at temperatures from $T = 0.3\,\mathrm{K}$ up to $T = 33.3\,\mathrm{K}$. As stated in Sec. 5.2.2, we omitted the step of heating the sample above T_c prior to individual measurements. As a consequence, the shape of the initial magnetization curve depends on a not well controlled temperature and field history and is therefore not considered. Thus, we exclusively discuss magnetization curves corresponding to a high-field cooling scenario in distinction from a situation after zero-field cooling (cf. Ref. [Bau17]). As stated above, our measurement procedure for field scans features six sweeps through the regime of non-collinear phases of which we only present the last full scan for each direction. A full set of all six sweeps is shown in appendix D.2.1. In the following, we refer to field values changing towards more positive values as increasing field and field values changing towards more negative values as decreasing field independent of the sign. Thus, e.g., decreasing field at negative field values corresponds to an increasing field magnitude.
In Fig. 5.14, we present field scans at $T = 0.3\,\mathrm{K}$ along all major symmetry directions of the crystal. Black and red lines denote increasing and decreasing field, respectively. Signatures of critical fields H_{c1} and H_{c2} are labeled for each curve. The superscripts $\uparrow$ and $\downarrow$ correspond to increasing and decreasing field magnitude, respectively. Most saliently, we observe a large hysteresis between $B = \pm\mu_0 H_{c2}$ for all field directions. Further similarities are spike-like disturbances of the otherwise smooth curves. Such irregularities spiking towards both positive and negative values are positioned at zero field for all curves. This is an artifact of data evaluation since we divide the

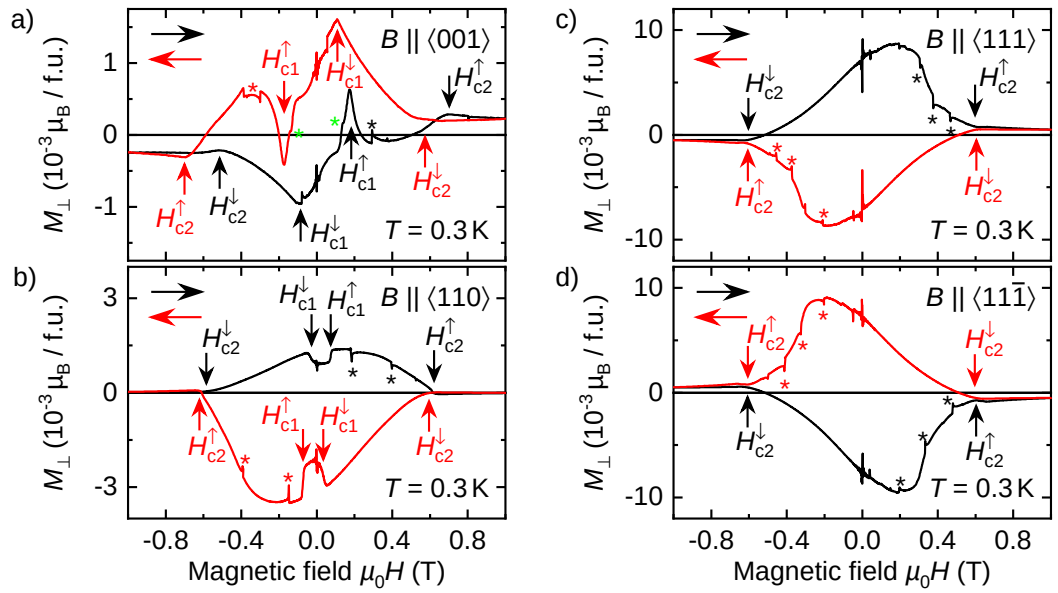

Figure 5.14: Anisotropic magnetization $M_\perp$ during field scans between $B = \pm 1\,\mathrm{T}$ at $T = 0.3\,\mathrm{K}$ and field vectors pointing along a) ⟨001⟩-, b) ⟨110⟩-, c) ⟨111⟩-, and d) ⟨11$\bar{1}$⟩-directions. Black lines denote increasing field, red lines denote decreasing field. The vertical arrows indicate positions of critical fields. Black and red asterisks mark spike-like irregularities of unknown origin. The green asterisks in panel a) highlight slight kinks which may represent a two-step transition at $H_{c1,<}^{\langle 001\rangle}$ and $H_{c1,>}^{\langle 001\rangle}$.

measured torque Γ by the applied field B to obtain the anisotropic magnetization $M_\perp$. Further disturbances at finite field are marked by the red and black asterisks in Fig. 5.14. They spike only towards zero magnetization and are found almost exclusively for increasing field magnitude. These disturbances are present already in the capacitance raw data.

The anisotropic magnetization for field along the ⟨001⟩-direction is depicted in Fig. 5.14 a). For increasing field, $M_\perp$ is nearly constant at a negative value between $B = -1\,\mathrm{T}$ and $-H_{c2}^{\downarrow}$ followed by a steady decrease to a sharp minimum at $-H_{c1}^{\downarrow}$. From there, $M_\perp$ increases through zero field until it reaches roughly the same value as at $-H_{c2}^{\downarrow}$. At this point, $M_\perp$ rapidly increases to a maximum at positive values at $+H_{c1}^{\uparrow}$. This increase exhibits a small kink as marked by the green asterisk. Above $+H_{c1}^{\uparrow}$, the magnetization quickly decreases back to negative values, passes a minimum and then slowly advances to positive values again. At $+H_{c2}^{\uparrow}$, a maximum is reached from which $M_\perp$ slightly decreases up to $B = +1\,\mathrm{T}$. The curve for decreasing field qualitatively matches the point mirror image of the described curve for increasing fields, but both curves appear to be slightly distorted towards positive values between $\pm H_{c2}$ which is best recognized by comparing the extrema at $\pm H_{c1}$. This asymmetry is more prominent in the torque data than in the magnetization and contrasts earlier torque measurements on MnSi which found little asymmetry of field scans along ⟨001⟩ [Bir09]. We attribute this to misalignment in the earlier experiments as we argue in appendix D.2.2. In our measurements, we further observe rather large hystereses at

both critical fields as illustrated by the significantly different field positions of $H_{c2}^{\uparrow}$ and $H_{c2}^{\downarrow}$ as well as $H_{c1}^{\uparrow}$ and $H_{c1}^{\downarrow}$ at both positive and negative field values. Moreover, we observe spike-like disturbances at decreasing field magnitude close to $H_{c1}^{\downarrow}$ as well as two discontinuous jumps (red asterisk). No such irregularities are present for fields applied along other directions.
In Fig. 5.14 b) we present the anisotropic magnetization for field along the $\langle 110 \rangle$-direction. For increasing field, $M_{\perp}$ is nearly constant at small positive values between $B = -1\,\mathrm{T}$ and $-H_{c2}^{\downarrow}$. From there, it slowly increases until a maximum followed by a rapid decrease is reached at $-H_{c1}^{\downarrow}$. Between $-H_{c1}^{\downarrow}$ and $+H_{c1}^{\uparrow}$, the magnetization is almost constant. After a rapid increase at $+H_{c1}^{\uparrow}$, the curve passes a broad maximum and then steadily decreases up to $+H_{c2}^{\uparrow}$, only just changing towards negative values. Up to $B = +1\,\mathrm{T}$, $M_{\perp}$ slightly increases at very small values. The anisotropic magnetization observed for decreasing field agrees qualitatively with the point mirror image of the described curve for increasing field, yet quantitatively the curves differ by a factor of $\sim$2.5. Hystereses at H_{c1} and H_{c2} are present, but small compared to the situation of field applied along the $\langle 001 \rangle$-direction.
The anisotropic magnetization for fields along $\langle 111 \rangle$- and $\langle 11\bar{1} \rangle$-directions is shown in Fig. 5.14 c) and d), respectively. Both situations are equal except for a reversal of the sign of $M_{\perp}$. We thus discuss the situation for field along $\langle 111 \rangle$ only. For increasing field, $M_{\perp}$ is negative and nearly constant between $B = -1\,\mathrm{T}$ and $-H_{c2}^{\downarrow}$. From there, the magnetization increases towards positive values and through zero field until a broad maximum is reached at $\sim$0.2 T. We find no signature of $-H_{c1}^{\downarrow}$ and it is uncertain whether the observed maximum corresponds to $+H_{c1}^{\uparrow}$. After the maximum, $M_{\perp}$ quickly decreases up to $+H_{c2}^{\uparrow}$ from where it further decreases slightly up to $B = +1\,\mathrm{T}$. The magnetization at decreasing field matches the point mirror image of the described curve for increasing field. Within the precision of our measurements, no hysteresis is found at H_{c2}. We note that for fields applied along the $\langle 111 \rangle$- or $\langle 11\bar{1} \rangle$-directions, absolute values of the anisotropic magnetization are substantially larger than for fields applied along the $\langle 110 \rangle$- or $\langle 001 \rangle$-directions. This is particularly intriguing given that $\langle 111 \rangle$ and $\langle 001 \rangle$ represent the easy and hard magnetic axes, respectively.
In Fig. 5.14 a), i.e. for field applied along the $\langle 001 \rangle$-direction, we observe hysteretic behavior also at fields $|B| > \mu_0 H_{c2}$. While it is not perceptible in Fig. 5.14 b) - d) due to scaling, such a hysteresis in the field-polarized state is found for all investigated field directions. Moreover, we observe equally hysteretic behavior in a second sample as well as in a different setup where the effect persists up to the highest field magnitudes studied, i.e. $B = \pm 14\,\mathrm{T}$. The respective magnetization curves are presented in appendix D.2.3.

Temperature evolution

We studied the evolution of the anisotropic magnetization during field scans with temperatures increasing from $T = 0.3\,\mathrm{K}$ up to $T = 33.3\,\mathrm{K}$. Selected magnetization curves are presented in Fig. 5.15. Top and bottom graphs correspond to field vectors

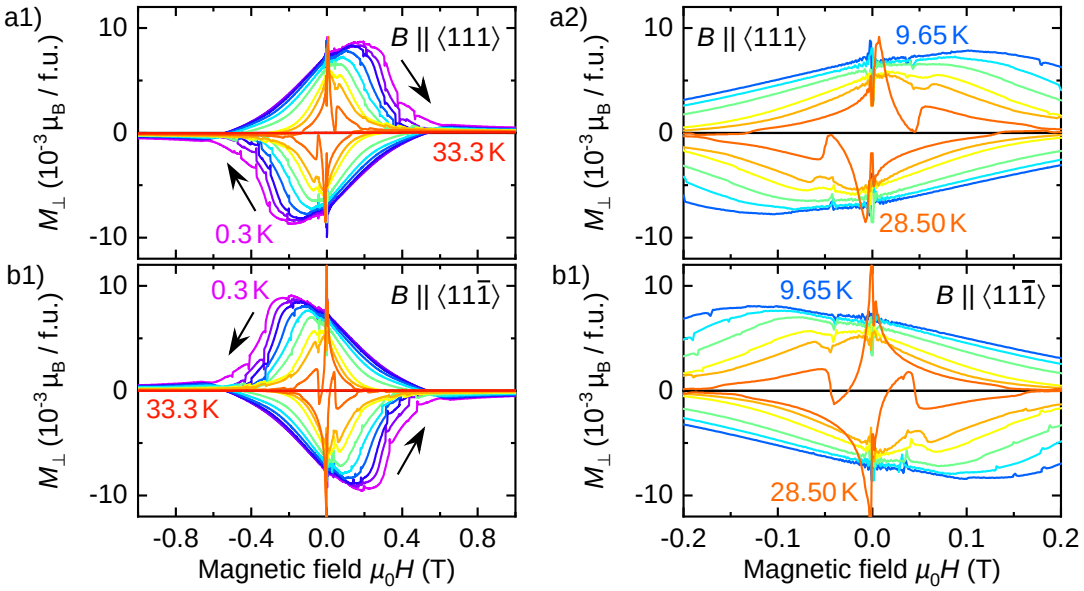

Figure 5.15: Temperature evolution of the anisotropic magnetization $M_\perp$ during field scans between $B = \pm 1\,\mathrm{T}$ and field vectors pointing along a1)-a2) ⟨111⟩- and b1)-b2) ⟨11$\bar{1}$⟩-directions. a1)-b1) Temperatures are set to $T = 0.3\,\mathrm{T}$, $T = 2\,\mathrm{K}$, $T = 5\,\mathrm{K}$, $T = 9.65\,\mathrm{K}$, $T = 14.2\,\mathrm{K}$, $T = 19.15\,\mathrm{K}$, $T = 23.75\,\mathrm{K}$, $T = 26\,\mathrm{K}$, $T = 28.5\,\mathrm{K}$, and $T = 33.3\,\mathrm{K}$. a2)-b2) Blow-ups of a1)-b1) to the low field regime and temperatures of $9.65\,\mathrm{K} \leq T \leq 28.5\,\mathrm{K}$.

applied along the ⟨111⟩- and ⟨11$\bar{1}$⟩-directions, respectively. From purple to red, the temperatures in the left hand side panels are set to $T = 0.3\,\mathrm{T}$, $T = 2\,\mathrm{K}$, $T = 5\,\mathrm{K}$, $T = 9.65\,\mathrm{K}$, $T = 14.2\,\mathrm{K}$, $T = 19.15\,\mathrm{K}$, $T = 23.75\,\mathrm{K}$, $T = 26\,\mathrm{K}$, $T = 28.5\,\mathrm{K}$, and $T = 33.3\,\mathrm{K}$. Panels on the right hand side show blow-ups to the low field regime and temperatures from $T = 9.65\,\mathrm{K}$ to $T = 28.5\,\mathrm{K}$. As discussed above, the magnetization curves obtained at $T = 0.3\,\mathrm{K}$ for field applied along ⟨111⟩ and ⟨11$\bar{1}$⟩ are equal up to a sign change of $M_\perp$. This observation essentially holds true at elevated temperatures. We thus describe magnetization curves for field along ⟨111⟩ only and point out minor differences where necessary. As further described for the low temperature curves, the decreasing field magnetization curve matches the increasing field curve's point mirror image. This observation is maintained for all studied temperatures.
Most evidently, the size of the hysteresis loop observed between $B = \pm\mu_0 H_{c2}$ decreases steadily with increasing temperature up to $T = 26\,\mathrm{K}$. During this evolution, the loop shrinks not only regarding $M_\perp$ but also along the field direction which reflects the well established reduction of H_{c2} with rising temperature (cf. Fig. 5.1 b)). In addition to the decreasing hysteresis, a new pair of extrema evolves close to zero field. While at temperatures up to $T = 19.15\,\mathrm{K}$, merely a flattening of the increasing magnetization curve is visible after passing through zero field, the increasing field curves at temperatures from $T = 23.75\,\mathrm{K}$ upwards exhibit a distinct maximum right after the applied field changes sign. This is followed by a minimum and another maximum which appears to correspond to the maximum already present at lower temperatures.

At $T = 28.5\,\mathrm{K}$, the new maximum after reversal of the field direction develops into a spike that surmounts the maxima of all other magnetization curves while apart from this narrow peak the magnetization is still lower when compared to that at lower temperatures. The following minimum is lowered such that the magnetization reaches zero. The transition from the minimum to the subsequent maximum is very rapid. From there, the magnetization slowly decays as observed at lower temperatures. For field applied along the $\langle 11\bar{1}\rangle$-direction, both spike-like maximum and the subsequent minimum are substantially more pronounced as compared to the situation with field applied along the $\langle 111\rangle$-direction. In order to discuss maxima and minima in agreement with the preceding description, we address the decreasing field curve for field along $\langle 11\bar{1}\rangle$ due to the sign reversal. Here, the magnetization begins to grow larger than that at lower temperatures already before the direction of the field is reversed. Further, $M_\perp$ changes sign back and forth whilst dropping to the following minimum and rising back up to the subsequent maximum.
In Fig. 5.15, we do not recognize signatures associated with the skyrmion lattice phase. This is owed to the scaling of the graphs. We observe signatures of the upper and lower transition fields $H_{\mathrm{a}1}$ and $H_{\mathrm{a}2}$ between conical state and skyrmion lattice phase during field scans along all major symmetry directions. Respective magnetization curves are presented in appendix D.2.4.
At $T = 33.3\,\mathrm{K}$, the anisotropic magnetization equals zero on the scale considered in Fig. 5.15. This reflects the absence of long-range magnetic order in the paramagnetic state at $T > T_{\mathrm{c}}$.
The evolution of the anisotropic magnetization during field scans at elevated temperatures for field vectors applied along the $\langle 001\rangle$- and $\langle 110\rangle$-directions is shown in appendix D.2.5. Similar to the evolution described above, new extrema evolve around zero field. In addition, the magnetization curves gradually change sign with increasing temperature and the prominent features are altered drastically.

5.4.3 Discussion

In this section, we appraise the presented results regarding magnetic anisotropy in the non-collinear phases of MnSi. We begin with general considerations on the origin of anisotropic magnetization in these states, discriminating between two contributions to $M_\perp$. On the one hand, the helical pitch vector $\hat{Q}$ or skyrmion lattice normal vector $\hat{N}$ of an ideal modulated spin structure is subject to an anisotropy potential. As addressed in Sec. 2.1.2, these potentials result from the total magnetic anisotropy energy of the full ensemble of magnetic moments. On the other hand, anharmonic deformations of helices or skyrmions arise due to the magnetic anisotropy energy of individual magnetic moments. Such distortions of the ideal structures may also contribute to $M_\perp$.
As stated before, the anisotropy potentials for $\hat{Q}$ and $\hat{N}$ in MnSi have been investigated using neutron scattering techniques [Bau17, Ada18]. However, it is non-trivial to infer the size of a contribution to $M_\perp$ even from a known anisotropy potential. For a pristine helix, the magnetic moments cancel each other so that no net magnetization

is observed on a macroscopic scale, i.e. $M_\perp$ is dominated by anharmonic effects in the helical state. In the conical phase, the anisotropy potential for the pitch vector depends strongly on the cone angle (cf. Sec. 2.1.2) which we do not know for a given field and temperature. For a skyrmion lattice, modeling $M_\perp$ requires extended calculations which are beyond the scope of this thesis.
Several neutron scattering studies have stated that anharmonic distortions constitute minor deviations from ideal spin structures which influence measurement results on the order of a few percent only (see Refs. [Bau17, Hal18] and refs. therein). In contrast, our experimental technique is highly sensitive to such deformations as we infer from the large signal during measurements in the helical state where the magnetization of an ideal helix vanishes. Again, modeling anharmonic effects and the resulting anisotropic magnetization requires theoretical efforts beyond the scope of the present work.
In addition to the intrinsic complexity of anisotropic magnetization and non-collinear magnetic order, we need to consider angular distortion. As discussed in Sec. 5.2, two effects are distinguished, namely the deviation of $\mathbf{M}$ from $\mathbf{B}$ and relative rotation of sample and field due to cantilever bending caused by the magnetic torque. The latter can in principle be estimated analogous to the procedure described for the field-polarized phase. Since we perform no further quantitative analysis in non-collinear phases, we omit such a correction estimate. For the former contribution, it is disputable whether the desired reference is still $\mathbf{M}$ or rather the direction of $\hat{Q}$ or $\hat{N}$. We can no longer calculate an angular correction via Eq. 5.6 since we do not know the magnitude m of the sample's magnetic moment. Our measurements yield no information on the direction of $\hat{N}$ or $\hat{Q}$. The question is therefore moot since none of both deviations can be estimated quantitatively. Still, we suggest large angles between $\mathbf{M}$ and $\mathbf{B}$ considering that we measure torque signals comparable to those observed in the field-polarized state while we expect a significantly smaller magnetization. In contrast, the deviation of $\hat{Q}$ or $\hat{N}$ from $\mathbf{B}$ is expected to be small [Bau17, Ada18].
As shown in Sec. 5.3.4, angular distortion results in slight shearing of torque curves recorded during rotation scans. The situation is more delicate for field scans. Here, torque-dependent bending of the cantilever during measurements causes a varying deviation of the magnetic field from the crystallographic direction under investigation. As we show in appendix D.2.2, deviations on the order of $\sim 1°$ can suffice to impose changes on the order of $\sim 100\,\%$ to the measured torque. Unfortunately, a quantitative estimate of these changes during our measurements is not feasible. Still, its potentially large influence must be kept in mind during interpretation.
On top of the issues discussed above, we note that the measured torque reflects only a projection of $M_\perp$ on the plane perpendicular to the cantilever's projection axis. Moreover, measurements in the field-polarized state using the AMI setup have shown significant disturbances of incomprehensible shape and origin. Given these circumstances, a sound understanding of the presented data is difficult at best. In particular, no quantitative analysis can be performed. We thus restrict ourselves to a qualitative discussion.

Rotation scans

For rotation scans involving only the skyrmion lattice phase, we observe magnetization curves of the shape described by Eq. 5.1. The same holds true for rotation scans addressing solely the conical state. This observation implies that, within these phases, the anisotropic magnetization is dominated by the anisotropy potential for the ordering vectors $\hat{N}$ and $\hat{Q}$ with only small contributions from anharmonicities. The minor irregularities encountered at $T = 0.3\,\mathrm{K}$ and $B = 300\,\mathrm{mT}$ may represent such corrections. As an alternative explanation, the irregularities may reflect the importance of higher order anisotropy terms at low temperatures similar to our discussion for the field-polarized state.
We observe no sign change of K_{eff} corresponding to a change of the cone angle (cf. Sec. 2.1.2). A tentative fitting procedure yields a value of $K_{\mathrm{eff}} \approx 370\,\mathrm{J/m^3}$ for the conical state at $T = 5\,\mathrm{K}$ and $B = 300\,\mathrm{mT}$. This is on the same order of magnitude as the anisotropy constants found for the field-polarized phase as well as the value $K_{\mathrm{eff}} = 545\,\mathrm{J/m^3}$ reported at $B \lesssim \mu_0 H_{\mathrm{c1}}$ and $T = 5\,\mathrm{K}$ [Bau17]. A direct comparison is not warranted since we do not know the cone angle α. Similarly, we obtain a value of $K_{\mathrm{eff}} \approx 48\,\mathrm{J/m^3}$ for the skyrmion lattice phase at $B = 200\,\mathrm{mT}$ and $T = 28.5\,\mathrm{K}$ which neither can be translated to a single-moment anisotropy constant K_1.
In contrast to conical and skyrmion lattice states, the behavior of magnetization curves differs distinctly from that described by Eq. 5.1 during measurements addressing the helical phase. As stated above, we expect the magnetization of an ideal helix to vanish and therefore $M_\perp$ to be dominated by anharmonic distortions in the helical state. This expectation is confirmed by the strong deviations from Eq. 5.1. Intriguingly, we observe rotational hysteresis independent of which contribution to $M_\perp$ dominates. Moreover, the absolute values of $M_\perp$ as well as its rotational hysteresis are of comparable size in both cases. The observed hysteresis implies that the magnetization vector "follows" the field vector with a certain lag during rotation. At this point, we can not offer any suggestion as to the origin of this lag or its decrease with rising temperature.
As stated above, our rotation scans at $B = 100\,\mathrm{mT}$ may include phase transitions between helical and conical state due to the anisotropy of H_{c1}. The influence of such transitions on the shape of the measured curves is unforeseeable and therefore inhibits an unambiguous interpretation. For a closer look at rotation scans in the helical phase, we refer to the measurement at $T = 28.5\,\mathrm{K}$ and $B = 50\,\mathrm{mT}$ illustrated in Fig. D.3 a). As described in appendix D.1.3, we observe a sawtooth-like behavior with an additional shoulder at $\langle 001 \rangle$ and a lack of the two-fold symmetry present in all other rotation scans. Further, the point symmetry with respect to $\langle 110 \rangle$-directions for magnetization curves recorded with opposing rotation senses is no longer maintained. We interpret this by means of the lower symmetry of the tetrahedral point group T as compared to cubic symmetry. In particular, the eight $\langle 111 \rangle$-directions which we treat as equivalent throughout this chapter are split into two groups of four equivalent directions. Strictly speaking, the [111]-direction is equivalent only to $[1\bar{1}\bar{1}]$, $[\bar{1}1\bar{1}]$ and $[\bar{1}\bar{1}1]$ whereas $[\bar{1}\bar{1}\bar{1}]$ is equivalent to $[\bar{1}11]$, $[1\bar{1}1]$ and $[11\bar{1}]$. This symmetry reduction is directly evident in Fig. D.3 a). Similarly, the difference between [001] and $[00\bar{1}]$

reflects the missing inversion symmetry of the crystal structure.
In contrast to measurements in the conical phase, the helical pitch vector does not follow the magnetic field vector in the helical state but remains pinned to a $\langle 111 \rangle$-direction. As reported in Ref. [Bau17], a field magnitude of $B = 50\,\mathrm{mT}$ applied along $\langle 111 \rangle$ is just enough to depopulate unfavorable domains. We suggest rather discontinuous switching between domains during field rotation at $B = 50\,\mathrm{mT}$ where (un-)favorable domains are (de-)populated at once. This is consistent with the sawtooth-like behavior as well as with the observation of a kink at $\langle 001 \rangle$-directions. At this point, the field vector encloses identical angles with two pairs of equivalent $\langle 111 \rangle$-directions which results in a double-transition [Bau17]. At the larger field of $B = 100\,\mathrm{mT}$, we expect continuous variations of domain populations during field rotations corresponding to the angle between field vector and equivalent $\langle 111 \rangle$-directions. Consequently, the respective magnetization curves exhibit a less sharp sawtooth-shape (cf. Fig. D.3 b)). Simultaneously, the two-fold symmetry consistent with cubic symmetry is restored. Consistent with our expectation, the sawtooth-shape sharpens and the kink at $\langle 001 \rangle$ is enhanced with lowering the temperature from $T = 28.5\,\mathrm{K}$ towards $T = 20\,\mathrm{K}$ (cf. Fig. D.2). On the contrary, the kink gradually disappears and the shape becomes smoother again with temperature decreasing further from $T = 20\,\mathrm{K}$ down to $T = 0.3\,\mathrm{K}$. At this point, we lack an explanation for such behavior.

Field scans

As illustrated in Fig. 5.14, the magnetization curves recorded during field scans at low temperatures exhibit signatures of almost all magnetic field-driven phase transitions in MnSi. For fields along all major symmetry directions, the second order transition from field-polarized to conical state is characterized by the onset of a larger slope and a larger hysteresis. The large anisotropic magnetization below H_{c2} is barely surprising given that non-collinear order enforces large deviations of individual magnetic moments from the field direction. This may explain the larger signal for field along $\langle 111 \rangle$-directions where individual moments are forced to point away from the easy axis whereas for field along $\langle 001 \rangle$, the moments are forced to point away from the hard axis. On the contrary, the large hysteresis is not expected. We address hysteretic behavior further below.
The transition between helical and conical state with changing field magnitude has been described in great detail in Ref. [Bau17]. Along the $\langle 111 \rangle$- and $\langle 11\bar{1} \rangle$-directions, we observe no signatures of H_{c1}. This is consistent with the predicted crossover transition for an anisotropy potential pinning $\hat{Q}$ along $\langle 111 \rangle$-directions below H_{c1}. Sharp features at H_{c1} may be observed for field along $\langle 111 \rangle$-directions when starting from a multi-domain state. As stated above, we do not address such a scenario in our experiments. For field vectors along $\langle 110 \rangle$- and $\langle 001 \rangle$-directions, the pitch vector reorients from the field direction towards the closest $\langle 111 \rangle$-directions at H_{c1}. For $\langle 110 \rangle$, the field encloses identical angles with a $\langle 111 \rangle$- and a $\langle 11\bar{1} \rangle$-direction and we observe changes of $M_{\perp}$ connected to a second order phase transition. For

$\langle 001 \rangle$, the field vector encloses identical angles with each a $\langle 111 \rangle$-, a $\langle \bar{1}11 \rangle$-, a $\langle 1\bar{1}1 \rangle$- and a $\langle \bar{1}\bar{1}1 \rangle$-direction which results in two subsequent second order transitions. For increasing field magnitude, we observe a hint of such a double transition. For both increasing and decreasing field, the low field side of the peak at $H_{c1}^{\uparrow}$ exhibits a slight kink as indicated by the green asterisks in Fig. 5.14. For decreasing field magnitude, no such kink is observed. Instead, the extremum at $H_{c1}^{\downarrow}$ is followed by a discontinuous irregularity for both increasing and decreasing field. Such perturbations are otherwise observed exclusively for increasing field magnitude. Their odd occurrence close to $H_{c1}^{\downarrow}$ may also hint at the specific quality of the transition.
Signatures of the first order transitions between conical and skyrmionic states are well visible in our field scans as illustrated in Fig. D.11. With the exception of decreasing field magnitude along $\langle 001 \rangle$, we observe distinct reductions of $M_{\perp}$ for all field and sweep directions. As stated in appendix D.2.4, this observation has already been reported in Ref. [Bir09] and was attributed to a reduced pinning of the skyrmionic spin structure to the crystal lattice as compared to the conical helix.
We can not explain the specific behavior of the anisotropic magnetization between $B = \pm\mu_0 H_{c2}$ even on a qualitative level. We specifically note that we do not observe any features explicitly indicating a sign change of the effective anisotropy constant K_{eff} as expected for a continuous transformation from the pristine helix to the field polarized limit (cf. Sec. 2.1.2). The main obstacle impeding qualitative interpretation is the reduced dimensionality of the measured torque. As described above, $M_{\perp}$ crucially depends on unknown parameters such as the precise deviation of $\hat{Q}$ from $\mathbf{B}$, the cone angle and the sum of anharmonic contributions of individual magnetic moments. In particular, $\mathbf{M}$ may point in an arbitrary direction so that even qualitative changes of our measured signal as, e.g., multiple sign changes in Fig. 5.14 a) may result from only small angular variations of a magnetization vector pointing mostly out of our experiment's field rotation plane. In order to gain further insights into the magnetization's behavior under non-collinear order, a technique capturing the full three-dimensional magnetization vector should be employed in future investigations.
Our inability of reconstructing the behavior of $\mathbf{M}$ under non-collinear magnetic order mostly prevents us from assessing its temperature dependence. The critical field H_{c2} continuously decreases with rising temperature consistent with the well-known phase diagram. For field along the $\langle 111 \rangle$- and $\langle 11\bar{1} \rangle$-directions, the magnetization in the conical phase also decreases with increasing temperature consistent with a decreasing ordered moment. In contrast, several features grow substantially for fields along $\langle 110 \rangle$ and $\langle 001 \rangle$. The origin of these increases as well as the gradual sign changes of magnetization curves remain unclear. The same holds true for the evolution of additional extrema between H_{c1} and zero field for field along $\langle 111 \rangle$ and $\langle 11\bar{1} \rangle$. While a connection to the transition between conical and helical phase may appear natural, it remains speculative at this point.
In our field scans, we detect a hysteresis of critical fields that depends strongly on the direction of the applied field and quickly fades with increasing temperature. A similar hysteresis has been reported at H_{c1} from SANS, magnetization and AC susceptibil-

ity measurements [Bau17]. The authors suggest that the observed hysteresis is a nonequilibrium effect due to large relaxation times caused by topologically protected disclinations. Such defects are expected to emerge, e.g., from topologically nontrivial domain walls [Li12]. Magnetic force microscopy (MFM) measurements on the cubic helimagnet FeGe have shown that relaxation times related to such defects can be on the order of hundreds to thousands of seconds [Dus16]. As described above, we observe large hysteresis of H_{c1} and H_{c2} for field along the $\langle 001 \rangle$-direction where four helical domains with pitch vectors $\hat{Q}$ along different $\langle 111 \rangle$-directions are degenerate with respect to the Zeeman energy. Smaller hystereses of H_{c2} and H_{c1} are found for field along the $\langle 110 \rangle$-direction where only two such domains are energetically favorable. For field along the $\langle 111 \rangle$-directions where a single domain is expected, we observe no notable hysteresis of the critical fields. The indicated correlation between critical field hysteresis and number of degenerate domains is only an ambiguous hint towards a connection between our observation and topological defects.

Beside the hysteresis of critical fields, $M_\perp$ exhibits a large hysteresis between $B = \pm\mu_0 H_{c2}$ and a comparatively small hysteresis for $|B| > \mu_0 H_{c2}$. These hystereses are observed similarly for fields applied along all major symmetry directions despite distinct differences in the behavior of $M_\perp$ beside that. While the hysteresis above H_{c2} gradually decays with increasing temperature and vanishes well below T_c, the hysteresis below H_{c2} persists up to the critical temperature. This different temperature dependence hints at different mechanism at the origin of the respective hysteresis. In particular, the hysteresis above H_{c2} decays similarly fast with temperature as the leading order anisotropy constants K_1 extracted from rotation scans at $\mu_0 H_{c2} < B \leq 1\,\mathrm{T}$. While this may seem suggestive, we are not aware of a mechanism intrinsic to magnetocrystalline anisotropy that leads to a field hysteresis of the magnetization.

For field along $\langle 001 \rangle$, similar hysteretic behavior has already been reported but remains unexplained [Bir09]. For a defect-free magnetic system in equilibrium, no such hysteresis is expected. It is therefore natural to suggest the topological defects discussed above as a possible origin. However, as stated before, such defects are expected to emerge from domain walls. For field scans along $\langle 111 \rangle$-directions, no formation of domains is expected. Still, we observe large hysteresis up to highest fields in this situation. This implies that, if topological defects are in fact at the heart of our observations, they must be stable over periods on the order of $10^4\,\mathrm{s}$ and in magnetic fields up to $B = 14\,\mathrm{T}$. To the best of our knowledge, neither experimental nor theoretical groundwork exists regarding an estimate of the contribution of topological defects to the anisotropic magnetization. Similar to undisturbed spin structures of non-collinear order in MnSi, modeling such a contribution requires theoretical efforts that are beyond the scope of the present thesis. We reinforce the statement made in Ref. [Bau17] that topological defects and their properties deserve further investigation.

Finally, we address the spike-like disturbances observed during field scans. It is notable that the spikes are always directed towards zero in distinction from the magnet-induced irregularities discussed in appendix C.3.2. Further, these pertur-

bations occur exclusively for increasing field magnitudes with the exception of $H_{c1}^{\downarrow}$ for field along $\langle 001 \rangle$ addressed above. Even more remarkably, spikes are in many cases observed at nearly identical field magnitudes for field scans along identical field directions but at different temperatures. This systematic behavior might indicate a origin related to the magnetic properties of the sample. In the light of the above discussion on defects and relaxation times, one may speculate whether the observed perturbations are signatures of relaxation processes. In particular, MFM measurements on FeGe have shown that magnetic edge dislocations can move through the material [Dus16]. Similar dynamical processes could lead to spike-like signatures in the torque as observed. However, further investigations are needed to rule out technical issues as an origin of these perturbations.

5.5 Conclusion

In the previous sections, we have presented our work on the magnetic anisotropy of MnSi. In this section, we give a short summary and provide a detailed outlook on potential further studies. We begin with our investigations of the field-polarized state followed by studies of modulated phases. Finally, we address possible technical improvements.

Concerning the field-polarized state, we show experimental results obtained from three samples in two setups and employ a bespoke fitting routine for extraction of anisotropy constants. We investigate the evolution of these constants with field magnitude and temperature and perform numerical calculations capturing the full complexity of the experiments in order to assess the reliability of our results. For the leading-order anisotropy constant K_1, we obtain stable results for various samples, setups and experimental uncertainties. The values exhibit a non-monotonic behavior with both temperature and field magnitude. A sign change in the temperature evolution demonstrates that extrapolation towards the phase diagram region of modulated states is not warranted. Similar to K_1, the next-to-leading-order anisotropy constant K_2 shows a non-monotonic dependence on field magnitude and on temperature for large fields. It appears likely that a sign change from positive no negative values with increasing temperature will be observed at higher field magnitudes. In contrast to K_1, values of K_2 exhibit significant fluctuations regarding setup, experimental uncertainties and data evaluation procedures. We further investigate the influence of cubic shape anisotropy. Within the precision of our measurements, we do not observe severe differences to a spherical shape. However, we observe a two-fold sine-shaped perturbation which, according to preliminary measurements on a cuboid of CSO, may arise due to shape anisotropy.

Several shortcomings of our studies may be addressed in further investigations. For instance, we discuss the temperature evolution of K_1 in terms of a fit function that does not represent a physical origin of the observed behavior. Theoretical efforts providing a comprehensive explanation for the non-monotonic evolution are desirable. Likewise, the behavior of K_1 with increasing field magnitude may be understood with the aid of sophisticated calculations considering subtle shifts of the multi-sheet

Fermi surface. In this respect, we have fulfilled our aim of providing benchmark data for an appropriate theoretical description of the electronic structure in MnSi. On the experimental side, further studies may address higher-order anisotropy constants. The importance of higher-order terms especially towards low temperatures and low field magnitudes has been indicated in our measurements. Calculations suggest that in the high-field limit the torque corresponding to K_1 vanishes when rotating around a $\langle 111 \rangle$-direction. While numerical simulations insinuate that the respective torque contribution remains finite due to deviations from the assumed high-field limit, such an experiment is still a promising opportunity to investigate K_2 with a better precision and reliability. Aside from that, our simulation suggests that measurements at a well-defined misalignment of rotation axis and a given high-symmetry direction may yield information on the chirality of the crystal. As a further step, the temperature evolution of anisotropy constants may be studied at larger field magnitudes. Finally, further investigations regarding shape anisotropy may be conducted by measuring cuboids and platelets. A profound knowledge of the influence of shape anisotropy may substantially alleviate future experiments.

We now turn to our measurements targeting non-collinear magnetic order in MnSi. We present experimental results of rotation scans and field scans. Rotation scans at various fields and temperatures demonstrate the dominance of different contributions to the anisotropic magnetization in different phases. Regardless of the dominant mechanism, we observe large rotational hysteresis below T_c. In principle, rotation scans addressing only the conical or the skyrmionic phase allow us to extract effective anisotropy constants. Without precise microscopic knowledge of the underlying spin structure, these values can not be related to single-moment anisotropy constants. Rotation scans addressing solely the helical phase reflect the reduced symmetry of the crystal structure as compared to the cubic symmetry of the Bravais lattice. Our field scans exhibit distinct signatures of all field-driven magnetic phase transitions in MnSi. We observe an asymmetry for opposing sweep directions and a hysteresis of critical fields both strongly depending on the field direction. Further, we find large hysteresis within modulated states as well as in the field-polarized state independent of the field direction and spike-like irregularities exhibiting systematic behavior. These observations hint at, but constitute no explicit evidence of the existence of topological defects stable over long time periods and at high magnetic fields. The specific behavior of the anisotropic magnetization in modulated states is subject to drastic alterations with increasing temperature.

Again, future investigations may improve experiments and their interpretation in various ways. Understanding our data addressing non-collinear magnetic order is fairly delicate mostly due to the limitations of the experimental technique. While it is possible to reconfigure the AMI setup such that magnetization components pointing out of the rotation plane are detected, we rather suggest utilization of a technique capturing the three-dimensional magnetization vector at once as proposed, e.g., in Refs. [Duf00, Ben06]. Further experimental tasks are investigations of the initial response of a spin helix to a small magnetic field in terms of anharmonic effects, the reorientation of the pitch vector under reversal of the rotation sense or tempera-

ture scans through the modulated phases. The latter has already been reported in Ref. [Bir09], but, as stated in appendix D.2.2, the respective experiments may also be improved. In addition to experimental efforts, theoretical studies are required in order to facilitate an understanding of torque measurements on non-collinear spin structures. Models of anharmonic perturbations as well as helical domain populations could allow for numerical simulations of the corresponding anisotropic magnetization. Finally, theoretical considerations on the emergence, magnetic signatures and stability of topological defects are desired.

We conclude that our experimental and theoretical approaches are appropriate for investigations of collinear magnetic systems. For comprehensive studies of non-collinear magnetic order, several theoretical and experimental improvements are required. A thorough investigation of magnetic anisotropy in MnSi paves the way for extensive studies on related compounds such as, e.g., CSO, FeGe or $Fe_xCo_{1-x}Si$. In the light of these future endeavors, we address some technical issues limiting our experiments that must be minded during or resolved prior to subsequent measurements.

We begin with the AMI setup. Here, the temperature is monitored and controlled on the probe more than 10 cm above the sample position. While this was not a problem for our experiments and procedures, monitoring the temperature directly on the sample stage is crucial for potential future measurements such as temperature scans through various magnetic phases, but also for temperature control utilized to create well-defined starting conditions for measurements. In addition, our measurements reveal the presence of substantial field gradients in the setup. A precise measurement of these gradients similar to our Hall probe investigation might facilitate future data evaluation. Finally, the analysis of AMI data indicates an additional perturbation of unknown shape and origin. A thorough investigation of the setup is required to identify and eliminate the source of this disturbance.

We now turn to the PPMS setup. Here, the torque data obtained from rotation scans on various samples featured a small perturbation at high frequencies. A similar observation during measurements on a different material points at a source related to the setup. Resolving this issue may allow for higher precision measurements. A particularly bad signal-to-noise ratio was observed during field scans in the PPMS setup. Due to the opaque software used for measuring, it is unclear whether the large noise is intrinsic to the cantilever or emerges from adverse operation or electronic configuration. This may be figured out by directly monitoring the cantilevers response. Finally, it is advisable to mind the shift observed between high- and low-temperature data as described in Sec. C.2.1. While the origin remains unexplained, we point out that such a shift may impose a quantitative error of $\sim$15 %.

A common issue of both setups is the problem of angular distortion. In particular, the unwanted rotation of the sample during measurements in the PPMS setup can have substantial influence on experimental results. This might be overcome by implementation of a feedback loop keeping the sample orientation constant independent of the exerted torque. As an alternative, one may measure the spring constants of the cantilevers used in experiment. If none of both solutions is applicable, the spring constants may be estimated, e.g., by means of finite element simulations.

Despite all issues described in the foregoing paragraphs, our data represents the first comprehensive set of anisotropy constants reported for the field-polarized state of MnSi. We regard this as a starting point for sophisticated quantitative investigations on the subtle role of magnetic anisotropy for a variety of phenomena in the context of cubic chiral helimagnets.

6 Summary and outlook

In this work, we investigated the anisotropic magnetization of two metallic compounds hosting correlated electron systems. Specifically, we studied the Fermi surface of the weak itinerant antiferromagnet CrB_2 by means of the dHvA effect and magnetocrystalline anisotropies in the archetypal helimagnet MnSi. We employed cantilever magnetometry in various modes and setups optimized for our specific measurement. In the following, we summarize the main results for each studied material.

6.1 CrB_2

Experiments on CrB_2 relied on longitudinal operation of CuBe cantilevers. We conducted measurements in three experimental setups. A dilution refrigerator combined with an axial superconducting magnet allowed for temperatures down to $\sim$60 mK in magnetic fields up to 14 T. Further, ^{3}He inserts providing temperatures down to $\sim$0.3 K were used in combination with a superconducting 15 T axial magnet and a resistive 35 T Bitter magnet.
Our measurements focused on a rather narrow angular range of 60° with field directions residing exclusively in the basal plane. We were able to identify 11 reliable dHvA frequencies and determined the effective masses of 8 corresponding orbits. The dHvA spectrum was complemented by an abundance of vague, but possibly real components.
We further performed DFT calculations of the electronic structure in CrB_2 taking into account the experimentally observed values for the spin spiral propagation vector and the size of the ordered moment. We found five bands to cross the Fermi energy yielding five FS sheets and ultimately resulting in a manifold of observable dHvA frequencies. Additionally, the expected signal strengths of frequency component were estimated from our calculations.
Although several well matching candidates are found, the variety of options inhibits an unambiguous allocation of experimentally observed frequencies to specific orbits on calculated FS sheets. Despite its richness, the spectrum deduced from calculations does not provide possible orbits for all experimentally observed frequencies. Moreover, we find strong discrepancies regarding the signal strength of experimental and theoretical orbits. While we did not observe the calculated frequency branches yielding the largest signal strength estimate, we obtained well-matching candidates for frequency components with a low signal strength estimate. Finally, the role of magnetic breakdown as well as an apparent mass enhancement of orbits on Cr-*d*-like bands raise questions that cannot be resolved within this work.

The presented results constitute a considerable advance of the experimental and theoretical state of the art regarding the determination of the CrB_2 Fermi surface. Yet there is plenty of room for further improvements. Our studies suggest that, compared to previous work, the observation of additional dHvA components was enabled by larger field magnitudes rather than by lower temperatures. Still, a combination of fields above 15 T with temperatures below 100 mK may allow for observation of further dHvA components. Moreover, the studied angular range should be extended and dHvA components should be tracked along symmetry planes orthogonal to the basal plane. The theoretical approach must be adjusted to include spin-orbit interactions and, for direct comparison, electronic structure calculations for the case of a triple-k spin arrangement should be carried out. A combination of the proposed experimental and theoretical enhancements may provide a conclusive picture of the real FS in CrB_2 which will constitute a milestone on the road to a comprehensive understanding of weak itinerant antiferromagnetism.

6.2 MnSi

For the investigation of MCAs in MnSi, we pursued two different experimental approaches. First, longitudinal CuBe cantilevers and ^{3}He-inserts allowing for temperatures down to 0.3 K were combined with a 2D vector magnet providing fields up to 4.5 T in all directions. A thorough Hall probe investigation was performed to map out the field centre and to obtain an estimate of field gradients present in the setup. Second, torsional silicon cantilevers incorporated in a commercially available setup were employed at temperatures down to 2 K and fields up to 14 T. Several issues regarding calibration, gravity and other spurious influences were resolved. We further established a method for high-precision alignment of single crystals with spherical shape on the cantilever sensors.
Rotation scans in the field-polarized state allowed us to extract anisotropy constants in leading and next-to-leading order. Regarding their evolution with field and temperature, we encountered surprising non-monotonic behavior even involving a sign change of K_1 at high temperatures and low field magnitudes. In order to assess our experimental results, we incorporated misalignment, field gradients and the unknown chirality of our samples in numerical simulations. Moreover, we estimated the influence of angular distortion. While K_1 is fairly robust against perturbations, K_2 exhibits large variations with respect to experimental uncertainties and data evaluation. Within the precision of our measurements, a cubic shape anisotropy showed no noticeable effect.
Our experiments confirm that torque magnetometry is a powerful tool for studies of magnetocrystalline anisotropy in collinear spin systems. The reported results constitute the first direct measurements of anisotropy constants in bulk MnSi. While a direct comparison is not possible, the values are on the same order of magnitude as those reported from indirect measurements. Still, we encounter a number of issues that may be resolved in future studies. For instance, chirality and next-to-leading or higher order anisotropy constants may be studied more precisely by measuring

the torque during rotations in a different symmetry plane. The shape anisotropy may be investigated by measuring cuboids and platelets. Further, the behavior at elevated temperatures may be studied at larger field magnitudes. A comprehensive understanding of the field and temperature evolution of anisotropy constants requires theoretical efforts involving a consideration of subtle changes of the multi-sheet Fermi surface.

Experiments in the non-collinear magnetic phases of MnSi comprised rotation and field scans. In both types of measurements we observed large hysteresis which hints at the presence of long-living topologial defects in the material. From rotation scans, we inferred that the anisotropic magnetization is dominated by an effective anisotropy potential for the helical pitch or lattice normal vector in the conical and skyrmionic phases, while in the helical state $M_{\perp}$ is dominated by anharmonic effects and, close to H_{c1}, domain population effects. Moreover, rotation scans addressing purely the helical phase reflected the low symmetry of the crystal structure. In field scans, we observed signatures of all field-driven magnetic phase transitions in MnSi. An asymmetry between opposing sweep directions is observed which's origin remains unresolved. The same holds true for remarkable alterations of the behavior at elevated temperatures.

In contrast to the field-polarized phase, interpreting measurements in the modulated phases is a more challenging task. In particular, huge theoretical efforts are necessary to enable quantitative analysis of our data. We conclude that torque magnetometry exhibits a rather limited capability for tackling the anisotropic magnetization in non-collinear spin systems. Still, the information gained from torque measurements may complement data obtained with other techniques in order to facilitate a full comprehensive picture.

Aside from the improvements suggested above, several technical issues may be resolved in future studies, a most urgent problem being angular distortion which occurs in both employed setups. Several possibilities to fix this issue have been proposed. Given the good results as well as the prospects pointed at, the work presented in this thesis may serve well as a groundwork for the thorough investigation of the subtle role of magnetocrystalline anisotropies in the material class of helimagnets.

A Magnets, cantilevers and alignment

This chapter is dedicated to additional information concerning the methodology throughout our work. In Sec. A.1 we give the equations employed for the calculation of longitudinal bending of a cantilever as well as the reduction factor for electrostatic calibration. The beam width uncertainty of wet-etched CuBe cantilevers is discussed in Sec. A.2. The generic calibration of the CuBe cantilevers utilized in the high field magnet laboratory in Nijmegen is presented in Sec. A.3. We show further results of the Hall probe investigation of the deployed vector magnet in Sec. A.4. Finally, we present x-ray scattering patterns obtained in the Laue camera during the alignment of spherical samples in Sec. A.5.

A.1 Calculation of cantilever bending lines and the reduction factor β

In Sec. 3.1.1, we present numeric values of the reduction factor *beta* for electrostatic calibration of longitudinal CuBe cantilevers. In Sec. 3.3.3, we estimate the maximum misalignment angle γ_r of a torsional silicon cantilever by calculating its longitudinal bending line. Both calculations were done following a mathematical framework adapting elasticity theory in order to address micromechanical cantilevers. Here, we briefly review the equations used for the purposes mentioned above. The full deduction can be found in [Wil04].
The position dependent deflection $D(x')$ of a uniform beam due to a bending moment $M(x')$ is given by

$$\frac{\partial^2 D(x')}{\partial x'^2} = \frac{-M(x')}{EI} \tag{A.1}$$

for small deviations. Here, E is the Young's modulus of the material and I is the areal moment of inertia. We consider a principal cantilever shape with rectangular paddle and beams as depicted in Fig. 3.3 a). We denote width and length of the beams by w and l, width and length of the paddle by W and L and the cantilever thickness by t. The areal moment of inertia is then given by $I_b = w \cdot t^3/12$ for a beam and $I_p = W \cdot t^3/12$ for the paddle. The two beams can be treated as one beam with width $2w$.
In order to determine the reduction factor β, we need to consider different bending of the lever due to a force and due to a torque. In [Wil04], an additional differentiation is made between a torque or force acting on a single point at the centre of the paddle

and the same torque or force acting distributed over the whole paddle area. Here, we restrict ourselves to the case of torques and forces acting on the paddle centre since this best resembles our experimental situation. To obtain the bending lines, Eq. A.1 must be integrated twice. Thereby we must differentiate between the beams and the parts of the paddle closer and farther away from the fixed end than the paddle centre, i.e.

$$D(x) = \begin{cases} D_1(x) \ , & 0 \leq x \leq L/2 \\ D_2(x) \ , & L/2 \leq x \leq L \\ D_3(x) \ , & L \leq x \leq \mathcal{L} \end{cases} \tag{A.2}$$

where x is zero at the *free* end of the cantilever and $\mathcal{L} = L + l$ is the total length of the cantilever. For a force F acting only on the centre of the paddle we obtain

$$D_1(x) = \frac{F}{EI_b}\left[\frac{x^3}{6} - \frac{Lx^2}{4} - \frac{\mathcal{L}lx}{2} + \frac{\mathcal{L}^3}{3} - \frac{L\mathcal{L}^2}{4}\right], \tag{A.3}$$

$$D_2(x) = \frac{F}{2EI_p}\left[\frac{x^3}{3} - \frac{Lx^2}{2} + \frac{L^3}{6}\right] + \frac{F}{2EI_b}\left[-l\mathcal{L}x + \frac{2\mathcal{L}^3}{3} - \frac{L\mathcal{L}^2}{2} - \frac{L^3}{6}\right], \tag{A.4}$$

$$D_3(x) = \frac{F}{2EI_p}\left[-\frac{L^2x}{4} + \frac{5L^3}{24}\right] + \frac{F}{2EI_b}\left[-l\mathcal{L}x + \frac{2\mathcal{L}^3}{3} - \frac{L\mathcal{L}^2}{2} - \frac{L^3}{6}\right]. \tag{A.5}$$

These equations have been used for the estimation of the angle γ_r in Sec. 3.3.3. From the bending lines, an expression for the mean deflection can be derived. Comparing the mean deviation resulting from a point force F and a point torque $\tau = F(l + L/2)$ yields the expression for the reduction factor:

$$\beta_\mathrm{p} = \frac{17I_bL^3 + 32I_pl(4\mathcal{L}^2 - 2L\mathcal{L} + L^2)}{8(L/2 + l)(24I_pl\mathcal{L} + 7I_bL^2)}. \tag{A.6}$$

In the case of distributed torque and force, β is given by

$$\beta_\mathrm{d} = \frac{2(3I_bL^3 + 5I_pl(4\mathcal{L}^2 - 2L\mathcal{L} + L^2))}{15(L/2 + l)(4I_pl\mathcal{L} + I_bL^2)}. \tag{A.7}$$

For the cantilever dimensions employed in the present work, the maximum difference between β_p and β_d is less than 2.5 %.

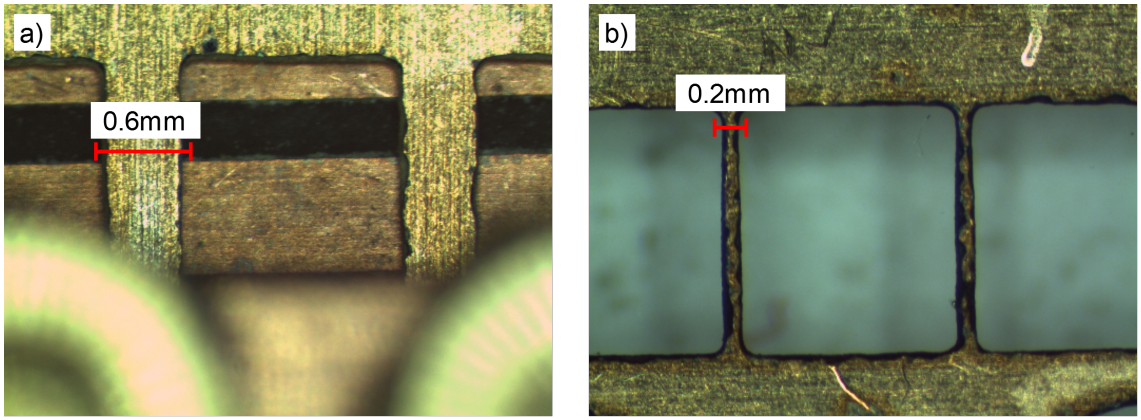

Figure A.1: Microscope images showing the beams of CuBe cantilevers prepared at TUM via wet chemical etching. The displayed scales denote the targeted beam widths.

A.2 Beam widths of CuBe cantilevers prepared by wet chemical etching

As mentioned in Sec. 3.1.1, the CuBe cantilevers employed in our experiments at TUM were fabricated from a foil by wet chemical etching. This process allowed poor control of the beam width d as shown in Fig. A.1. The microscope images depict beams of cantilevers that have been used for anisotropy measurements. The cantilever shown in a) has a targeted beam width of 600 µm, for the sensor in b) d was set to 200 μm. In both images we notice distinctly smaller widths of the finished beams. According to calculations, the reduced beam widths change the reduction factor β for electrostatic calibration by less than 1.5 % in both cases.

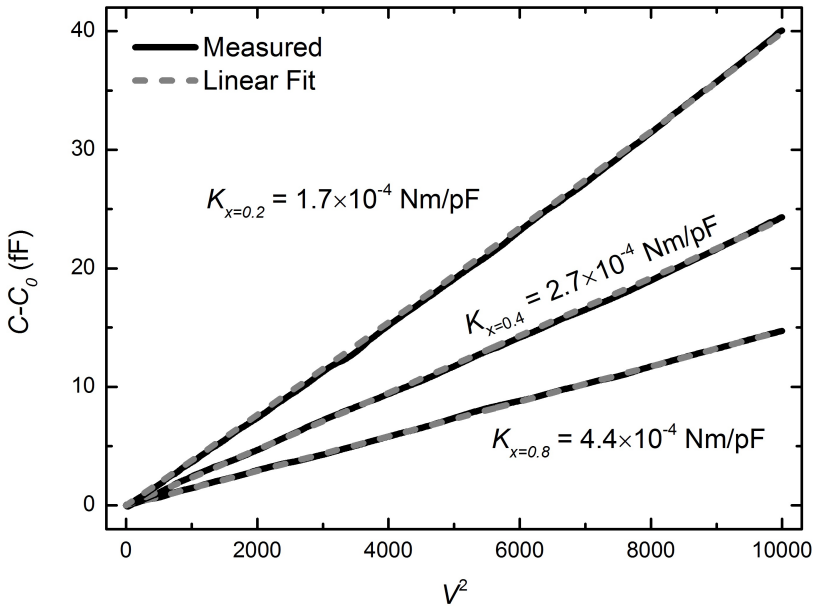

Figure A.2: Generic calibration for the cantilevers used at HFML. Change in capacitance is plotted versus the square of the voltage applied to the plates. The x in the index of the calibration constants K corresponds to the beam width d as defined in Fig. 3.3.

A.3 Generic calibration of cantilevers at HFML

Due to time constraints, no electrostatic calibration was performed during our measurements at HFML. Fortunately, the absolute torque values are not important for the interpretation of our experiments. Nevertheless, there is a generic calibration for the HFML type of cantilever as shown in Fig. A.2. Following Eq. 3.10, the deviation of capacitance C from its zero-voltage value C_0 is plotted versus the square of the applied voltage V. Black solid lines represent measured data, linear fits are depicted as gray dashed lines. The calibration constants calculated from the fit results are given in the figure. Here, x denotes the beam width of the respective cantilever. As stated in the main text, the given values were not used for data evaluation.

A.4 Hall probe measurements within the AMI vector magnet

During the Hall probe measurements described in Sec. 3.3.1, we performed rotations and sweeps of the magnetic field as during our measurements. The results are described in this chapter. None of the issues discussed in the following sections was reflected to a notable level in our measurements.

A.4.1 Rotations

Hall resistances recorded during field rotations are shown in Fig. A.3. Graphs on the left show data where the sensor for horizontal field was placed in the split coil field centre, graphs on the right show data where the vertical field sensor was centered in the solenoid field. Note that vertical and horizontal field centres are not at the same position. The magnetic field magnitude was set to 0.5 T, 1 T and 4.5 T in the top, middle and bottom graphs, respectively. Alike our sample measurements, we ramped the field up to the desired value, then rotated the field consecutively 720° in positive sense, 720° in negative sense and 720° in positive sense again.
All recorded curves resemble the expected sine with a 90° phase shift between y- and z-coil. The amplitudes scale linearly with the field magnitude. Amplitudes are slightly decreased for sensors not located in the field centre. At $B = 0.5\,\mathrm{T}$ we observe an angular offset of ∼7° on the y-coil, i.e. for horizontal field, between positive and negative rotation sense. No such offset is visible at higher fields in Fig. A.3, yet at 1 T an offset of ∼3° is still present. However, an effect of this offset could not be recognized in our measurements. At 4.5 T slight irregularities on both coils are vaguely visible around 0° and 180°. We review these deviations closer in the following figures.
Figures A.4 and A.5 show several blow-ups of Fig. A.3 e) and f), respectively. Graphs in a) cover the full range depicted in Fig. A.3, graphs b) to e) focus on smaller segments as marked in a). All blow-ups illustrate deviations of the recorded Hall resistances from the ideal sine shape in the region where the solenoid field is close to zero and the split coil field is close to an extremum. The Hall sensor probing the split coil field is depicted in Figs. A.4 b)-c) and A.5 b)-c). When centred in the split coil, it displays a small hysteretic drop of the Hall resistance near the extremum. The drop corresponds to a field drop of ∼100 mT over an angular range of ∼10°. When the sensor is not located in the field centre, we merely observe a drop in the shape of two sharp peaks at the edges of the hysteretic region. The Hall sensor probing vertical field is depicted in Figs. A.4 d)-e) (not field-centred) and A.5 d)-e) (field-centred). In both cases it exhibits a small hysteresis near zero field. Both angular range and the field gap of ∼100 mT match the hysteretic drop of the split coil.
While the discussed observations imply a substantial deviation of the magnet system from its ideal behavior, we find no signatures in our measured signal that could be attributed to these deviations. We thus ignore the disturbances and assume ideal magnet behavior in our data analysis.

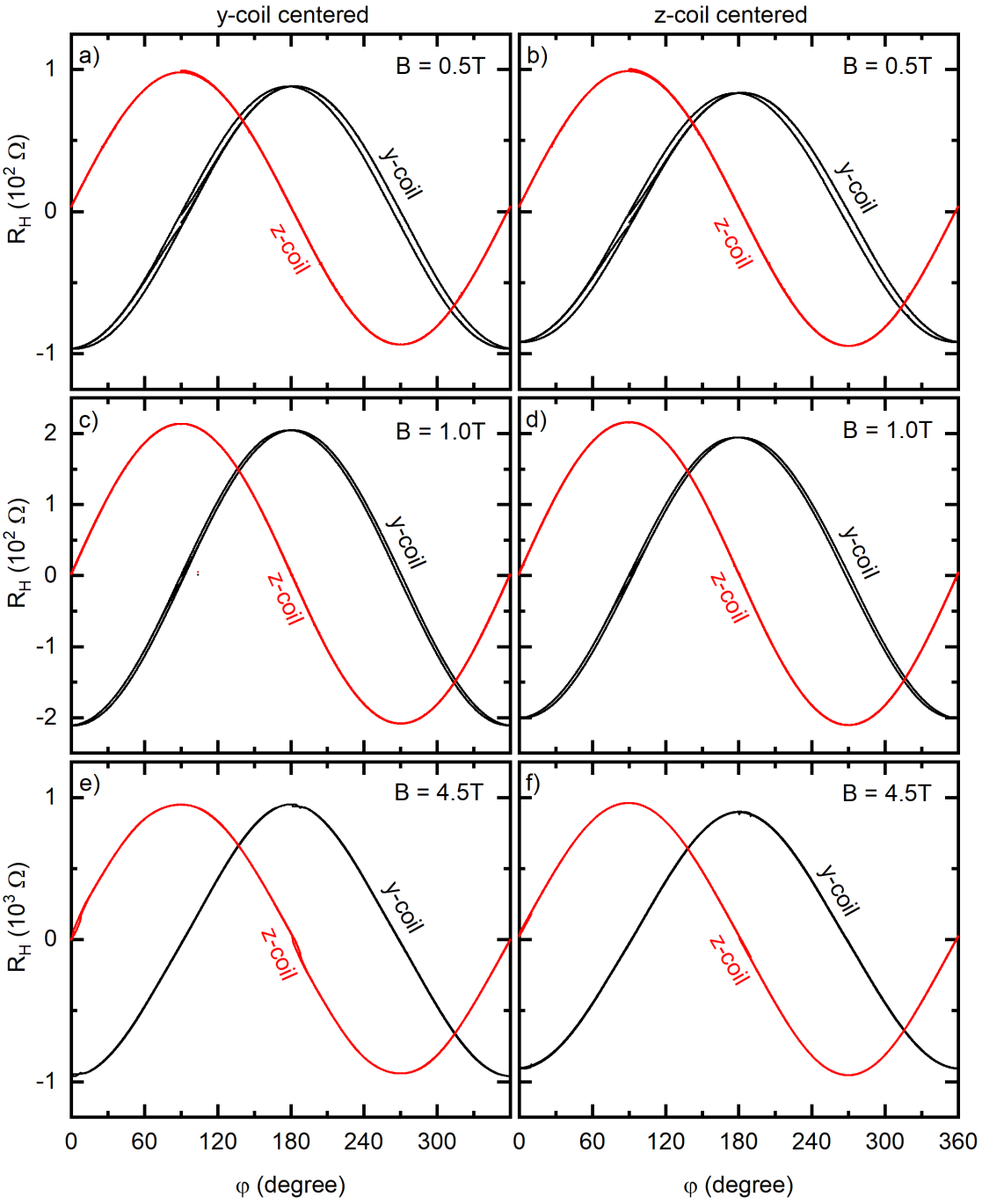

Figure A.3: Hall resistance measured during field rotations at various fields.

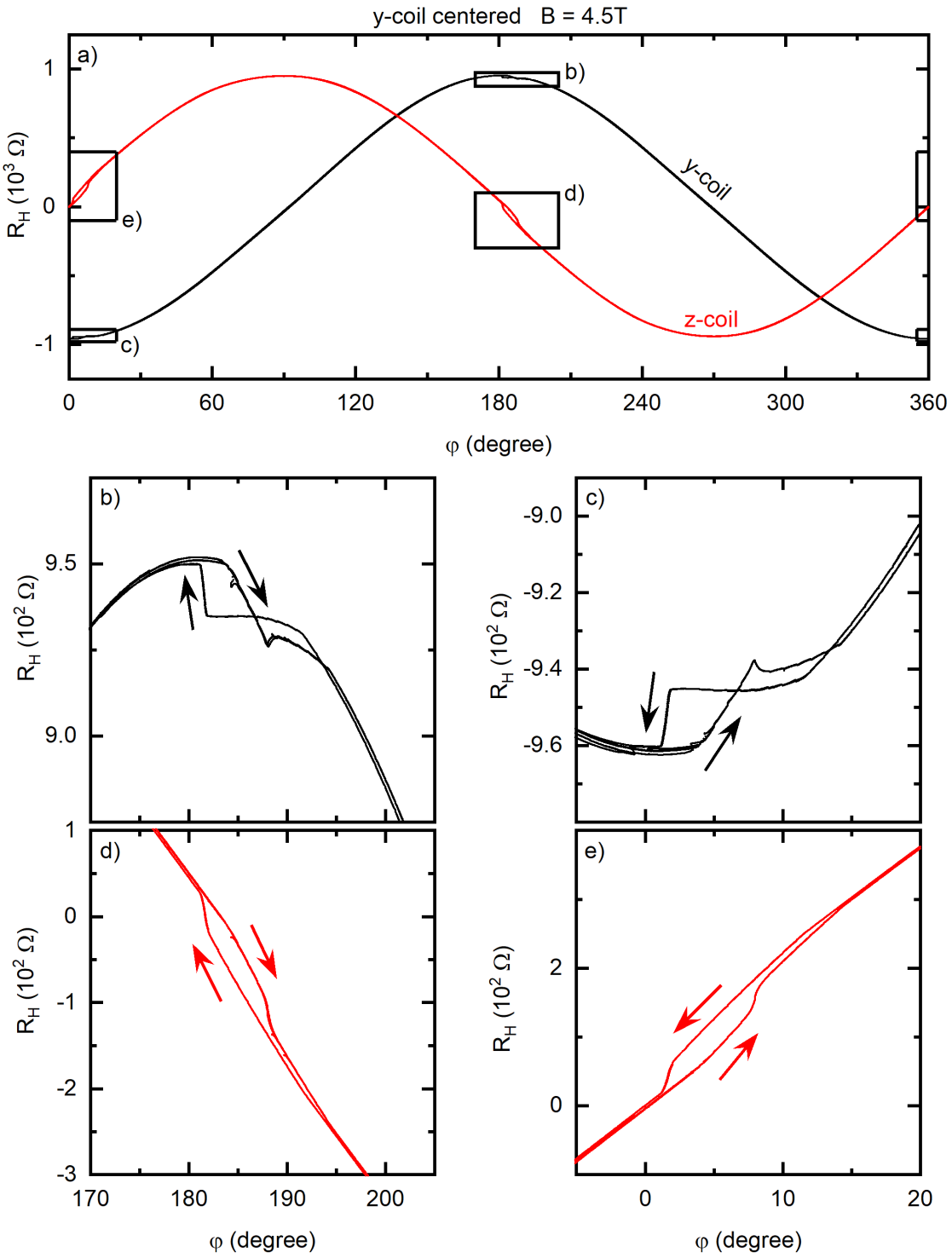

Figure A.4: Hall resistance measured during field rotations. b)-e) show magnifications of the sections marked in a).

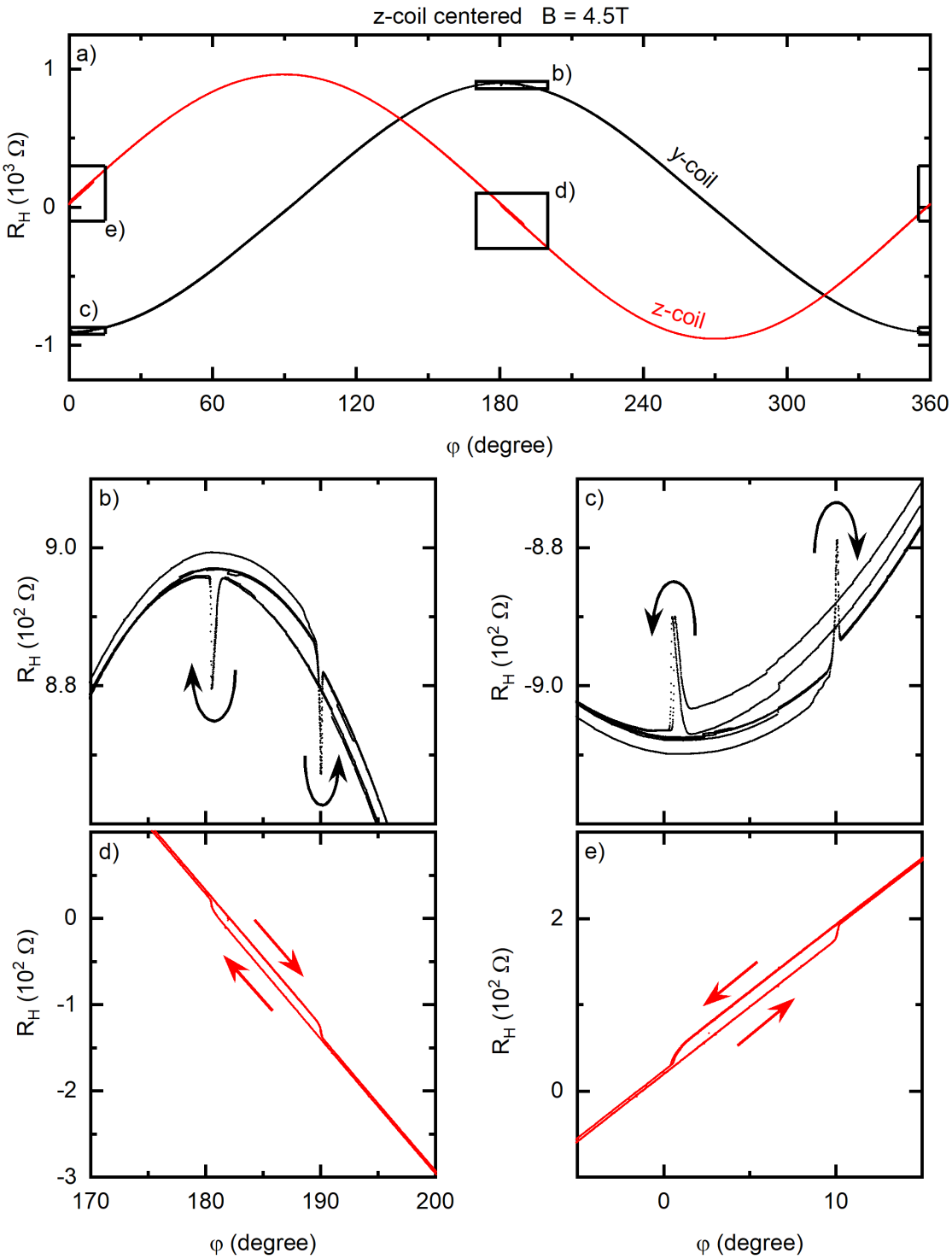

Figure A.5: Hall resistance measured during field rotations. b)-e) show magnifications of the sections marked in a).

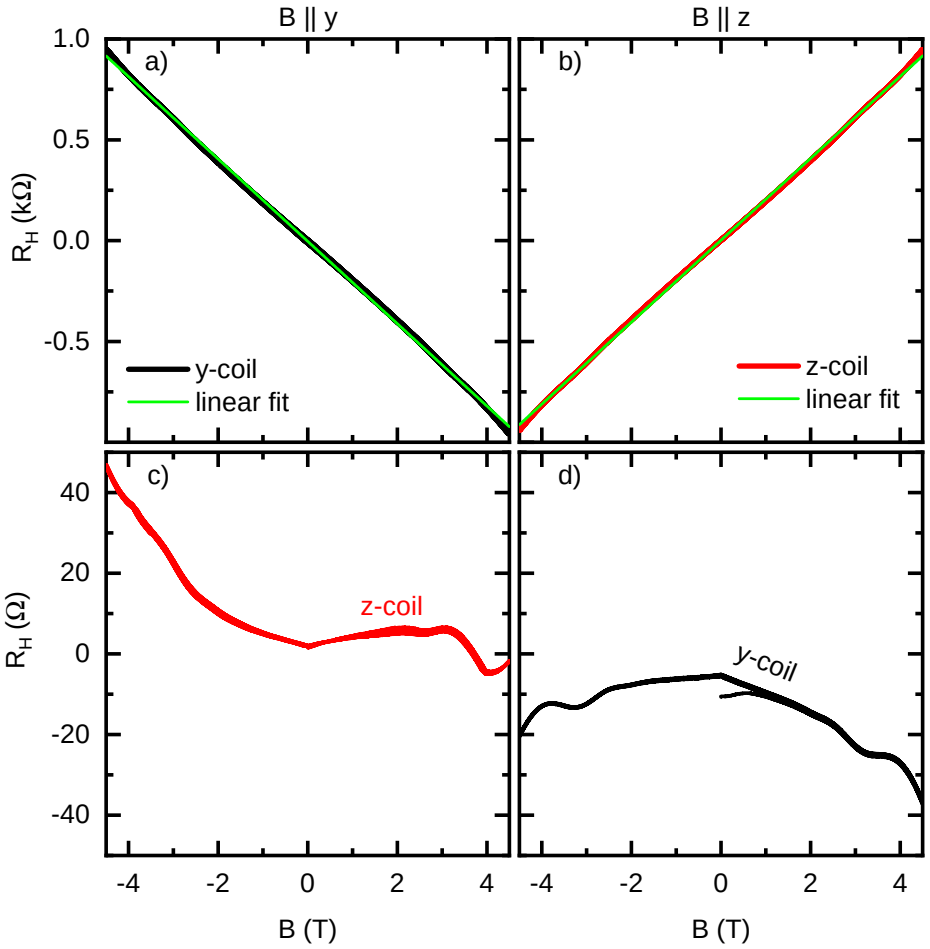

Figure A.6: Hall resistance recorded during field sweeps in a) y-direction and b) z-direction.

A.4.2 Field sweeps

Field sweeps with both coils were performed while centering the Hall sensor for the respective direction in the corresponding field centre. As for our sample measurements, one measurement consists of six consecutive sweeps where the first one starts from zero towards positive fields and the last one runs from positive fields to zero. In between we sweep the field twice from positive to negative values and back. For the Hall probe investigation, the full range of the split coil of 4.5 T was exploited. The results are shown in Fig. A.6 where the top graphs depict the Hall sensor located in the respective field centre and the bottom graph illustrates the respective other one. In the left graphs, the horizontal Hall sensor is centred, on the right the vertical sensor is centred. The green lines in Fig. A.6 a) and b) represent linear fits to the Hall resistance. While a slight deviations from perfect linearity may be recognized, the overall shape of the Hall resistances is grasped very well by the fits for both coils. From Fig. A.6 c) and d) we observe that both Hall sensors are also influenced by a field perpendicular to their sensitive direction. However, the amplitude at 4.5 T

corresponds to a field of roughly 200 mT. Considering contributions due to imperfect alignment, the remaining signal may be deemed negligible.

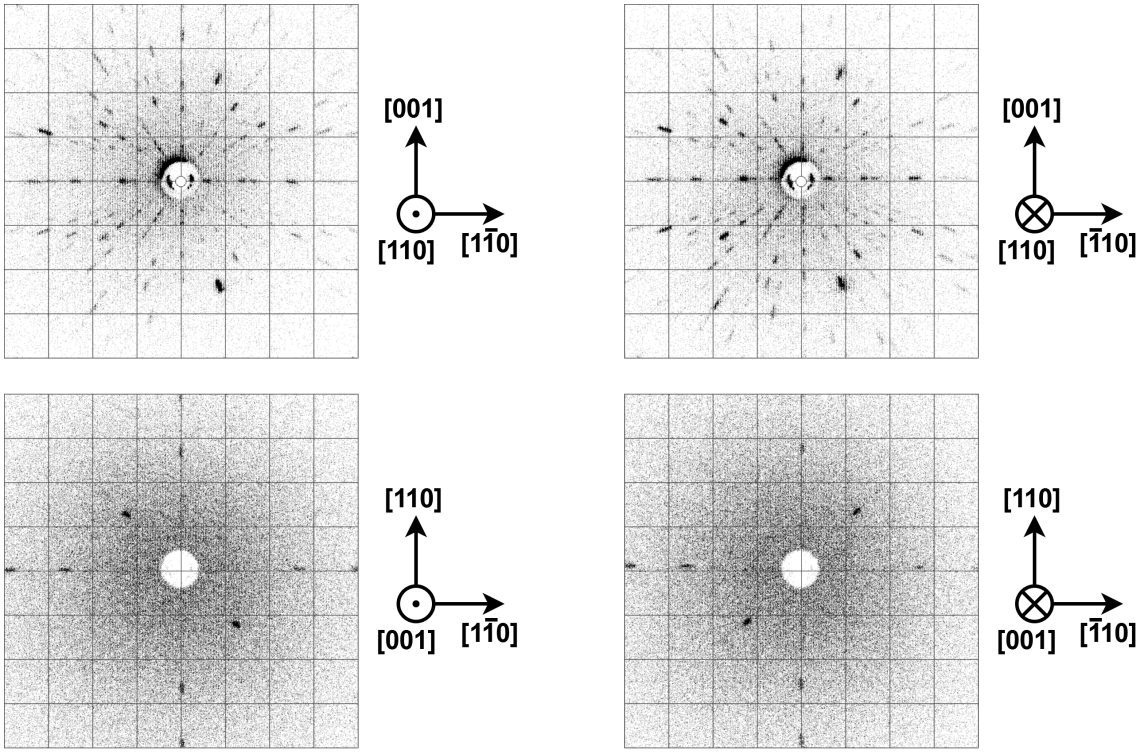

Figure A.7: X-ray images obtained in the Laue camera from the spherical MnSi sample. Images on the left show the sample on the goniometer, images on the right the sample on the cantilever. The top images correspond to the gluing process to the longitudinal cantilever, the bottom images to the torsional one.

A.5 X-ray images of a spherical MnSi sample in the Laue camera

As illustrated in Fig. 3.11, the sample was first oriented with respect to the x-ray beam while being attached to the goniometer and then glued to a cantilever. X-ray images were recorded in both situations as depicted in Fig. A.7. Images on the left side correspond to samples mounted on the goniometer, images on the right show samples glued to the cantilever. The top images were taken when mounting the sample to a longitudinal CuBe cantilever, the bottom images refer to the usage of a torsional cantilever. Due to the different projection axes of the two cantilever types, the orientation on the goniometer was chosen differently. Slight deviations of the scattering patterns on the right compared to the left ones are visible. In particular, both samples appear to have tilted around the [1$\bar{1}$0]-direction during transfer from goniometer to cantilever. However, the tilts amount to less than 1.5° in both cases and are thus of minor significance for our measurements.

B DFT calculations on CrB_2

B.1 Electronic structure of non-magnetic CrB_2

We performed electronic structure calculations for the paramagnetic state of CrB_2 to assess the sensitivity of the Fermi surface to magnetic order. The same software and parameters as for calculations in the cycloidal state were used. Figure B.1 shows the resulting density of states (DOS). The black line denotes the total DOS, the red, green and blue lines represent the DOS arising from Cr-d, B-s and B-p states, respectively. The results look fairly similar to earlier works [Bra13a, Liu75]. At the Fermi level, set to zero in this plot, the largest contribution originates from Cr-d states. While B-p states still make a notable contribution, the DOS due to B-s states is negligible.

The band structure of the paramagnetic state is shown in Fig. B.2. The point size represents the B-p character of the bands. In full agreement with Ref. [Bra13a], we find that two bands crossing the Fermi level near the A-point exhibit dominant B-p character, while in the rest of the Brillouin zone, bands exhibit mostly Cr-d character near E_F.

We present the Fermi surface sheets of all four contributing bands in Fig. B.3. The pockets corresponding to the B-p-like bands are visible as spheres in Fig. B.3 c) and d). Here, we find a single copy of this sphere centered around the A-point for each band. In the spin spiral state reported above, we find two copies for each band. These are shifted away from A along the $\mathbf{q}_{110}$-direction by $\pm|\mathbf{q}|/2$, i.e., in the ferromagnetic state with $|\mathbf{q}| = 0$, the spheres are still degenerate and centered on the A-point, but with increasing length of the ordering wave vector, they are shifted apart from each other. In the collinear antiferromagnetic state with $|\mathbf{q}| = 0.5\,|\mathbf{q}_{110}|$, they reside close to the H-point, at $|\mathbf{q}| = 1\,|\mathbf{q}_{110}|$ the spheres are again degenerate and centered around M.

The B-p-like spheres are shifted, but not altered significantly in size or shape when introducing magnetic order. In contrast, the remaining Fermi sheets in Fig. B.3 a) and b) as well as the K-centered pocket in c) are of predominantly Cr-d character. These pockets show no clear similarity to the Fermi surface sheets obtained for the magnetically ordered state.

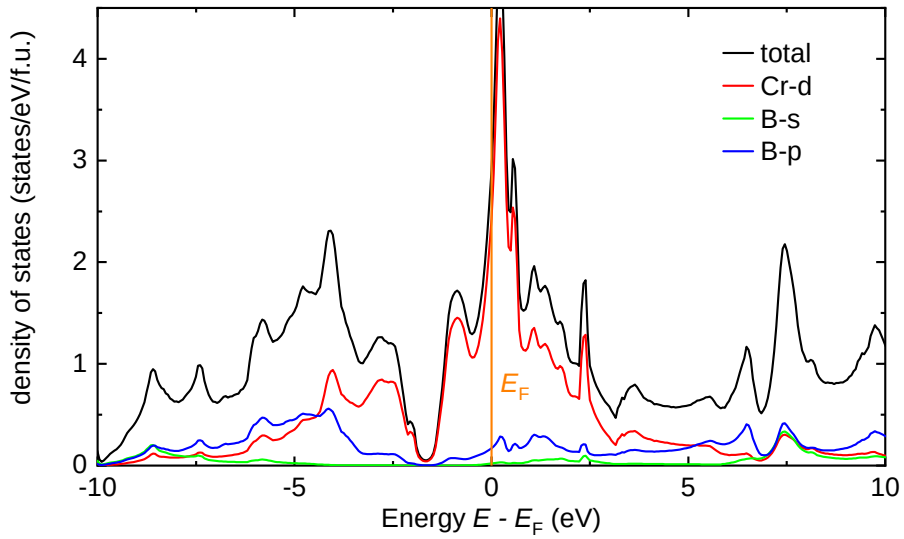

Figure B.1: Density of states (DOS) of paramagnetic CrB_2. The main contribution stems from Cr-*d* states (red). B-*p* also contribute to a notable extent while B-*s* states are negligible.

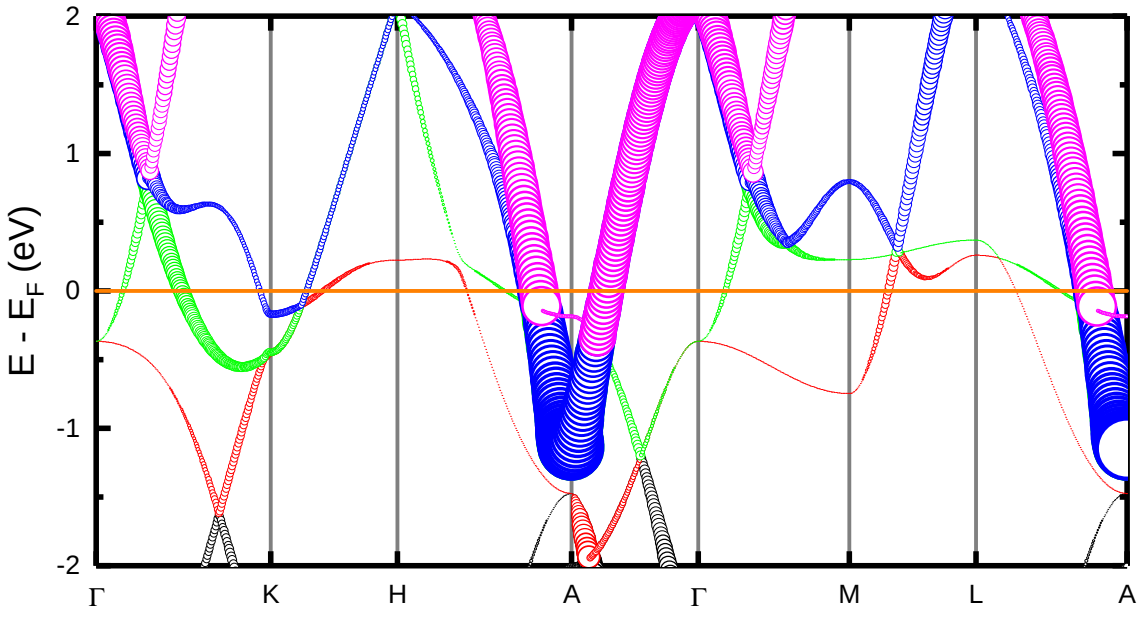

Figure B.2: Band structure of non-magnetic CrB_2. The point size resembles the B-*p* character. In total, four bands cross the Fermi energy. Dominant B-*p* character is found for two of them close to the A-point. The other bands have predominantly Cr-*d* character.

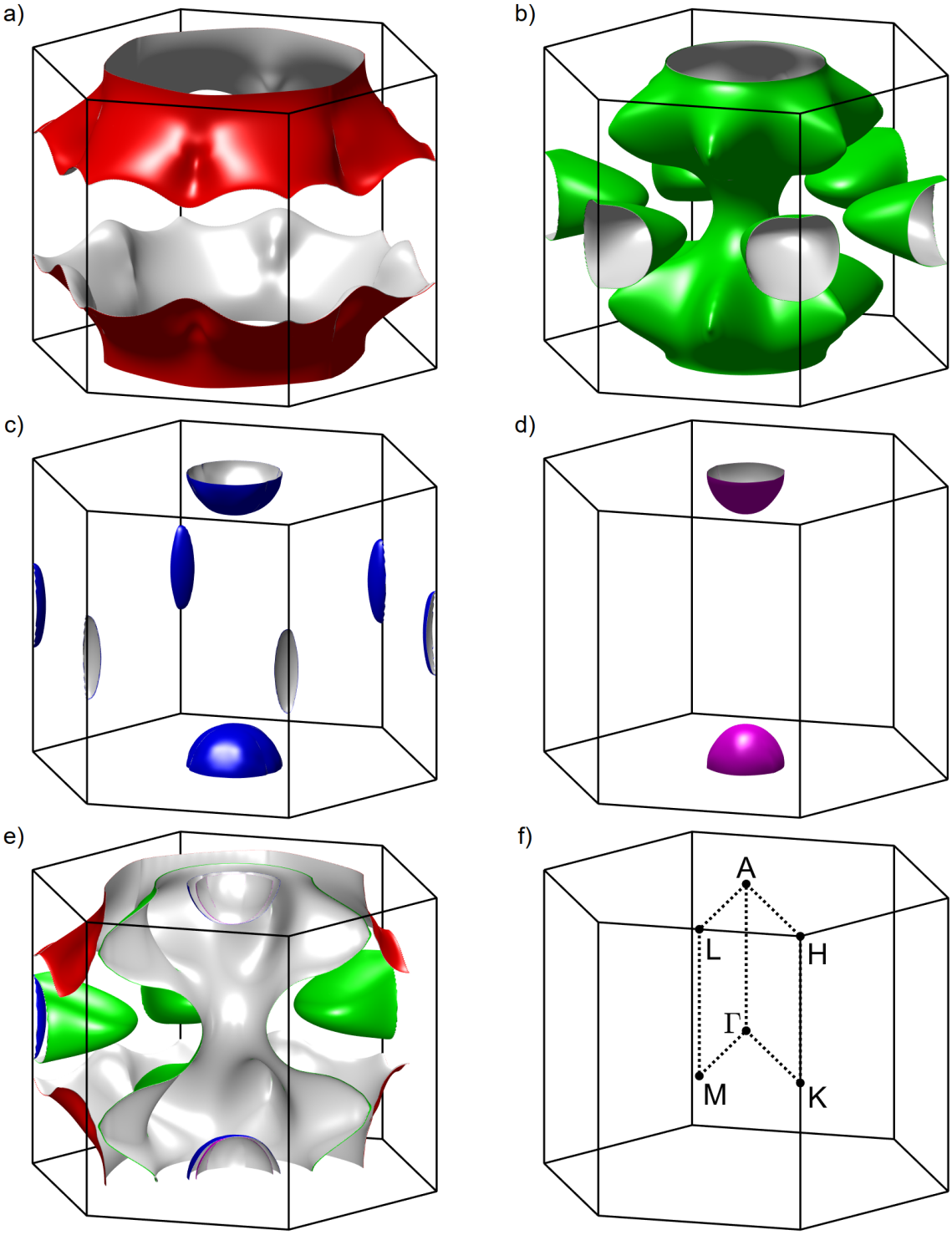

Figure B.3: Fermi surface resulting from the non-magnetic band structure calculation as separate bands in a) - d) and combined in e). The colors correspond to the bands presented in Fig. B.2. The pockets with predominant B-*p* character are the spheres around the A-points in c) and d). The FS sheets in e) are cut along $\mathbf{q}_{100}$ for clarity. f) Symmetry points of the Brillouin zone.

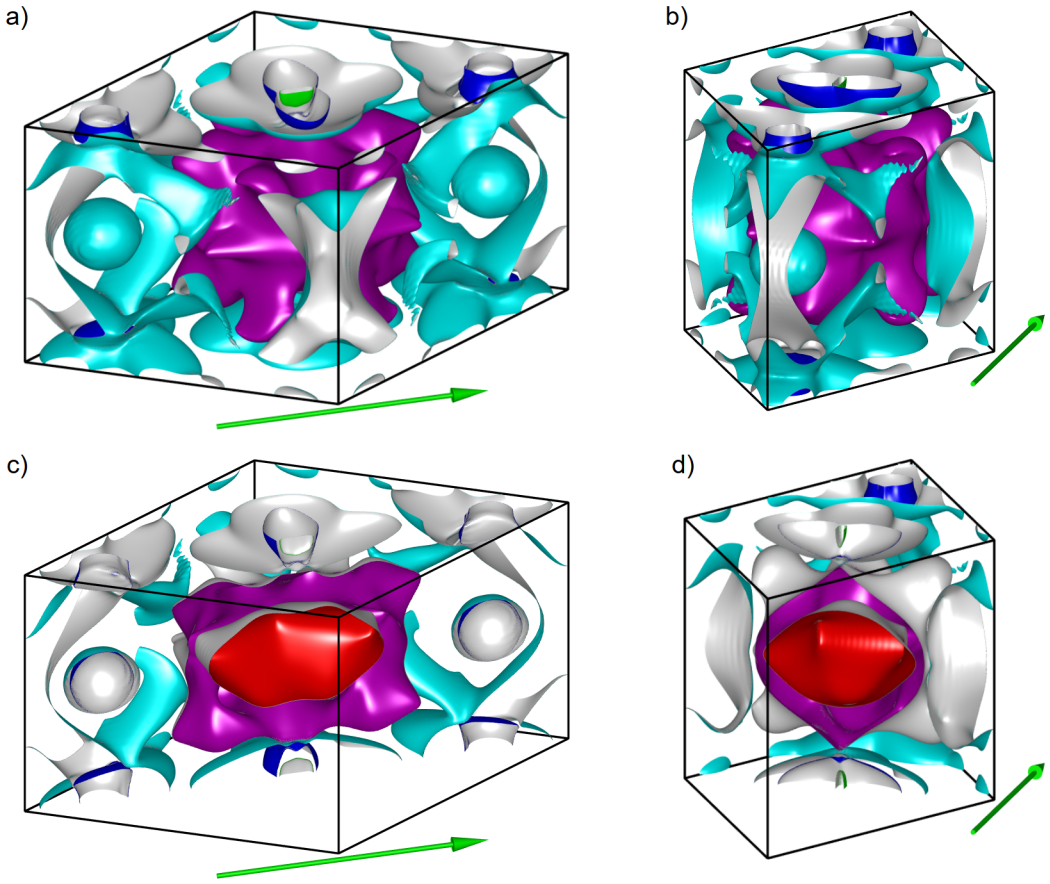

Figure B.4: Fermi surface calculated for a simple spin cycloid in CrB_2. The sheets arising from all five contributing bands are included. Green arrows illustrate the direction of the propagation vector. a) - b) FS sheets in the full RUC from different perspectives. c) FS sheets are cut along $\mathbf{q}_{110}$. d) FS sheets are cut orthogonal to $\mathbf{q}_{110}$.

B.2 Alternative representation of the CrB_2 Fermi surface

In Ch. 4 the results of electronic structure calculations for a simple spin cycloidal state of CrB_2 have been presented. The Fermi surface sheets arising from individual bands were plotted separately in Fig. 4.13 to allow for a thorough examination of individual sheets. However, the interplay and possible contact points between the sheets of separate bands was merely sketched by means of Figs. 4.19 and 4.20.
Here, further representations of the Fermi surface are shown for the sake of a more complete picture. In Figs. B.4 and B.5 the Fermi surfaces originating from all five bands are plotted together in the reciprocal unit cell and the Brillouin zone, respectively. The sheet colors are chosen analogous to the representation in Fig. 4.13. Green arrows represent $\mathbf{q}_{110}/2$. The sheets are plotted in the full cells from two

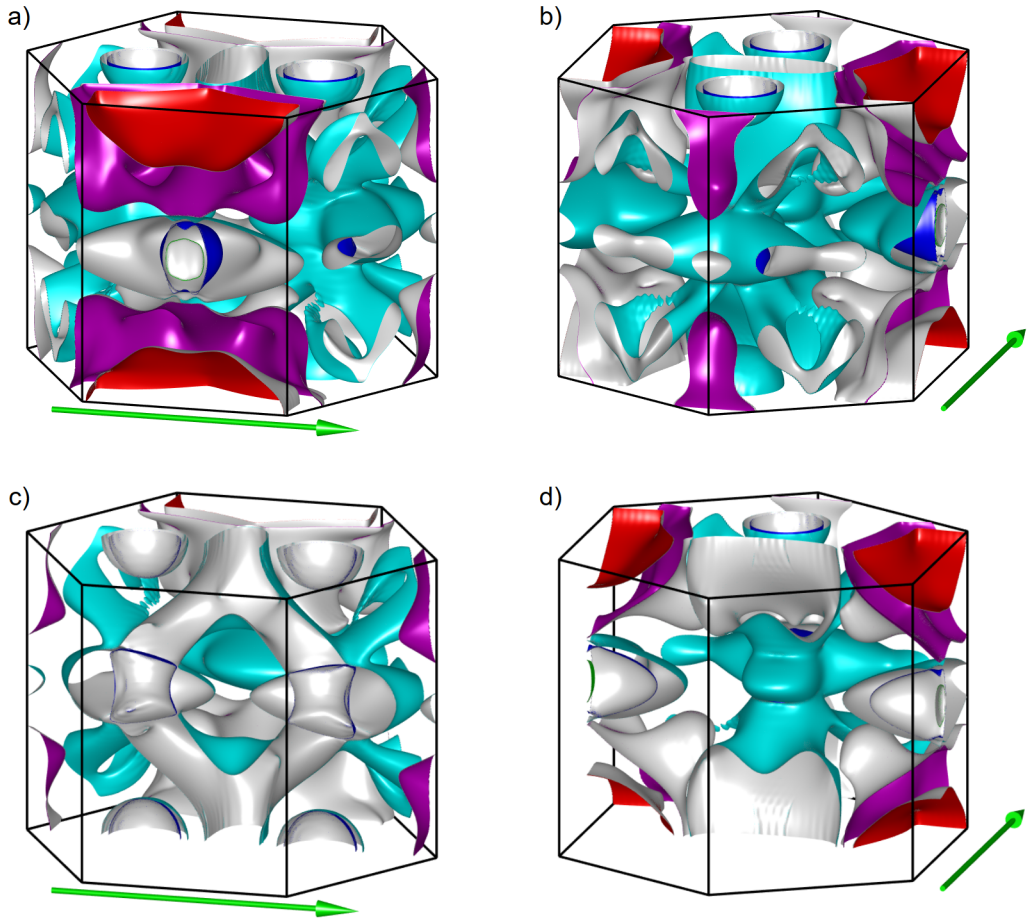

Figure B.5: Fermi surface calculated for a simple spin cycloid in CrB_2. The sheets arising from all five contributing bands are included. Green arrows illustrate the direction of the propagation vector. a) - b) FS sheets in the full BZ from different perspectives. c) FS sheets are cut along $\mathbf{q}_{110}$. d) FS sheets are cut orthogonal to $\mathbf{q}_{110}$.

different perspectives in parts a) and b) of the respective figures. In parts c) and d), the sheets only fill half the cell. They are cut along $\mathbf{q}_{110}$ in c) and orthogonal to $\mathbf{q}_{110}$ in d). A representation of separate bands in the Brillouin zone appears useful only for the complex FS sheets arising from band 21. A respective illustration is presented in B.3.

B.3 Extremal orbits on the CrB_2 Fermi surface

In Sec. 4.4.4 we discussed the implications of the calculated CrB_2 Fermi surface for the dHvA effect. Observable oscillations in the magnetization arise from extremal charge carrier orbits on single or multiple FS pockets. Some of the single sheet orbits discussed in Sec. 4.4.4 are illustrated in Fig. B.6. The Fermi surface sheets of individual bands are plotted separately for clarity with the same coloring as in Fig. 4.13. The green arrows represent the direction of the propagation vector. In Fig. B.6 a) - d) the yellow orbits correspond to $\varphi = 0°$. The green orbits correspond to $\varphi = 90°$ which in a three domain configuration discussed in Sec. 4.4.4 is mapped back to $\varphi = 30°$ with a propagation vector shifted by 120°. The same holds for the red and blue orbits in Fig. B.6 e). In Fig. B.6 c), orbits yielding dHvA frequencies above the experimental threshold of 5 kT were excluded for clarity.
For band 19 in Fig. B.6 a) and band 23 in Fig. B.6 e) we observe a single extremal orbit as discussed by means of Fig. 4.14. Similarly, single extremal orbits run on the spherical and dumbbell-shaped pockets of band 22 in Fig. B.6 d). For band 20 in Fig. B.6 b) we find a single extremal orbit in one direction and several, partly degenerate orbits in another direction. This is reflected in Fig. 4.14 by the single continuous frequency with several split-offs. Similarly, the elongated M'-centered pocket of band 22 exhibits a single orbit in one direction but multiple orbits for the orthogonal field direction. For band 21 in Fig. 4.13 c) we find a large number of orbits for both displayed field directions. For a more lucid illustration of several orbits on band 21 discussed with respect to Figs. 4.16 and 4.18, we turn to a representation in the Brillouin zone.

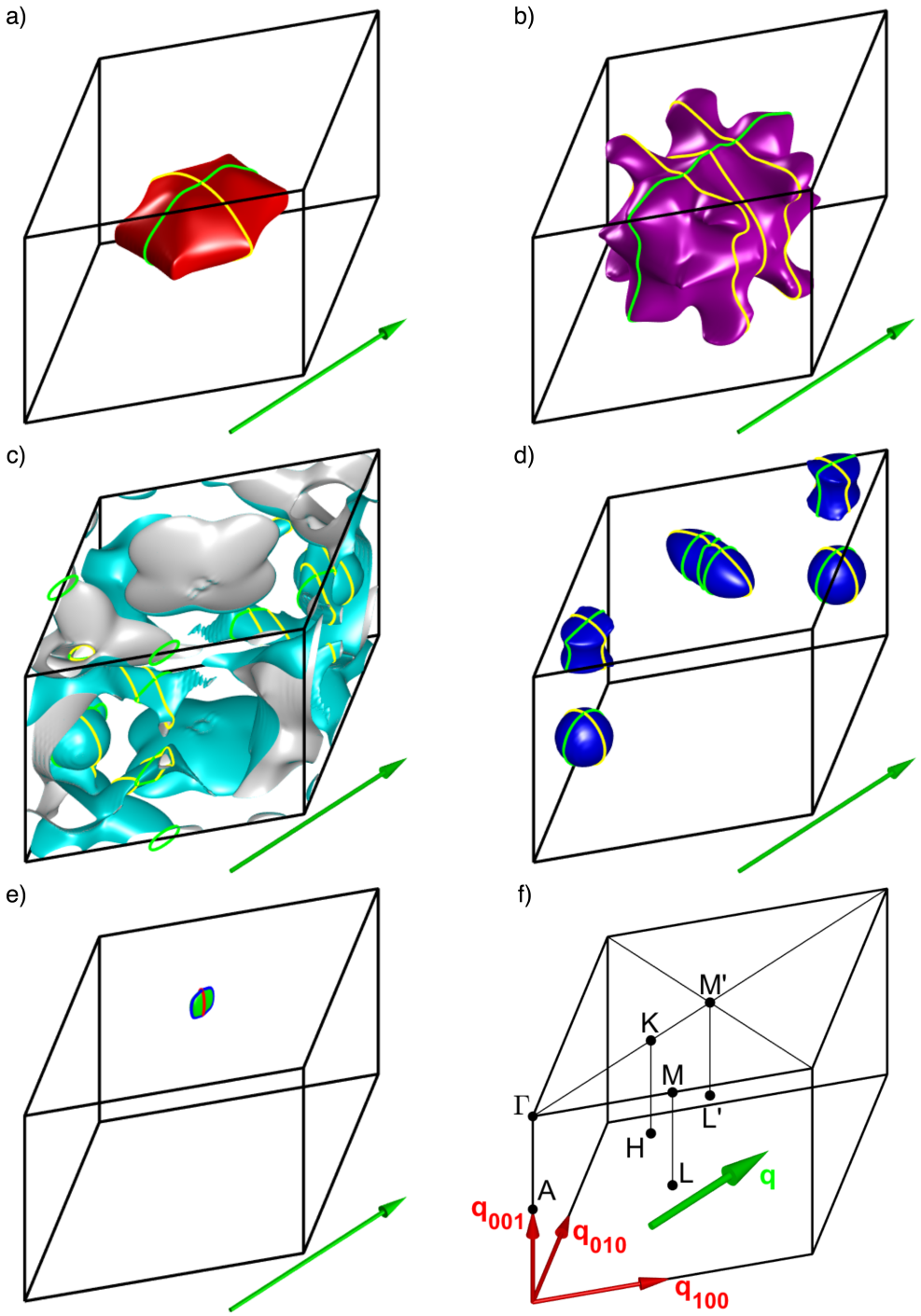

Figure B.6: a)-e) Fermi surface sheets calculated for CrB_2 in the RUC together with extremal orbits. Green arrows represent $\mathbf{q}_{110}/2$. f) Directions (red arrows scaled to half length) and symmetry points in the RUC.

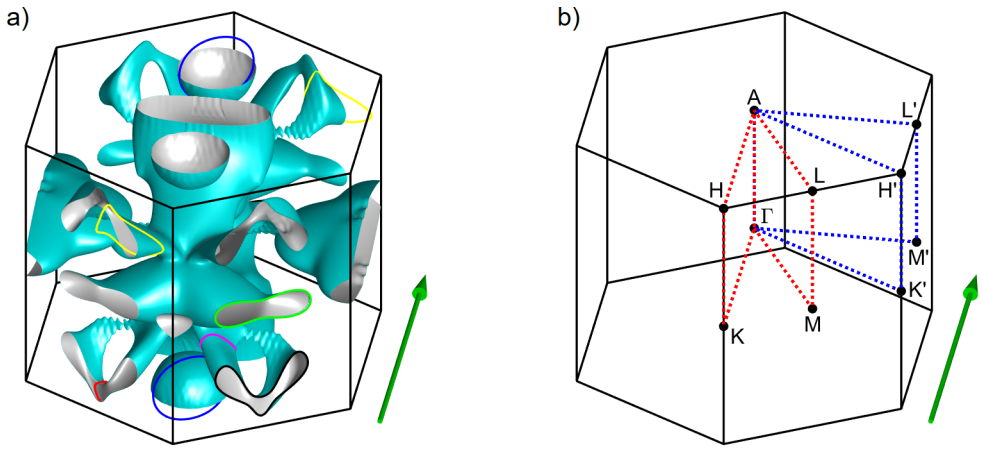

Figure B.7: a) Fermi surface of band 21 in the BZ together with selected extremal orbits. b) Symmetry points in the Brillouin zone. Green arrows indicate the direction of the propagation vector.

In Fig. B.7 a) the FS sheet resulting from band 21 is shown within the Brillouin zone. The green arrow depicts $\mathbf{q}_{110}$, i.e., the field direction for $\varphi = 0°$. Selected extremal orbits are displayed for the experimental angle $\varphi = 30°$. The orbits depicted in blue run around the spherical FS pockets. They correspond to the frequencies colored blue in Fig. 4.16 and masses depicted as blue triangles in Fig. 4.18. The orbit depicted in green is centered around M and results in frequencies colored green in Fig. 4.16 and masses represented by the green triangles in Fig. 4.18. Note that said values in Figs. 4.16 and 4.18 also include a copy of the green orbit centered on the equivalent M-point on the left front BZ surface. The remaining orbits in Fig. B.7 a) correspond to frequencies depicted gray in Fig. 4.16 and represented by triangles in Fig. 4.18. The colors of the corresponding triangles match the colors of the orbits in Fig. B.7 a) except for the red orbit which is colored cyan in Fig. 4.18. Again, several copies of these orbits exist within the BZ which are not shown in the plot.

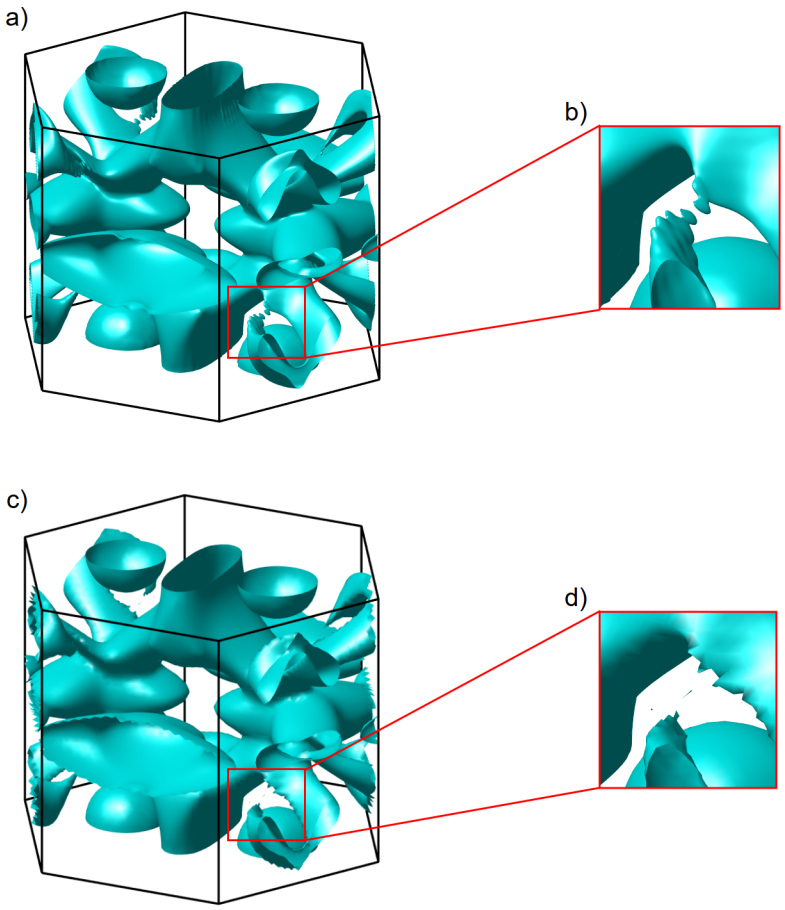

Figure B.8: Fermi surface sheet arising from band 21. a) Strong interpolation after FS calculation. b) Magnification of a) with focus on a small, disconnected junction. c) No interpolation after FS calculation. d) Magnification of c) with focus on the same junction as in b).

B.4 Resolution limit of the DFT calculation

In Sec. 4.5 we argued that the low frequency branch at 5 - 15 T contained in the SKEAF output is not reliable due to the limited resolution of the FS calculation. We illustrate this in Fig. B.8. The FS sheet of band 21 is displayed with strong interpolation in a) and b) and without interpolation in c) and d). Comparing a) and c), no pronounced difference is found in the overall shape of the FS sheets. However, comparing the magnifications in b) and d) we note a distinct difference. Extremal orbits around the narrow part of the FS pocket in b) can easily be constructed for which there is no clear evidence in the original FS calculation.

C Torque in the field-polarized phase of MnSi

In this appendix we provide additional information on the torque investigations on MnSi in the field-polarized state. Section C.1 covers general topics, Secs. C.2 and C.3 are dedicated to specific information concerning rotating sample and rotating field setups, respectively.

C.1 General

We briefly review the benefit of including the K_2-term in our fit procedure in the following section.

C.1.1 Benefit of including the K_2-term in the fit function

In our discussion of rotation scans in the field-polarized phase, we reach the conclusion that the second anisotropy K_2 can not be determined reliably from our experiments. For the determination of the high temperature scaling factor of PPMS data on the MnSi sphere, we set K_2 to zero manually to avoid unwanted effects due to this parameter. Regarding AMI data, the behavior of K_2 depends mainly on the choice of evaluation method rather than on our experimental data. This raises the question if including the K_2-term in the fit function during evaluation is reasonable at all.
To address this question, we directly compare the result of a fit with K_2 as free parameter to that of a fit with $K_2 = 0$. In Fig. C.1 we show the torque curve measured at $B = 1\,\mathrm{T}$ and $T = 2\,\mathrm{K}$ as black line in both panels. The green line in panel a) represents a fit including the K_2-term as described in the main text. The red line in panel b) depicts a fit where K_2 has been fixed to zero. Evidently, the inclusion of K_2 remarkably improves the match of fit function and experimental data. Due to this distinct improvement, we choose to stick with the evaluation procedure including K_2 as fit parameter.
Despite the excellent agreement of data and fit, we have to be aware that K_2 may actually differ substantially from our fitted values and the deviation of data and fit in Fig. C.1 b) may be caused by some perturbation not related to magnetic anisotropy. In particular, this imposes an additional uncertainty on the values obtained for K_1. We compare values for K_1 obtained from fitting with and without the K_2-term over the full experimental temperature and field range and find substantial difference below $\sim$20 K. Qualitatively, we observe that the low temperature values of K_1 at different field magnitudes lie substantially closer together when excluding the K_2-term from

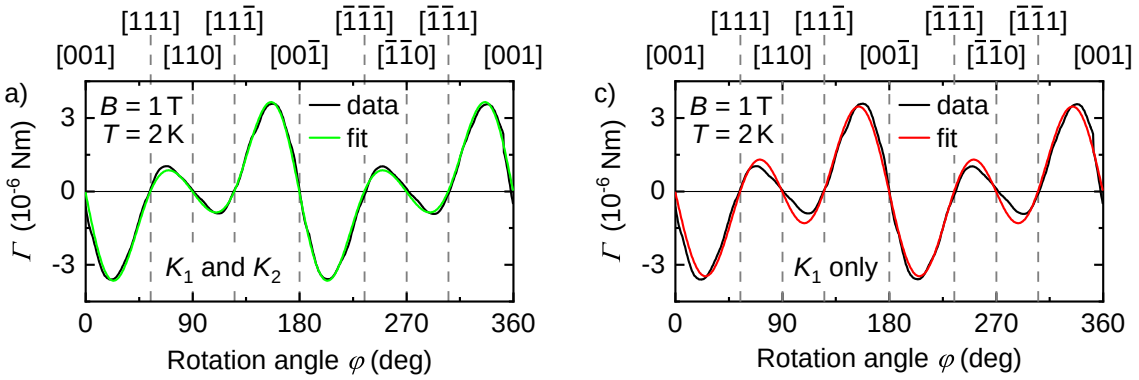

Figure C.1: Torque data (black lines) measured at $B = 1\,\mathrm{T}$ and $T = 2\,\mathrm{K}$ together with fits (red and green lines) according to Eq. 5.1. a) K_2 is included as fit parameter. b) K_2 is fixed to zero for the fit.

the fit. Quantitatively, values of K_1 are larger by up to 28 % when neglecting the K_2-term during evaluation for fields up to 4 T. At higher fields, K_1 is larger by up to 14 % when including the K_2-term. This observation relates to the sign change of fitted values for K_2 in the field magnitude dependence.

C.2 Rotating sample setup

In Sec. C.2.1 we discuss the mismatch of measurements at high and low temperature measurements on the spherical sample and explain our approach to combine both regimes. Section C.2.2 is dedicated to the additional curve correction performed for data on the cubic sample. We present the measurement errors in the temperature dependence of K_1 and K_2 in Sec. C.2.3 and the torque curves acquired on the cubic sample in Sec. C.2.4.

C.2.1 Scaling of high-temperature data from the spherical sample

During acquisition of torque data from the spherical sample, we encountered an irregularity of unknown origin. While being completely consistent apart from that, data acquired before and after a specific date differed from each other by a fixed factor of ∼7/8. As a consequence, data acquired above and below 16.5 K differed by the same factor. This is illustrated in Fig. C.2 a) by means of K_1 which exhibits a distinct kink between 16 K and 17 K (arrows). As further illustration, the mean curves of zero field rotation scans at all temperatures above and below 16.5 K are plotted in Fig. C.2 b) as gray and black line, respectively.
The red horizontal lines in Fig. C.2 b) denote our estimate $\pm\Gamma_\mathrm{G}$ of the maximum torque exerted on the cantilever by the sample weight. This estimate is obtained via

$$\Gamma = \mathbf{r} \times \mathbf{F}_\mathrm{G} \tag{C.1}$$

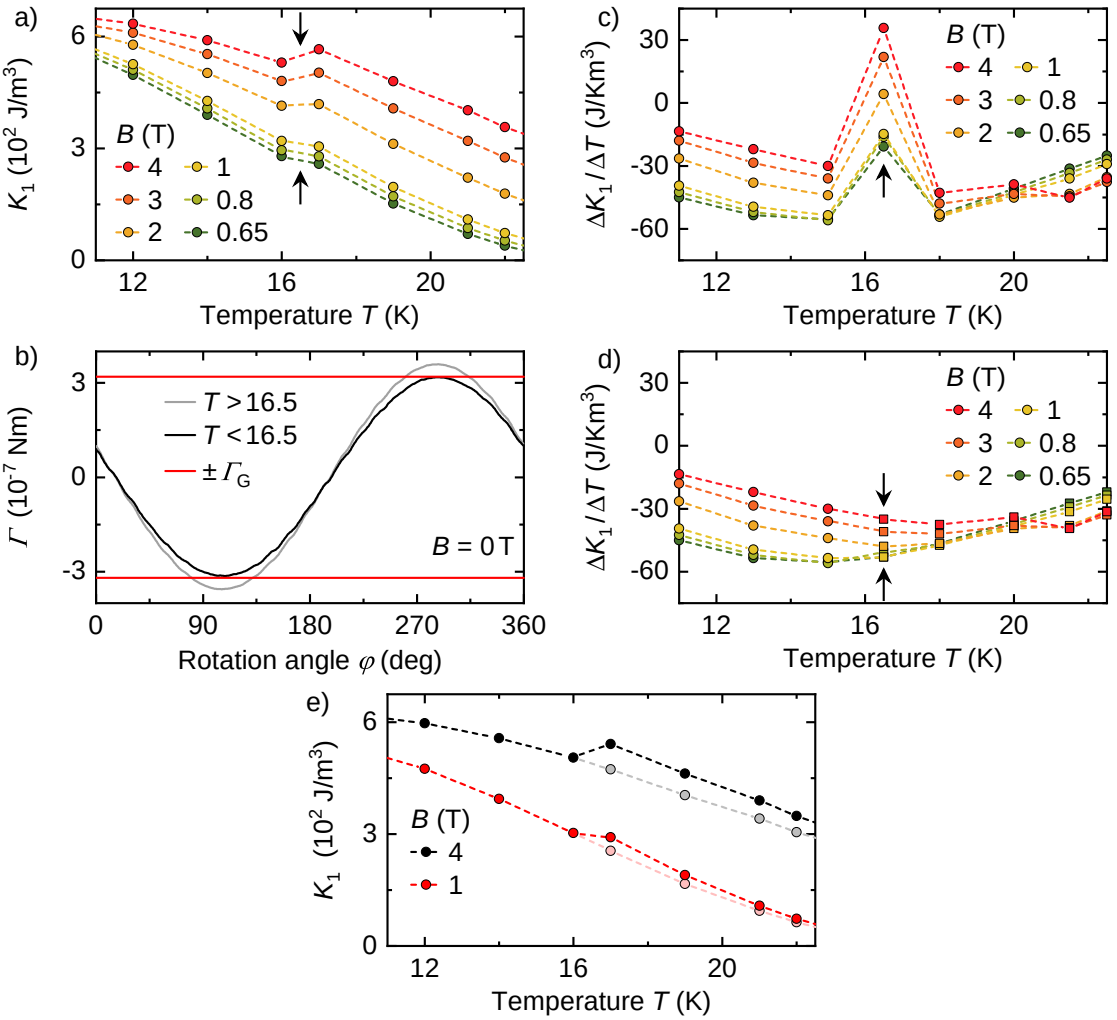

Figure C.2: a) Anisotropy constants K_1 extracted from data on the spherical sample for various fields plotted versus temperature. The arrows mark a distinct kink between the data points at 16 and 17 K. b) The black and gray lines represent the mean curves of all zero-field measurements below and above 16.5 K, respectively. The value Γ_G marked by the red lines corresponds to the maximum torque exerted on the cantilever due to the sample weight. c) and d) show the derivative of K_1 with respect to the temperature before and after rescaling the high temperature data. While c) shows a distinct outlier between 16 and 17 K, the derivatives in d) exhibit smooth curves for all fields. e) Temperature evolution of anisotropy constants K_1 at $B = 1$ T and $B = 4$ T. Faint lines and symbols represent high-temperature data scaled to match low-temperature data.

where $\mathbf{r}$ is the vector from the point where the sample is glued to the cantilever to the samples centre of mass and $\mathbf{F}_\mathrm{G}$ is the weight force acting on the sample. Obviously, Γ is maximal at $\mathbf{r} \perp \mathbf{F}_\mathrm{G}$ and thus

$$\Gamma_\mathrm{G} = |\mathbf{r}| \cdot |\mathbf{F}_\mathrm{G}| \approx r_\mathrm{sphere} \cdot m_\mathrm{sphere} \cdot g \tag{C.2}$$

with mass $m_\mathrm{sphere} \approx 30\,\mathrm{mg}$ and radius $r_\mathrm{sphere} \approx 1.05\,\mathrm{mm}$ of the sample. Strikingly, the zero field torque curve exhibits extrema very close to $\pm\Gamma_\mathrm{G}$ for temperatures below 16.5 K. In addition, the low temperature data matches well with data obtained on the cubic sample where no such irregularity occurred. We thus assume the low temperature data to be measured correctly and scale the high temperature data to achieve a consistent data set. However, as we have no explanation for the scaling, this assumption remains somewhat doubtful and must be kept in mind for a conclusive discussion of our data.
In order to determine the scaling factor, we considered the derivative of K_1 with respect to temperature while setting $K_2 = 0$ during evaluation. This is in equal shares due to the facts that K_2 is not a reliable quantity and that it is about to approach zero in the temperature region of interest. The discontinuity of K_1 is well visible in its derivative as illustrated in Fig. C.2 c) (arrow). By manual adjustment, we find that the scaling factor 7/8 minimizes the discontinuity to a satisfying extent. This is illustrated in Fig. C.2 d) where no discontinuity in the derivative of K_1 can be recognized by the bare eye. The same holds true for K_1 which is shown in Fig. C.2 e). The semi-transparent lines and symbols represent the scaled values which yield a continuous temperature evolution.

C.2.2 Node-correction of data from the cubic sample

In Sec. 3.3.2 we reported that the rotating sample setup yields a finite torque signal even for an empty cantilever. In Fig. 3.7 a) we showed a somewhat two-fold angular variation of this signal. In principle, this angular dependence is spurios to our data and should be removed if possible. In practice, its influence is small enough that it can be neglected in the case of the spherical sample. However, the cubic sample's volume is smaller by a factor of $\sim$5 which makes it necessary to account for the sensors angular dependence to be considered. In particular when the torque signal is decreased by elevated temperatures, a proper separation of sample and sensor induced torque is crucial. Here, we describe our procedure for the estimation of the sensor's contribution to our angle dependent torque signal.
Figure C.3 a) shows torque curves measured on the cubic sample at 1 T and various temperatures from 2 K up to 23 K. The zero field curves and the mean values have already been subtracted as described in Sec. 5.2.1. For undisturbed measurements, the torque curves of different temperatures are expected to intersect in nodes positioned exactly at $\Gamma = 0$. A blowup of the area marked by the black rectangle in Fig. C.3 a) is shown in panel b). Black circles denote nodes which are positioned at finite torque. We attribute these finite torque values to the two-fold symmetric signal arising already from the empty cantilever.

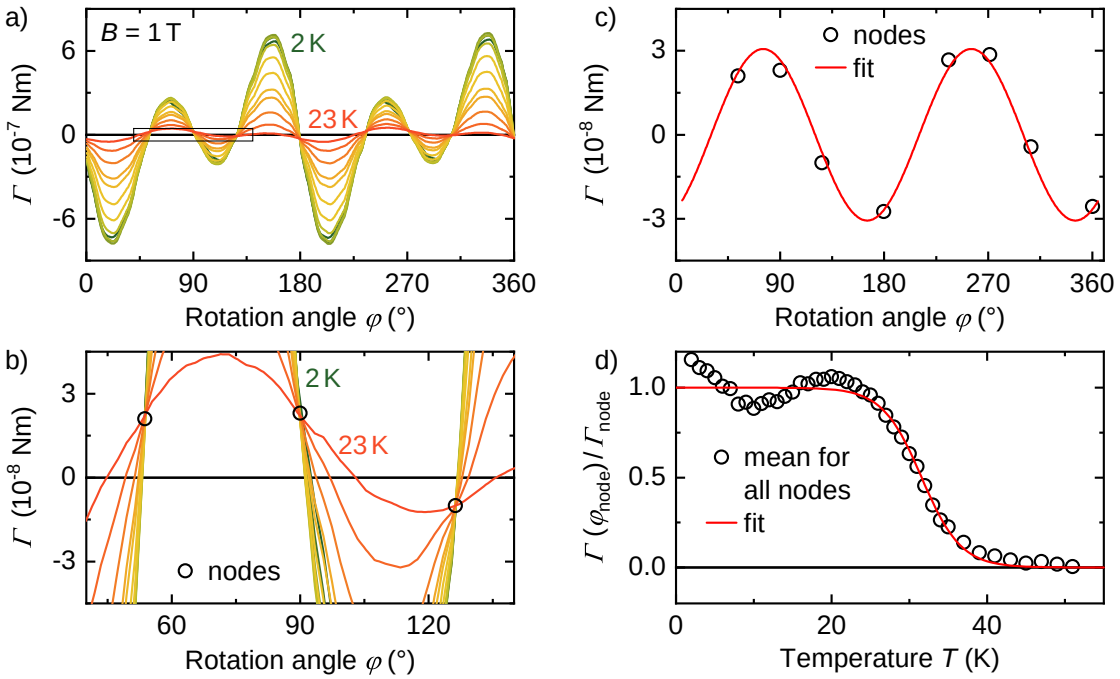

Figure C.3: a) Torque curves measured on a cubic sample in the rotating sample setup at $B = 1\,\mathrm{T}$ and various temperatures between $T = 2\,\mathrm{K}$ and $T = 23\,\mathrm{K}$. The zero-field curve and mean value have already been subtracted. b) Magnification of a). The black circles denote nodal points of torque curves at various temperatures. c) Nodal points in the whole angular regime. The red line represents a sine-shaped fit. d) Torque magnitude measured at nodal point positions relative to the torque value of nodal points versus temperature. The red line represents a fit (for function see main text).

Figure C.3 c) shows all nodes observed in the full angle range as black circles. Similar to Fig. 3.7 a), their distribution implies a two-fold angular dependence. In order to model the cantilevers contribution, we apply

$$\Gamma_{\mathrm{node}}(\varphi) = a_1 \cdot \sin[2(\varphi - a_2)] + a_3 \tag{C.3}$$

as a fit function to the nodes. The fit is shown as red line in Fig. C.3 c). Before the resulting torque curve can be subtracted from our measurements, we need to determine the temperature reduction factor $R(T)$ since the cantilever's contribution to the angular dependent torque decreases at high temperatures. In order to include this decrease in our model, we interpolate the torque measured at a given temperature to the node positions φ_{node}. We divide the obtained values by the corresponding torque values $\Gamma_{\mathrm{node}}(\varphi_{\mathrm{node}})$ of the fit to the nodes and form the average value of this ratio for all nodes. The resulting values are plotted versus temperature in Fig. C.3 d) as black circles. To estimate the reduction factor, we apply

$$R(T) = \left[\exp\left(\frac{T - b_1}{b_2}\right) + 1\right]^{-1} \tag{C.4}$$

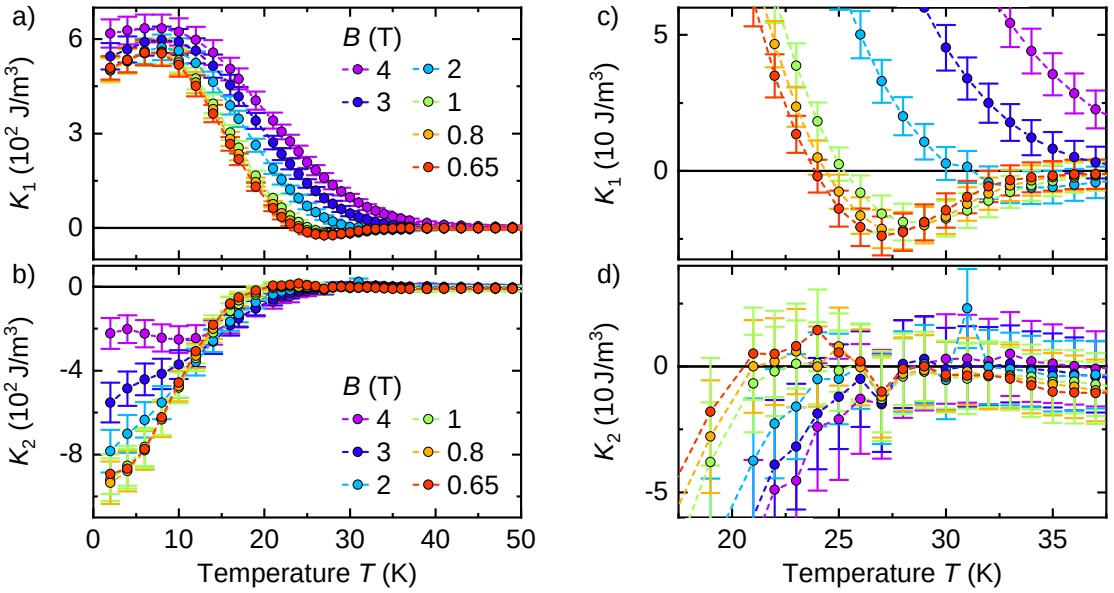

Figure C.4: Anisotropy constants at magnetic fields from $B = 0.65\,\mathrm{T}$ to $B = 4\,\mathrm{T}$ versus temperature. a) shows K_1, b) shows K_2. c) and d) show blow-ups of a) and b), respectively.

as a fit function. The fit is depicted by the red line in Fig. C.3 d). Finally, we subtract $\Gamma_{\mathrm{node}}(\varphi) \cdot R(T)$ from our measured torque curves to account for the sensor's influence.
A look at Fig. 3.7 a) shows that the torque induced by the cantilever changes with field magnitude. The described correction process was thus performed separately for the temperature series at 1T and 4T. The series of measurements at 2 K and various magnetic fields was not corrected for the sensor's influence since the sample's torque signal at this temperature is large enough to neglect the sensor's contribution.

C.2.3 Measurement errors in the temperature dependence of K_1 and K_2

Error bars have been left out of the presentation of the temperature evolution of K_1 and K_2 in Fig. 5.5 c) and d) for clarity. To convey an impression of the temperature dependence of the errors displayed in Fig. 5.4 c) and d), we present the respective graphs including error bars in Fig. C.4 a) and b). Blow-ups of the high-temperature regime are shown in Fig. C.4 c) and d). As described in the main text, these error bars include fits' 95 % confidence bounds, a relative error of 5 % and a static error of $5\,\mathrm{J/m^3}$ for K_1 and $10\,\mathrm{J/m^3}$ for K_2, respectively. The higher static error for K_2 is owed to the weaker influence of K_2 on the measured torque compared to K_1 (cf. Sec. 2.1.2). Additional errors may arise from angular distortion (cf. Fig. 5.2), misalignment (cf. Sec. 5.3.3) and unclarified events scaling the absolute values (cf. Sec. C.2.1). Due to these influences and the complex shape of the fit function, outliers are still possible as we see at $B = 2\,\mathrm{T}$ and $T = 31\,\mathrm{K}$ in Fig. C.4 d).

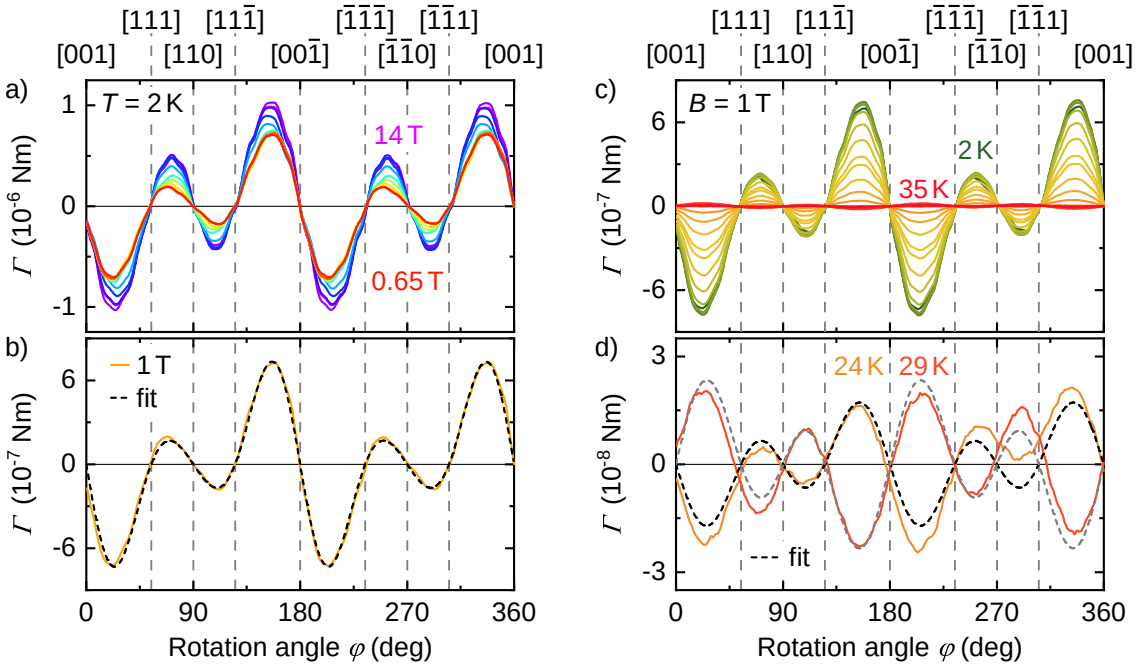

Figure C.5: Torque curves measured on the cubic sample in the rotating sample setup. a) Torque at $T = 2\,\mathrm{K}$ and magnetic fields from $B = 0.65\,\mathrm{T}$ to $B = 14\,\mathrm{T}$. b) Torque at $T = 2\,\mathrm{K}$ and $B = 1\,\mathrm{T}$. The dashed black line denotes a fit yielding K_1 and K_2. c) Torque at $B = 1\,\mathrm{T}$ and selected temperatures from $T = 2\,\mathrm{K}$ up to $T = 35\,\mathrm{K}$. d) Torque at $B = 1\,\mathrm{T}$ and temperatures of $T = 24\,\mathrm{K}$ and $T = 29\,\mathrm{K}$. Dashed lines denote fits.

C.2.4 Torque data from the cubic sample

In Sec. 5.3.1, we show anisotropy constants K_1 and K_2 extracted from rotation scans on a cubic sample. Here we present the underlying torque curves for various fields and temperatures. In Fig. C.5 a) we show the field magnitude dependent torque curves at $T = 2\,\mathrm{K}$ and fields from $0.65\,\mathrm{T}$ up to $14\,\mathrm{T}$. The curve at $B = 1\,\mathrm{T}$ is additionally shown in Fig. C.5 b) as solid line with the corresponding fit shown as dashed line. Panels a) and b) constitute a cubic sample analogue to Fig. 5.4 a) and b) in the main text and yield the same key observations as described in Sec. 5.3.1. Likewise, Fig. C.5 c) and d) constitute the cubic sample analogue to Fig. 5.5 a) and b). In Fig. C.5 c), a representative set of torque curves is shown at $B = 1\,\mathrm{T}$ and temperatures from $2\,\mathrm{K}$ up to $35\,\mathrm{K}$. The curves at $T = 24\,\mathrm{K}$ and $T = 29\,\mathrm{K}$ are additionally shown as solid lines in Fig. C.5 d) together with the corresponding fits depicted by dashed lines. The temperature dependent torque data on the cubic sample reproduces the results obtained from the MnSi sphere and described in Sec. 5.3.1.

C.2.5 Phenomenological fit to the temperature evolution of K_1

In Fig. 5.10 we show fits to the temperature evolution of the anisotropy constant K_1 experimentally obtained from the PPMS setup for $B = 1\,\mathrm{T}$ and $B = 4\,\mathrm{T}$. Here, we

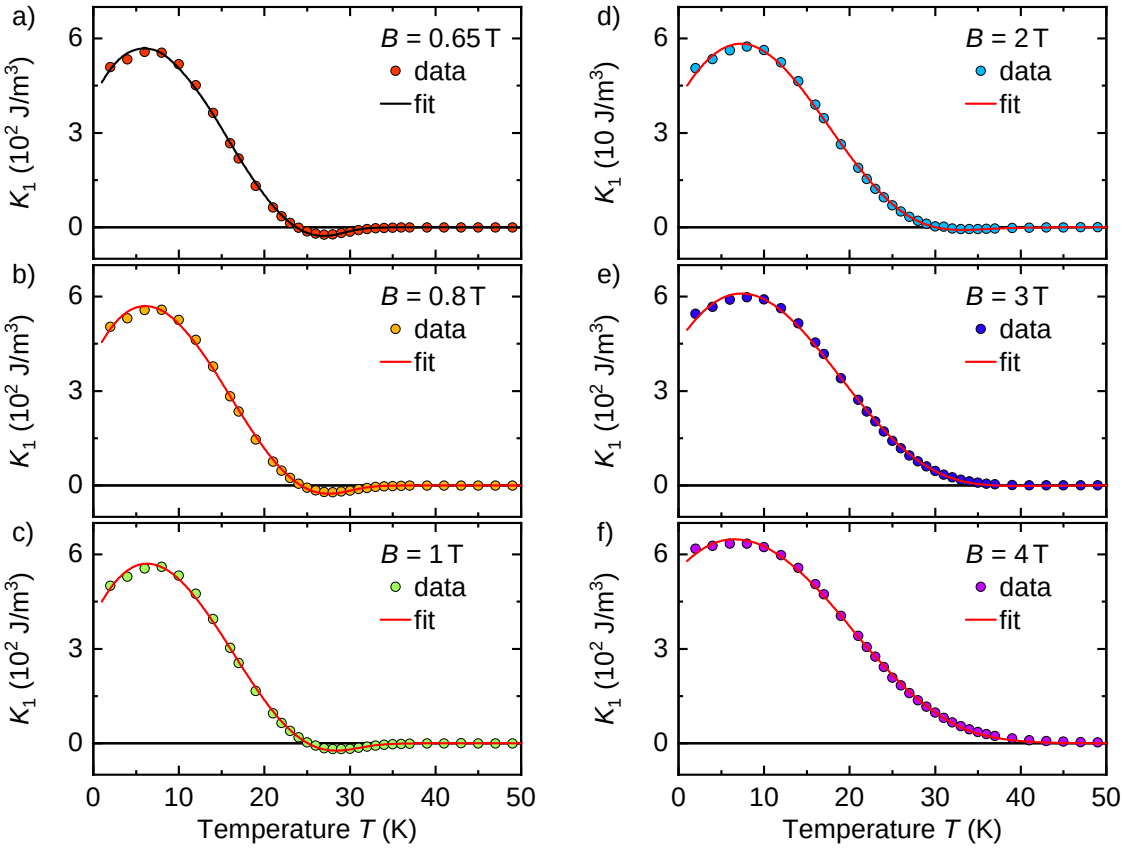

Figure C.6: Temperature evolution of anisotropy constant K_1 at a) $B = 0.65\,\mathrm{T}$, b) $B = 0.8\,\mathrm{T}$, c) $B = 1\,\mathrm{T}$, d) $B = 2\,\mathrm{T}$, e) $B = 3\,\mathrm{T}$ and f) $B = 4\,\mathrm{T}$. Solid lines denote fits according to Eq. 5.8.

present the same graphs for all six field magnitudes at which temperature dependent measurements were recorded. The graphs are shown in Fig. C.6. Fit function and results are discussed in Sec. 5.3.4.

C.3 Rotating field setup

In this section we present some measurements on the MnSi sample acquired in the rotating field setup. In Sec. C.3.1 we show exemplary measurements on a cubic sample. Sections C.3.2 and C.3.3 are dedicated to flaws of the capacitive readout and rotational hysteresis, respectively. We present additional data on the temperature dependent torque in Sec. C.3.5 and the field magnitude dependent anisotropy constants in Sec. C.3.4. The fit parameters related to field gradients are presented in Sec. C.3.6 and physically interpreted in Sec. C.3.7. Finally, we compare measurements and simulation at different misalignment angles γ_r in Sec. C.3.8.

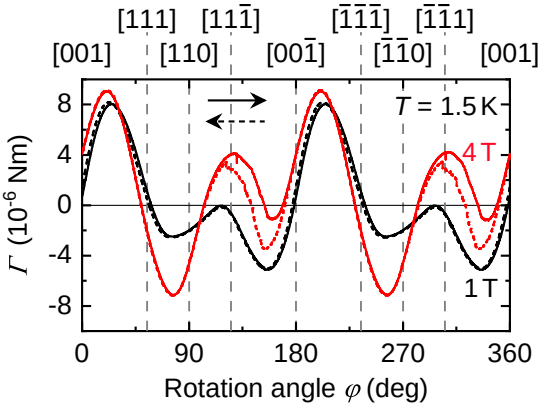

Figure C.7: Torque curves measured on the cubic sample in the rotating field setup at $T = 1.5\,\mathrm{K}$ and magnetic fields of $B = 1\,\mathrm{T}$ and $B = 4\,\mathrm{T}$.

C.3.1 Measurements on a cubic sample

As described in Sec. 3.3.3, the alignment of cantilever and magnet as well as the sample position relative to the field centre were poorly controlled during our measurements on the cubic MnSi sample in the rotating field setup. Moreover, the probe utilized for these measurements featured a magnetic capillary as stated in Sec. 3.3.1. As a result, torque curves recorded in this configuration were strongly deformed. This is examplarily shown in Fig. C.7 for measurements at a temperature of $T = 1.5\,\mathrm{K}$ and field magnitudes of $B = 1\,\mathrm{T}$ (black) and $B = 4\,\mathrm{T}$ (red). Solid lines represent rotations in the positive rotation sense, dashed lines depict rotations in the negative rotation sense.
The torque curves recorded at $B = 1\,\mathrm{T}$ distinctly deviate from the ideal shape. This may stem from the poor position and orientation control of the sample. In particular, a significant vertical distance between sample position and field centre may impose severe field gradients on the sample. Yet the principal shape of the expected pattern is still maintained at $B = 1\,\mathrm{T}$. In contrast, the curve recorded at $B = 4\,\mathrm{T}$ is altered to an extent that renders evaluation impossible. In particular, the minima at $\sim$160° and $\sim$340° are lifted so much that they are no longer the global minima. These are now represented by the minima at $\sim$80° and $\sim$260° which have been lowered. However, the global maxima at $\sim$20° and $\sim$200° remain in place. As a consequence, the sign changes between the global extrema and between the local extrema no longer correspond to the [001]- and the [110]-directions. We suggest these deformations to be caused by stronger vertical field gradients at this larger field magnitude.
In addition to the deformation of the principal shape, a hysteretic eye has opened up in the region of the now local extrema. We find no evidence for such a large rotational hysteresis in the field-polarized state with any of our other anisotropy measurement configurations. Thus it appears natural to attribute the hysteresis to a technical issue of the specific configuration. We suggest that the observed hysteresis is caused by hysteretic magnetic switching of the capillary during rotation at fields above $\sim$1.5 T. In the picture of this suggestion, the probe is pulled from its free-hanging position

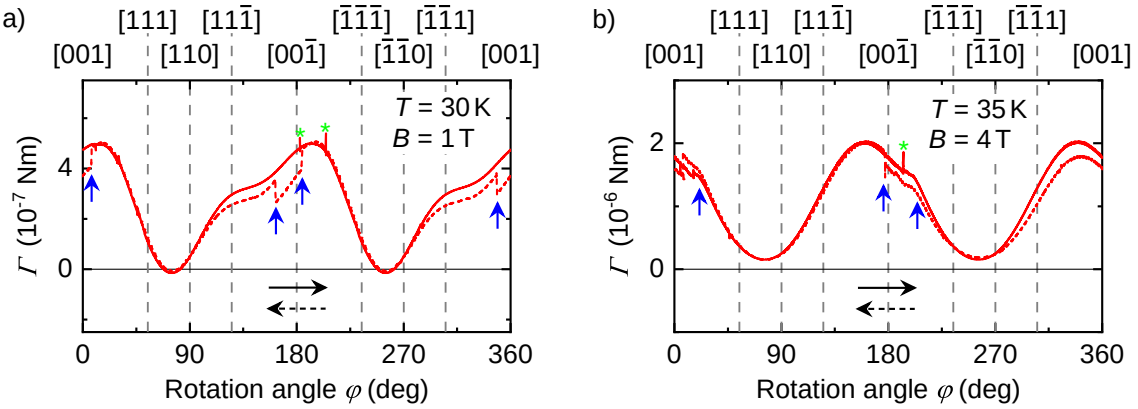

Figure C.8: Torque curves measured on the spherical sample in the rotating field setup. Blue arrows and green asterisks mark features we devote to readout errors due to magnetic flux jumps rather than actual magnetic torque signal from the sample. a) Torque at $T = 30\,\mathrm{K}$ and $B = 1\,\mathrm{T}$. b) Torque at $T = 35\,\mathrm{K}$ and $B = 4\,\mathrm{T}$.

in the middle of the magnet bore to the bore's edges by the magnetic force acting on the capillary. Depending on the capillary's magnetization direction, the probe is pulled to either one side of the bore or the other. A switching of this direction during rotation thus changes the angle between cantilever and gravity, field direction and field gradients' directions. These changes can be sufficient to explain the observed hysteresis. Due to the strong disturbances, a proper evaluation of the data obtained on the cubic sample in the rotating field setup is out of question.

C.3.2 Spurious features in the capacitive readout induced by magnetic flux jumps

The superconducting split coil providing horizontal field exhibited large flux jumps during operation. As a consequence, capacitance readout was disturbed in the form of individual spikes, discontinuous capacitance jumps or excessive noise. This is illustrated in Fig. C.8. Panel a) shows the torque measured at $B = 1\,\mathrm{T}$ and $T = 30\,\mathrm{K}$. Green asterisks mark individual spikes, blue arrows mark discontinuous jumps. These readout errors are easy to correct by scrapping individual points to remove a spike or shifting the region between two discontinuous jumps.
Panel b) displays the torque measured at $B = 4\,\mathrm{T}$ and $T = 35\,\mathrm{K}$. Again, an individual spike is marked by the green asterisk. In the region between the blue arrows the otherwise smooth torque curve appears rather scrawly during both up- and downsweep. This may be caused by excessive noise smoothed out by the capacitance bridge's internal averaging. Such a readout error is harder to correct, but may be overcome by appropriately smoothing the curve. If this is not possible, the error may severely disturb our fitting procedure (cf. Fig. C.11 c)).
We note that all shown examples of erroneous readout appear close to $\varphi = 0°$ or $\varphi = 180°$, i.e. in the regime in which the field of the split coil is close to zero. Thus

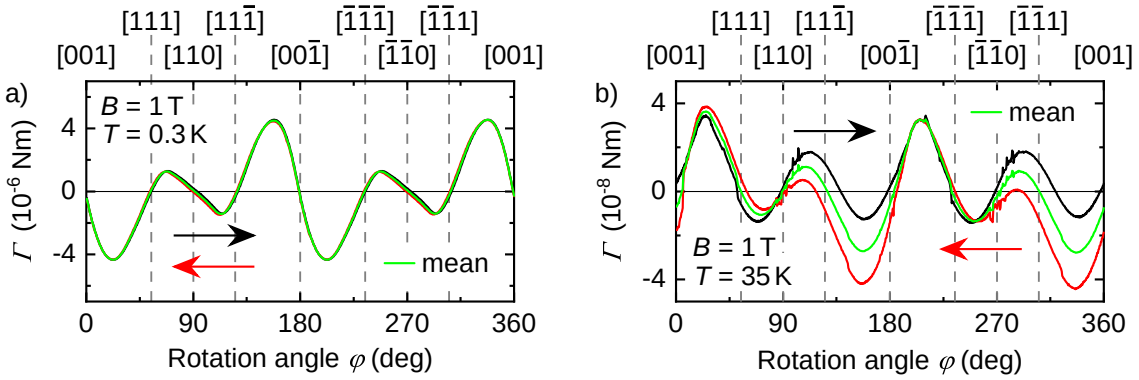

Figure C.9: Torque curves measured on the spherical sample in the rotating field setup at $B = 1\,\mathrm{T}$ and temperatures of a) $T = 0.3\,\mathrm{K}$ and b) $T = 35\,\mathrm{K}$. Black and red lines denote opposite directions of rotation, green lines represent the mean between "up"- and "down" rotations.

it appears reasonable to attribute such errors to flux jumps near sign reversal of the split coil's field.

C.3.3 Rotational hysteresis

During rotation scans in the AMI setup, we recorded the angular dependence of torque with both rotation senses. At field magnitudes below H_{c2} we observe a large rotational hysteresis that results from the magnetic state of the sample (cf. Sec. 5.4.1). Above H_{c2}, the sample is in a field-polarized state and we do not expect rotational hysteresis from the sample.
In Fig. C.9 a) we present the torque measured at $B = 1\,\mathrm{T}$ and $T = 0.3\,\mathrm{K}$ for positive (black) and negative (red) rotation sense. The rotational hysteresis is barely visible by eye. The small angular deviation corresponds to the hysteresis of the magnet system as discussed in Sec. A.4.1. We take the mean of both rotation sense curves (green line) for evaluation.
In Fig. C.9 b) we present the torque measured at $B = 1\,\mathrm{T}$ and $T = 35\,\mathrm{K}$ for both rotation senses as black and red lines. Here, a distinct rotational hysteresis is observed that comprises a vertical rather than a horizontal shift. We suggest that this hysteresis results from an altered evolution of the field gradient vector as a result of differently pronounced hystereses in the solenoid and the split coil. The same hysteresis is present but negligible at 0.3 K where the absolute torque signal is two orders of magnitude larger than at 35 K. The method of taking the average of both rotation senses is applied to high temperature measurements, too. As illustrated in Fig. C.9 b), the mean curve (green line) is distinctly less distorted from the ideal shape than the measured torque.

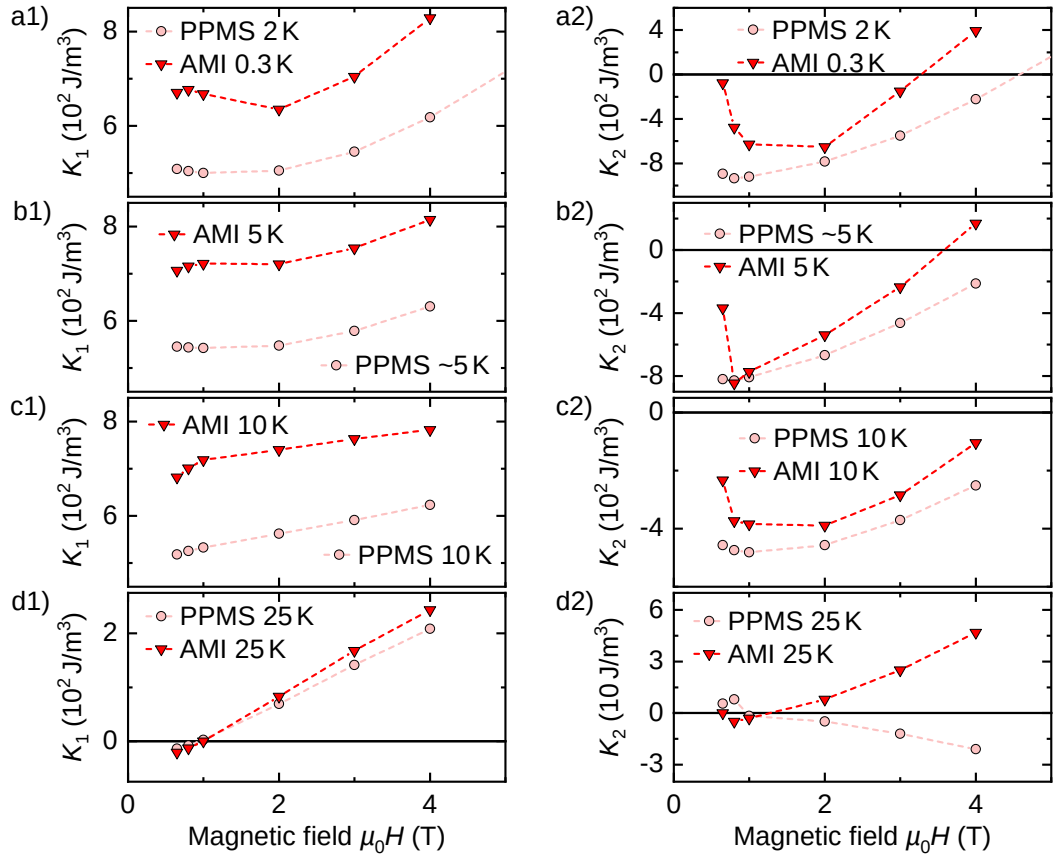

Figure C.10: Dependence of K_1 and K_2 on magnetic field magnitude at temperatures of a) 0.3 K, b) 5 K, c) 10 K and d) 25 K.

C.3.4 Magnetic field dependence of torque and anisotropy constants

We present anisotropy constants K_1 and K_2 extracted from AMI data with the direct fitting method employing Eq. 5.2 in dependence of the applied field magnitude. We carried out rotation scans at six field magnitudes from 0.65 T up to 4 T at several temperatures. Regarding the evolution described along the PPMS data (cf. Sec. 5.3.1), this covers the low field regime only. Thus an extended discussion of the field dependence is inadequate.

Anisotropy constants extracted from AMI data are presented as triangles in Fig. C.10. Graphs on the left hand side show K_1, graphs on the right hand side depict K_1. From top to bottom, the data corresponds to temperatures at 0.3 K, 5 K, 10 K and 25 K. For comparison, PPMS data have been included as semi-transparent circles. However, no PPMS data are available at 0.3 K and 5 K. In Fig. C.10 a1), we show the lowest available temperature in the PPMS of 2 K. In Fig. C.10 b1), we show the arithmetic mean of the values extracted at 4 K and 6 K.

Similar to the temperature dependence presented in Sec. 5.3.2, K_1 extracted from AMI data resembles the behavior obtained from the PPMS data but yields values

that are ∼30 % larger especially at low temperatures. At 25 K, we observe the sign change at ∼1 T in both data sets. For K_2, we observe little agreement of AMI and PPMS data. K_2 derived from AMI data has a stronger tendency towards positive values compared to K_2 from PPMS data. At 25 K, AMI and PPMS data exhibit similar behaviors with opposite sign. The comparison of the anisotropy constants' field magnitude evolution substantiates our conclusion that K_1 can be determined with an uncertainty of several tens of percent while K_2 cannot be determined even qualitatively from our experiments.

C.3.5 Additional temperature dependent torque data and anisotropy constants

In this section we present the torque during rotation scans at $B = 4\,\mathrm{T}$ and a comparison of our various data sets of K_1 and K_2 extracted from temperature dependent AMI data. Torque curves at $B = 4\,\mathrm{T}$ and temperatures from $T = 0.3\,\mathrm{K}$ up to $T = 35\,\mathrm{K}$ are presented in Fig. C.11 a). As for the data at $B = 1\,\mathrm{T}$ presented in Fig. 5.7 a), we observe the expected shape due to magnetocrystalline anisotropy at low temperatures and a simple sine-shape at high temperatures. As described in Sec. 5.3.2, we can fit these curves via Eq. 5.2.
Figure C.11 b) shows the torque curves measured at $T = 30\,\mathrm{K}$ and $T = 35\,\mathrm{K}$ as solid lines together with the respective fits as dashed lines in analogy to Fig. 5.7 b). We find a good agreement of measurement and fit. Figure C.11 c) shows the same torque curves after subtraction of Γ_g as solid lines together with fits according to Eq. 5.1 as dashed lines in analogy to Fig. 5.7 c). Here, we still find a good agreement for the measurement at $T = 30\,\mathrm{K}$ with only minor deviations around $\varphi = 20°$ and $\varphi = 200°$. In contrast, the curve at $T = 35\,\mathrm{K}$ exhibits large deviations from the ideal shape resulting in a bad fit outcome. The observed deviations are caused by perturbations described in appendix C.3.2. The good agreement of fit and measured torque at $T = 30\,\mathrm{K}$ confirms that we can neglect such perturbations except for measurements at highest temperatures and fields. Under these conditions, the error of K_1 and K_2 becomes larger than the value.
Figure C.11 d) shows the gradient contribution obtained from fitting and normalized with respect to the sample's magnetic moment M as solid lines. As described in Sec. 5.3.2, we use interpolated values from an existing data set for the magnetic moment M. In full analogy to Fig. 5.7 d), we obtain very different curves at different temperatures but small variations between measurements at high temperatures. The mean of the four high-temperature curves is depicted as dashed line. As described in the main text, we used this mean as a fixed gradient model during evaluation.
All four sets of extracted values of K_1 and K_2 are presented in Fig. C.11 e) and f), respectively. This includes the values extracted by direct fitting via Eq. 5.2 as circles, subtraction of individual gradients and fitting via Eq. 5.1 as upwards pointing triangles, subtraction of the mean gradient derived at $B = 1\,\mathrm{T}$ and fitting via Eq. 5.1 as downward pointing triangles and subtraction of the mean gradient derived at $B = 4\,\mathrm{T}$ and fitting via Eq. 5.1 as squares. Dashed lines are drawn by

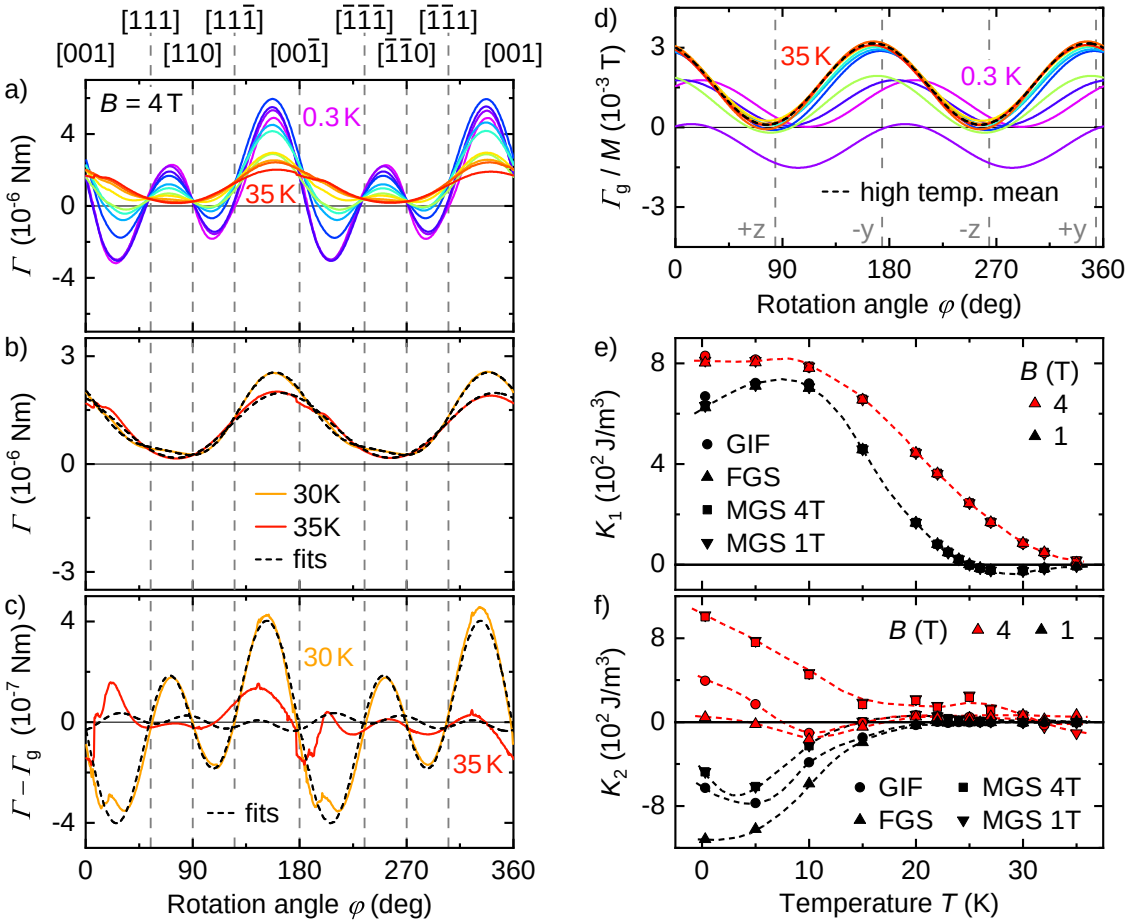

Figure C.11: Temperature dependence of torque and anisotropy constants. a) Torque curves as measured in the rotating field setup at $B = 4\,\mathrm{T}$ and temperatures from $T = 0.3\,\mathrm{K}$ to $T = 35\,\mathrm{K}$. b) Torque as measured at $B = 1\,\mathrm{T}$ and $T = 30\,\mathrm{K}$ and $T = 35\,\mathrm{K}$. Dashed lines represent fits according to Eq. 5.2. c) Torque at $B = 4\,\mathrm{T}$ and $T = 30\,\mathrm{K}$ and $T = 35\,\mathrm{K}$ after subtraction of fitted gradient contributions. Dashed lines represent fits according to Eq. 5.1. d) Fitted gradient contributions to the torque at $B = 4\,\mathrm{T}$ and temperatures from $T = 0.3\,\mathrm{K}$ to $T = 35\,\mathrm{K}$. The dashed line represents the mean of four gradient torque curves at high temperatures. e)-f) Anisotropy constants at K_1 and K_2 at magnetic fields of $B = 1\,\mathrm{T}$ and $B = 4\,\mathrm{T}$ versus temperature for different approaches to the gradient problem.

hand as a guide to the eye. We find excellent agreement of all data sets for K_1 with small outliers only at the lowest measured temperature. For K_2 we obtain large quantitative and qualitative differences. Only the data sets for the two fixed gradient approaches coincide which is somewhat surprising since a distinct difference between both gradient contributions is observed. The blatant inconsistency of the other data sets once again substantiates our assessment that K_2 is beneficial for our evaluation yet not determinable as a physical quantity from our experiments.

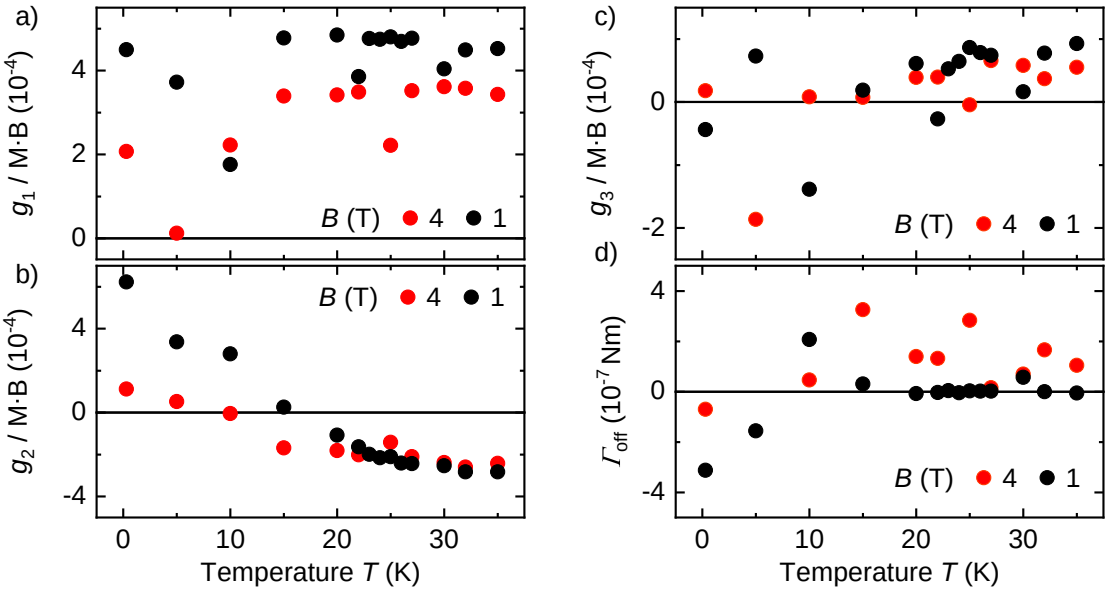

Figure C.12: Parameters a) Γ_{off}, b) g_1, c) g_2 and d) g_3 as obtained from fitting torque data with Eq. 5.2.

C.3.6 Fit parameters g_i and Γ_{off}

We present values of the fit parameters g_1, g_2, g_3 and Γ_{off} obtained from fitting the AMI torque data as measured via Eq. 5.2. For comparability, we normalize the gradient parameters with respect to the applied field's magnitude B and the sample's magnetic moment M. We use interpolated values from an existing data set for the magnetic moment M as described in Sec. 5.3.2.

Values of g_1, g_2 and g_3 obtained by fitting are shown in Fig. C.12 a), b) and c), respectively. In agreement with Figs. 5.7 d) and C.11 d) and in contradiction to the physical picture of a fixed gradient, we find values for the gradient parameters g_1, g_2 and g_3 widely varying with field and temperature. While values for g_1 remain nearly constant at high temperatures, there is still a distinct difference between values for $B = 1\,\text{T}$ and $B = 4\,\text{T}$. This difference becomes small at high temperatures for g_2 but only after a sign change for both fields which precludes any physical interpretation. g_3 also contains sign changes and exhibits a large scatter.

Fitted values of the parameter Γ_{off} are shown in Fig. C.12 d). We obtain values on the order of $10^{-7}\,\text{Nm}$ which is large compared to values obtained by fitting Eq. 5.1 to PPMS data. We have no physical explanation for such a shift, but finite values of Γ_{off} may occur due to deformations of the torque curves from ideal shape. Further, the presence of gradients shifts the symmetry line of a torque curve away from zero. We discuss this in more detail in the following section.

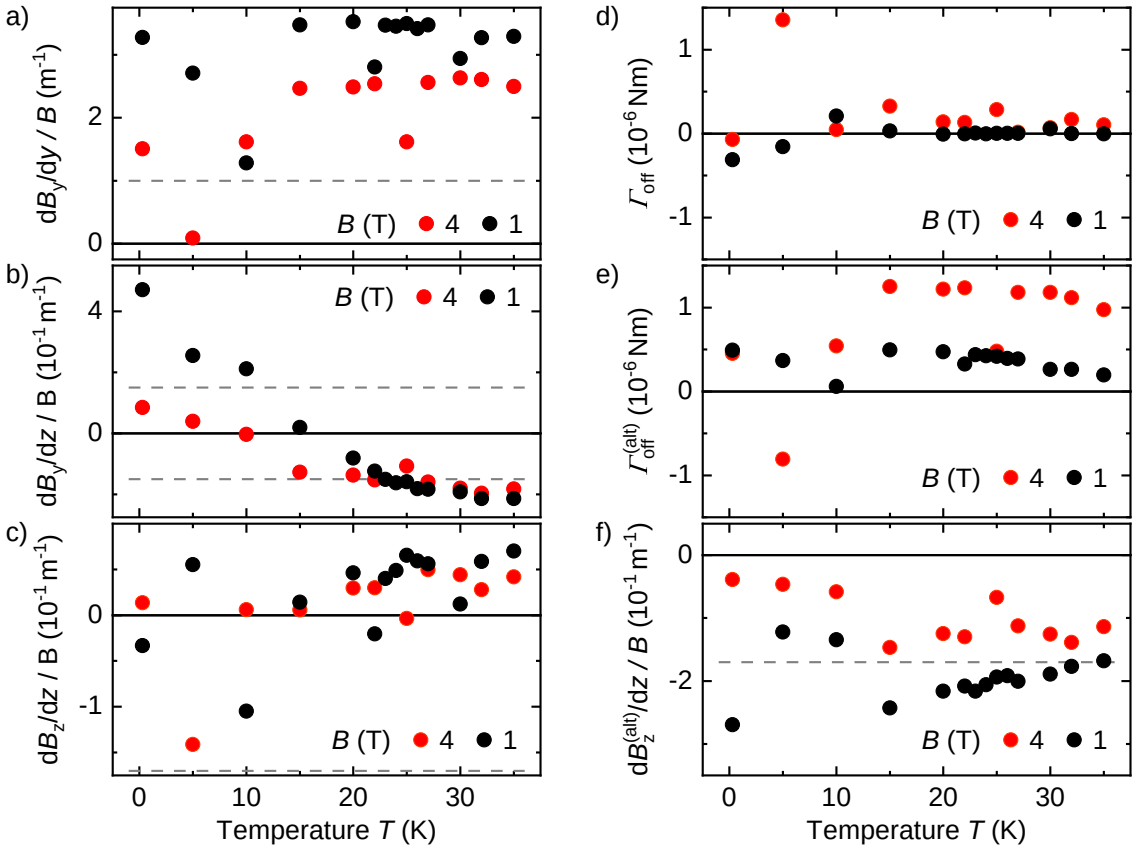

Figure C.13: a)-c) Magnitude of field gradients relevant to our experiments as obtained from fitting. d) Linear torque offset Γ_{off} as obtained from fitting. Gray dashed lines represent maximum estimates for the respective gradient's magnitudes. e) Linear torque offset Γ_{off} introduced by rescaling $\mathrm{d}B_{\mathrm{y}}/\mathrm{d}y$ and $\mathrm{d}B_{\mathrm{z}}/\mathrm{d}z$. f) Magnitude of $\mathrm{d}B_{\mathrm{z}}/\mathrm{d}z$ obtained by rescaling $\mathrm{d}B_{\mathrm{y}}/\mathrm{d}y$ to $1\,\mathrm{m}^{-1}$. The gray dashed lines represents the maximum estimate for the gradient's magnitude.

C.3.7 Magnitude of field gradients in the AMI vector magnet

In this section, we discuss the magnitude of field gradients as inferred from fitting parameters. With the help of numerical simulations, values of g_1, g_2 and g_3 can be interpreted as field gradients $\mathrm{d}B_{\mathrm{y}}/\mathrm{dy}$, $\mathrm{d}B_{\mathrm{y}}/\mathrm{dz}$ and $\mathrm{d}B_{\mathrm{z}}/\mathrm{dz}$, respectively. We plot the respective gradients per field magnitude in Fig. C.13 a), b) and c). The dashed horizontal lines represent our maximum estimates for the gradients as discussed in Sec. 3.3.1. We obtain values grossly exceeding these limits for the gradients of the split coil field B_{y}.

Equation 5.2 is overdefined by the terms g_1, g_3 and Γ_{off} since a cosine-term with linear offset is fully defined by two parameters. As a consequence, we can rescale the gradients shown in Fig. C.13 a) without altering the shape of the resulting torque by simultaneously adjusting the vertical solenoid gradient $\mathrm{d}B_{\mathrm{z}}/\mathrm{dz}$ and the offset Γ_{off} shown in Fig. C.13 d). In an attempt to create a gradient parameter set consistent

with our considerations in Sec. 3.3.1, we scale all values of $\mathrm{d}B_\mathrm{y}/\mathrm{dy}$ down to our maximum estimate of $1\,\mathrm{m}^{-1}$. The values of Γ_off and $\mathrm{d}B_\mathrm{z}/\mathrm{dz}$ necessary to keep the torque unchanged are presented in Fig. C.13 e) and f), respectively. We obtain values larger than $1 \cdot 10^{-6}\,\mathrm{Nm}$ for Γ_off and values clearly exceeding our maximum estimate for $\mathrm{d}B_\mathrm{z}/\mathrm{dz}$.
The variation of field gradients does not comply with our physical perception of a fixed field gradient and their magnitude suggested by our fit results grossly exceeds our maximum estimates which are based on experimental Hall sensor data. In addition, values suggested by our fit results for Γ_off are on the same order of magnitude as our torque signals' amplitudes which lacks physical explanation. All these observations hint at the existence of large additional perturbations of our experiments. Within the scope of this thesis, we were unable to identify their origin.

C.3.8 Measurements at different misalignment γ_r

We repeated some rotation scans performed at $\gamma_\mathrm{r} = 9°$ at otherwise identical conditions and $\gamma_\mathrm{r} = 0°$. Simulations suggest that the comparison of the respective torque curves should allow to determine the sample's chirality. Unfortunately, this was not the case with our results. We illustrate this in Fig. C.14. Panels a1), b1) and c1) display experimental torque curves, panels a2), b2) and c2) show simulated torque. The field magnitude is $B = 1\,\mathrm{T}$ in all cases. The temperature is $T = 0.3\,\mathrm{K}$ in a1) and a2) and $T = 5\,\mathrm{K}$ in b1), b2), c1) and c2). Simulated torque curves include the experimental misalignment. Black lines denote torque curves at $\gamma_\mathrm{r} = 0°$. Red continuous lines represent torque measured at $\gamma_\mathrm{r} = 9°$, red and green dashed lines depict torque simulated for $\gamma_\mathrm{r} = 9°$ in right-handed and left-handed MnSi, respectively.
The simulations show different alterations of the torque curve by introduction of the misalignment for left- and right-handed MnSi. For left-handed crystals, the local extrema both shift towards positive values whereas they move towards negative values in right-handed MnSi. The global extrema decrease for both chiralities, yet we observe a larger decrease of the maximum in left-handed and a larger decrease of the minimum in right-handed crystals. Unfortunately, the experimental torque shows a mixture of both alterations. The local extrema slightly shift towards positive values as simulated for left-handed MnSi. At the same time, the change of the global minimum is larger than that of the global maximum as simulated for right-handed MnSi. Further, the global maximum does not decrease, but increases with finite γ_r. This contradiction prohibits the determination of our sample's chirality from experimental data.
Beside the height of the extrema, also the angular position of the inflection point between the global extrema shifts in different directions for right- and left-handed MnSi. This is visible for simulated torque in Fig. C.14 a2), b2) and c2) and further illustrated by the fitting parameter δ_r in Fig. C.14 d). Obviously, the inflection point shifts to larger angles for left-handed and towards lower angles for right-handed MnSi. According to the fit parameter δ_r, the inflection point of experimental torque

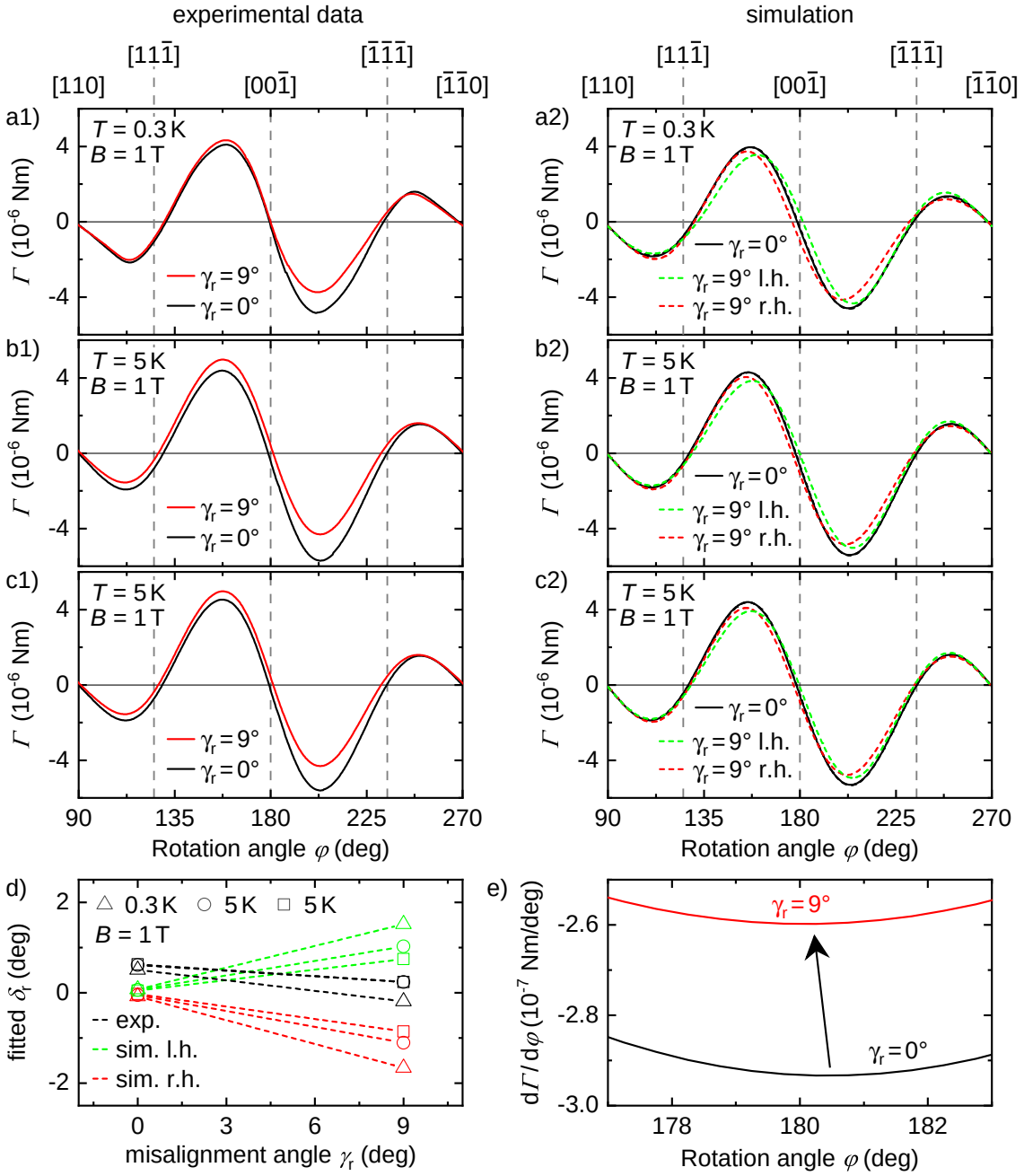

Figure C.14: Comparison of data obtained at $\gamma_r = 9°$ and $\gamma_r = 0°$. a)-c) Experimental (left) and simulated (right) torque curves. d) Misalignment δ_r obtained from fits of experimental torque curves and simulations for both left- and right-handed MnSi. e) Derivative of torque curve fits around the extremum at 180°.

curves shifts towards lower angles. This can not be recognized in Fig. C.14 a1), b1) and c1) where the red line rather appears to be shifted to larger angles around ⟨001⟩. However, this impression results from a vertical shift rather than a horizontal one. For confirmation, we show the derivative of the fit to the measured torque curve in Fig. C.14 e). Here, we note that the minimum moves towards lower angles when changing γ_r from 0° to 9°. Due to the contradictory behavior of the extrema, we still refrain from assigning a chirality.
The alteration of the experimental torque curve when changing γ_r is not consistent with the simulated torque. This suggests that while changing γ_r, we inadvertently change some other quantity as well. As an example, small changes of the horizontal position of the sample may result in a different horizontal field gradient.

D Anisotropic magnetization in the modulated states of MnSi

In this appendix we provide additional information on the torque investigations in the modulated states of MnSi. Analogous to Sec. 5.4, we discuss $M_\perp = \Gamma/B$ instead of the measured torque Γ. Section D.1 is dedicated to field rotations. In Sec. D.2, we address field scans at fixed orientations.

D.1 Field rotations

In the following, we present additional data recorded during field rotations at field magnitudes $B < \mu_0 H_{c2}$. In Sec. D.1.1, we show a full set of magnetization curves including six full rotations. Section D.1.2 is dedicated to the temperature evolution of magnetization curves at $B = 0.1\,\mathrm{T}$ and Sec. D.1.3 addresses the evolution of magnetization curves with increasing field magnitude at a fixed temperature of $T = 28.5\,\mathrm{K}$.

D.1.1 Full rotation measurement data

As described in Sec. 5.2.2, each rotation scan in the rotating field setup comprises six full rotations of the magnetic field vector. In chronological order, we perform two full rotations in the positive rotation sense followed by two full rotations in the negative rotation sense and then two more rotations in the positive rotation sense. This means that the rotation sense is reversed twice during a complete rotation scan. As further stated, we show only the last full rotations for each rotation sense when discussing the data in Sec. 5.4.1 and appendices D.1.2 and D.1.3. As a consequence, the presented magnetization curves do not include regimes of reorientation after a reversal of the rotation sense.
In this section, we present a full set of magnetization curves during six rotations. Figure D.1 a) shows the first and second rotations in the positive rotation sense as black continuous and red dashed lines, respectively, followed by first and second rotations in the negative rotation sense depicted by a green continuous and a blue dashed line, respectively. All curves begin and end at $\varphi = 96°$. It is evident that, after a short period of reorientation, the first and second rotations yield identical magnetization curves for each rotation sense. Figure D.1 b) shows the second rotation in the negative rotation sense again for reference which is follow by a third and fourth rotation in the positive rotation sense. These are depicted as solid magenta and dashed cyan lines. Again, both rotations in the positive rotation sense yield

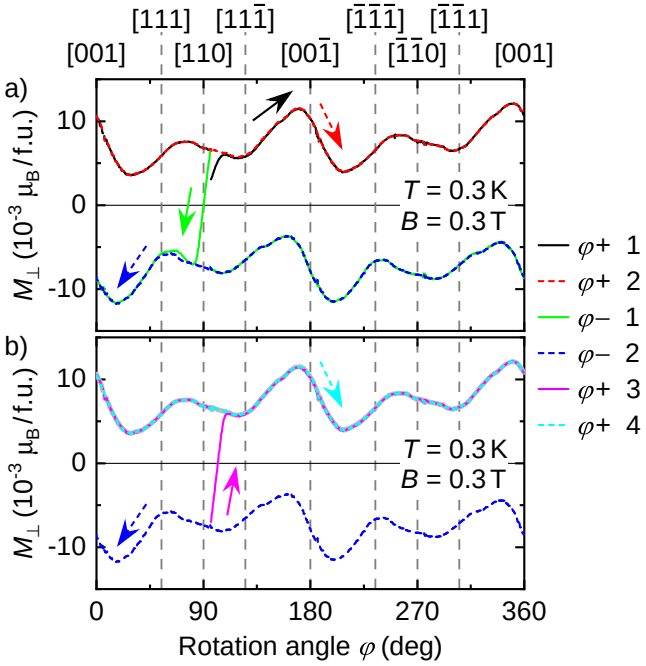

Figure D.1: Anisotropic magnetization $M_\perp$ measured during field rotations at $B = 0.3\,\mathrm{T}$ and $T = 0.3\,\mathrm{K}$. The curves are recorded in chronological order as indicated by the legend: a) Two full rotations in the positive rotation sense ($\varphi+$ 1 and $\varphi+$ 2) are followed by two full rotations in the negative rotation sense ($\varphi-$ 1 and $\varphi-$ 2). b) Then two more full rotations are performed in the positive rotation sense ($\varphi+$ 3 and $\varphi+$ 4). The rotation labelled "$\varphi+$ 2" is included in panel b) as gray continuous line. All rotations begin and end at $\varphi = 96°$.

identical results after a short period of reorientation. The second rotation in the positive rotation sense is included in Fig. D.1 b) as gray solid line and coincides perfectly with the fourth rotation in the positive rotation sense. The magnetization curves shown as continuous and dashed lines in Fig. 5.13 a) of the main text are identical to the cyan and blue dashed lines in Fig. D.1, respectively.

D.1.2 Temperature evolution at 0.1 T

In Sec. 5.4.1, we showed magnetization curves recorded during rotation scans at $B = 0.3\,\mathrm{T}$ and temperatures from $T = 0.3\,\mathrm{K}$ up to $T = 28.5\,\mathrm{K}$. In this section, we provide additional data measured at $B = 0.1\,\mathrm{T}$ and temperatures from $T = 0.3\,\mathrm{K}$ up to $T = 35\,\mathrm{K}$. The corresponding magnetization curves are shown in Fig. D.2. Panels are ordered such that the temperature increases from a) to h). Continuous and dashed lines denote positive and negative rotation sense, respectively. Consistent with the measurements at $B = 0.3\,\mathrm{T}$, we observe a large rotational hysteresis at low temperatures that decreases with increasing temperature and vanishes at T_c. Temperatures above T_c are displayed in panel h). Here, we observe a very small $\sin(2\beta)$-shaped signal shifted towards positive values. We attribute this to the presence of field gradients as discussed extensively for measurements in the field-

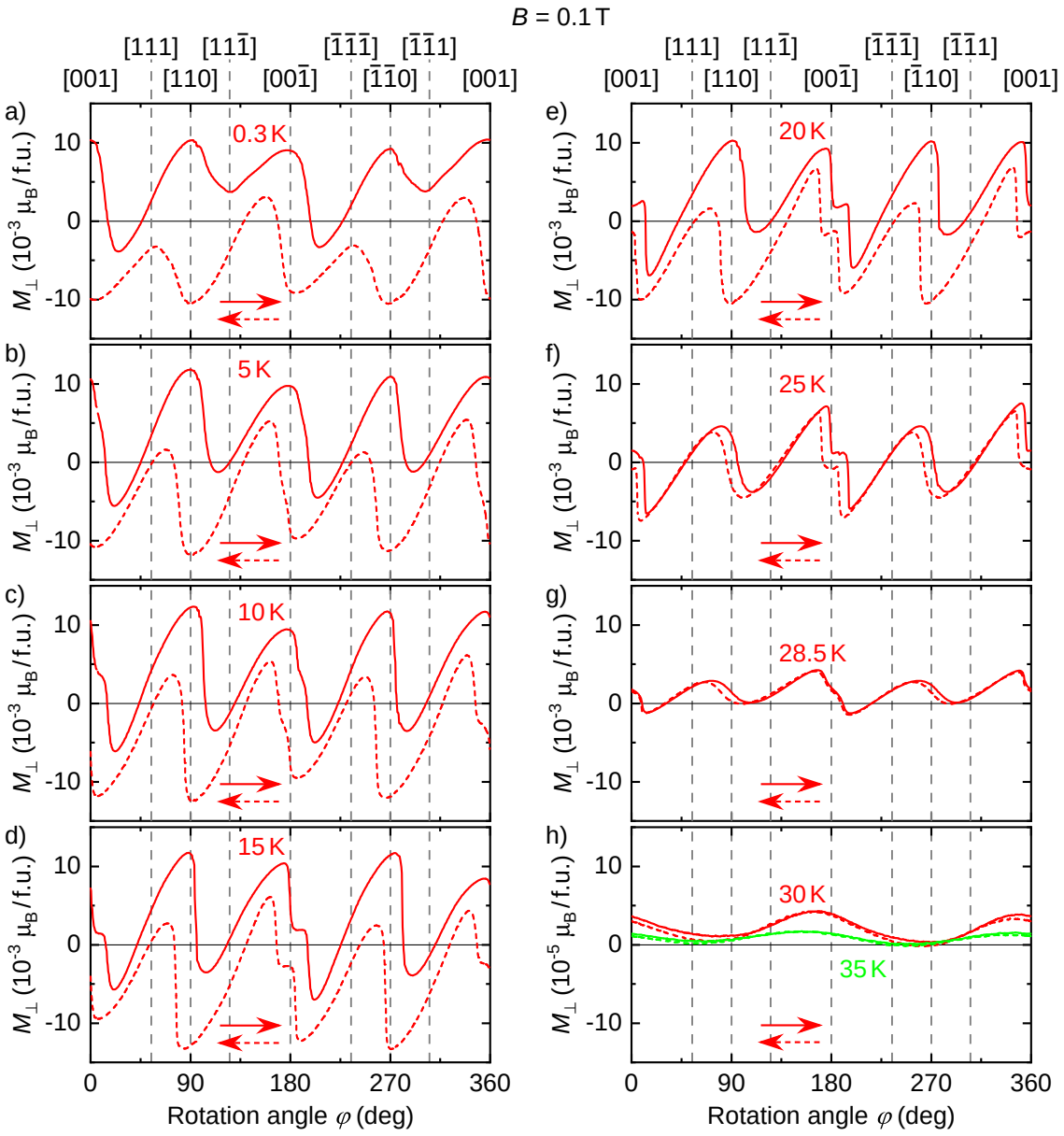

Figure D.2: Temperature evolution of the anisotropic magnetization $M_\perp$ during field rotations at $B = 0.1\,\mathrm{T}$. Continuous lines denote positive rotation sense, dashed lines denote negative rotation sense.

polarized state. Temperatures just below T_c, i.e. $T = 28.5\,\mathrm{K}$ and $T = 25\,\mathrm{K}$ are displayed in panels g) and f), respectively. The magnetization curves resemble to some extent the shape described by Eq. 5.1 with global maxima and minima around $\langle 001 \rangle$-directions and local maxima and minima around $\langle 110 \rangle$-directions. However, there are two distinct differences to that behavior: (i) There is an additional shoulder between the global extrema around the $\langle 001 \rangle$-direction and (ii) between their extrema, the curves resemble a smoothed sawtooth shape rather than a sinusoidal behavior. As a tendency, these deviations are more pronounced at $T = 25\,\mathrm{K}$ compared to

$T = 28.5\,\mathrm{K}$. Towards lower temperatures, magnetization curves maintain four pairs of maxima and minima as well as a two-fold symmetry, but the relative heights as well as the positions of the extrema are shifted such that the shape described by Eq. 5.1 is no longer resembled. The additional shoulder between the extrema around the $\langle 001 \rangle$-direction decreases below $T = 15\,\mathrm{K}$ and vanishes below $T = 10\,\mathrm{K}$.
As we argue in Sec. 5.4.3, a straightforward interpretation of anisotropic magnetization data in non-collinear phases is difficult at best. For the measurements exclusively involving the conical phase, we observe smooth curves following a known behavior (cf. Sec. 5.4.1). Still, a quantitative evaluation is not possible within this thesis. For the data presented in this section, we encounter two additional issues that impede the understanding of our observations: (i) Due to the anisotropy of $H_{\mathrm{c1}} \approx 0.1\,\mathrm{T}$, the phase boundary between helical and conical phase may be crossed during rotation. (ii) In the helical phase, the pitch vector of the helix is pinned to $\langle 111 \rangle$-directions. While the applied field may not be sufficient to reorient the pitch vector towards the field direction as in the conical phase, it is significantly larger than the $\sim$50 mT needed to depopulate unfavorable domains. As a consequence, domains with helical pitch vectors along different $\langle 111 \rangle$-directions may continuously be de- and repopulated during field rotation. Understanding the anisotropic magnetization resulting from such dynamics requires extensive efforts in the form of theoretical considerations and numerical simulations and is therefore a task for future investigations.

D.1.3 Field dependence at 28.5 K

In Secs. 5.4.1 and D.1.2, we showed rotation scans at fixed field magnitudes of $B = 100\,\mathrm{mT}$ and $B = 300\,\mathrm{mT}$ and various temperatures that addressed helical and conical states, but not the skyrmion lattice phase. In this section, we present rotation scans at a fixed temperature of $T = 28.5\,\mathrm{K}$ and field magnitudes from $B = 50\,\mathrm{mT}$ up to $B = 300\,\mathrm{mT}$ thus addressing all three states of non-collinear magnetic order in MnSi. Magnetization curves are depicted in Fig. D.3. Panels are ordered such that the field magnitude increases from a) to h). Continuous and dashed lines denote positive and negative rotation sense, respectively. Consistent with rotation scans at various temperatures, we observe only small rotational hystereses.
All magnetization curves presented in Fig. D.3 b) - h) exhibit four pairs of maxima and minima and a two-fold symmetry. Field magnitudes of $B = 130\,\mathrm{mT}$ and $B = 300\,\mathrm{mT}$ are displayed in panels c) and d), respectively. Here, only the conical phase is stabilized and the corresponding magnetization curves exhibit a shape described by Eq. 5.1 in consistence with Sec. 5.4.1. As shown in panel f), the same behavior is observed at $B = 180\,\mathrm{mT}$ and $B = 200\,\mathrm{mT}$ where solely the skyrmion lattice phase is addressed. At the intermediate field magnitudes $B = 165\,\mathrm{mT}$ and $B = 250\,\mathrm{mT}$ depicted in panels e) and g), respectively, the relative heights and position of the extrema still resemble this shape, but we find distinct deviations from the sinusoidal behavior around the $\langle 001 \rangle$-direction. At $B = 150\,\mathrm{mT}$ illustrated in panel d), smaller deviations are observed around $\langle 110 \rangle$-directions. We suggest that these deviations are caused by transitions between conical state and skyrmion

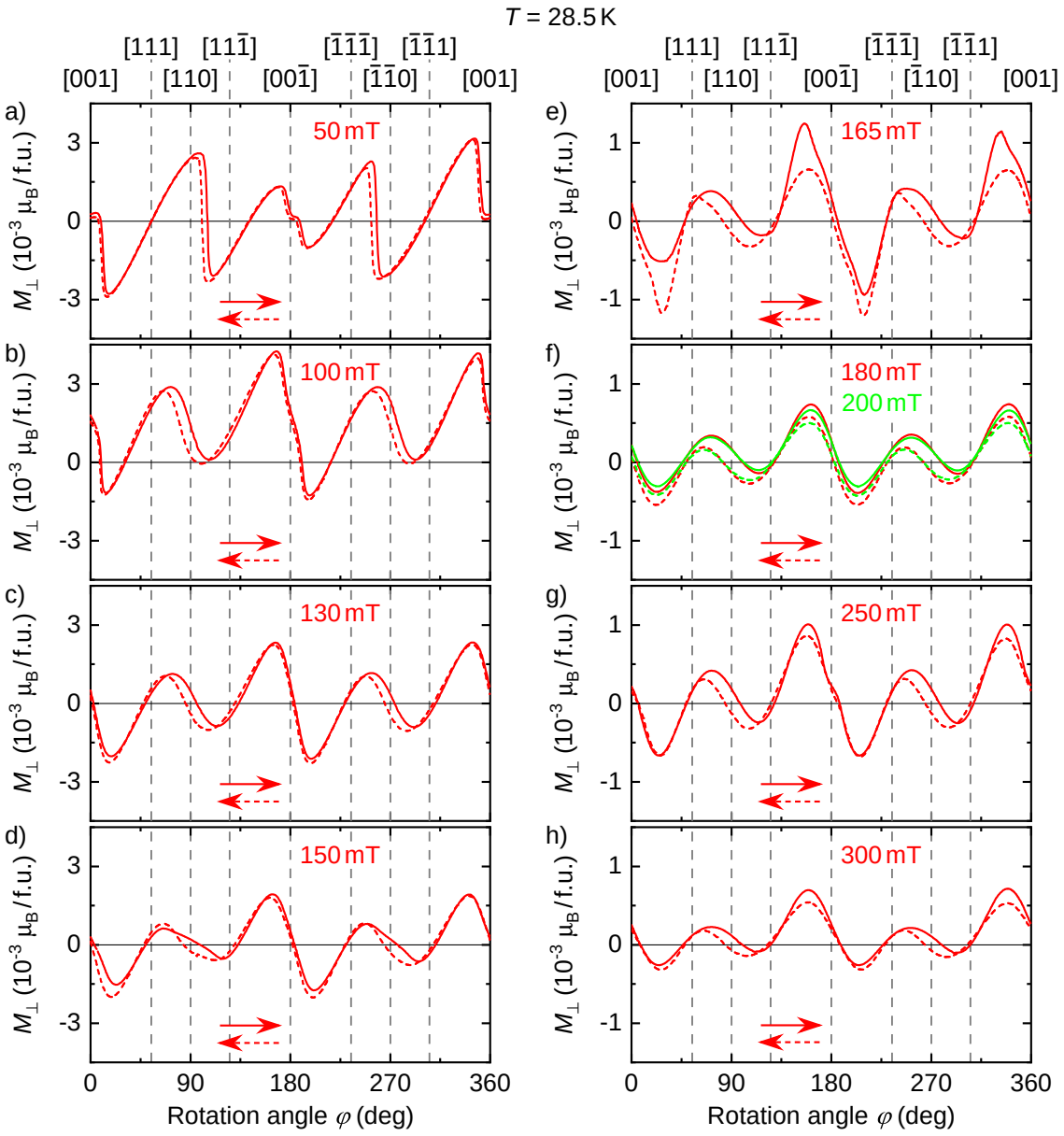

Figure D.3: Anisotropic magnetization $M_\perp$ during field rotations at $T = 28.5\,\mathrm{K}$ and field magnitudes from $B = 50\,\mathrm{mT}$ up to $B = 300\,\mathrm{mT}$. Continuous lines denote positive rotation sense, dashed lines denote negative rotation sense.

lattice phase during rotation due to the anisotropy of the critical fields H_{a1} and H_{a2}. Similarly, the magnetic order may change between helical and conical state during rotation at $B = 100\,\mathrm{mT}$ due to the anisotropy of H_{c1}. As already discussed in Sec. D.1.2 and shown again in panel b), the magnetization at this field magnitude resembles the behavior described by Eq. 5.1 with an additional shoulder at $\langle 001 \rangle$ and a tendency towards sawtooth-like behavior between its extrema.
At the lowest applied field magnitude of $B = 50\,\mathrm{mT}$ displayed in panel a), solely the helical phase is present. However, the field magnitude may be sufficient to cause

de- and repopulation of domains during rotation. We observe a more pronounced sawtooth-like behavior as well as a more distinct shoulder at ⟨001⟩ as compared to $B = 100\,\mathrm{mT}$. In addition, the heights and positions of extrema are shifted such that the well-known shape is no longer resembled. In particular, while ⟨001⟩-directions still represent centres of point symmetry for the magnetization curves of positive and negative rotation sense, this is no longer the case for ⟨110⟩-directions. More strikingly, the two-fold symmetry of the magnetization curves is broken in that the extrema around ⟨001⟩ are larger by a factor of ∼2 compared to the extrema around $\langle 00\bar{1}\rangle$. As stated in Sec. D.1.2, constructing a model capable of a sound and quantitative explanation for our observations is a task for future investigations.

D.2 Field scans

In this section, we present additional data recorded during field scans at fixed orientations. In Sec. D.2.1, we show a full set of field scans including six consecutive sweeps. We address deviations of field vectors from high symmetry directions in Sec. D.2.2 and hysteresis above H_{c2} in Sec. D.2.3. Signatures of the skyrmion lattice phase are presented in Sec. D.2.4. Section D.2.5 is dedicated to the temperature evolution of field scans with field vectors along ⟨001⟩- and ⟨110⟩-directions.

D.2.1 Full field scan data

As described in Sec. 5.2.2, our measurement procedure for field scans included six consecutive field sweeps. In chronological order, we first ramped the field up from zero to $B = +1\,\mathrm{T}$ followed by two iterations of sweeping down to $B = -1\,\mathrm{T}$ and back up to $B = +1\,\mathrm{T}$. Finally, the field was ramped back to $B = 0\,\mathrm{T}$. As further stated, we only present the last full sweep for each direction when discussing our data in Sec. 5.4.2 and appendices D.2.2, D.2.3, D.2.4 and D.2.5. In Fig. D.4, we present a full set of magnetization curves obtained from all six sweeps of a field scan at $T = 5\,\mathrm{K}$ and field applied along the ⟨111⟩-direction. Panel a) only includes the first three sweeps for clarity. In panel b), all six sweeps are displayed.
The initial magnetization curve starting from zero field is displayed as black continuous line. As stated in Sec. 5.2.2, we did not control field and temperature to provide a well-defined starting point for our field scan measurements. Consequently, the shape of the initial magnetization curve may depend on a poorly controlled starting point and is not further considered for interpretation. The diverging values towards zero field are an artifact of data evaluation owed to the fact that $B = 0$ is not crossed during this sweep. Subsequent to this initial magnetization, the field is swept down to $B = -1\,\mathrm{T}$ (red dashed line) and back up to $B = +1\,\mathrm{T}$ (dashed green line). We observe the behavior described in the main text for the respective experimental situation. After that, the field is once again ramped down to $B = -1\,\mathrm{T}$ (blue solid line) and back up to $B = +1\,\mathrm{T}$ (magenta solid line). We observe ideal coincidence of the first and second sweeps for increasing and decreasing field, respectively. The same

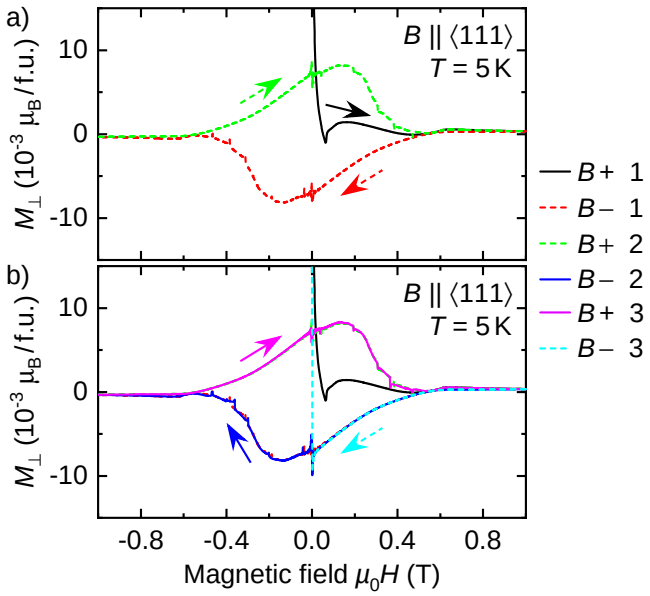

Figure D.4: Anisotropic magnetization $M_\perp$ during field scans between $B = \pm 1\,\mathrm{T}$ at $T = 5\,\mathrm{K}$ and field along $\langle 111 \rangle$. The curves are recorded in chronological order as indicated by the legend: a) The field is swept from 0 T up to +1 T ($B+$ 1), down to −1 T ($B-$ 1) and back up to +1 T ($B+$ 2). b) The consecutive sweeps down to −1 T and back to +1 T ($B-$ 2 and $B+$ 3) closely match the preceding curves. In a final sweep, the field is set back to zero ($B-$ 3).

holds true for the final sweep to $B = 0\,\mathrm{T}$ depicted as cyan dashed line. Again, the divergence at zero field is an artifact of data evaluation due to the curve terminating before reaching zero field.
The reproducibility of magnetization data during consecutive field sweeps in contrast to the initial sweep confirms that the behavior in the non-collinear states depends on field and temperature history and that we bring our sample into a well defined state by applying a sufficiently large field. In this work, we only address situations where we start from such a high-field state corresponding to a single domain with a unique helical pitch vector. Studying the anisotropic magnetization during the initial response of the material to an applied field in a situation of several equally populated domains after zero-field cooling may yield further insights. This is a task for future investigations.

D.2.2 Deviation from high symmetry directions

In Sec. 5.4.2, we stated that we observe a small asymmetry of the magnetization curves measured for increasing and decreasing field for a field vector applied along the $\langle 001 \rangle$-direction. We further stated that this asymmetry is more salient in the torque than in the magnetization. We show this in Fig. D.5 a) where we present the torque as measured during a field scan at $T = 5\,\mathrm{K}$ and field applied along $\langle 001 \rangle$. The continuous and dashed lines denote increasing and decreasing field, respectively. Note

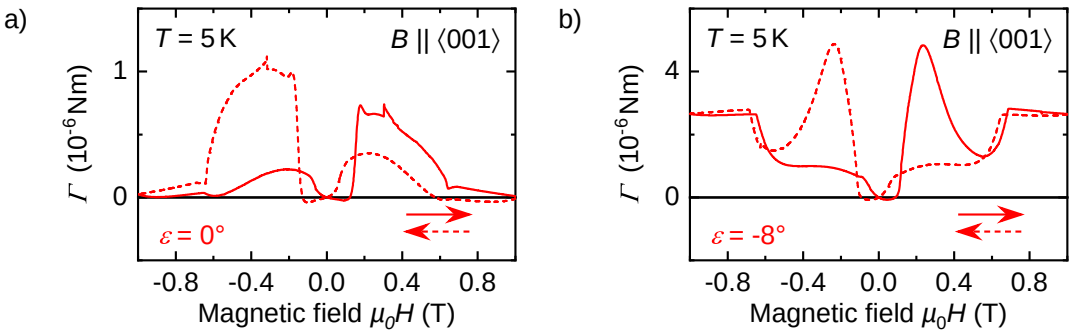

Figure D.5: Torque as measured during field scans between $B = \pm 1\,\mathrm{T}$ at $T = 5\,\mathrm{K}$ and field vector (nearly) along the $\langle 001 \rangle$-direction. Continuous lines denote increasing field, dashed lines denote decreasing field. a) Ideal alignment of B and $\langle 001 \rangle$. b) B and $\langle 001 \rangle$ are off by 8°.

that a point symmetry with respect to the origin for the anisotropic magnetization translates to a line symmetry with respect to zero field for the torque. In Fig. D.5 a), we find a distinct deviation from such a symmetry.
The observed asymmetry contrasts the results of Ref. [Bir09] in which torque curves obtained with an experimental approach similar to ours are presented. In this earlier work, the torque observed during field scans for field nominally aligned along the $\langle 001 \rangle$-direction exhibits little to no asymmetry regarding an inversion of the field direction. However, the relative orientation of field and sample has not been controlled as well during these previous measurements as compared to the present work. In our experiments, we investigated the evolution of the anisotropic magnetization for field vectors increasingly deviating from the crystal's high symmetry directions. For this purpose, we denote the angle between the applied field vector and the $\langle 001 \rangle$-direction for deviations along the rotation plane of our setup (cf. Sec 3.3.3) by ε. The sign of ε corresponds to deviations following the positive and negative rotation sense as defined in Sec. 5.2.2.
In Fig. D.5 b), we present the torque measured during a field scan at $T = 5\,\mathrm{K}$ and a field vector deviating from the $\langle 001 \rangle$-directions by $\varepsilon = -8°$. No asymmetry regarding an inversion of the field direction is observed. We further recognize that the absolute values of the torque signal at fields $|B| < \mu_0 H_{c2}$ are larger by a factor of $\sim$5 as compared to $\varepsilon = 0°$. This poses the question whether the asymmetry present at $\varepsilon = 0°$ actually vanishes or is merely masked by superposition of a large symmetric signal at field vectors deviating from $\langle 001 \rangle$. A closer look shows that the difference between the maxima at $\varepsilon = -8°$ is smaller by a factor of $\sim$9 compared to $\varepsilon = 0°$. We suggest that the great symmetry of torque curves presented in Ref. [Bir09] is owed to suboptimal alignment. The origin of the asymmetry observed in our measurements remains unresolved.
We performed field scans for various deviations from the $\langle 001 \rangle$-direction between $\varepsilon = -8°$ and $\varepsilon = +8°$. For the sake of completeness, we show the evolution of the magnetization curves in direct comparison to $\varepsilon = 0°$ in Fig. D.6. Continuous and dashed lines correspond to increasing and decreasing field, respectively. The

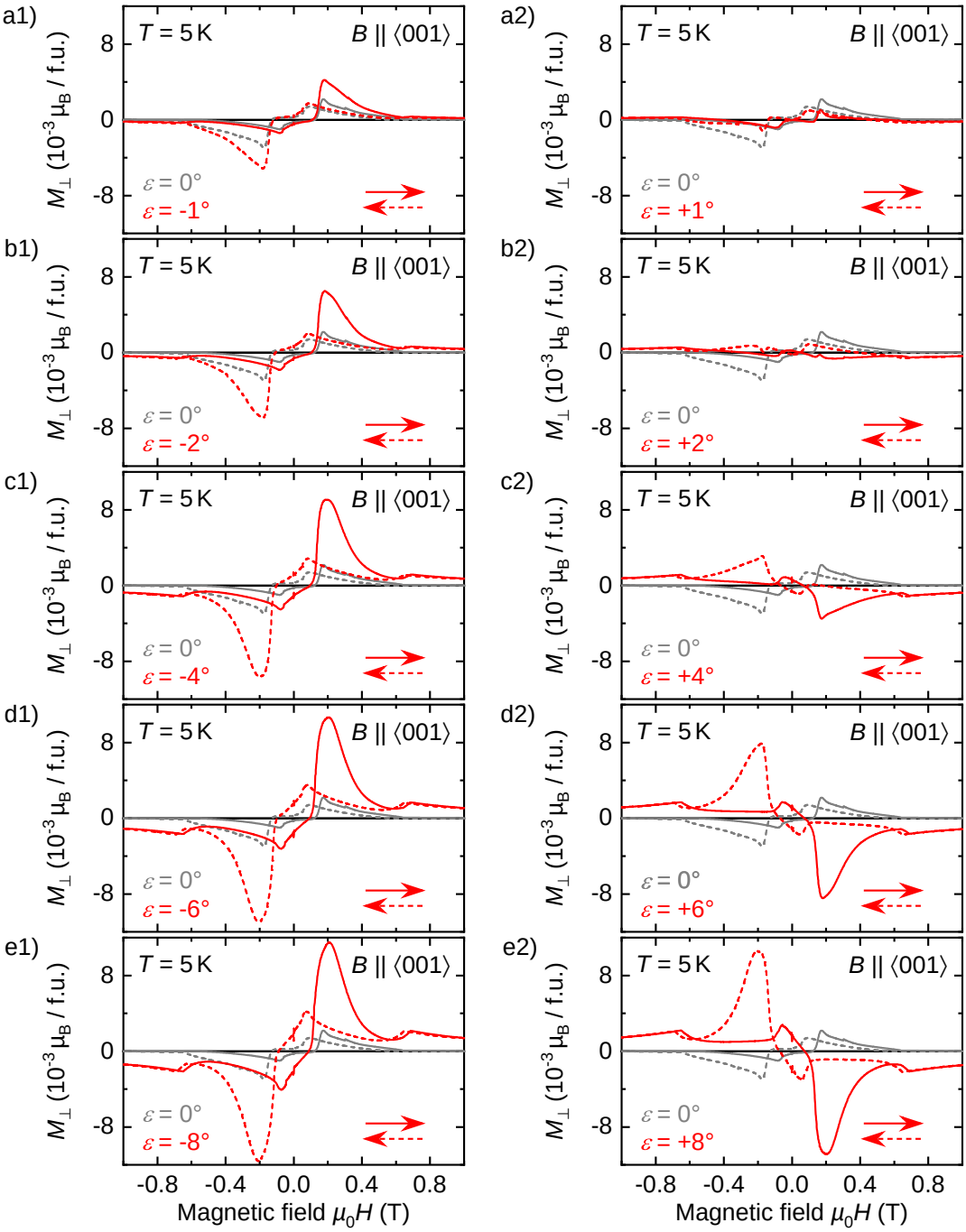

Figure D.6: Evolution of the anisotropic magnetization $M_\perp$ during field scans between $B = \pm 1\,\mathrm{T}$ at $T = 5\,\mathrm{K}$ and increasing deviation angles ε between field vector and the $\langle 001 \rangle$-direction. Continuous lines denote increasing field, dashed lines denote decreasing field.

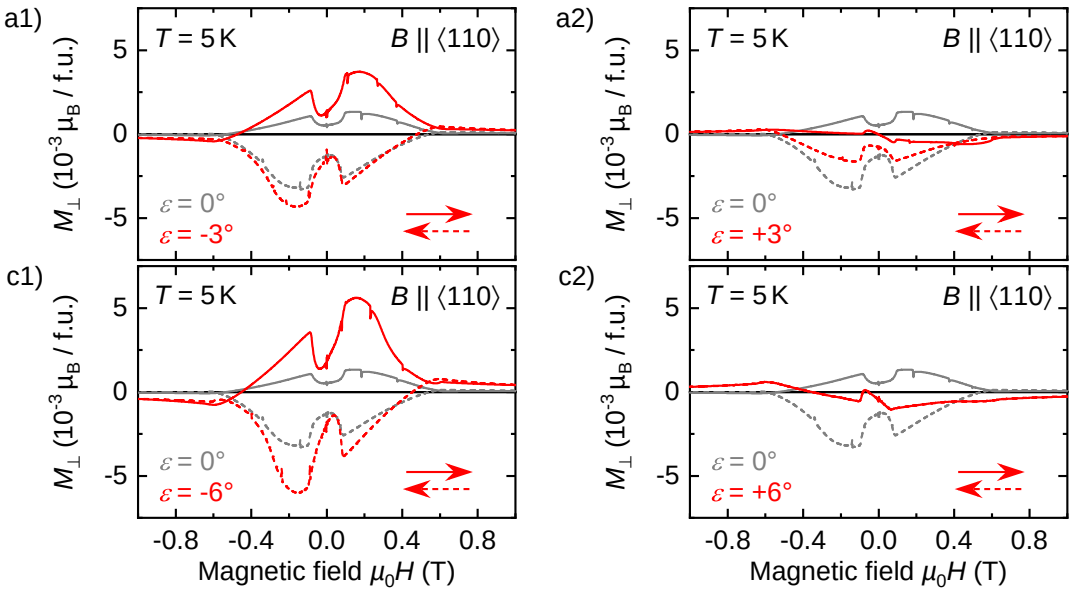

Figure D.7: Evolution of the anisotropic magnetization $M_\perp$ during field scans between $B = \pm 1\,\mathrm{T}$ at $T = 5\,\mathrm{K}$ and increasing deviation angles ε between field vector and the $\langle 110\rangle$-direction. Continuous lines denote increasing field, dashed lines denote decreasing field.

magnetization curves at $\varepsilon = 0°$ are included in all graphs as gray lines. Panels are ordered such that the deviation increases from top to bottom. Panels on the left hand side correspond to negative values of ε, panels on the right hand side show positive values of ε. We observe substantial differences in the magnetization already for deviations of $\varepsilon = \pm 1°$. This may be important for the interpretation of our data considering that the relative orientation of sample and field may change during field scans due to sample rotation caused by the investigated torque (cf. Sec. 5.2). The curves at $\varepsilon = +8°$ appear to be symmetric to those at $\varepsilon = -8°$ regarding a sign change of $M_\perp$. For both signs of ε, the large symmetric signal decreases towards the small asymmetric shape with decreasing deviation. Intriguingly, the sign change of the salient features in $M_\perp$ does not occur at $\varepsilon = 0°$ but rather around $\varepsilon = +2°$. Similar to the origin of the asymmetry at $\varepsilon = 0°$, we can not present an explanation of the observed behavior at this point.

As as described in Sec. 5.4.2, the observed asymmetry between increasing and decreasing field magnetization curves was even more pronounced for field along the $\langle 110\rangle$-direction than for field along $\langle 001\rangle$. We therefore also investigated the evolution of anisotropic magnetization with field vectors increasingly deviating from $\langle 110\rangle$. Again, we denote the deviation angle along the rotation plane by ε. The magnetization curves are depicted in Fig. D.7. Continuous and dashed lines correspond to increasing and decreasing field, respectively. The magnetization curves at $\varepsilon = 0°$ are included in all graphs as gray lines. Panels are ordered such that the deviation increases from top to bottom. Panels on the left hand side correspond to negative values of ε, panels on the right hand side show positive values of ε. At negative values of ε,

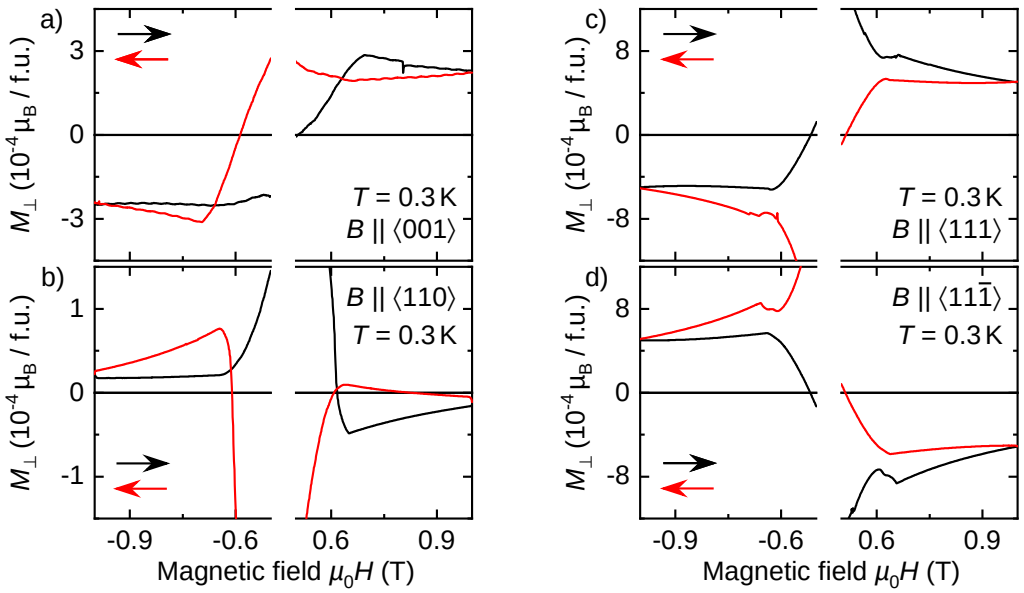

Figure D.8: Anisotropic magnetization $M_\perp$ during field scans between $B = \pm 1\,\mathrm{T}$ at $T = 0.3\,\mathrm{K}$ and field vectors pointing along a) ⟨001⟩-, b) ⟨110⟩-, c) ⟨111⟩-, and d) ⟨11$\bar{1}$⟩-directions. Black lines denote increasing field, red lines denote decreasing field.

we observe larger and more symmetric magnetization curves similar to the situation around ⟨001⟩. At positive values of ε, the magnetization curves of increasing and decreasing field coincide at $\varepsilon = +6°$. This may constitute a point of sign reversal similar to that described for $\varepsilon = +2°$ and the ⟨001⟩-direction.

D.2.3 Hysteresis above H_{c2}

In Sec. 5.4.2, we claim that we observe hysteretic behavior during field scans along all major symmetry directions for $|B| > \mu_0 H_{c2}$. To substantiate this statement, we present a blow-up of Fig. 5.14 of the main text to the high field regime in Fig. D.8. The magnetization curves at $T = 0.3\,\mathrm{K}$ and field vectors aligned along ⟨001⟩-, ⟨110⟩-, ⟨111⟩-, and ⟨11$\bar{1}$⟩-directions are depicted in panels a), b), c) and d), respectively. Black and red lines denote increasing and decreasing fields, respectively. Field hystereses at field magntiudes $|B| > \mu_0 H_{c2}$ are well recognizable in all graphs. In order to rule out technical issues connected to the setup or impurities of the sample as possible origins of this hysteresis, we present anisotropic magnetization data obtained with a different sample as well as in a different setup in the following. The evolution of field hysteresis in the field-polarized state in briefly addressed in Sec. D.2.5.
In Fig. D.9, we show magnetization curves obtained with the cubic MnSi sample in the rotating field setup. Continuous and dashed lines denote increasing and decreasing field, respectively, during field scans at $T = 1.5\,\mathrm{K}$ and a deviation angle ε of less than 2° between field vector and the ⟨001⟩-direction. Different colors correspond to different fields $\pm B_{\mathrm{max}}$ at which the sweep direction is reversed. We observe field hysteresis at $|B| > \mu_0 H_{c2}$ up to the highest field magnitudes studied, i.e. $B = \pm 3\,\mathrm{T}$.

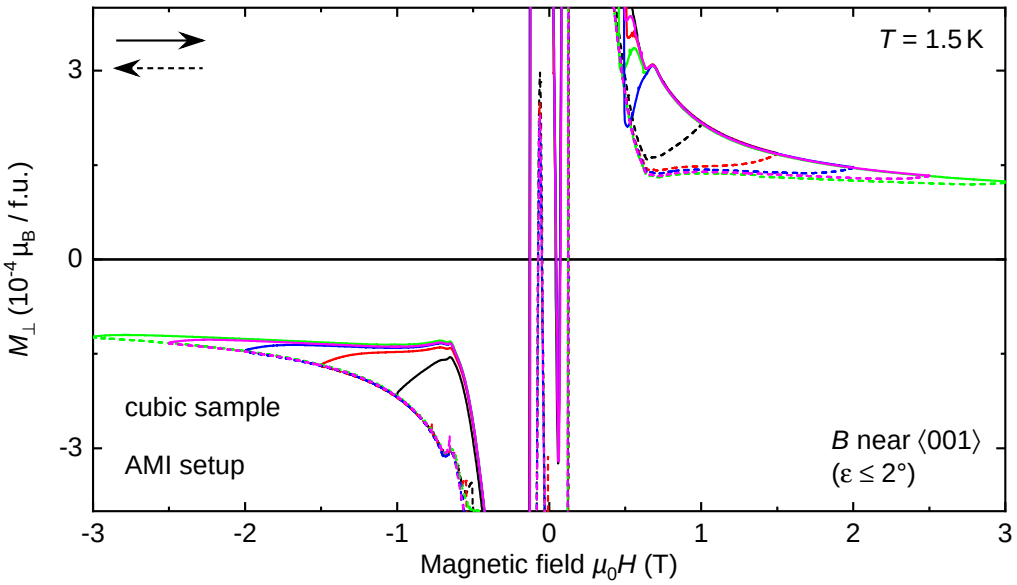

Figure D.9: Anisotropic magnetization $M_\perp$ during field scans measured on the cubic sample in the rotating field setup at $T = 1.5\,\mathrm{K}$ and field vector pointing less than 2° away from the ⟨001⟩-direction. Different colors correspond to different turning points B_{max}. Continuous lines denote increasing field, dashed lines denote decreasing field.

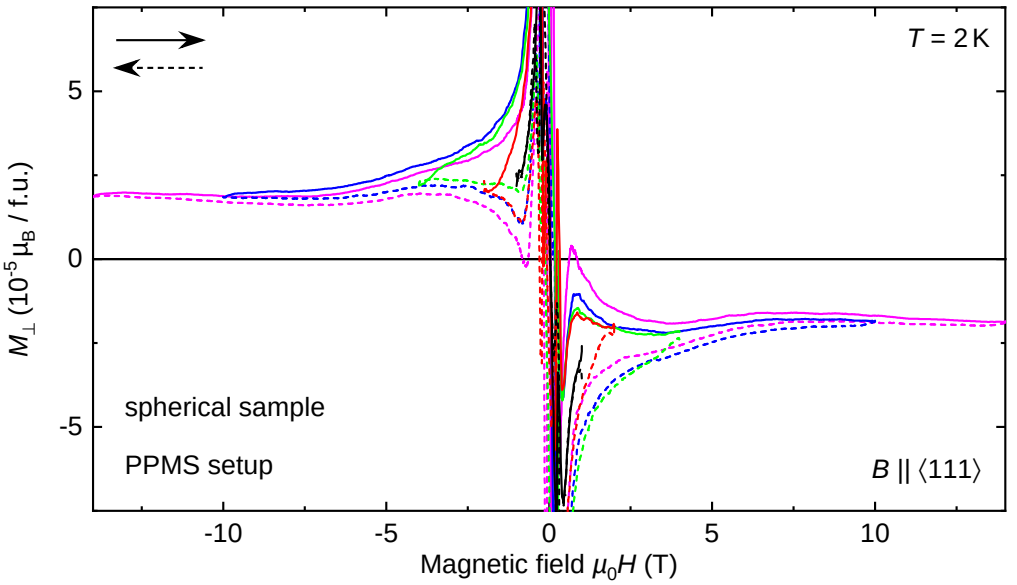

Figure D.10: Anisotropic magnetization $M_\perp$ during field scans measured on the spherical sample in the rotating sample setup at $T = 2\,\mathrm{K}$ and field vector along the ⟨111⟩-direction. Different colors correspond to different turning points B_{max}. Continuous lines denote increasing field, dashed lines denote decreasing field.

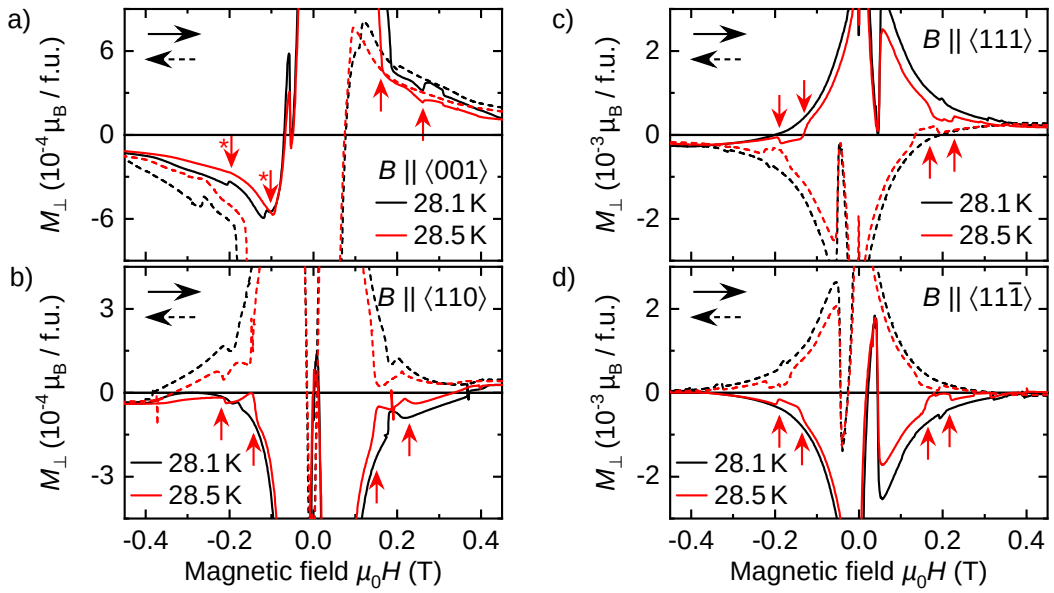

Figure D.11: Anisotropic magnetization $M_\perp$ during field scans between $B = \pm 1\,\mathrm{T}$ at temperatures of $T = 28.1\,\mathrm{K}$ (black) and $T = 28.5\,\mathrm{K}$ (red). Field is applied along the a) $\langle 001 \rangle$-, b) $\langle 110 \rangle$-, c) $\langle 111 \rangle$-, and d) $\langle 11\bar{1} \rangle$-directions. Continuous lines denote increasing field, dashed lines denote decreasing field. From left to right, the red arrows in each panel mark $H_{a2}^{\downarrow}$, $H_{a1}^{\downarrow}$, $H_{a1}^{\uparrow}$ and $H_{a2}^{\uparrow}$ of the increasing field curves at $T = 28.5\,\mathrm{K}$. The asterisks in panel a) highlight the ambiguity of the respective features.

In Fig. D.10, we show magnetization curves obtained with the spherical MnSi sample in the rotating sample setup. Continuous and dashed lines denote increasing and decreasing field, respectively, during field scans at $T = 2\,\mathrm{K}$ and a field vector applied along the $\langle 111 \rangle$-direction. Again, different colors correspond to different fields $\pm B_{\mathrm{max}}$ at which the sweep direction is reversed. We observe field hysteresis at $|B| > \mu_0 H_{c2}$ up to the highest field magnitudes studied, i.e. $B = \pm 14\,\mathrm{T}$. The consistent observation of field hysteresis in various measurement configurations rules out issues related to specific samples or setups and thus strongly indicates an origin connected to the magnetic properties of MnSi.

D.2.4 Field scans through the skyrmion lattice phase

In Sec. 5.4.2, we claim to observe signatures of the critical fields H_{a1} and H_{a2} at which MnSi undergoes a transition from the conical state to the skyrmion lattice phase and vice versa. In order to substantiate this statement, we present the respective anisotropic magnetization data in Fig. D.11. Black and red lines correspond to temperatures of $T = 28.1\,\mathrm{K}$ and $T = 28.5\,\mathrm{K}$, respectively. Continuous and dashed lines denote increasing and decreasing field, respectively. From a) to d), the graphs depict situations with field vectors applied along the $\langle 001 \rangle$-, $\langle 110 \rangle$-, $\langle 111 \rangle$-, and $\langle 11\bar{1} \rangle$-directions. Signatures of transitions between conical state and skyrmion lattice phase are marked by red arrows for the increasing field curve at $T = 28.5\,\mathrm{K}$. From

left to right, the arrows in each panel denote $H_{a2}^{\downarrow}$, $H_{a1}^{\downarrow}$, $H_{a1}^{\uparrow}$, and $H_{a2}^{\uparrow}$. As in the main text, the superscripts $\uparrow$ and $\downarrow$ denote increasing and decreasing field magnitude, respectively.
In general, the anisotropic magnetization is reduced within the skyrmion lattice phase as compared to the conical phase. This has already been observed in Ref. [Bir09] and was attributed to a low pinning of the skyrmion lattice to the atomic lattice of MnSi. For the $\langle 111 \rangle$- and $\langle 11\bar{1} \rangle$-directions, such a reduction is well perceptible at $T = 28.5\,\mathrm{K}$ for both increasing and decreasing field magnitude in both field sweep directions. In contrast, the curves at $T = 28.1\,\mathrm{K}$ exhibit no notable sign of a transition between conical and skyrmion lattice phase. We observe a hysteresis of critical fields which is small enough to be attributed to the superconducting magnet's hysteresis.
For field along the $\langle 110 \rangle$-direction, signatures at $T = 28.5\,\mathrm{K}$ are well visible for both field sweep directions and increasing as well as decreasing field magnitude. In addition, narrower minima are visible at $T = 28.1\,\mathrm{K}$, again, for both field sweep directions and increasing as well as decreasing field magnitude. This indicates that the skyrmion lattice phase is stabilized over a smaller field range as compared to $T = 28.5\,\mathrm{K}$ in consistence with the reported phase diagram [Bau12].
For field applied along $\langle 001 \rangle$, a distinct reduction of the anisotropic magnetization is found for increasing field magnitude at both temperatures and for both sweep directions. For decreasing field magnitude, no unambiguous signatures of the investigated phase transition are observed. The minimum and the slight kink marked by the red arrows and asterisks may correspond to the transition, but since the torque between these features is not notably reduced compared to its surrounding progression, we refrain from an association to the skyrmion lattice phase.

D.2.5 Temperature evolution for field along $\langle 001 \rangle$- and $\langle 110 \rangle$-directions

In Sec. 5.4.2, we present the evolution of the anisotropic magnetization during field scans with increasing temperature for field vectors applied along the $\langle 111 \rangle$- and $\langle 11\bar{1} \rangle$-directions. In this section, we provide additional temperature dependent data for field scans along the $\langle 001 \rangle$- and $\langle 110 \rangle$-directions.
The anisotropic magnetization during field scans for field along the $\langle 001 \rangle$-direction is shown in Fig. D.12 for temperatures from $T = 0.3\,\mathrm{K}$ up to $T = 33.3\,\mathrm{K}$. Continuous and dashed lines denote increasing and decreasing field, respectively. In Sec. 5.4.2, we stated that curves measured for increasing and decreasing field are point symmetric to each other except for minor quantitative differences. Since this observation is maintained for all investigated temperatures, we describe only the increasing field curves. The behavior at $T = 0.3\,\mathrm{K}$ has been described in detail in the main text. At slightly elevated temperatures, the minimum at negative values following the sharp maximum at $H_{c1}^{\uparrow}$ is lifted. At $T = 0.75\,\mathrm{K}$, the minimum resides at positive values, at $T = 2\,\mathrm{K}$, the curve does no longer exhibit a minimum between $H_{c1}^{\uparrow}$ and $H_{c2}^{\uparrow}$. Simultaneously, $M_{\perp}$ develops a plateau at small negative values between zero field and the beginning of the peak at $H_{c1}^{\uparrow}$. At temperatures from $T = 14.2\,\mathrm{K}$ upwards, this

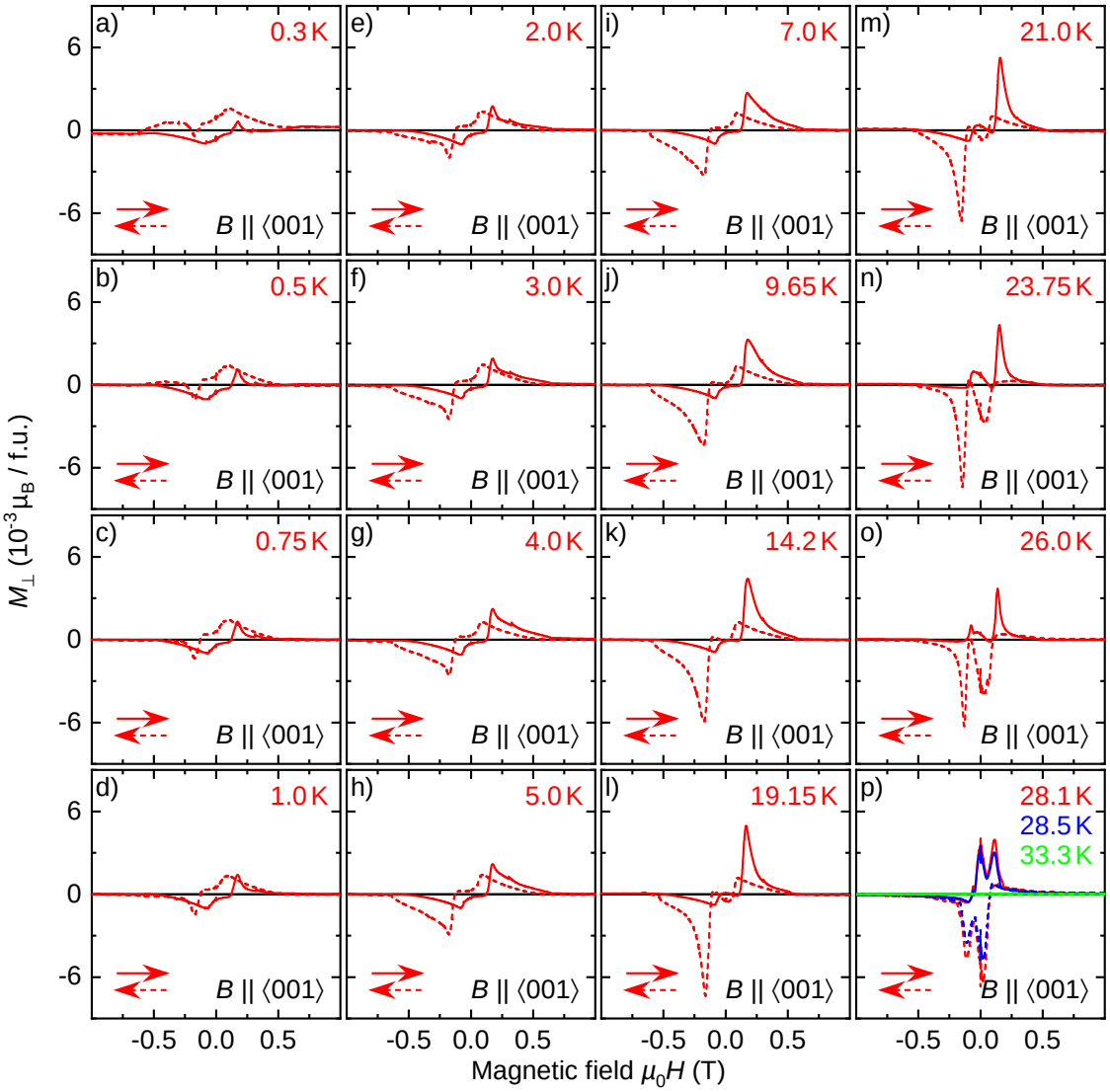

Figure D.12: Temperature evolution of the anisotropic magnetization $M_\perp$ during field scans between $B = \pm 1\,\mathrm{T}$ for field along $\langle 001 \rangle$ and temperatures from $T = 0.3\,\mathrm{K}$ up to $T = 33.3\,\mathrm{K}$. Continuous lines denote increasing field, dashed lines denote decreasing field.

plateau evolves into a pair of extrema comprising a maximum around $B = 0\,\mathrm{T}$ and a minimum right before the peak at $H_{c1}^{\uparrow}$. With the temperature further increasing, the maximum is lifted to larger positive values and becomes comparable to the peak at $H_{c1}^{\uparrow}$ at $T = 28.5\,\mathrm{K}$. The subsequent minimum remains at small negative values up to $T = 26\,\mathrm{K}$. At $T = 28.1\,\mathrm{K}$ and $T = 28.5\,\mathrm{K}$, the minimum is also lifted to larger positive values.
The peak at $H_{c1}^{\uparrow}$ steadily increases with rising temperature up to $T = 21\,\mathrm{K}$ from where it slightly decreases again up to $T = 28.5\,\mathrm{K}$. In contrast, the minimum at $-H_{c1}^{\downarrow}$ remains unaltered for most of the investigated temperature range. Only at $T = 23.75\,\mathrm{K}$ and $T = 26\,\mathrm{K}$, the minimum is strongly decreased to almost zero. At temperatures of $T = 28.1\,\mathrm{K}$ and $T = 28.5\,\mathrm{K}$, it is recovered with roughly half its size

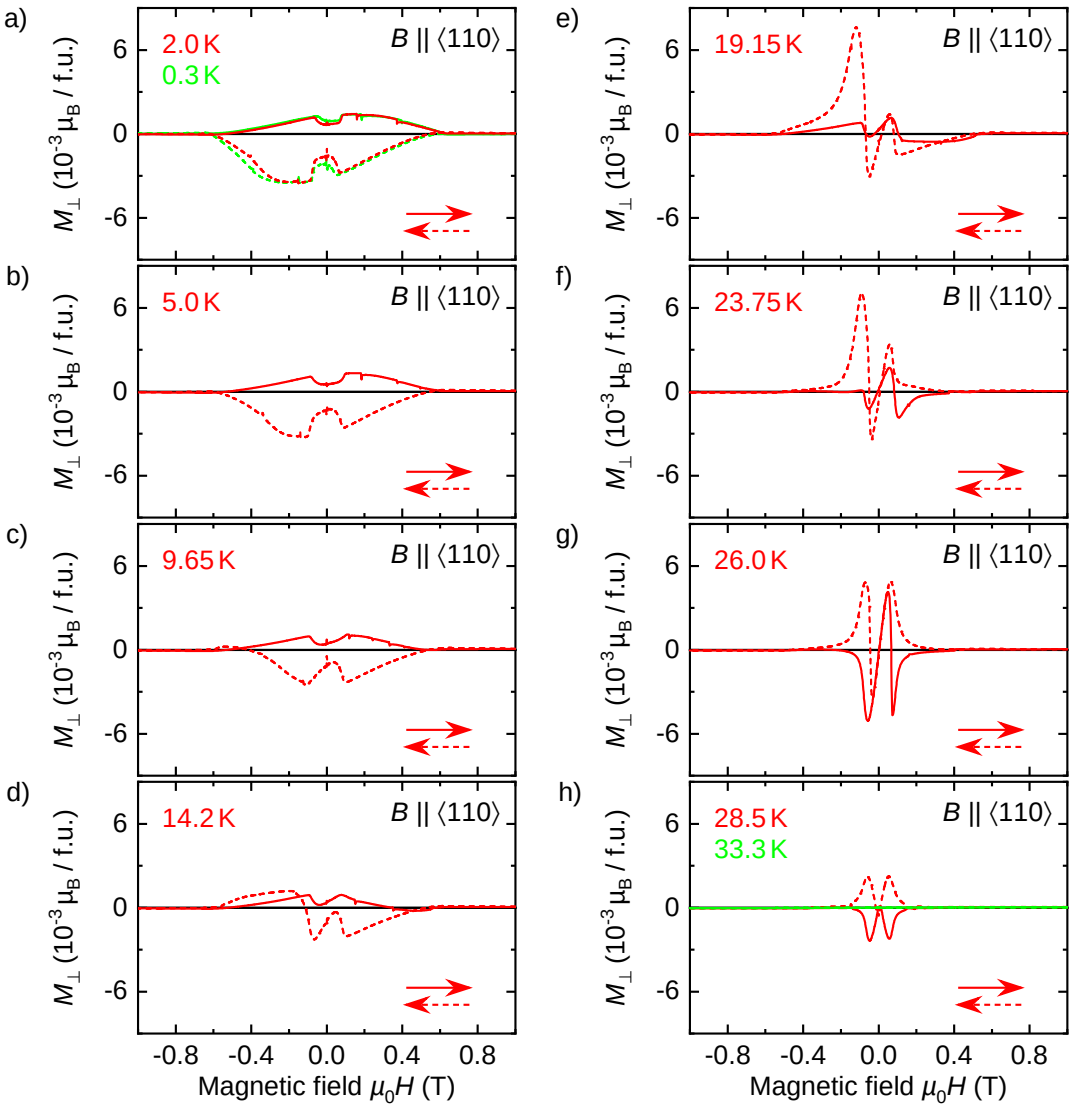

Figure D.13: Temperature evolution of the anisotropic magnetization $M_\perp$ during field scans between $B = \pm 1\,\mathrm{T}$ for field along $\langle 110 \rangle$ and temperatures from $T = 0.3\,\mathrm{K}$ up to $T = 33.3\,\mathrm{K}$. Continuous lines denote increasing field, dashed lines denote decreasing field.

at low temperatures. At $T = 33.3\,\mathrm{K}$, the anisotropic magnetization is zero on the scale shown in Fig. D.12. As stated in the main text, this behavior is expected due to the absence of long-range magnetic order in the paramagnetic state at $T > T_\mathrm{c}$. The anisotropic magnetization during field scans for field along the $\langle 110 \rangle$-direction is shown in Fig. D.13 for temperatures from $T = 0.3\,\mathrm{K}$ up to $T = 33.3\,\mathrm{K}$. Continuous and dashed lines denote increasing and decreasing field, respectively. In Sec. 5.4.2, we stated that curves measured for increasing and decreasing field are point symmetric to each other regarding only their qualitative behavior. This observation is maintained for most of the investigated temperatures. Therefore, we describe only the increasing field curves and address deviations of the decreasing field curve where appropriate. The behavior at $T = 0.3\,\mathrm{K}$ has been described in detail in the main text. For mildly

elevated temperatures of $T = 2\,\mathrm{K}$ and $T = 5\,\mathrm{K}$, the only qualitative difference is that the minimum at $H_{c2}^{\uparrow}$ resides at positive values. At $T = 9.65\,\mathrm{K}$, this evolution is reversed. At the same temperature, the almost constant behavior between the rapid decrease and increase at $-H_{c1}^{\downarrow}$ and $H_{c1}^{\uparrow}$, respectively, begins to evolve into a steady increase replacing the rapid increase at $H_{c1}^{\uparrow}$. With rising temperature, the minimum at $-H_{c1}^{\downarrow}$ is lowered reaching negative values at $T = 19.15\,\mathrm{K}$. At temperatures of $T = 23.75\,\mathrm{K}$ and above, the increase of the magnetization between $-H_{c2}^{\downarrow}$ and $-H_{c1}^{\uparrow}$ has vanished. The point of sign reversal and the minimum of $M_{\perp}$ close to $H_{c2}^{\uparrow}$ gradually shift towards $H_{c1}^{\uparrow}$ between $T = 9.65\,\mathrm{K}$ and $T = 19.15\,\mathrm{K}$. Simultaneously, the minimum is lowered. This results in a rapid decrease between the maximum at $H_{c1}^{\uparrow}$ and the subsequent minimum followed by a slower increase up to $H_{c2}^{\uparrow}$. Here, the quantitative differences between increasing and decreasing field curves are most pronounced in the form of the minimum (maximum) following $\pm H_{c1}^{\uparrow}$ for increasing (decreasing) field which is substantially larger for decreasing field. In a final step, the maximum at $H_{c1}^{\uparrow}$ is lowered to almost zero at $T = 28.1\,\mathrm{K}$. As for the other field directions, the magnetization is basically zero at $T = 33.3\,\mathrm{K} > T_c$.
It is interesting to note that, for field along $\langle 001 \rangle$, the magnetization curve between $B = \pm\mu_0 H_{c2}$ constantly resides at more positive values for decreasing field than for increasing field at low temperatures whereas the opposite situation applies to the high temperature limit. For field along $\langle 110 \rangle$, a similar turnaround is observed. Here, the increasing field curves reside at more positive values at low temperatures and at more negative values at high temperatures. A further pecularity is noted for $T = 26\,\mathrm{K}$ and field along the $\langle 110 \rangle$-direction. Here, the increasing and decreasing field curves coincide around zero field apparently resulting in two separate hysteresis loops at purely positive and purely negative fields.
In Sec. D.2.3, we showed hysteretic behavior for field magnitudes $|B| > \mu_0 H_{c2}$ during field scans at low temperatures. This phenomenon was observed for field vectors applied along all major symmetry directions and persisted up to the highest field magnitudes studied. In this work, we did not perform field scans to field magnitudes larger than 1 T at elevated temperatures. However, the data displayed in Figs. 5.15, D.12, and D.13 shows that the hysteresis in the field-polarized state gradually decays between $T = 9.65\,\mathrm{K}$ and $T = 23.75\,\mathrm{K}$. This roughly corresponds to the temperature range over which K_1 decays from its low temperature value to zero for field magnitudes $B \leq 1\,\mathrm{T}$.
We further highlighted hysteresis of critical fields at $B = 0.3\,\mathrm{K}$ and fields along $\langle 001 \rangle$ and $\langle 110 \rangle$ in Fig. 5.14 a) and b), respectively. This hysteresis quickly fades with increasing temperature. At $T \lesssim 5\,\mathrm{K}$, it is already small enough to be attributed to the magnet's hysteresis.

Bibliography

[Ada11] T. Adams, S. Mühlbauer, C. Pfleiderer, F. Jonietz, A. Bauer, A. Neubauer, R. Georgii, P. Böni, U. Keiderling, K. Everschor, M. Garst and A. Rosch: *Long-Range Crystalline Nature of the Skyrmion Lattice in MnSi*, Phys. Rev. Lett. **107**, 217206 (2011).

[Ada12] T. Adams, A. Chacon, M. Wagner, A. Bauer, G. Brandl, B. Pedersen, H. Berger, P. Lemmens and C. Pfleiderer: *Long-Wavelength Helimagnetic Order and Skyrmion Lattice Phase in* Cu_2OSeO_3, Phys. Rev. Lett. **108**, 237204 (2012).

[Ada18] T. Adams, M. Garst, A. Bauer, R. Georgii and C. Pfleiderer: *Response of the Skyrmion Lattice in MnSi to Cubic Magnetocrystalline Anisotropies*, Phys. Rev. Lett. **121**, 187205 (2018).

[Alb15] S. G. Albert: *Torque magnetometry on graphene and Fermi surface properties of* VB_2 *and* MnB_2 *single crystals studied by the de Haas-van Alphen effect*, Ph.D. thesis, Technische Universität München (2015).

[Ama36] E. Amaldi and E. Fermi: *On the Absorption and the Diffusion of Slow Neutrons*, Physical Review **50**, 899 (1936).

[Ard06] W. Arden: *Future Semiconductor Material Requirements and Innovations as Projected in the ITRS 2005 Roadmap*, Materials Science and Engineering: B **134**, 104 (2006).

[Avi03] M. A. Avila, S. L. Bud'ko, C. Petrovic, R. A. Ribeiro, P. C. Canfield, A. V. Tsvyashchenko and L. N. Fomicheva: *Synthesis and properties of* YbB_2, Journal of Alloys and Compounds **358**, 56 (2003).

[Bak80] P. Bak and M. H. Jensen: *Theory of Helical Magnetic Structures and Phase Transitions in MnSi and FeGe*, Journal of Physics C: Solid State Physics **13**, L881 (1980).

[Bar48] J. Bardeen and W. H. Brattain: *The Transistor, A Semi-Conductor Triode*, Phys. Rev. **74**, 230 (1948).

[Bar69] R. G. Barnes and R. B. Creel: *Chromium-like antiferromagnetic behavior of* CrB_2, Physics Letters A **29**, 203 (1969).

[Bau10] A. Bauer, A. Neubauer, C. Franz, W. Münzer, M. Garst and C. Pfleiderer: *Quantum phase transitions in single-crystal* $Mn_{1-x}Fe_xSi$ *and* $Mn_{1-x}Co_xSi$*: Crystal growth, magnetization, ac susceptibility, and specific heat*, Phys. Rev. B **82**, 064404 (2010).

[Bau12] A. Bauer and C. Pfleiderer: *Magnetic phase diagram of MnSi inferred from magnetization and ac susceptibility*, Phys. Rev. B **85**, 214418 (2012).

[Bau13] A. Bauer, M. Garst and C. Pfleiderer: *Specific Heat of the Skyrmion Lattice Phase and Field-Induced Tricritical Point in MnSi*, Phys. Rev. Lett. **110**, 177207 (2013).

[Bau14a] A. Bauer: *Investigation of itinerant antiferromagnets and cubic chiral helimagnets*, Ph.D. thesis, Technische Universität München (2014).

[Bau14b] A. Bauer, A. Regnat, C. G. F. Blum, S. Gottlieb-Schönmeyer, B. Pedersen, M. Meven, S. Wurmehl, J. Kuneš and C. Pfleiderer: *Low-temperature properties of single-crystal CrB_2*, Physical Review B **90**, 064414 (2014).

[Bau16a] A. Bauer, G. Benka, A. Regnat, C. Franz and C. Pfleiderer: *Ultra-High Vacuum Compatible Preparation Chain for Intermetallic Compounds*, Review of Scientific Instruments **87**, 113902 (2016).

[Bau16b] A. Bauer, A. Neubauer, W. Münzer, A. Regnat, G. Benka, M. Meven, B. Pedersen and C. Pfleiderer: *Ultra-High Vacuum Compatible Induction-Heated Rod Casting Furnace*, Review of Scientific Instruments **87**, 063909 (2016).

[Bau16c] A. Bauer and C. Pfleiderer: *Generic aspects of skyrmion lattices in chiral magnets*, in J. Seidel (ed.), *Topological Structures in Ferroic Materials: Domain Walls, Vortices and Skyrmions*, Springer International Publishing, 2016, 1–28.

[Bau17] A. Bauer, A. Chacon, M. Wagner, M. Halder, R. Georgii, A. Rosch, C. Pfleiderer and M. Garst: *Symmetry breaking, slow relaxation dynamics, and topological defects at the field-induced helix reorientation in MnSi*, Phys. Rev. B **95**, 024429 (2017).

[Ben06] L. Benito, J. I. Arnaudas and A. del Moral: *High-Sensitivity Vector Magnetometer for Measuring Magnetic Torque at Low Temperatures*, Review of Scientific Instruments **77**, 025101 (2006).

[Bir77] R. R. Birss, G. J. Keeler and C. H. Shepherd: *Temperature Dependence of the Magnetocrystalline Anisotropy Energy of Nickel in the (100) Plane*, Journal of Physics F: Metal Physics **7**, 1683 (1977).

[Bir09] F. Birkelbach: *Aufbau eines Drehmomentmagnetometers*, Zulassungsarbeit, Technische Universität München, 2009.

[Bog89] A. N. Bogdanov and D. A. Yablonskii: *Thermodynamically stable "vortices" in magnetically ordered crystals. The mixed state of magnets*, Soviet Physics JETP **68**, 101 (1989).

[Bog94] A. Bogdanov and A. Hubert: *Thermodynamically Stable Magnetic Vortex States in Magnetic Crystals*, Journal of Magnetism and Magnetic Materials **138**, 255 (1994).

[Boz51] R. M. Bozorth: *Ferromagnetism*, Van Nostrand, 1951.

[Bra13a] M. Brasse: *Magnetization of correlated electron systems: MnSi thin films, CrB2 single crystals and two-dimensional electron systems in MgZnO/ZnO*, Ph.D. thesis, Technische Universität München (2013).

[Bra13b] M. Brasse, L. Chioncel, J. Kuneš, A. Bauer, A. Regnat, C. G. F. Blum, S. Wurmehl, C. Pfleiderer, M. A. Wilde and D. Grundler: *de Haas–van Alphen effect and Fermi surface properties of single-crystal CrB_2*, Physical Review B **88**, 155138 (2013).

[Bru93] P. Bruno: *Physical origins and theoretical models of magnetic anisotropy*, in *Ferienkurse des Forschungszentrums Jülich*, chap. 24, FZ Jülich, 1993, 24.1–24.29.

[Buh13] S. Buhrandt and L. Fritz: *Skyrmion lattice phase in three-dimensional chiral magnets from Monte Carlo simulations*, Phys. Rev. B **88**, 195137 (2013).

[Bur77] J. Burd, M. Huq and E. Lee: *The Determination of Magnetic Anisotropy Constants from Torque Curves*, Journal of Magnetism and Magnetic Materials **5**, 135 (1977).

[Buz01] C. Buzea and T. Yamashita: *Review of the superconducting properties of MgB_2*, Superconductor Science and Technology **14**, R115 (2001).

[Cal60] E. Callen and H. Callen: *Anisotropic Magnetization*, Journal of Physics and Chemistry of Solids **16**, 310 (1960).

[Car58] W. J. Carr: *Temperature Dependence of Ferromagnetic Anisotropy*, Phys. Rev. **109**, 1971 (1958).

[Cha18] A. Chacon, L. Heinen, M. Halder, A. Bauer, W. Simeth, S. Mühlbauer, H. Berger, M. Garst, A. Rosch and C. Pfleiderer: *Observation of Two Independent Skyrmion Phases in a Chiral Magnetic Material*, Nature Physics **14**, 936 (2018).

[Che01] X. L. Chen, Q. Y. Tu, M. He, L. Dai and L. Wu: *The bond ionicity of MB_2 (M = Mg, Ti, V, Cr, Mn, Zr, Hf, Ta, Al and Y)*, Journal of Physics: Condensed Matter **13**, L723 (2001).

[Chi64] S. Chikazumi: *Physics of Magnetism*, Wiley, 1964.

[Cho75] A. Cho and J. Arthur: *Molecular Beam Epitaxy*, Progress in Solid State Chemistry **10**, 157 (1975).

[Coh61] M. H. Cohen and L. M. Falicov: *Magnetic Breakdown in Crystals*, Physical Review Letters **7**, 231 (1961).

[Con69] J. H. Condon and J. H. Wellendorf: *Torque measurements of magnetic properties of MnSi*, Bulletin of the American Physical Society **14**, 386 (1969).

[Dat90] S. Datta and B. Das: *Electronic Analog of the Electro-optic Modulator*, Applied Physics Letters **56**, 665 (1990).

[Din52a] R. B. Dingle: *Some Magnetic Properties of Metals. I. General Introduction, and Properties of Large Systems of Electrons*, Proceedings of the Royal Society of London. Series A, Mathematical and Physical Sciences **211**, 500 (1952).

[Din52b] R. B. Dingle: *Some Magnetic Properties of Metals. II. The Influence of Collisions on the Magnetic Behaviour of Large Systems*, Proceedings of the Royal Society of London. Series A, Mathematical and Physical Sciences **211**, 517 (1952).

[Dmi12] V. Dmitriev, D. Chernyshov, S. Grigoriev and V. Dyadkin: *A Chiral Link between Structure and Magnetism in MnSi*, Journal of Physics: Condensed Matter **24**, 366005 (2012).

[Duf00] D. Dufeu, E. Eyraud and P. Lethuillier: *An Efficient 8 T Extraction Vector Magnetometer with Sample Rotation for Routine Operation*, Review of Scientific Instruments **71**, 458 (2000).

[Dus16] A. Dussaux, P. Schoenherr, K. Koumpouras, J. Chico, K. Chang, L. Lorenzelli, N. Kanazawa, Y. Tokura, M. Garst, A. Bergman, C. L. Degen and D. Meier: *Local Dynamics of Topological Magnetic Defects in the Itinerant Helimagnet FeGe*, Nature Communications **7**, 12430 (2016).

[Dzy58] I. Dzyaloshinsky: *A Thermodynamic Theory of "Weak" Ferromagnetism of Antiferromagnetics*, Journal of Physics and Chemistry of Solids **4**, 241 (1958).

[Dzy64] I. E. Dzyaloshinskii: *Theory of Helicoidal Structures in Antiferromagnets. I. Nonmetals*, Soviet Physics JETP **19**, 960 (1964).

[Eis85a] J. P. Eisenstein: *High-precision torsional magnetometer: Application to two-dimensional electron systems*, Applied Physics Letters **46**, 695 (1985).

[Eis85b] J. P. Eisenstein, H. L. Störmer, V. Narayanamurti and A. C. Gossard: *High precision de Haas-van Alphen measurements on a two-dimensional electron gas*, Superlattices and Microstructures **1**, 11 (1985).

[Eve12] K. Everschor: *Current-Induced Dynamics of Chiral Magnetic Structures*, Ph.D. thesis, Universität Köln (2012).

[Fun77] S. Funahashi, Y. Hamaguchi, T. Tanaka and E. Bannai: *Helical magnetic structure in CrB_2*, Solid State Communications **23**, 859 (1977).

[Gar16] M. Garst: *Topological skyrmion dynamics in chiral magnets*, in J. Seidel (ed.), *Topological Structures in Ferroic Materials: Domain Walls, Vortices and Skyrmions*, Springer International Publishing, 2016, 29–53.

[Gib93] G. A. Gibson and S. Schultz: *Magnetic force microscope study of the micromagnetics of submicrometer magnetic particles*, Journal of Applied Physics **73**, 4516 (1993).

[Gol65] A. Goldstein, S. J. Williamson and S. Foner: *Low Frequency Field Modulation Differential Magnetometer; Applications to the De Haas-Van Alphen Effect*, Review of Scientific Instruments **36**, 1356 (1965).

[Gor75] W. Gordon and S. B. Soffer: *A galvanomagnetic investigation of TiB_2, NbB_2 and ZrB_2*, Journal of Physics and Chemistry of Solids **36**, 627 (1975).

[Gri73] R. Griessen: *A capacitance torquemeter for de Haas-van Alphen measurements*, Cryogenics **13**, 375 (1973).

[Gri10] S. V. Grigoriev, D. Chernyshov, V. A. Dyadkin, V. Dmitriev, E. V. Moskvin, D. Lamago, T. Wolf, D. Menzel, J. Schoenes, S. V. Maleyev and H. Eckerlebe: *Interplay between crystalline chirality and magnetic structure in* $Mn_{1-x}Fe_xSi$, Phys. Rev. B **81**, 012408 (2010).

[Gro12] R. Gross and A. Marx: *Festkörperphysik*, Oldenbourg Verlag, 2012.

[Haa30] W. J. de Haas and P. M. van Alphen: *The dependence of the susceptibility of diamagnetic metals upon the field*, Proc. Netherlands Roy. Acad. Sci. **33**, 1106 (1930).

[Haa84] T. Haavasoja, H. L. Störmer, D. J. Bishop, V. Narayanamurti, A. C. Gossard and W. Wiegmann: *Magnetization measurements on a two-dimensional electron system*, Surface Science **142**, 294 (1984).

[Hal18] M. Halder, A. Chacon, A. Bauer, W. Simeth, S. Mühlbauer, H. Berger, L. Heinen, M. Garst, A. Rosch and C. Pfleiderer: *Thermodynamic evidence of a second skyrmion lattice phase and tilted conical phase in* Cu_2OSeO_3, Phys. Rev. B **98**, 144429 (2018).

[Her15] F. Herzog: *Spin-orbit interaction and confinement effects in low-dimensional electron systems studied by torque magnetometry and anisotropic magnetotransport*, Ph.D. thesis, Technische Universität München (2015).

[Hoh64] P. Hohenberg and W. Kohn: *Inhomogeneous Electron Gas*, Phys. Rev. **136**, B864 (1964).

[Hub98] A. Hubert and R. Schäfer: *Magnetic Domains*, Springer Berlin Heidelberg, 1998.

[Hui17] Huiming Bu: *5 Nanometer Transistors Inching Their Way into Chips*, IBM Research Blog, https://www.ibm.com/blogs/think/2017/06/5-nanometer-transistors, 2017.

[Ish76] Y. Ishikawa, K. Tajima, D. Bloch and M. Roth: *Helical Spin Structure in Manganese Silicide MnSi*, Solid State Communications **19**, 525 (1976).

[Jan08] M. Janoschek: *Investigation of the chiral magnets* $NdFe_3(^11BO_3)_4$ *and MnSi by means of neutron scattering*, Ph.D. thesis, Technische Universität München (2008).

[Joh96] M. T. Johnson, P. J. H. Bloemen, F. J. A. den Broeder and J. J. de Vries: *Magnetic Anisotropy in Metallic Multilayers*, Reports on Progress in Physics **59**, 1409 (1996).

[Kai94] G. Kaiser: *A Friendly Guide to Wavelets*, Birkhäuser, 1994.

[Kan63] J. Kanamori: *4 – anisotropy and magnetostriction of ferromagnetic and antiferromagnetic materials*, in *Magnetism: A treatise on Modern Theory and Materials*, 1963, 127–203.

[Kar12] E. A. Karhu, U. K. Rößler, A. N. Bogdanov, S. Kahwaji, B. J. Kirby, H. Fritzsche, M. D. Robertson, C. F. Majkrzak and T. L. Monchesky: *Chiral modulations and reorientation effects in MnSi thin films*, Phys. Rev. B **85**, 094429 (2012).

[Kar16] K. Karube, J. S. White, N. Reynolds, J. L. Gavilano, H. Oike, A. Kikkawa, F. Kagawa, Y. Tokunaga, H. M. Rønnow, Y. Tokura and Y. Taguchi: *Robust Metastable Skyrmions and Their Triangular–Square Lattice Structural Transition in a High-Temperature Chiral Magnet*, Nature Materials **15**, 1237 (2016).

[Kas70] M. Kasaya and T. Hihara: *Magnetic Structure of MnB_2*, Journal of the Physical Society of Japan **29**, 336 (1970).

[Kay09] E. Kaya, Y. Kousaka, K. Kakurai, M. Takeda and J. Akimitsu: *Spherical neutron polarimetry studies on the magnetic structure of single crystal $Cr_{1-x}Mo_xB_2$ (x=0, 0.15)*, Physica B: Condensed Matter **404**, 2524 (2009).

[Kef55] F. Keffer: *Temperature Dependence of Ferromagnetic Anisotropy in Cubic Crystals*, Phys. Rev. **100**, 1692 (1955).

[Key01] R. W. Keyes: *Fundamental limits of silicon technology*, Proceedings of the IEEE **89**, 227 (2001).

[Kit78] Y. Kitaoka, H. Yasuoka, T. Tanaka and Y. Ishizawa: *Nuclear magnetic resonance of ^{1}1B in CrB_2*, Solid State Communications **26**, 87 (1978).

[Kit80] Y. Kitaoka and H. Yasuoka: *NMR Investigations on the Spin Fluctuations in Itinerant Antiferromagnets III. CrB_2*, Journal of the Physical Society of Japan **49**, 493 (1980).

[Kli80] K. v. Klitzing, G. Dorda and M. Pepper: *New Method for High-Accuracy Determination of the Fine-Structure Constant Based on Quantized Hall Resistance*, Phys. Rev. Lett. **45**, 494 (1980).

[Kny76] E. A. Knyshev, V. M. Novgorodtsev, U. S. Plyshevski, V. A. Kobyakov, Z. G. Stepanova, V. V. Svistunov and A. R. Becketov: *Synthesis of transition metal borides and their properties*, Journal of the Less Common Metals **47**, 273 (1976).

[Kob16] N. Kobayashi, K. Hyodo and A. Sakuma: *Effects of Spin Fluctuation on the Magnetic Anisotropy Constant of Itinerant Electron Magnets*, Japanese Journal of Applied Physics **55**, 100306 (2016).

[Koh65] W. Kohn and L. J. Sham: *Self-Consistent Equations Including Exchange and Correlation Effects*, Phys. Rev. **140**, A1133 (1965).

[Kon74] E. Kondorsky: *A review of the theory of magnetic anisotropy in Ni*, IEEE Transactions on Magnetics **10**, 132 (1974).

[Lam06] D. Lamago, R. Georgii, C. Pfleiderer and P. Böni: *Magnetic-Field Induced Instability Surrounding the A-Phase of MnSi: Bulk and SANS Measurements*, Physica B: Condensed Matter **385-386**, 385 (2006).

[Leb89] B. Lebech, J. Bernhard and T. Freltoft: *Magnetic Structures of Cubic FeGe Studied by Small-Angle Neutron Scattering*, Journal of Physics: Condensed Matter **1**, 6105 (1989).

[Leb95] B. Lebech, P. Harris, J. S. Pedersen], K. Mortensen, C. Gregory, N. Bernhoeft, M. Jermy and S. Brown: *Magnetic Phase Diagram of MnSi*, Journal of Magnetism and Magnetic Materials **140-144**, 119 (1995).

[Li12] F. Li, T. Nattermann and V. L. Pokrovsky: *Vortex Domain Walls in Helical Magnets*, Phys. Rev. Lett. **108**, 107203 (2012).

[Lif54] I. M. Lifshitz and A. M. Kosevich: *On the theory of the de Haas-van Alphen effect for particles with an arbitrary dispersion law*, Doklady Akademii Nauk **96**, 963 (1954).

[Lif55] I. M. Lifshitz and A. M. Kosevich: *Theory of Magnetic Susceptibility in Metals at Low Temperatures*, Zh. eksp. teor. fiz. **29**, 730 (1955).

[Liu75] S. H. Liu, L. Kopp, W. B. England and H. W. Myron: *Energy bands, electronic properties, and magnetic ordering of* CrB_2, Physical Review B **11**, 3463 (1975).

[Lom76] N. R. Lomb: *Least-Squares Frequency Analysis of Unequally Spaced Data*, Astrophysics and Space Science **39**, 447 (1976).

[Lup99] C. Lupien, B. Ellman, P. Grütter and L. Taillefer: *Piezoresistive torque magnetometry below 1 K*, Applied Physics Letters **74**, 451 (1999).

[Mü09] S. Mühlbauer, B. Binz, F. Jonietz, C. Pfleiderer, A. Rosch, A. Neubauer, R. Georgii and P. Böni: *Skyrmion Lattice in a Chiral Magnet*, Science **323**, 915 (2009).

[Man00] Manual: *Physical Property Measurement System Hardware Manual*, Quantum Design, 2000.

[Man16] Manual: *Horizontal Rotator Option Users's Manual*, Quantum Design, 2016.

[Man17] Manual: *Torque Magnetometer Option Users's Manual*, Quantum Design, 2017.

[Mar04] R. M. Martin: *Electronic Structure: Basic Theory and Practical Methods*, Cambridge University Press, 2004.

[Mat85] K. Matsuzawa, T. Ukai, S. Ohtsuka and N. Mori: *Anisotropy Energy for the Ordered* Ni_3Al *Crystal*, Journal of Applied Physics **57**, 3238 (1985).

[Mat04] A. J. Matthews, A. Usher and C. D. H. Williams: *A low-temperature high-sensitivity torsion balance magnetometer with in situ stator adjustment*, Review of Scientific Instruments **75**, 2672 (2004).

[Mer59] K. Merkle: *Ueber die ferromagnetische Anisotropie und ihre quantentheoretische Behandlung durch ein Einelektronenmodell*, Z. Naturforschg. **14 a**, 938 (1959).

[Mic07] C. Michioka, Y. Itoh, K. Yoshimura, Y. Watabe, Y. Kousaka, H. Ichikawa and J. Akimitsu: *NMR studies of single crystal chromium diboride*, Journal of Magnetism and Magnetic Materials **310**, e620 , proceedings of the 17th International Conference on Magnetism (2007).

[Mit97] A. I. Mitsek and V. A. Mitsek: *Ni Magnetic Anisotropy Model*, physica status solidi (b) **199**, 549 (1997).

[Moo65] G. E. Moore: *Cramming more components onto integrated circuits*, Electronics **38**, 114 (1965).

[Mor60] T. Moriya: *Anisotropic Superexchange Interaction and Weak Ferromagnetism*, Phys. Rev. **120**, 91 (1960).

[Mor69] N. Mori: *Calculation of Ferromagnetic Anisotropy Energies for Ni and Fe Metals*, Journal of the Physical Society of Japan **27**, 307 (1969).

[Mor74] N. Mori, Y. Fukuda and T. Ukai: *Ferromagnetic Anisotropy Energies of Ni and Fe Metals –Band Model–*, Journal of the Physical Society of Japan **37**, 1263 (1974).

[Mor85] T. Moriya: *Spin Fluctuations in Itinerant Electron Magnetism*, vol. 56, Springer Berlin Heidelberg, 1985.

[Mor09] T. Mori, T. Takimoto, A. Leithe-Jasper, R. Cardoso-Gil, W. Schnelle, G. Auffermann, H. Rosner and Y. Grin: *Ferromagnetism and electronic structure of TmB_2*, Physical Review B **79**, 104418 (2009).

[Nag01] J. Nagamatsu, N. Nakagawa, T. Muranaka, Y. Zenitani and J. Akimitsu: *Superconductivity at 39 K in magnesium diboride*, Nature **410**, 63 (2001).

[Nak17] T. Nakajima, H. Oike, A. Kikkawa, E. P. Gilbert, N. Booth, K. Kakurai, Y. Taguchi, Y. Tokura, F. Kagawa and T.-h. Arima: *Skyrmion Lattice Structural Transition in MnSi*, Science Advances **3**, e1602562 (2017).

[Neu11] A. Neubauer, J. Bœuf, A. Bauer, B. Russ, H. v. Löhneysen and C. Pfleiderer: *Ultra-High Vacuum Compatible Image Furnace*, Review of Scientific Instruments **82**, 013902 (2011).

[Nov07] V. V. Novikov and A. V. Matovnikov: *Low-temperature heat capacity of dysprosium diboride*, Journal of Thermal Analysis and Calorimetry **88**, 597 (2007).

[Ono77] F. Ono: *Temperature and Magnetization Dependences of the Magneto-Crystalline Anisotropy Energy of Ni*, Journal of the Physical Society of Japan **43**, 1194 (1977).

[Ons52] L. Onsager: *Interpretation of the de Haas-van Alphen effect*, The London, Edinburgh, and Dublin Philosophical Magazine and Journal of Science **43**, 1006 (1952).

[Ort12] L. Ortenzi, I. I. Mazin, P. Blaha and L. Boeri: *Accounting for spin fluctuations beyond local spin density approximation in the density functional theory*, Physical Review B **86**, 064437 (2012).

[Par08] S. S. P. Parkin, M. Hayashi and L. Thomas: *Magnetic Domain-Wall Racetrack Memory*, Science **320**, 190 (2008).

[Per92] J. P. Perdew and Y. Wang: *Accurate and simple analytic representation of the electron-gas correlation energy*, Physical Review B **45**, 13244 (1992).

[Pfl97] C. Pfleiderer, G. J. McMullan, S. R. Julian and G. G. Lonzarich: *Magnetic quantum phase transition in MnSi under hydrostatic pressure*, Phys. Rev. B **55**, 8330 (1997).

[Pri66] M. G. Priestley: *Pulsed-Field de Haas-van Alphen Effect in Thallium*, Physical Review **148**, 580 (1966).

[Qiu00] Z. Q. Qiu and S. D. Bader: *Surface Magneto-Optic Kerr Effect*, Review of Scientific Instruments **71**, 1243 (2000).

[Rah11] M. Rahman: *Applications of Fourier Transforms to Generalized Functions*, WIT Press, 2011.

[Reg19] A. Regnat: *Low-temperature properties and magnetic structure of CrB_2, MnB_2, and CuMnSb*, Ph.D. thesis, Technische Universität München (2019).

[Rei16] M. Reiner, A. Bauer, M. Leitner, T. Gigl, W. Anwand, M. Butterling, A. Wagner, P. Kudejova, C. Pfleiderer and C. Hugenschmidt: *Positron Spectroscopy of Point Defects in the Skyrmion-Lattice Compound MnSi*, Scientific Reports **6**, 29109 (2016).

[Rou12] P. M. C. Rourke and S. R. Julian: *Numerical extraction of de Haas–van Alphen frequencies from calculated band energies*, Computer Physics Communications **183**, 324 (2012).

[San91] L. M. Sandratskii: *Symmetry analysis of electronic states for crystals with spiral magnetic order. I. General properties*, Journal of Physics: Condensed Matter **3**, 8565 (1991).

[Sca82] J. D. Scargle: *Studies in astronomical time series analysis. II. Statistical aspects of spectral analysis of unevenly spaced data.*, The Astrophysical Journal **263**, 835 (1982).

[Sch00] M. P. Schwarz, D. Grundler, I. Meinel, C. Heyn and D. Heitmann: *Micromechanical cantilever magnetometer with an integrated two-dimensional electron system*, Applied Physics Letters **76**, 3564 (2000).

[Sch07] E. Schrüfer: *Elektrische Messtechnik*, Hanser, 2007.

[Sch12] T. Schulz, R. Ritz, A. Bauer, M. Halder, M. Wagner, C. Franz, C. Pfleiderer, K. Everschor, M. Garst and A. Rosch: *Emergent Electrodynamics of Skyrmions in a Chiral Magnet*, Nature Physics **8**, 301 (2012).

[Sch15] T. Schwarze, J. Waizner, M. Garst, A. Bauer, I. Stasinopoulos, H. Berger, C. Pfleiderer and D. Grundler: *Universal Helimagnon and Skyrmion Excitations in Metallic, Semiconducting and Insulating Chiral Magnets*, Nature Materials **14**, 478 (2015).

[Sho64] D. Shoenberg and P. J. Stiles: *The de Haas-Van Alphen Effect in Alkali Metals*, Proceedings of the Royal Society A: Mathematical, Physical and Engineering Sciences **281**, 62 (1964).

[Sho84] D. Shoenberg: *Magnetic oscillations in metals*, Cambridge University Press, 1984.

[Sho09] Sholl, D. S. and Steckel, J. A.: *What is density functional theory?*, in *Density Functional Theory*, John Wiley & Sons, Ltd, 2009, 1–33.

[Sig82] T. I. Sigfusson and G. G. Lonzarich: *Magnetocrystalline Anisotropy in the Weak Itinerant Ferromagnet Ni_3Al*, Physica Scripta **25**, 720 (1982).

[Sko08] R. Skomski: *Simple models of magnetism*, Oxford University Press, 2008.

[Smi10] J. O. Smith: *Mathematics of the Discrete Fourier Transform (DFT): With Audio Applications*, BookSurge, 2010.

[Spr06] J. I. Springborn, N. Ruhe, C. Heyn, M. A. Wilde, D. Heitmann and D. Grundler: *Gate-controlled de Haas-van Alphen effect in an interacting two-dimensional electron system*, Physica E: Low-dimensional Systems and Nanostructures **34**, 172 (2006).

[Sta68] R. W. Stark and L. R. Windmiller: *Theory and technology for measuring the de haas-van alphen type spectra in metal*, Cryogenics **8**, 272 (1968).

[Sta17] I. Stasinopoulos, S. Weichselbaumer, A. Bauer, J. Waizner, H. Berger, S. Maendl, M. Garst, C. Pfleiderer and D. Grundler: *Low Spin Wave Damping in the Insulating Chiral Magnet Cu_2OSeO_3*, Applied Physics Letters **111**, 032408 (2017).

[Szp84] B. Szpunar: *The Temperature Dependence of the Anisotropy Constants for Nickel*, Physics Letters A **102**, 63 (1984).

[Tat65] E. Tatsumoto, T. Okamoto, N. Iwata and Y. Kadena: *Temperature Dependence of the Magnetocrystalline Anisotropy Constants K_1 and K_2 of Nickel*, Journal of the Physical Society of Japan **20**, 1541 (1965).

[Tem88] I. M. Templeton: *A high-sensitivity torsional magnetometer for two-dimensional electron systems*, Journal of Applied Physics **64**, 3570 (1988).

[Vaj01] P. Vajeeston, P. Ravindran, C. Ravi and R. Asokamani1: *Electronic structure, bonding, and ground-state properties of AlB_2-type transition-metal diborides*, Physical Review B **63**, 045115 (2001).

[Van18] J. T. VanderPlas: *Understanding the Lomb–Scargle Periodogram*, The Astrophysical Journal Supplement Series **236**, 16 (2018).

[Vle37] J. H. van Vleck: *On the Anisotropy of Cubic Ferromagnetic Crystals*, Phys. Rev. **52**, 1178 (1937).

[Was96] A. Wasserman and M. Springford: *The influence of many-body interactions on the de Haas-van Alphen effect*, Advances in Physics **45**, 471 (1996).

[Web16] Website: *High Field Magnet Laboratory*, Radboud University Nijmegen, https //www.ru.nl/hfml, 2016.

[Wel67] P. Welch: *The Use of Fast Fourier Transform for the Estimation of Power Spectra: A Method Based on Time Averaging over Short, Modified Periodograms*, IEEE Transactions on Audio and Electroacoustics **15**, 70 (1967).

[Wie98] S. A. J. Wiegers, A. S. van Steenbergen, M. E. Jeuken, M. Bravin, P. E. Wolf, G. Remenyi, J. A. A. J. Perenboom and J. C. Maan: *A sensitive and versatile torque magnetometer for use in high magnetic fields*, Review of Scientific Instruments **69**, 2369 (1998).

[Wil98] M. Willemin, C. Rossel, J. Brugger, M. H. Despont, H. Rothuizen, P. Vettiger, J. Hofer and H. Keller: *Piezoresistive cantilever designed for torque magnetometry*, Journal of Applied Physics **83**, 1163 (1998).

[Wil04] M. A. Wilde: *Magnetization measurements on low-dimensional electron systems in high-mobility GaAs and SiGe heterostructures*, Ph.D. thesis, Universität Hamburg (2004).

[Wil20a] M. A. Wilde: priv. comm. (2020).

[Wil20b] M. A. Wilde, M. Dodenhöft, A. Niedermayr, A. Bauer, M. M. Hirschmann, K. Alpin, A. P. Schnyder and C. Pfleiderer: *Magnetic-Field-controlled topological protectorates of the Fermi surface in MnSi*, unpublished (2020).

[Win66] L. R. Windmiller: *de Haas-van Alphen Effect and Fermi Surface in Antimony*, Physical Review **149**, 472 (1966).

[Win68] L. R. Windmiller and J. B. Ketterson: *Techniques and Instrumentation for Measuring the de Haas-van Alphen Effect in Metals*, Review of Scientific Instruments **39**, 1672 (1968).

[Xi08] X. X. Xi: *Two-Band Superconductor Magnesium Diboride*, Reports on Progress in Physics **71**, 116501 (2008).

[Zen54] C. Zener: *Classical Theory of the Temperature Dependence of Magnetic Anisotropy Energy*, Phys. Rev. **96**, 1335 (1954).

Acknowledgments

I would like to express my gratitude to all the people who contributed to this work and who supported me during my time as a PhD student. In particular, I want to thank

- Dr. Marc A. Wilde for his overall guidance, his friendly attitude and the genuine discussion of countless question, no matter how small,
- Prof. Dr. Christian Pfleiderer for admitting me into his group, his sincere sympathy and his relentless optimism,
- Prof. Dr. Rudi Hackl for immediately stepping in as my mentor and examiner when needed,
- Dr. Andreas Bauer for providing CrB_2 and MnSi samples as well as for many quick answers and fruitful discussions,
- Prof. Dr. Dirk Grundler for the opportunity to begin my studies at E10 and for introducing me to the world of academic research,
- Prof. Dr. Markus Garst for helpful discussions regarding anisotropy in helimagnets in general and the implementation of numerical simulation in particular,
- Dr. Olga Young and Prof. Dr. Uli Zeitler for their unlimited commitment to supporting our measurements at HFML,
- Alexander Regnat, Marco Halder, Matthias Dodenhöft and Arthur Niedermayr for their help with performing and understanding measurements and calculations on CrB_2,
- Vivek Kumar, Georg Benka and Michelle Hollricher for their assistance concerning the PPMS,
- Susanne Mayr and her coworkers at the physics department's crystal laboratory for patient assistance with sample orientation,
- Manfred Pfaller, Manfred Reither and their coworkers at the physics department's central workshop,
- my former colleagues at E10: Matthias Brasse, Stephan Albert, Florian Herzog and Stefanos Chalkidis, my cantilever co-workers, as well as Thomas Schwarze, Florian Brandl, Florian Heimbach, Ioannis Stasinopoulos, Stefan Mändl, Haiming Yu and Vinayak Bhat,

- all postdocs, doctoral, master, bachelor and working students at E21 and E51 including but not limited to Christoph Hugenschmidt, Astrid Schneidewind, Grace Causer, Dennis Mettus, Alfonso Chacon, Christoper Duvinage, Steffen Säubert, Felix Rucker, Marc Seifert, Tobias Simmeth, Alexander Engelhardt, Franz Haslbeck, Pau Jorba, Markus Kleinhans, Christian Oberleitner, Tomek Schulz, Jan Spallek, Anh Tong, Andreas Wendl, Jonas Kindervater, Christoph Schnarr, Alexander Book, Henrik Gabold, Josef Ketels, Ran Tang, Jingfan Ye, Carolina Burger, Nico Huber, Michael Lampl, Christoph Resch, Laura Stapf, Leonie Spitz, Lukas Vogl, Lukas Worch and André Deyerling

- organizational and technical staff at both chairs: Claudine Voelcker, Thomas Rapp, Thomas Neukel, Johannes Seitz, Stephan Lichtenauer and Herbert Hetzl at E10 as well as Lisa Seitz, Martina Meven, Astrid Mühlberg, Martina Michel and Stefan Giemsa at E21/E51,

- Markus Wiesinger and Peter Weiser for sharing the burden of the wire bonder, as well as Fabian Klemm and many other members of the TUM Graduate Council for their moral support.

- Finally, I want to thank my parents for their unlimited support at all times and for being a safe haven whenever needed.

This research has received funding from the Transregio program TRR 80: "From Electronic Correlations to Functionality" of the Deutsche Forschungsgemeinschaft, the German Excellence Initiative via Nanosystems Initiative Munich (NIM), and from the ERC Advanced Grant 788031: "Extreme Quantum Matter in Solids" which is gratefully acknowledged.